DEPARTMENT OF PHYSICS
INDIAN INSTITUTE OF TECHNOLOGY MADRAS
CHENNAI 600036

OBSERVATIONAL IMPRINTS OF NON-TRIVIAL INFLATIONARY DYNAMICS OVER LARGE AND SMALL SCALES

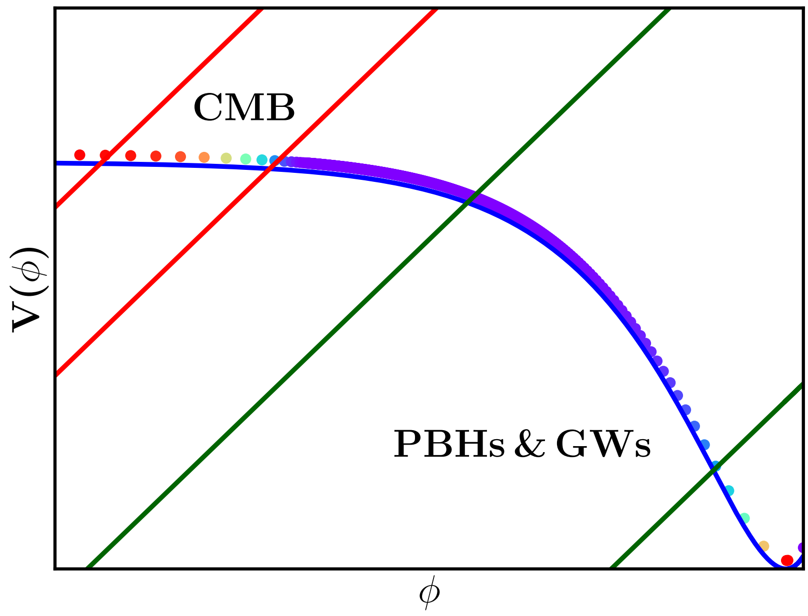

A thesis

Submitted by

H. V. RAGAVENDRA

For the award of the degree

of

DOCTOR OF PHILOSOPHY

January 2022

DEPARTMENT OF PHYSICS
INDIAN INSTITUTE OF TECHNOLOGY MADRAS
CHENNAI 600036

OBSERVATIONAL IMPRINTS OF NON-TRIVIAL INFLATIONARY DYNAMICS OVER LARGE AND SMALL SCALES

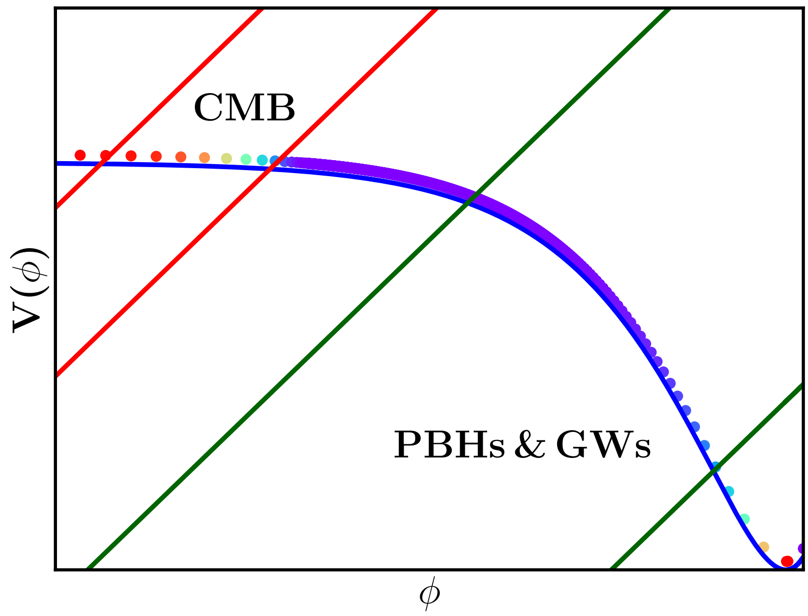

A thesis

Submitted by

H. V. RAGAVENDRA

For the award of the degree

of

DOCTOR OF PHILOSOPHY

January 2022

தெய்வத்தால் ஆகா தெனினும்
श्रमेण सर्वं साध्यम्

<u>THESIS CERTIFICATE</u>

This is to undertake that the thesis titled *Observational imprints of non-trivial inflationary dynamics over large and small scales* submitted by me to the Indian Institute of Technology Madras, for the award of Ph.D. is a bonafide record of the research work done by me under the supervision of Prof. L. Sriramkumar. The contents of this thesis, in full or in parts, have not been submitted to any other Institute or University for the award of any degree or diploma.

Chennai 600036

Date: January 26, 2022

Research Scholar

[H. V. RAGAVENDRA]

Research Guide

List of Publications

The publications arising out of the work described in this thesis are as follows.

• **Publications in refereed journals**

1. **H. V. Ragavendra**, P. Saha, L. Sriramkumar and J. Silk, *Primordial black holes and secondary gravitational waves from ultra slow roll and punctuated inflation*, Phys. Rev. D **103**, 083510 (2021) [arXiv:2008.12202 [astro-ph.CO]].

2. **H. V. Ragavendra**, L. Sriramkumar and J. Silk, *Could PBHs and secondary GWs have originated from squeezed initial states?*, JCAP **05**, 010 (2021) [arXiv:2011.09938 [astro-ph.CO]].

• **Publications in conference proceedings**

3. **H. V. Ragavendra**, D. Chowdhury and L. Sriramkumar, *Unique contributions to scalar bispectrum in 'just enough inflation'*, in *Workshop on Frontiers in High Energy Physics 2019* (University of Hyderabad, Hyderabad, India, October 14–17, 2019), Eds. A. Giri and R. Mohanta (Springer Nature, Singapore, 2020), pp. 39–47 [arXiv:1906.03942 [astro-ph.CO]].

• **Preprints**

4. **H. V. Ragavendra**, D. Chowdhury and L. Sriramkumar, *Suppression of scalar power on large scales and associated bispectra*, arXiv:2003.01099 [astro-ph.CO], submitted for publication.

5. **H. V. Ragavendra**, *Accounting for scalar non-Gaussianity in secondary gravitational waves*, arXiv:2108.04193 [astro-ph.CO], submitted for publication.

ACKNOWLEDGEMENTS

I am extremely thankful to my supervisor Prof. L. Sriramkumar for guiding me during the course of my thesis work. I am grateful for his knowledge, patience and support that aided my development throughout the course of this program.

I thank the members of my doctoral committee — Prof. K. G. Arun, Dr. Dawood Kothawala, Prof. Arul Lakshminarayan and Prof. James Libby — for their time, advice, and support.

I place on record my thanks to the High Performance Computing Environment of the Indian Institute of Technology Madras for providing means to perform various intense numerical computations involved in my research. I also thank the cluster computing facility at the Department of Physics for providing access and support during the testing and development of my codes.

I am grateful to my collaborators — Dr. Debika Chowdhury, Dr. Pankaj Saha, and Prof. Joseph Silk — who were integral parts of various projects constituting this thesis.

I should also thank several faculty members beyond Indian Institute of Technology Madras, *viz.* Dr. Dhiraj Hazra, Dr. Rajeev Kumar Jain, Prof. Jérôme Martin, Prof. Shiv Sethi, and Dr. V. Sreenath. They contributed much to my understanding of various aspects of cosmology through interactions and useful discussions at various points during the course of my thesis work.

I wish to thank each of my colleagues with whom I was fortunate to share workspace at different times — Rathul Nath Raveendran, Debika Chowdhury, Jaffino Stargen, Nirmalya Kajuri, Krishnamohan Parattu, Sagarika Tripathy, Suvashis Maity, Debottam Nandi, Rahul Kothari, Pankaj Saha, Sampurn Anand, Ashmita Das and Sukannya Bhattacharya. Each of them enriched the working environment and contributed to my learning in their own way during their respective periods of stay.

I thank my close set of friends beyond my research group at the institute — S. Sarath Srinivas, G. Swaminath Bharadwaj and Malayaja Chutani — with whom I was involved in various para-academic activities that made the duration of my Ph.D. all the more valuable and memorable.

Importantly, I thank my family for understanding and encouraging me during these years. I owe my parents for their steadfast support through difficult times and uncertain circumstances.

Lastly, I thank numerous people, known and unknown, whose work I may have

benefited from, directly or indirectly, during the course of my learning, which adds to the debts of gratitude that I cannot readily repay in kind but only hope that my work in future may serve as many as well, if not more.

ABSTRACT

KEYWORDS: Inflation, Cosmic Microwave Background, Primordial Black Holes, Secondary Gravitational Waves, Primordial non-Gaussianity

The inflationary epoch is a period of accelerated expansion of the universe that occurs during the early stages of the radiation dominated era (for reviews, see, for instance, Refs. [1–5]). A suitable duration of inflation ensures the observed extent of homogeneity, isotropy and spatial curvature of the universe. It also provides a natural mechanism for the generation of perturbations that are imprinted as tiny anisotropies in the cosmic microwave background (CMB). The study of properties of the quantum fluctuations of the field driving inflation and the corresponding signatures on the CMB anisotropies offers us insight into the physics operating at the earliest stages of the universe (for the latest constraints on inflation from the CMB, see Ref. [6]). Yet, there are numerous inflationary models that lead to a reasonably good fit to the CMB data at the level of two-point functions [7]. Hence, it is important to study the correlations at higher orders, especially the non-Gaussianities arising from three-point functions, in order to break the degeneracy amongst the various models. It also becomes important to consider complementary observables over scales smaller than the CMB scales, which can help us capture the complete picture of the dynamics of the fields during the inflationary epoch. One possible probe over small scales is the population of primordial black holes (PBHs) that can contribute to the cold dark matter density today. Primordial scalar power with enhanced amplitude over small scales lead to copious production of PBHs when these scales re-enter the Hubble radius at later epochs [8, 9]. Such enhancement in scalar power also sources second order tensor perturbations thereby generating secondary gravitational waves (GWs) [10, 11]. Various direct and indirect constraints have emerged over the last decade on the population of PBHs and the amplitude of GWs (in this regard, see, for instance, Refs. [12–15]). This thesis is aimed at evaluating the observational imprints associated with non-trivial inflationary scenarios over a wide range of scales and utilize the above-mentioned observables to constrain the dynamics.

We shall briefly outline below the different problems we have investigated involving the non-trivial dynamics of inflation driven by a single, canonical, scalar field, which lead to strong features over large or small scales. The goal of these investigations has been to address some of the issues of current interest in the literature, particularly in the context of non-Gaussianities generated in these scenarios and their direct or indirect role on the observables.

• *Unique contributions to the scalar bispectrum in 'just enough inflation':* A scalar field rolling down a potential with a large initial velocity results in inflation of a finite duration. Such a scenario suppresses the scalar power on large scales improving the fit to the cosmological data. In this work [16], we find that the scenario leads to a hitherto unexplored situation wherein the boundary terms of the cubic order action dominate the contributions to the scalar bispectrum over the bulk terms. We show that the consistency relation governing the non-Gaussianity parameter $f_{_{\rm NL}}$ is violated on large scales and that the contributions at the initial time can substantially enhance the value of $f_{_{\rm NL}}$.

• *Suppression of scalar power on large scales and associated bispectra:* A sharp cut-off in the primordial scalar power spectrum on large scales has been known to improve the fit to the CMB data when compared to the more standard, nearly scale invariant power spectrum that arises in slow roll inflation. Over the last couple of years, there has been a resurgent interest in arriving at such power spectra in models with kinetically dominated initial conditions for the background scalar field which leads to inflation of specific duration. In an earlier work [16], we had numerically investigated the characteristics of the scalar bispectrum generated in such models. In this work [17], we compare the scenario with two other competing scenarios (*viz.* punctuated inflation and a model due to Starobinsky) which also suppress the scalar power in a roughly similar fashion on large scales. We further consider two other scenarios involving inflation of a finite duration, one wherein the scalar field begins on the inflationary attractor and another wherein the field starts with a smaller velocity and evolves towards the attractor. These scenarios too exhibit a sharp drop in power on large scales if the initial conditions on the perturbations for a range of modes are imposed on super-Hubble scales as in the kinetically dominated model. We compare the performance of all the models against the Planck CMB data at the level of scalar and tensor power spectra. The model wherein the background field always remains on the inflationary attractor is interesting for the reason that it permits analytical calculations of the scalar power and bispectra. We also compare the amplitudes and shapes of the scalar non-Gaussianity parameter $f_{_{\rm NL}}$ in all these cases which lead to scalar power spectra of similar form. Interestingly, we find that, in the models wherein the initial conditions on the perturbations are imposed on super-Hubble scales, the consistency relation governing the scalar bispectrum is violated for the large scale modes, whereas the relation is satisfied for all the modes in the other scenarios. These differences in the behavior of the scalar bispectra can conceivably help us observationally discriminate between the various models which lead to scalar power spectra of roughly similar shape.

• *PBHs and secondary GWs from ultra slow roll and punctuated inflation:* The primordial scalar power spectrum is well constrained by the cosmological data on large scales, primarily from the observations of the anisotropies in the CMB. Over the last few years, it has been recognized that a sharp rise in power on small scales will lead to enhanced formation of PBHs and also generate secondary GWs of higher and, possibly, detectable amplitudes. It is well understood that scalar power spectra with COBE normalized amplitude on the CMB scales and enhanced amplitudes on smaller scales can be generated due to deviations from slow roll in single, canonical scalar field models of inflation. In fact, an epoch of so-called ultra slow roll inflation can lead to the desired amplification. We find that scenarios which lead to ultra slow roll can be broadly classified into two types, one wherein there is a brief departure from inflation (a scenario referred to as punctuated inflation) and another wherein such a departure does not arise. In this work [18], we consider a set of single field inflationary models involving the canonical scalar field that lead to ultra slow roll and punctuated inflation and examine the formation of PBHs as well as the generation of secondary GWs in these models. Apart from considering specific models, we reconstruct potentials from certain functional choices of the first slow roll parameter leading to ultra slow roll and punctuated inflation and investigate their observational signatures. In addition to the secondary tensor power spectrum, we calculate the secondary tensor bispectrum in the equilateral limit in these scenarios. Moreover, we calculate the inflationary scalar bispectrum that arises in all the cases and discuss the imprints of the scalar non-Gaussianities on the extent of PBHs formed and the amplitude of the secondary GWs generated.

- *Could PBHs and secondary GWs have originated from squeezed initial states?:* The production of PBHs and secondary GWs due to enhanced scalar power on small scales have garnered considerable attention in the recent literature. Often, the mechanism considered to arrive at such increased power involves a modification of the standard slow roll inflationary dynamics, achieved with the aid of fine-tuned potentials. In this work [19], we investigate another well known method to generate features in the power spectrum wherein the initial state of the perturbations is assumed to be squeezed states. The approach allows one to generate features even in slow roll inflation with a specific choice for the Bogoliubov coefficients characterizing the squeezed initial states. Also, the method is technically straightforward to implement since the Bogoliubov coefficients can be immediately determined from the form of the desired spectrum with increased scalar power at small scales. It is known that, for squeezed initial states, the scalar bispectrum is strongly scale dependent and the consistency condition governing the scalar bispectrum in the squeezed limit is violated. In fact, the non-Gaussianity parameter $f_{\rm NL}$ characterizing the scalar bispectrum proves to be inversely proportional to the squeezed mode and this dependence enhances its amplitude at large wave numbers making it highly sensitive to even a small deviation from the standard Bunch-Davies vacuum. These aspects can possibly aid in leading to enhanced formation of PBHs and generation of secondary GWs. However, we find that: (i) the desired form of the squeezed initial states may be challenging to achieve from a dynamical mechanism, and (ii) the backreaction due to the excited states severely limits the extent of deviation from the Bunch-Davies vacuum at large wave numbers. We argue that, unless the issue of backreaction is circumvented, squeezed initial states cannot lead to a substantial increase in power on small scales that is required for enhanced formation of PBHs and generation of secondary GWs.

- *Accounting for scalar non-Gaussianity in secondary GWs:* It is well known that enhancement in the primordial scalar perturbations over small scales generate detectable amplitudes of secondary GWs, by sourcing the tensor perturbations at the second order. These stochastic GWs are expected to carry the imprints of the primordial non-Gaussianities. The scalar bispectrum that is typically produced in models of inflation leading to significant secondary GWs is non-trivial and highly scale dependent. In this work [20], we present a method to account for such general, scale dependent scalar bispectrum arising from inflationary models in the calculation of the spectral density of secondary GWs. Using this method, we compute the contributions arising from the scalar bispectrum to the amplitude of secondary GWs in two specific models of inflation driven by the canonical scalar field. We find that these non-Gaussian contributions can be highly model dependent and have to be consistently taken into account while estimating the total amplitude of the secondary GWs. Beyond the models considered, we emphasize that the method discussed is robust, free from assumptions about the shape of the bispectrum and generalizes earlier approaches adopted in the literature. We argue that this method of accounting for scalar bispectrum will be helpful in future computations of secondary GWs for exotic models that generate larger amplitudes of scalar non-Gaussianities.

TABLE OF CONTENTS

LIST OF TABLES

LIST OF FIGURES

ABBREVIATIONS

BBO	Big Bang Observer
CE	Cosmic Explorer
CHI	Critical-Higgs Inflation
DECIGO	DECi-hertz Interferometer Gravitational wave Observatory
CMB	Cosmic Microwave Background
COBE	Cosmic Background Explorer
EROS	Experience pour la Recherche d'Objets Sombres
ET	Einstein Telescope
FIRAS	Far-InfraRed Absolute Spectrophotometer
GWs	Gravitational Waves
HCO	Hard Cut-Off
LIGO	Laser Interferometer Gravitational-Wave Observatory
LISA	Laser Interferometer Space Antenna
MACHOs	Massive Astrophysical Compact Halo Objects
MAGIS	Matter-wave Atomic Gradiometer Interferometric Sensor
OGLE	Optical Gravitational Lensing Experiment
PBHs	Primordial Black Holes
PI	Punctuated Inflation
PL	Power Law power spectra
PTA	Pulsar Timing Array
QP	Quadratic Potential
RS	Reconstructed Scenario
SKA	Square Kilometre Array
SMI	Starobinsky Model I
SMII	Starobinsky Model II
SMD	SMI with a dip added to the potential
USR	Ultra Slow Roll
WMAP	Wilkinson Microwave Anisotropy Probe

NOTATIONS

The notations used in this thesis have been listed below in the order of their appearance in the thesis.

Notation	Description
$\hbar$	Reduced Planck's constant, $1.054 \times 10^{-34}\,\mathrm{J\,s}$
c	Speed of light, $299792458\,\mathrm{m\,s^{-1}}$
$M_{_{\mathrm{Pl}}}$	Reduced Planck mass, $2.435 \times 10^{18}\,\mathrm{GeV/c^2}$
G	Universal gravitational constant, $6.674 \times 10^{-11}\,\mathrm{N\,kg^{-2}\,m^2}$
t	Cosmic time
$\boldsymbol{x}$	Position vector
η	Conformal time
N	E-fold
$a(t)$	Scale factor describing the universe
H	Hubble parameter
H_0	Hubble constant: value of the Hubble parameter today
h	Parameter describing the Hubble constant as: $H_0 = 100\,h\,\mathrm{km\,s^{-1}\,Mpc^{-1}}$
K	Spatial curvature
ρ	Energy density
w	Equation of state parameter
p	Pressure
ρ_{cr}	Critical energy density
ϕ	Scalar field
$V(\phi)$	Potential for the scalar field ϕ
V_0	Parameter determining the energy scale of potential in the models of SMI, SMII, USR1, USR2, PI1, PI3 and CHI
η_{i}	Conformal time when the initial conditions are imposed on perturbations
η_{e}	Conformal time close to the end of inflation
$H_{_{\mathrm{I}}}$	Value of the Hubble parameter during inflation
V_ϕ	Derivative of the potential V with respect to the scalar field ϕ
$V_{\phi\phi}$	Double derivative of the potential V with respect to ϕ

Notation	Description
ϵ_n	n-th slow roll parameter
$\Omega_{\rm r}$	Dimensionless energy density of radiation at present
$\Omega_{\rm m}$	Dimensionless energy density of non-relativistic matter at present
Ω_K	Density parameter associated with the present value of the spatial curvature
$\Omega_{\rm c}$	Density parameter of cold dark matter in the universe at present
λ	Comoving wavelength, strength of the dip added in case of SMD
k	Comoving wave number of the perturbations
$\mathcal{H}$	Conformal Hubble parameter
$\mathcal{R}(\eta, \boldsymbol{x})$	Curvature perturbation at the spacetime coordinates $(\eta, \boldsymbol{x})$
$\gamma_{ij}(\eta, \boldsymbol{x})$	Primary tensor perturbation at the spacetime coordinates $(\eta, \boldsymbol{x})$
$h_{ij}(\eta, \boldsymbol{x})$	Secondary tensor perturbation at the spacetime coordinates $(\eta, \boldsymbol{x})$
$S_2[\mathcal{R}]$	Second order action governing the curvature perturbations
$S_2[\gamma_{ij}]$	Second order action governing the primary tensor perturbations
f_k	Fourier mode of the scalar perturbations, corresponding to the wave number k
v_k	Fourier mode of the Mukhanov-Sasaki variable for the scalar perturbations, corresponding to the wave number k
g_k	Fourier mode of the primary tensor perturbations, corresponding to the wave number k
u_k	Fourier mode of the Mukhanov-Sasaki variable for the tensor perturbations, corresponding to the wave number k
$\mathcal{P}_{\rm S}(k)$	Power spectrum of the curvature perturbations
$\mathcal{P}_{\rm T}(k)$	Power spectrum of the primary tensor perturbations
$S_3[\mathcal{R}]$	Third order action governing the curvature perturbations
$\mathcal{L}_2$	Second order Lagrangian density associated with the action governing the curvature perturbation $\mathcal{R}$
$S_3^{\rm B}[\mathcal{R}]$	Temporal boundary terms associated with the third order action governing the curvature perturbations
$k_{\rm T}$	$k_1 + k_2 + k_3$

Notation	Description
$G(\boldsymbol{k}_1, \boldsymbol{k}_2, \boldsymbol{k}_3)$	Bispectrum of the scalar perturbations involving the wave vectors $\boldsymbol{k}_1, \boldsymbol{k}_2, \boldsymbol{k}_3$
$G_{_C}(\boldsymbol{k}_1, \boldsymbol{k}_2, \boldsymbol{k}_3)$	The C-th term of the nine contributions to $G(\boldsymbol{k}_1, \boldsymbol{k}_2, \boldsymbol{k}_3)$
$\mathcal{G}_{_C}(\boldsymbol{k}_1, \boldsymbol{k}_2, \boldsymbol{k}_3)$	The integral corresponding to $G_{_C}(\boldsymbol{k}_1, \boldsymbol{k}_2, \boldsymbol{k}_3)$
κ	Cut-off parameter introduced in $\mathcal{G}_{_C}$ to choose the correct perturbative vacuum
$f_{_{\rm NL}}(\boldsymbol{k}_1, \boldsymbol{k}_2, \boldsymbol{k}_3)$	Non-Gaussianity parameter corresponding to the scalar bispectrum
$A_{_{\rm S}}$	Amplitude of primordial scalar power spectrum
$n_{_{\rm S}}$	Spectral index of primordial scalar power spectrum
r	Primordial tensor-to-scalar ratio
τ	Optical depth due to reionization
$\theta_{_{\rm MC}}$	Acoustic scale of the CMB
k_*	Pivot scale
ℓ	Multipole
C_ℓ	CMB angular power spectrum corresponding to the multipole ℓ
δ	Density contrast of matter perturbations
σ^2	Variance of matter perturbations
$\delta_{\rm c}$	Threshold value of density contrast beyond which matter fluctuations are likely to collapse into PBHs
$\mathcal{P}(\delta)$	Probability density describing the matter perturbations
$P_\delta(k)$	Power spectrum of density contrast δ
$W(k\,R)$	Window function to smoothen the distribution of density contrast over the length scale R
γ_*	Parameter quantifying the efficiency of collapse of density contrast into PBHs
$g_{*,k}$	Relativistic degrees of freedom at the time when density contrast corresponding to wave number k collapses into PBHs
$g_{*,\rm eq}$	Relativistic degrees of freedom at the time of radiation-matter equality
M	Mass of PBH corresponding to the length scale R
$M_{\rm eq}$	Mass within Hubble radius at the epoch of radiation and matter equality, $5.83 \times 10^{47}\,\mathrm{kg}$
β	Fraction of matter perturbations that collapse to form PBHs
$f_{_{\rm PBH}}$	Fraction of PBHs constituting dark matter in the current universe

Notation	Description
Φ, Ψ	Bardeen potentials
$\mathcal{T}(k\,\eta)$	Transfer function relating the Bardeen potential to the primordial curvature perturbation $\mathcal{R}_{\boldsymbol{k}}$ corresponding to the wave number k at a given time η
h_k	Fourier mode of the secondary tensor perturbations corresponding to the wave number k
$e_i(\boldsymbol{k}),\ \bar{e}_i(\boldsymbol{k})$	Unit vectors in the plane perpendicular to the wave vector $\boldsymbol{k}$
$e_{ij}^{\lambda}(\boldsymbol{k})$	Polarization tensor of GWs corresponding to the wave vector $\boldsymbol{k}$, with the index $\lambda = (+, \times)$ denoting the two states of polarization
$e^{\lambda}(\boldsymbol{k}, \boldsymbol{p})$	Contraction of the polarization tensor of GWs corresponding to wave vector $\boldsymbol{k}$ with the wave vector $\boldsymbol{p}$, *i.e.* $e^{\lambda}(\boldsymbol{k}, \boldsymbol{p}) = e_{ij}^{\lambda}(\boldsymbol{k})\, p^i\, p^j$
$\mathcal{P}_h(k, \eta)$	Power spectrum of the secondary tensor perturbations corresponding to wave number k at a given time η
$\overline{\mathcal{P}_h(k, \eta)}$	$\mathcal{P}_h(k, \eta)$ averaged over small time scales
f	Frequency corresponding to a given wave number k
$\Omega_{\mathrm{GW}}(f)$	Density parameter of gravitational waves corresponding to frequency f
m	Mass of the inflaton when described by potentials such as QP and PI2
ϕ_{i}	Value of the scalar field at the beginning of its evolution
$\epsilon_{1\mathrm{i}}$	Value of the first slow roll parameter at the beginning of the evolution of ϕ
N_1	E-fold at the onset of inflation in scenarios with kinetic dominated initial conditions, Parameter determining the onset of ultra slow in RS
N_*	E-fold at which the pivot scale k_* leaves the Hubble radius, when counted from the end of inflation
k_{i}	Wave number corresponding to initial time of inflation, *i.e.* $k_{\mathrm{i}} = -1/\eta_{\mathrm{i}}$
ϕ_0	Value of the scalar field at which the slope changes in the potential of SMII, Value of the field at inflection the point of USR and PI models, Location of dip introduced in case of SMD
k_0	Wave number that exits Hubble radius when the slope changes in the model of SMII
A_+	Slope of the potential in the first stage of SMII
A_-	Slope of the potential in the second stage of SMII
ΔA	Difference between the slopes in SMII, *i.e.* $A_- - A_+$

Notation	Description
$\Delta\phi$	Parameter determining the change of slope in the smoothened form of the potential in SMII, width of the dip added in case of SMD
$\alpha(k),\ \beta(k)$	Bogoliubov coefficients that describe the mode function in a non-vacuum initial state
$\Delta\chi^2$	Difference between the χ^2 of a given model and the case with PL power spectra *i.e.* $\Delta\chi^2 = \chi^2_{\mathrm{model}} - \chi^2_{\mathrm{PL}}$
$f_{\mathrm{NL}}^{\mathrm{CR}}$	Expression of f_{NL} given by the consistency relation in the squeezed limit
α, β	Parameters describing the potential in USR1
A, f_{ϕ}	Parameters describing the potential in USR2
B	Parameter describing the potential in PI1
c_0, c_1, c_2, c_3	Parameters describing the potential in PI3
$\mathcal{S}$	Intrinsic entropy perturbation
$\mathcal{S}_k$	Fourier mode associated with intrinsic entropy perturbation corresponding to the wave number k
δp^{NA}	Non-adiabatic component of the pressure perturbation
c_{A}	Adiabatic speed of the scalar perturbations
$\epsilon_1^{\mathrm{I}}(N)$	Parametrization of ϵ_1 in RS1
$\epsilon_1^{\mathrm{II}}(N)$	Parametrization of ϵ_1 in RS2
$\epsilon_1^{\mathrm{III}}(N), \epsilon_1^{\mathrm{IV}}(N)$	Truncated versions of RS1
ϵ_{1a}	Parameter in RS to achieve initial slow roll value of ϵ_1
ϵ_{2a}	Parameter in RS to achieve initial slow roll behavior of ϵ_1
ϵ_{1b}	Parameter in RS that determines the minimum value of ϵ_1
N_2	Parameter denoting the e-fold at the end of inflation in RS
ΔN_1	Parameter determining the rapidity of transition from slow roll to ultra slow roll in RS
ΔN_2	Parameter determining the rapidity of transition from ultra slow roll to end of inflation in RS
N_{i}	E-fold at the beginning of field evolution in RS
H_{i}	Value of Hubble parameter at N_{i} in RS
$G_h^{\lambda_1\lambda_2\lambda_3}(\boldsymbol{k}_1, \boldsymbol{k}_2, \boldsymbol{k}_3)$	Bispectrum of the secondary tensor perturbations corresponding to wave vectors $\boldsymbol{k}_1, \boldsymbol{k}_2, \boldsymbol{k}_3$ and polarizations $\lambda_1, \lambda_2, \lambda_3$
$S_h^{\lambda_1\lambda_2\lambda_3}(\boldsymbol{k}_1, \boldsymbol{k}_2, \boldsymbol{k}_3)$	Shape function associated with $G_h^{\lambda_1\lambda_2\lambda_3}(\boldsymbol{k}_1, \boldsymbol{k}_2, \boldsymbol{k}_3)$
$\delta(k)$	Ratio of the Bogoliubov coefficients, *i.e.* $\delta(k) = \beta(k)/\alpha(k)$
$\mathcal{P}_{\mathrm{S}}^{0}(k)$	Scale invariant part of a scalar power spectrum containing features

Notation	Description
$g(k)$	Function characterizing the feature over an otherwise scale invariant spectrum, *i.e.* $\mathcal{P}_{\mathrm{S}}(k) = \mathcal{P}_{\mathrm{S}}^{0}(k)\,[1+g(k)]$
γ	Parameter determining the strength of the feature when $g(k)$ is chosen to be a lognormal function
k_{f}	Wave number corresponding to the location of the peak of the feature in the spectrum
Δ_k	Width of the feature of lognormal function in the spectrum
k_{min}	$k_1/10$, with k_1 being the smallest wave number of observational interest
$\mathcal{R}^{\mathrm{G}}(\boldsymbol{x},\eta)$	Gaussian component of the perturbation $\mathcal{R}$ at $(\boldsymbol{x},\eta)$
$\mathcal{R}^{\mathrm{G}}_{\boldsymbol{k}}(\eta)$	Gaussian component of the perturbation in Fourier space $\mathcal{R}_{\boldsymbol{k}}(\eta)$
$\mathcal{P}_{\mathrm{C}}(k)$	Correction to the scalar power spectrum due to f_{NL}
$\mathcal{P}^{\mathrm{M}}_{\mathrm{S}}(k)$	Scalar power spectrum accounting for $\mathcal{P}_{\mathrm{C}}(k)$
ρ_{I}	Background energy density during inflation
$\rho_{\mathcal{R}}$	Energy density of the curvature perturbations during inflation
$\rho^{(1)}_{\mathcal{R}}$	Contribution to $\rho_{\mathcal{R}}$ due to modes in the sub-Hubble domain
$\rho^{(2)}_{\mathcal{R}}$	Contribution to $\rho_{\mathcal{R}}$ due to modes in the super-Hubble domain
$\mathcal{P}^{(2-i)}_{h}(k)$	Contributions to the secondary tensor power spectrum due to scalar non-Gaussianity at the level of f^{2}_{NL}
$\mathcal{P}^{(4-i)}_{h}(k)$	Contributions to the secondary tensor power spectrum due to scalar non-Gaussianity at the level of f^{4}_{NL}
a, b, c, μ	Parameters describing the potential in CHI

CHAPTER 1
INTRODUCTION

In this age of precision cosmology, the inflationary scenario constitutes an essential ingredient of the prevailing standard model of cosmology (for textbooks in this context, see Refs. [21–29]; for reviews, see Refs. [1–5, 30–36]). Inflation refers to an epoch of accelerated expansion of the universe during its earliest stage of evolution, soon after big bang. It was originally introduced to explain the observed level of statistical isotropy and flatness over large scales in the current universe. When compared to the other alternatives which attempt to provide similar solutions, inflation proves to be more appealing because of the minimal level of modeling that is required and the attractor behavior in phase space. Apart from resolving the problems mentioned above, inflation also provides a natural mechanism to explain the origin of the primordial perturbations over corresponding scales. During inflation, the quantum fluctuations present at small scales within a causally connected region are rapidly stretched to seed the perturbations in the epochs that follow. These perturbations evolve and are imprinted as small anisotropies in the otherwise isotropic cosmic microwave background (CMB). They grow further to form galaxies and the large scale structure observed in the current universe. It is by studying these perturbations through the statistics of their distribution that we are able gather insight about the epoch of their origin. Modeling the dynamics of inflation and constraining it using observations are truly remarkable for the reason that they allow us to probe the physics operating at the highest energy scales. We need to emphasize that these scales are way beyond the energies that can be accessed by terrestrial particle accelerators. In this thesis, we shall be discussing the correlations of the primordial perturbations generated during inflation and the constraints we can arrive on the mechanisms at play in the early universe from the various observational data. To begin with, let us quickly understand the essential aspects of inflation, the generation of the perturbations and the calculation of the two-point and three-point correlation functions which can be constrained by the observations.

This introductory chapter is organized as follows. In Sec. 1.1, we shall start with a discussion on the manner in which inflation provides a causal explanation for large scale isotropy. We shall describe as to how inflation can be driven by a canonical scalar field that is minimally coupled to gravitation. We shall also describe the generation and evolution of perturbations during this epoch and outline the computation of the two-point and three-point correlations that characterize the perturbations. These correlations predicted by different models shall then be used to arrive at constraints on the parameters describing the models when compared against relevant observational phenomena. In Sec. 1.2, we shall discuss the current and upcoming observational datasets that help us constrain inflationary models, *viz.* the anisotropies observed in the CMB, the possibility of primordial black holes (PBHs) constituting a fraction of cold dark matter today and the amplitude of stochastic gravitational waves (GWs) that can be measured by current and future observatories. In Sec. 1.3, we shall briefly outline the problems analyzed in the subsequent chapters of the thesis.

Before we proceed further, let us clarify a few points regarding the conventions and notations that we shall follow in this thesis. Throughout this thesis, we shall work with natural units wherein $\hbar = c = 1$, and define the Planck mass to be $M_{_{\mathrm{Pl}}} = (8\,\pi\,G)^{-1/2}$. Note that Latin indices shall represent the spatial coordinates, except for k which shall be reserved for denoting the wave number. We shall work in $(3+1)$-spacetime dimensions, and adopt the signature of the metric to be $(-,+,+,+)$. We shall assume the background to be the spatially flat Friedmann-Lemaître-Robertson-Walker (FLRW) universe, with a being the scale factor. An overdot and an overprime shall denote differentiation with respect to the cosmic time and the conformal time coordinates. Moreover, N shall represent the number of e-folds — defined as $\mathrm{d}N = \mathrm{d}\ln a$ or, equivalently, $a(N) \propto \mathrm{e}^N$ — a convenient, dimensionless unit of time to quantify the expansion of space.

1.1 INFLATION

Various cosmological observations — such as, for example, the anisotropies in the CMB [37, 38], the distribution of the large scale structure [39–43] and the supernovae data [44–46] — suggest that the universe today is statistically isotropic and spatially flat over large scales. Moreover, the observations point to the fact that the inhomogeneities were small at earlier times and at large scales today. Besides, the CMB data constrains the energy density associated with spatial curvature to be $\Omega_K = 0.001 \pm 0.002$ (see Ref. [38]; in this regard, however, also see Refs. [47, 48]). Motivated by the above mentioned observations and the cosmological principle, in this thesis, we shall assume that the background is described by the spatially flat FLRW universe. Such a universe is described by the line-element

$$\mathrm{d}s^2 = -\mathrm{d}t^2 + a^2(t)\,\mathrm{d}\boldsymbol{x}^2 = a^2(t)\,(-\mathrm{d}\eta^2 + \mathrm{d}\boldsymbol{x}^2), \tag{1.1}$$

where t denotes the cosmic time coordinate, $\boldsymbol{x}$ represents the spatial coordinates, and η is called the conformal time coordinate. The function $a(t)$ denotes the scale factor that quantifies the expansion of the spatial coordinates with respect to cosmic time. The dynamics of the FLRW metric is governed by the following Friedmann equations:

$$H^2 = \frac{1}{3\,M_{_{\rm Pl}}^2}\,\rho, \tag{1.2a}$$

$$\frac{\ddot{a}}{a} = -\frac{1}{6\,M_{_{\rm Pl}}^2}\,(\rho+3\,p), \tag{1.2b}$$

where ρ and p denote the energy density and pressure of the total matter content of the universe. The quantity H is the Hubble parameter, which is defined as $H = \dot{a}/a$. These equations are valid for the entire history of expansion of the universe. In this thesis, we shall primarily focus on solving them during the epoch of inflation.

In Fig. 1.1, we have illustrated the behavior of comoving length scales and the comoving Hubble radius as functions of e-folds N, during different epochs of the universe, as dictated by the energy and density and pressure of the corresponding epochs (see, for instance, Refs. [21, 29]). Note that a range of scales enter the comoving Hubble radius during the epochs dominated by radiation or matter. The observables over the large scales associated with the CMB, *i.e.* from $1\,\mathrm{Mpc}$ to $10^4\,\mathrm{Mpc}$ are highly isotropic, with anisotropies of order 10^{-4} or less. To explain such a level of isotropy, it is compelling to demand that these scales of cosmological interest were in causal contact before they entered the Hubble radius during the later epochs. Otherwise, we would be forced to impose isotropic initial conditions over such scales by hand, when they were outside the Hubble radius. For the scales to emerge from inside the Hubble radius during the early stages of their evolution, we need an epoch wherein the comoving Hubble radius decreases with time, *i.e.* ${\rm d}(a\,H)^{-1}/{\rm d}t < 0$. Since $H = \dot{a}/a$, this implies $\ddot{a} > 0$. Hence, a phase with accelerated expansion of the scale factor is invoked to address this issue. This is the epoch of inflation, hypothesized to occur during the early stages of the radiation dominated epoch. The behavior of scale factor during inflation is often conveniently modeled as $a(t) \propto \exp{(H_{_{\rm I}}\,t)}$, where $H_{_{\rm I}}$ is a constant. This leads to the comoving Hubble radius during this phase decrease as $(a\,H)^{-1} \propto a^{-1}$, thereby ensuring that all scales emerge from inside the Hubble radius when evolved from a sufficiently early time. Note that the second Friedmann equation (1.2b) suggests that the universe will go through accelerated expansion (*i.e.* $\ddot{a} > 0$) provided $(\rho + 3\,p) < 0$. In the next subsection, we shall discuss how such a condition for inflation can be easily achieved with a scalar field driving the background.

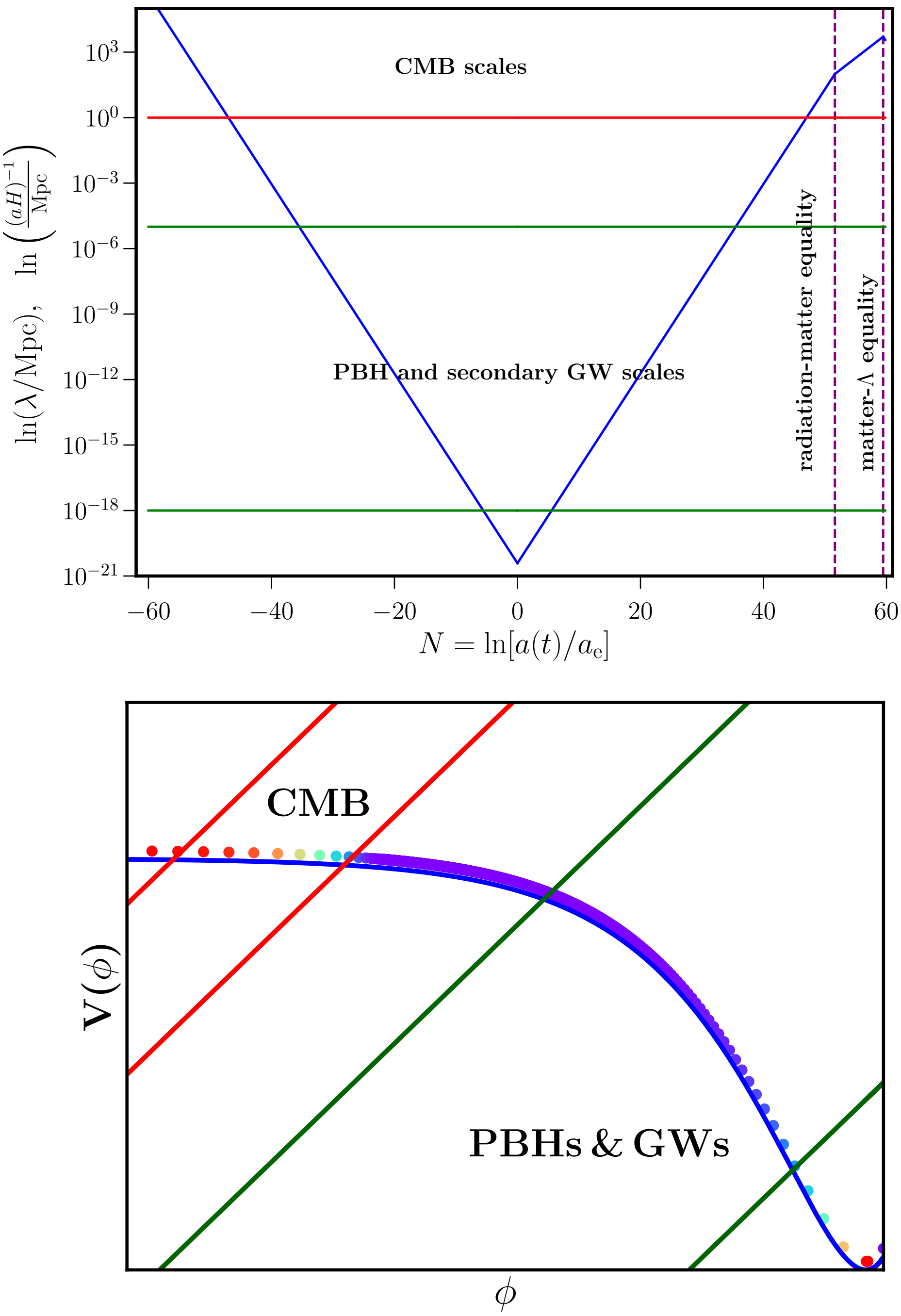

Figure 1.1: The behavior of the comoving Hubble radius of the universe beginning with inflation and through the radiation and matter dominated epochs have been plotted as a function of e-folds (on top). In the figure, we have also indicated the comoving wave numbers associated with the CMB and smaller scales. It is easy to see that the period of inflation ensures that the scales observed today begin inside a causally connected region, *i.e.* they lie within the Hubble radius. We have also illustrated schematically (at the bottom) a correspondence between the scales of observation and the evolution of the field over the potential, when inflation is driven by a canonical scalar field.

1.1.1 Evolution of the background

Inflation is typically modeled as driven by a canonical scalar field, say, ϕ, that is minimally coupled to gravitation (see, for example, the reviews [1–5, 30–36] as well as references therein). The potential, say, $V(\phi)$, driving inflation is required to be smooth to achieve what is called as the slow roll evolution of the field. The equation of motion governing the scalar field in a FLRW background is given by

$$\ddot{\phi} + 3\,H\,\dot{\phi} + V_{\phi} = 0, \tag{1.3}$$

where $V_{\phi} = \mathrm{d}V/\mathrm{d}\phi$. The energy density ρ and pressure p associated with the scalar field are found to be

$$\rho = \frac{\dot{\phi}^2}{2} + V(\phi), \tag{1.4a}$$

$$p = \frac{\dot{\phi}^2}{2} - V(\phi). \tag{1.4b}$$

When the field is slowly rolling as mentioned above, the kinetic energy is subdominant to the potential, *i.e.* $\dot{\phi}^2/2 \ll V(\phi)$. Hence, in such situations, we obtain the relation between the pressure and energy density to be $p \simeq -\rho$. This ensures that the condition for accelerated expansion — *viz.* $(\rho + 3\,p) < 0$ — is satisfied, leading to inflation. Apart from the condition that the velocity of the field is small, *i.e.* $\dot{\phi}^2/2 \ll V(\phi)$, if we demand that $\ddot{\phi} \ll 3\,H\,\dot{\phi}$, then the acceleration of the field also remains small thereby ensuring a sufficient duration of inflation. Depending on the energy scale at which inflation occurs, a minimum duration of inflation is required for all modes of cosmological interest to emerge from inside the Hubble radius. We shall now illustrate how such an evolution can be achieved using a well known potential as an example.

Consider the model of inflation originally introduced by Starobinsky [49]. This model is arrived at by adding a term that is quadratic in the Ricci scalar to the original Einstein-Hilbert action in the Jordan frame. In the Einstein frame, the model can be described by the following potential:

$$V(\phi) = \frac{V_0}{8}\left[1 - \exp\left(-\sqrt{\frac{2}{3}}\,\frac{\phi}{M_{_{\mathrm{Pl}}}}\right)\right]^2. \tag{1.5}$$

Notice that the potential has its minimum at $\phi = 0$ and tends to a constant when $\phi \gg M_{_{\mathrm{Pl}}}$. If one starts far away from the minimum of the potential, one finds that the friction or the drag term $3\,H\,\dot{\phi}$ in the equation of motion (1.3) slows down the field even when it has a large initial velocity. In other words, the drag term makes the kinetic energy of the field sub-dominant to the potential energy, *i.e.* $\dot{\phi}^2/2 \ll V(\phi)$, during the course of the evolution. The small velocity of the field leads to a situation wherein its acceleration is small so that the equation of motion for the field simplifies to

$$3\,H\,\dot{\phi} \simeq -V_{\phi}. \tag{1.6}$$

Therefore, when the field begins its evolution sufficiently away from the minimum of the potential, one can obtain the required duration of inflation so as to ensure that the cosmological scales emerge from inside the Hubble radius. As the field approaches the minimum of the potential, it is found that the velocity of field increases and inflation is naturally terminated. Thereafter, the field oscillates at the bottom of the potential. During this epoch, the energy from the inflaton is expected to be transferred to radiation leading to the conventional radiation dominated phase of the hot big bang model.

The evolution of the field in the Starobinsky model (1.5) can be easily solved analytically, using the two conditions that ensure that the field rolls slowly for an adequate period of time, *viz.* $\dot{\phi}^2/2 \ll V(\phi)$ and $\ddot{\phi} \ll 3\,H\,\dot{\phi}$. These conditions are referred to as the slow roll approximation and they prove to be helpful in calculations of observable quantities as well. However, non-trivial potentials that we shall encounter in later chapters can lead to a violation of the slow roll conditions and hence it may not be possible to readily obtain analytical solutions for the evolution of the field in such cases. In order to study the evolution of the field in a generic situation, we have developed a code to numerically solve and compute the relevant quantities of interest for a given inflationary potential describing a single, canonical scalar field. The code works with the e-fold N as the independent variable and it solves the background equations (1.2a) and (1.3) using the fifth-order Runge-Kutta method to arrive at the evolution of the field [50, 51]. The step size is made adaptive such that one can discern non-trivial features during the evolution without losing precision. We shall remark more about this code later when we discuss perturbations and the evaluation of the inflationary power spectra.

In Fig.1.2, we have presented the evolution of the field in the Starobinsky model, arrived at using the above-mentioned code. We have illustrated the behavior of the field at equal intervals of e-folds as it evolves across the potential. It can be readily inferred from the figure that the field rolls slowly when it is away from the minimum and it gathers velocity as it approaches the minimum. Around the minimum, the field oscillates with a large range of velocity. In the figure, we have also plotted the trajectory

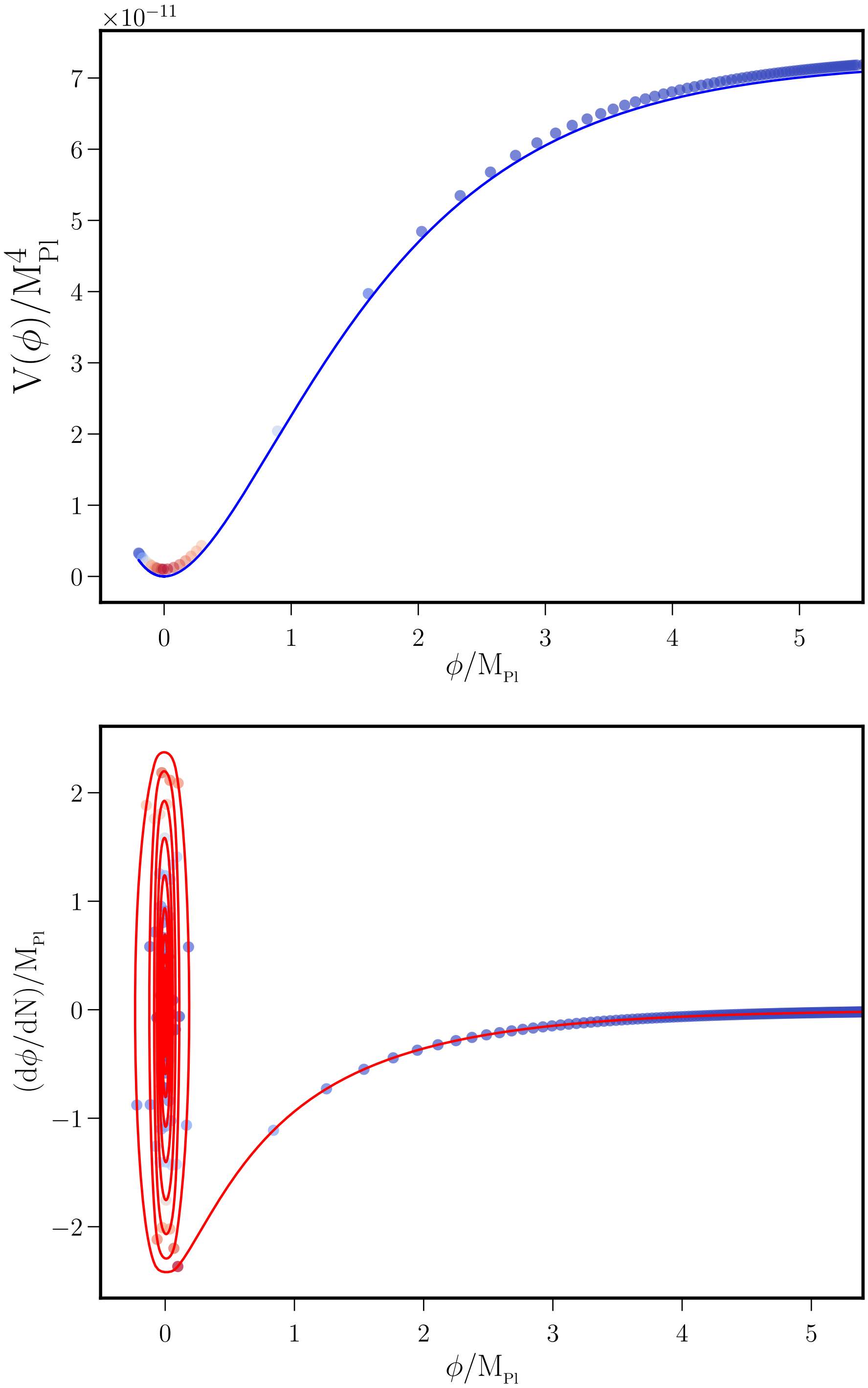

Figure 1.2: The evolution of the scalar field in the case of the Starobinsky model (1.5) has been plotted (on top) along with the corresponding trajectory of the field in phase space (at the bottom). The dots in the plots represent the evolution of the field over equal intervals of e-folds. We have also indicated the velocity of the field at different points in the potential, when it is rolling slowly during the early stages (with $\epsilon_1 \sim 10^{-4}$, in blue) and when it is rolling fast after the end of inflation (with $0 \leq \epsilon_1 \leq 3$, in red).

of the field in the phase space ϕ–$\mathrm{d}\phi/\mathrm{d}N$. As is evident from the trajectory in phase space, the field evolves with low kinetic energy during most of its evolution. At late times, it spirals with rapid changes in velocity until it loses all the kinetic energy and settles down at $\phi = \mathrm{d}\phi/\mathrm{d}N = 0$.

In order to gain a better understanding of the dynamics of the evolution of the field, it is convenient to define the so-called the slow roll parameters ϵ_n as follows:

$$\epsilon_1 = -\frac{\mathrm{d}\ln H}{\mathrm{d}N}, \tag{1.7a}$$

$$\epsilon_{n+1} = \frac{\mathrm{d}\ln \epsilon_n}{\mathrm{d}N}, \quad \text{for } n \geq 1. \tag{1.7b}$$

The first slow roll parameter is a crucial parameter because, combined with the Friedmann equations, it can be rewritten as

$$\epsilon_1 = \frac{1}{2\,M_{_{\mathrm{Pl}}}^2}\left(\frac{\mathrm{d}\phi}{\mathrm{d}N}\right)^2. \tag{1.8}$$

Note that, ϵ_1 quantifies the kinetic energy of the scalar field in a dimensionless fashion. In inflationary models which permit slow roll, such as the Starobinsky model (1.5), ϵ_1 is initially small when the value of the scalar field is large. At later stages, as the field approaches the minimum of the potential, the value of the parameter crosses unity, leading to the termination of inflation. Thereafter, the value of ϵ_1 varies between zero and 3, indicating the oscillations of the field at the bottom of the potential, which is reflected in the inspiralling trajectory in phase space [*cf.* Fig. 1.2].

In terms of these parameters, the slow roll approximation corresponds to $\epsilon_n \ll 1$. It is also interesting to note that these parameters can be related to the shape of the potential. For instance, in the slow roll approximation, the first two slow roll parameters can be expressed as

$$\epsilon_1 \simeq \frac{M_{_{\mathrm{Pl}}}^2}{2}\left(\frac{V_\phi}{V}\right)^2, \tag{1.9a}$$

$$\epsilon_2 \simeq 2M_{_{\mathrm{Pl}}}^2\left[\left(\frac{V_\phi}{V}\right)^2 - \frac{V_{\phi\phi}}{V}\right], \tag{1.9b}$$

where $V_{\phi\phi} = \mathrm{d}^2V/\mathrm{d}\phi^2$. As we shall see later, these parameters play crucial roles in the calculations of the power and bi-spectra of the perturbations.

1.1.2 Perturbations and power spectra

Having discussed the dynamics of the homogeneous background, let us turn to the perturbations over the background. These are perturbations arising from the metric as well as the scalar field and they can be decomposed into scalar, vector and tensor components (for detailed discussions, see, for example, Refs. [1, 52, 53]). The vector perturbations are known to decay rapidly in an inflating universe in the absence of corresponding sources. Therefore, we shall focus on the scalar and tensor perturbations.

Let $\mathcal{R}$ and γ_{ij} denote the scalar and the tensor perturbations. The action governing these perturbations at the quadratic order are given by [52, 54]

$$\mathcal{S}_2[\mathcal{R}] = \frac{1}{2}\int \mathrm{d}\eta \int \mathrm{d}^3\boldsymbol{x}\; z^2 \left[\mathcal{R}'^2 - (\partial\mathcal{R})^2\right], \tag{1.10a}$$

$$\mathcal{S}_2[\gamma_{ij}] = \frac{M_{_{\mathrm{Pl}}}^2}{8}\int \mathrm{d}\eta \int \mathrm{d}^3\boldsymbol{x}\; a^2 \left[\gamma_{ij}'^2 - (\partial\gamma_{ij})^2\right], \tag{1.10b}$$

where $z = \sqrt{2\,\epsilon_1}\, M_{_{\mathrm{Pl}}}\, a$, with ϵ_1 being the first slow roll parameter. Let $\mathcal{R}_{\boldsymbol{k}}$ and $\gamma_{ij}^{\boldsymbol{k}}$ denote the Fourier modes associated with the scalar and tensor perturbations, respectively. On varying the above action, we arrive at the following differential equations that govern the dynamics of these modes:

$$\mathcal{R}_{\boldsymbol{k}}'' + 2\,\frac{z'}{z}\,\mathcal{R}_{\boldsymbol{k}}' + k^2\,\mathcal{R}_{\boldsymbol{k}} = 0, \tag{1.11a}$$

$$\gamma_{ij}^{\boldsymbol{k}\,\prime\prime} + 2\,\frac{a'}{a}\,\gamma_{ij}^{\boldsymbol{k}\,\prime} + k^2\,\gamma_{ij}^{\boldsymbol{k}} = 0. \tag{1.11b}$$

On quantization, the Fourier modes are elevated to be operators, denoted as $\hat{\mathcal{R}}_{\boldsymbol{k}}$ and $\hat{\gamma}_{ij}^{\boldsymbol{k}}$. The scalar and tensor power spectra $\mathcal{P}_{_{\mathrm{S}}}(k)$ and $\mathcal{P}_{_{\mathrm{T}}}(k)$ are defined in terms of these operators through the relations

$$\langle \hat{\mathcal{R}}_{\boldsymbol{k}}(\eta_{\mathrm{e}})\, \hat{\mathcal{R}}_{\boldsymbol{k}'}(\eta_{\mathrm{e}})\rangle = \frac{2\,\pi^2}{k^3}\,\mathcal{P}_{_{\mathrm{S}}}(k)\;\delta^{(3)}\,(\boldsymbol{k}+\boldsymbol{k}'), \tag{1.12a}$$

$$\langle\, \hat{\gamma}_{ij}^{\boldsymbol{k}}(\eta_{\mathrm{e}})\, \hat{\gamma}_{\boldsymbol{k}'}^{ij}(\eta_{\mathrm{e}})\,\rangle = \frac{2\,\pi^2}{k^3}\,\mathcal{P}_{_{\mathrm{T}}}(k)\;\delta^{(3)}(\boldsymbol{k}+\boldsymbol{k}'), \tag{1.12b}$$

where η_{e} is the conformal time at late times, close to the end of inflation. We should mention that, in the above expressions, the expectation values on the left hand side are to be evaluated in the specified initial quantum state, which we shall assume to be the Bunch-Davies vacuum, unless we mention otherwise. Let f_k and g_k denote the positive frequency modes (associated with the Bunch-Davies vacuum) in terms of which the operators $\hat{\mathcal{R}}_{\boldsymbol{k}}$ and $\hat{\gamma}_{ij}^{\boldsymbol{k}}$ are decomposed. Then, in terms of the quantities f_k and g_k, the power spectra $\mathcal{P}_{_{\rm S}}(k)$ and $\mathcal{P}_{_{\rm T}}(k)$ can be expressed as

$$\mathcal{P}_{_{\rm S}}(k) = \frac{k^3}{2\,\pi^2}\,\vert f_k(\eta_{\rm e})\vert^2, \tag{1.13a}$$

$$\mathcal{P}_{_{\rm T}}(k) = 4\,\frac{k^3}{2\,\pi^2}\,\vert g_k(\eta_{\rm e})\vert^2. \tag{1.13b}$$

Let us now briefly describe the evaluation of the scalar power spectrum in the standard case of slow roll inflation. Let us introduce quantities called the Mukhanov-Sasaki variables defined as $v_k = z\, f_k$, $u_k = (M_{_{\rm Pl}}/\sqrt{2})\, a\, g_k$. In terms of these variables, the equations of motion (1.11) governing the perturbations become (see, for instance, the reviews [1–5, 30–36]):

$$v_k'' + \left(k^2 - \frac{z''}{z}\right)\, v_k = 0, \tag{1.14a}$$

$$u_k'' + \left(k^2 - \frac{a''}{a}\right)\, u_k = 0. \tag{1.14b}$$

The initial conditions on the scalar and tensor Mukhanov-Sasaki variables are imposed when the modes satisfy the conditions $k \gg \sqrt{z''/z}$ and $k \gg \sqrt{a''/a}$, respectively. These typically correspond to the condition that the modes are well inside the Hubble radius, *i.e.* they are in the sub-Hubble domain. The initial conditions corresponding to the Bunch-Davies vacuum are given by

$$v_k = u_k = \frac{1}{\sqrt{2\,k}}\,{\rm e}^{-i\,k\,\eta}, \tag{1.15a}$$

$$v_k' = u_k' = -i\,\sqrt{\frac{k}{2}}\,{\rm e}^{-i\,k\,\eta}. \tag{1.15b}$$

Note that, in terms of the Mukhanov-Sasaki variables, the scalar and tensor spectra (1.13) reduce to the following forms:

$$\mathcal{P}_{_{\rm S}}(k) = \frac{k^3}{2\,\pi^2}\,\left(\frac{\vert v_k\vert}{z}\right)^2, \tag{1.16a}$$

$$\mathcal{P}_{_{\rm T}}(k) = \frac{8}{M_{_{\rm Pl}}^2}\,\frac{k^3}{2\,\pi^2}\,\left(\frac{\vert u_k\vert}{a}\right)^2. \tag{1.16b}$$

In the slow roll approximation, one can easily arrive at analytical solutions that describe the evolution of the Mukhanov-Sasaki variables. On utilizing the solutions, one can calculate the power spectra at late times when $k \ll \sqrt{z''/z}$ and $k \ll \sqrt{a''/a}$, which often correspond to the condition that the modes are well outside the Hubble radius, *i.e.* they are in the super-Hubble domain. The scalar and tensor power spectra evaluated in the super-Hubble limit can be expressed as

$$\mathcal{P}_{\mathrm{S}}(k) \simeq \frac{H_{\mathrm{I}}^2}{8\,\pi^2\,M_{_{\mathrm{Pl}}}^2\,\epsilon_1}, \tag{1.17a}$$

$$\mathcal{P}_{\mathrm{T}}(k) \simeq \frac{2\,H_{\mathrm{I}}^2}{\pi^2\,M_{_{\mathrm{Pl}}}^2}, \tag{1.17b}$$

where H_{I} denotes the nearly constant value of the Hubble parameter in slow roll inflation. We should mention that the background quantities in these expressions are to be evaluated at the time when the modes leave the Hubble radius. These power spectra depend on the inflationary models of interest. They enable us to compare them against the observations and thereby arrive at constraints on the models.

While in simple situations such as slow roll inflation, the scalar and tensor power spectra can be evaluated analytically, one has to resort to numerical computations in order to arrive at the power spectra in non-trivial scenarios involving departures from slow roll. The exact scalar and tensor power spectra can be arrived at by solving equations (1.11) numerically. As in the case of the background, these equations are usually solved with the e-fold N as the independent variable, which allows us to efficiently capture the evolution of the modes. As we mentioned above, the Bunch-Davies initial conditions on the scalar and tensor perturbations are imposed at early times in a domain wherein $k \gg \sqrt{z''/z}$ and $k \gg \sqrt{a''/a}$. The modes are evolved from these initial conditions, and the power spectra are evaluated at late times such that $k \ll \sqrt{z''/z}$ and $k \ll \sqrt{a''/a}$. In a typical slow roll model, one finds that $\sqrt{z''/z} \simeq \sqrt{a''/a} \simeq \sqrt{2}\,a\,H$. Therefore, the above conditions correspond to the modes being in the sub-Hubble [*i.e.* when $k \gg (a\,H)$] and the super-Hubble [*i.e.* when $k \ll (a\,H)$] domains, respectively. While, analytically, one imposes the Bunch-Davies conditions in the limit $k \gg (a\,H)$, numerically, one often finds that it is adequate if the initial conditions on the perturbations are imposed when $k \simeq 10^2\,(a\,H)$. Moreover, theoretically, the spectra are to be evaluated in the super-Hubble limit $k \ll (a\,H)$. However, other than in a few peculiar models, the amplitude of the curvature perturbation f_k quickly freezes once the modes leave the Hubble radius. Due to this reason, the power spectra are numerically evaluated typically when $k \simeq 10^{-5}\,(a\,H)$ (see, for instance, Refs. [55, 56]). Later in certain cases, we shall explicitly note the situations where the modes were evolved beyond this condition and the spectra are computed close to the end of inflation.

Let us now mention a few details about the code used for the computation of the power spectra. It is a Fortran package developed independently as a part of this thesis work. We would like to mention here that we have made the code available at

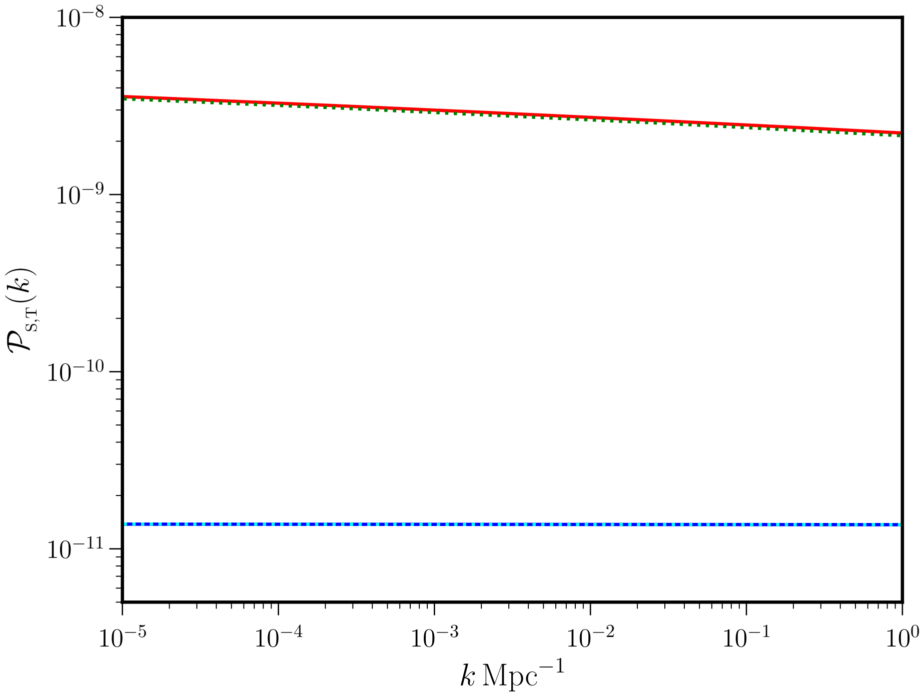

Figure 1.3: The power spectra of the scalar (in red) and tensor (in blue) perturbations obtained in the case of the Starobinsky model (1.5) have been presented. The exact numerical spectra are plotted (as solid lines) along with the analytical estimates arrived at using the slow roll approximation (indicated as green and cyan dots). The analytical estimates agree very well with the numerical results. We find that the relative difference is of the order of 1%.

the following URL: https://gitlab.com/ragavendrahv/pbs.git. It solves the background evolution for a given inflationary potential and parameters using an adaptive routine of fifth order Runge-Kutta method, as we pointed out earlier. Then, it solves for the Fourier modes of the scalar and tensor perturbations using the same method for a given number of points of wave numbers. The code is modular, capable of multi-threaded processing and hence time efficient. It is quite model independent as it can be employed to solve the background and the perturbations for any inflationary model driven by a single, canonical scalar field. As we shall describe in Chap. 2, a version of this code, with suitable modifications, was used in conjunction with CosmoMC for comparing various inflationary models against the CMB data. The power spectra obtained using the code for the Starobinsky model is presented in Fig. 1.3. We have presented both the numerical and the analytical estimates for the scalar and tensor power spectra $\mathcal{P}_{\mathrm{S}}(k)$ and $\mathcal{P}_{\mathrm{T}}(k)$ over the range of modes associated with the CMB scales. Evidently, the analytical estimates and the exact numerical results agree very well.

1.1.3 The third order action and the contributions to the scalar bispectrum

We shall now turn to the computation of the three-point correlation generated during inflation. In this thesis, we shall focus mainly on the three-point auto correlation of the scalar perturbations, *viz.* the scalar bispectrum. The scalar bispectrum is the three-point function of the curvature perturbation in Fourier space, and it is defined in terms of the operator $\hat{\mathcal{R}}_{\boldsymbol{k}}$ that we had introduced earlier as follows [57, 58]:

$$\langle \hat{\mathcal{R}}_{\boldsymbol{k}_1}(\eta_{\mathrm{e}})\, \hat{\mathcal{R}}_{\boldsymbol{k}_2}(\eta_{\mathrm{e}})\, \hat{\mathcal{R}}_{\boldsymbol{k}_3}(\eta_{\mathrm{e}})\rangle = (2\,\pi)^3\, \mathcal{B}_{_{\mathrm{S}}}(\boldsymbol{k}_1, \boldsymbol{k}_2, \boldsymbol{k}_3)\, \delta^{(3)}(\boldsymbol{k}_1+\boldsymbol{k}_2+\boldsymbol{k}_3). \tag{1.18}$$

Recall that, η_{e} is a time close to the end of inflation and, in this expression, the expectation value on the left hand side is to be evaluated in the perturbative vacuum [52, 53, 59]. Note that the three wave vectors $(\boldsymbol{k}_1, \boldsymbol{k}_2, \boldsymbol{k}_3)$ form the edges of a triangle. For convenience, we shall hereafter set

$$\mathcal{B}_{_{\mathrm{S}}}(\boldsymbol{k}_1, \boldsymbol{k}_2, \boldsymbol{k}_3) = (2\,\pi)^{-9/2}\, G(\boldsymbol{k}_1, \boldsymbol{k}_2, \boldsymbol{k}_3) \tag{1.19}$$

and refer to $G(\boldsymbol{k}_1, \boldsymbol{k}_2, \boldsymbol{k}_3)$ as the scalar bispectrum.

In order to evaluate the scalar bispectrum, one requires the action describing the curvature perturbation at the third order. For the case of inflation driven by a canonical scalar field, it can be shown that, at the third order, the action governing the curvature perturbation $\mathcal{R}$ can be expressed as (see, for instance, Refs. [52, 53, 60, 61])

$$\begin{aligned}
\mathcal{S}_3[\mathcal{R}] &= M_{_{\mathrm{Pl}}}^2 \int_{\eta_{\mathrm{i}}}^{\eta_{\mathrm{e}}} \mathrm{d}\eta \int \mathrm{d}^3\boldsymbol{x}\, \biggl[a^2\, \epsilon_1^2\, \mathcal{R}\, \mathcal{R}'^2 + a^2\, \epsilon_1^2\, \mathcal{R}\, (\partial\mathcal{R})^2 \\
&\quad - 2\, a\, \epsilon_1\, \mathcal{R}'\, (\partial\mathcal{R})\, (\partial\chi) + \frac{a^2}{2}\, \epsilon_1\, \epsilon_2'\, \mathcal{R}^2\, \mathcal{R}' + \frac{\epsilon_1}{2}\, (\partial\mathcal{R})\, (\partial\chi)\, \partial^2\chi \\
&\quad + \frac{\epsilon_1}{4}\, \partial^2\mathcal{R}\, (\partial\chi)^2 + 2\, \mathcal{F}(\mathcal{R})\, \frac{\delta\mathcal{L}_2}{\delta\mathcal{R}}\biggr],
\end{aligned} \tag{1.20}$$

where, as we have mentioned earlier, $\epsilon_2 = \mathrm{d}\ln\epsilon_1/\mathrm{d}N$ is the second slow roll parameter, while $\partial^2\chi = a\,\epsilon_1\,\mathcal{R}'$. The quantity $\mathcal{F}(\mathcal{R})$ is given by

$$\begin{aligned}
\mathcal{F}(\mathcal{R}) &= \frac{\epsilon_2}{4}\, \mathcal{R}^2 + \frac{1}{a\, H}\, \mathcal{R}\, \mathcal{R}' + \frac{1}{4\, a^2\, H^2}\Bigl\{-(\partial\mathcal{R})\, (\partial\mathcal{R}) + \partial^{-2}[\partial_i\, \partial_j\, (\partial_i\mathcal{R}\, \partial_j\mathcal{R})]\Bigr\} \\
&\quad + \frac{1}{2\, a^2\, H}\Bigl\{(\partial\mathcal{R})\, (\partial\chi) - \partial^{-2}[\partial_i\, \partial_j\, (\partial_i\mathcal{R}\, \partial_j\chi)]\Bigr\}
\end{aligned} \tag{1.21}$$

and $\mathcal{L}_2$ denotes the Lagrangian density associated with the action governing the curvature perturbation at the second order [*cf.* Eq. (1.10a)]. Note that η_{i} is the conformal time when the initial conditions are imposed on the perturbations and η_{e} is the conformal time close to the end of inflation, when the power and bi-spectra are evaluated. Typically, in analytical calculations, one assumes that $\eta_{\rm i} \to -\infty$ and $\eta_{\rm e} \to 0^-$.

The third order action (1.20) is arrived at from the original action governing the system of the gravitational and scalar fields. A set of temporal and spatial boundary terms are often ignored in arriving at the above action [52, 53, 61]. The spatial boundary terms do not contribute to the scalar bispectrum under any condition. However, in cases such as a scenario involving inflation of a finite duration or in situations involving an epoch of ultra slow roll, one finds that the temporal boundary terms can contribute non-trivially. These temporal boundary terms are given by [61]

$$\begin{aligned}
\mathcal{S}_3^{\rm B}[\mathcal{R}] &= M_{_{\rm Pl}}^2 \int_{\eta_{\rm i}}^{\eta_{\rm e}} {\rm d}\eta \int {\rm d}^3\boldsymbol{x}\, \frac{\rm d}{{\rm d}\eta}\biggl\{-9\, a^3 H\, \mathcal{R}^3 + \frac{a}{H}\,(1-\epsilon_1)\,\mathcal{R}\,(\partial\mathcal{R})^2 \\
&\quad - \frac{1}{4\,a\,H^3}\,(\partial\mathcal{R})^2\,\partial^2\mathcal{R} - \frac{a\,\epsilon_1}{H}\,\mathcal{R}\,\mathcal{R}'^2 - \frac{a\,\epsilon_2}{2}\,\mathcal{R}^2\,\partial^2\chi \\
&\quad + \frac{1}{2\,a\,H^2}\,\mathcal{R}\,\left(\partial_i\partial_j\mathcal{R}\,\partial_i\partial_j\chi - \partial^2\mathcal{R}\,\partial^2\chi\right) \\
&\quad - \frac{1}{2\,aH}\,\mathcal{R}\,\left[\partial_i\partial_j\chi\,\partial_i\partial_j\chi - (\partial^2\chi)^2\right]\biggr\}. \qquad (1.22)
\end{aligned}$$

It should be mentioned here that, in standard slow roll inflation, apart from the term involving ϵ_2, none of the above terms contribute either at early or at late times. The term involving ϵ_2 contributes non-trivially at late times, and this contribution is often absorbed through a field redefinition (in this context, see, for example, Refs. [52, 61]). However, it is important to clarify that, in this thesis, we do not carry out any field redefinition. We shall explicitly calculate all the contributions due to the bulk and the boundary terms (1.20) and (1.22).

The bispectrum $G(\boldsymbol{k}_1, \boldsymbol{k}_2, \boldsymbol{k}_3)$ can be arrived at by using the third order action described above and the standard rules of perturbative quantum field theory [52, 53, 60, 61]. It can be shown that the scalar bispectrum can be expressed as (see, for instance, Refs. [56, 60])

$$\begin{aligned}
G(\boldsymbol{k}_1, \boldsymbol{k}_2, \boldsymbol{k}_3) &= \sum_{C=1}^{9} G_{_C}(\boldsymbol{k}_1, \boldsymbol{k}_2, \boldsymbol{k}_3) \\
&= M_{_{\rm Pl}}^2 \sum_{C=1}^{6} \Bigl[f_{k_1}(\eta_{\rm e})\, f_{k_2}(\eta_{\rm e})\, f_{k_3}(\eta_{\rm e})\, \mathcal{G}_{_C}(\boldsymbol{k}_1, \boldsymbol{k}_2, \boldsymbol{k}_3) \\
&\quad + \text{complex conjugate}\Bigr] \\
&\quad + G_7(\boldsymbol{k}_1, \boldsymbol{k}_2, \boldsymbol{k}_3) + G_8(\boldsymbol{k}_1, \boldsymbol{k}_2, \boldsymbol{k}_3) + G_9(\boldsymbol{k}_1, \boldsymbol{k}_2, \boldsymbol{k}_3), \qquad (1.23)
\end{aligned}$$

where, as we mentioned earlier, f_k are the positive frequency Fourier modes associated with the curvature perturbation, while $\eta_{\rm e}$ denotes the conformal time close to the end of inflation. The quantities $\mathcal{G}_{_C}(\boldsymbol{k}_1, \boldsymbol{k}_2, \boldsymbol{k}_3)$ represent six integrals that involve the scale factor, the slow roll parameters, the modes f_k and their time derivatives f_k'. They correspond to the six bulk terms appearing in the cubic order action (1.20) and are described by the following expressions:

$$\mathcal{G}_1(\boldsymbol{k}_1, \boldsymbol{k}_2, \boldsymbol{k}_3) = 2\,i \int_{\eta_{\rm i}}^{\eta_{\rm e}} {\rm d}\eta\; a^2\, \epsilon_1^2\, \left(f_{k_1}^{*}\, f_{k_2}'^{*}\, f_{k_3}'^{*} + \text{two permutations}\right), \tag{1.24a}$$

$$\mathcal{G}_2(\boldsymbol{k}_1, \boldsymbol{k}_2, \boldsymbol{k}_3) = -2\,i\; \left(\boldsymbol{k}_1\cdot\boldsymbol{k}_2 + \text{two permutations}\right) \int_{\eta_{\rm i}}^{\eta_{\rm e}} {\rm d}\eta\; a^2\, \epsilon_1^2\, f_{k_1}^{*}\, f_{k_2}^{*}\, f_{k_3}^{*}, \tag{1.24b}$$

$$\mathcal{G}_3(\boldsymbol{k}_1, \boldsymbol{k}_2, \boldsymbol{k}_3) = -2\,i \int_{\eta_{\rm i}}^{\eta_{\rm e}} {\rm d}\eta\; a^2\, \epsilon_1^2\, \left(\frac{\boldsymbol{k}_1\cdot\boldsymbol{k}_2}{k_2^2}\, f_{k_1}^{*}\, f_{k_2}'^{*}\, f_{k_3}'^{*} + \text{five permutations}\right), \tag{1.24c}$$

$$\mathcal{G}_4(\boldsymbol{k}_1, \boldsymbol{k}_2, \boldsymbol{k}_3) = i \int_{\eta_{\rm i}}^{\eta_{\rm e}} {\rm d}\eta\; a^2\, \epsilon_1\, \epsilon_2'\, \left(f_{k_1}^{*}\, f_{k_2}^{*}\, f_{k_3}'^{*} + \text{two permutations}\right), \tag{1.24d}$$

$$\mathcal{G}_5(\boldsymbol{k}_1, \boldsymbol{k}_2, \boldsymbol{k}_3) = \frac{i}{2} \int_{\eta_{\rm i}}^{\eta_{\rm e}} {\rm d}\eta\; a^2\, \epsilon_1^3\, \left(\frac{\boldsymbol{k}_1\cdot\boldsymbol{k}_2}{k_2^2}\, f_{k_1}^{*}\, f_{k_2}'^{*}\, f_{k_3}'^{*} + \text{five permutations}\right), \tag{1.24e}$$

$$\mathcal{G}_6(\boldsymbol{k}_1, \boldsymbol{k}_2, \boldsymbol{k}_3) = \frac{i}{2} \int_{\eta_{\rm i}}^{\eta_{\rm e}} {\rm d}\eta\, a^2\, \epsilon_1^3\, \left[\frac{k_1^2\, \left(\boldsymbol{k}_2\cdot\boldsymbol{k}_3\right)}{k_2^2\, k_3^2}\, f_{k_1}^{*}\, f_{k_2}'^{*}\, f_{k_3}'^{*} + \text{two permutations}\right]. \tag{1.24f}$$

These integrals are to be evaluated from a sufficiently early time ($\eta_{\rm i}$), when the modes are typically well inside the Hubble radius, until very late times, which can be conveniently chosen to be a time close to the end of inflation ($\eta_{\rm e}$). We should mention here that the last term in action (1.20) involving $\mathcal{F}(\mathcal{R})\,(\delta\mathcal{L}_2/\delta\mathcal{R})$ actually vanishes when we assume that the curvature perturbation satisfies the linear equation of motion [*cf.* Eqs. (1.11a) and (1.14a)].

In the expression (1.23) for the scalar bispectrum, the terms $G_7(\boldsymbol{k}_1, \boldsymbol{k}_2, \boldsymbol{k}_3)$, $G_8(\boldsymbol{k}_1, \boldsymbol{k}_2, \boldsymbol{k}_3)$ and $G_9(\boldsymbol{k}_1, \boldsymbol{k}_2, \boldsymbol{k}_3)$ are the contributions that arise due to the boundary terms (1.22) associated with the third order action governing the curvature perturbation. The contribution $G_7(\boldsymbol{k}_1, \boldsymbol{k}_2, \boldsymbol{k}_3)$ is due to the term containing ϵ_2 in the boundary term (1.22), and it can be expressed as

$$\begin{aligned} G_7(\boldsymbol{k}_1, \boldsymbol{k}_2, \boldsymbol{k}_3) &= -i\, M_{_{\rm Pl}}^2\, f_{k_1}(\eta_{\rm e})\, f_{k_2}(\eta_{\rm e})\, f_{k_3}(\eta_{\rm e}) \\ &\quad\times \left[a^2 \epsilon_1 \epsilon_2\, f_{k_1}^{*}(\eta)\, f_{k_2}^{*}(\eta)\, f_{k_3}'^{*}(\eta) + \text{two permutations}\right]_{\eta_i}^{\eta_{\rm e}} \end{aligned}$$

$$+ \text{complex conjugate}. \tag{1.25}$$

In standard slow roll inflation, the contribution at $\eta_{\rm i}$ vanishes with the introduction of a regulator (which is required to choose the perturbative vacuum, as we shall discuss soon), and it is only the term evaluated towards end of inflation that contributes. Among the boundary terms, we have chosen to write this term separately as it is this contribution that is often taken into account (in slow roll inflation) through a field redefinition [52, 60, 61]. However, as we had mentioned, we shall not carry out any field redefinition and explicitly calculate the contributions due to the bulk as well as the boundary terms.

The two terms $G_8(\boldsymbol{k}_1, \boldsymbol{k}_2, \boldsymbol{k}_3)$ and $G_9(\boldsymbol{k}_1, \boldsymbol{k}_2, \boldsymbol{k}_3)$ are the contributions due to the remaining temporal boundary terms of the cubic order action in Eq. (1.22). The contributions $G_9(\boldsymbol{k}_1, \boldsymbol{k}_2, \boldsymbol{k}_3)$ and $G_8(\boldsymbol{k}_1, \boldsymbol{k}_2, \boldsymbol{k}_3)$ arise due to terms with and without $\mathcal{R}'$, respectively. They are given by the following expressions:

$$\begin{aligned}
G_8(\boldsymbol{k}_1, \boldsymbol{k}_2, \boldsymbol{k}_3) &= i\, M_{_{\rm Pl}}^2\, f_{k_1}(\eta_{\rm e})\, f_{k_2}(\eta_{\rm e})\, f_{k_3}(\eta_{\rm e})\, \left[\frac{a}{H}\, f_{k_1}^\ast(\eta)\, f_{k_2}^\ast(\eta)\, f_{k_3}^\ast(\eta)\right]_{\eta_{\rm i}} \\
&\quad \times \biggl\{54\, (a\, H)^2 + 2\, (1-\epsilon_1)\, (\boldsymbol{k}_1\cdot\boldsymbol{k}_2 + \boldsymbol{k}_1\cdot\boldsymbol{k}_3 + \boldsymbol{k}_2\cdot\boldsymbol{k}_3) \\
&\quad + \frac{1}{2\, (a\, H)^2}\left[(\boldsymbol{k}_1\cdot\boldsymbol{k}_2)\, {k_3}^2 + (\boldsymbol{k}_1\cdot\boldsymbol{k}_3)\, {k_2}^2 + (\boldsymbol{k}_2\cdot\boldsymbol{k}_3)\, {k_1}^2\right]\biggr\}_{\eta_{\rm i}} \\
&\quad + \text{complex conjugate}, \qquad (1.26\text{a})\\
G_9(\boldsymbol{k}_1, \boldsymbol{k}_2, \boldsymbol{k}_3) &= i\, M_{_{\rm Pl}}^2\, f_{k_1}(\eta_{\rm e})\, f_{k_2}(\eta_{\rm e})\, f_{k_3}(\eta_{\rm e}) \\
&\quad \times \biggl\{\frac{\epsilon_1}{2\, H^2}\, f_{k_1}^\ast(\eta)\, f_{k_2}^\ast(\eta)\, f_{k_3}'^\ast(\eta) \\
&\quad \times, \left[k_1^2 + k_2^2 - \left(\frac{\boldsymbol{k}_1\cdot\boldsymbol{k}_3}{k_3}\right)^2 - \left(\frac{\boldsymbol{k}_2\cdot\boldsymbol{k}_3}{k_3}\right)^2\right] \\
&\quad - \frac{a\, \epsilon_1}{H}\, f_{k_1}^\ast(\eta)\, f_{k_2}'^\ast(\eta)\, f_{k_3}'^\ast(\eta)\, \left[2 - \epsilon_1 + \epsilon_1\, \left(\frac{\boldsymbol{k}_2\cdot\boldsymbol{k}_3}{k_2\, k_3}\right)^2\right]\biggr\}_{\eta_{\rm i}}^{\eta_{\rm e}} \\
&\quad + \text{two permutations} + \text{complex conjugate}. \qquad (1.26\text{b})
\end{aligned}$$

Note that, because $G_8(\boldsymbol{k}_1, \boldsymbol{k}_2, \boldsymbol{k}_3)$ involves only $\mathcal{R}$ (and not $\mathcal{R}'$), its contribution at late times (*i.e.* at $\eta_{\rm e}$) vanishes identically in any scenario. Moreover, both the boundary terms $G_8(\boldsymbol{k}_1, \boldsymbol{k}_2, \boldsymbol{k}_3)$ and $G_9(\boldsymbol{k}_1, \boldsymbol{k}_2, \boldsymbol{k}_3)$ generally do not contribute in inflationary scenarios that do not have a finite duration. But, as we shall see, in non-trivial scenarios such as models with kinetically dominated or ultra slow roll epochs towards the beginning or end of inflation, these boundary terms can contribute significantly.

In inflationary models which permit slow roll, the different contributions to the bispectrum can be computed analytically using the slow roll approximation. One finds that, in such situations, the dominant contributions to the bispectrum arise due to $G_1(\boldsymbol{k}_1, \boldsymbol{k}_2, \boldsymbol{k}_3)$, $G_2(\boldsymbol{k}_1, \boldsymbol{k}_2, \boldsymbol{k}_3)$, $G_3(\boldsymbol{k}_1, \boldsymbol{k}_2, \boldsymbol{k}_3)$ and $G_7(\boldsymbol{k}_1, \boldsymbol{k}_2, \boldsymbol{k}_3)$. These contributions can be expressed in terms of the Hubble and the first two slow roll parameters as follows:

$$\begin{aligned}
G_1(\boldsymbol{k}_1, \boldsymbol{k}_2, \boldsymbol{k}_3) &= \frac{H_{\mathrm{I}}^4}{16\, M_{_{\mathrm{Pl}}}^4\, \epsilon_1}\, \frac{1}{(k_1\, k_2\, k_3)^3} \\
&\quad \times \left[k_2^2\, k_3^2 \left(\frac{1}{k_{_{\mathrm{T}}}} + \frac{k_1}{k_{_{\mathrm{T}}}^2}\right) + \text{ two permutations}\right], \qquad (1.27\mathrm{a}) \\
G_2(\boldsymbol{k}_1, \boldsymbol{k}_2, \boldsymbol{k}_3) &= \frac{H_{\mathrm{I}}^4}{16\, M_{_{\mathrm{Pl}}}^4\, \epsilon_1}\, \frac{(\boldsymbol{k}_1 \cdot \boldsymbol{k}_2 + \boldsymbol{k}_2 \cdot \boldsymbol{k}_3 + \boldsymbol{k}_3 \cdot \boldsymbol{k}_1)}{(k_1\, k_2\, k_3)^3} \\
&\quad \times \left[-k_{_{\mathrm{T}}} + \frac{(k_1\, k_2 + k_2\, k_3 + k_3\, k_1)}{k_{_{\mathrm{T}}}} + \frac{k_1\, k_2\, k_3}{k_{_{\mathrm{T}}}^2}\right], \qquad (1.27\mathrm{b}) \\
G_3(\boldsymbol{k}_1, \boldsymbol{k}_2, \boldsymbol{k}_3) &= \frac{-H_{\mathrm{I}}^4}{16\, M_{_{\mathrm{Pl}}}^4\, \epsilon_1}\, \frac{1}{(k_1\, k_2\, k_3)^3} \\
&\quad \times \Biggl\{ \left[(\boldsymbol{k}_1 \cdot \boldsymbol{k}_2)\, k_3^2 + (\boldsymbol{k}_1 \cdot \boldsymbol{k}_3)\, k_2^2\right] \left(\frac{1}{k_{_{\mathrm{T}}}} + \frac{k_1}{k_{_{\mathrm{T}}}^2}\right) \\
&\quad + \text{two permutations} \Biggr\}, \qquad (1.27\mathrm{c}) \\
G_7(\boldsymbol{k}_1, \boldsymbol{k}_2, \boldsymbol{k}_3) &= \frac{H_{\mathrm{I}}^4\, \epsilon_2}{32\, M_{_{\mathrm{Pl}}}^4\, \epsilon_1^2}\, \frac{1}{(k_1\, k_2\, k_3)^3}\, \left(k_1^3 + k_2^3 + k_3^3\right), \qquad (1.27\mathrm{d})
\end{aligned}$$

where $k_{_{\mathrm{T}}} = k_1 + k_2 + k_3$. The sum of these four terms gives us the analytical estimate of the scalar bispectrum in slow roll inflation.

As in the case of the power spectra, one has to resort to numerical computations to evaluate the scalar bispectrum in non-trivial scenarios involving deviations from slow roll inflation. To arrive at the exact value of the bispectrum in a generic situation, we compute all the terms [*cf.* Eqs. (1.23), (1.24), (1.25) and (1.26)] numerically. The limits of the integral in Eqs. (1.24) are chosen such that η_{i} corresponds to a suitable time when all modes are sufficiently inside the Hubble radius, and η_{e} corresponds to a time when all the modes are in the super-Hubble regime. These are ensured by choosing η_{i} to be the time when the smallest of the three wave numbers involved in the integrals satisfies $k \simeq 10^2\, (a\, H)$. Similarly, η_{e} is chosen when the largest of wave numbers satisfies $k \simeq 10^{-5}\, (a\, H)$. We should mention that the integrals in Eqs. (1.24) implicitly include a cut-off function of the form $\exp\, [-\kappa\, k_{_{\mathrm{T}}}/(3\, \sqrt{z''/z})]$. During slow roll, this function is approximately given by $\exp\, [-\kappa\, k_{_{\mathrm{T}}}/(3\, a\, H)]$. Such a cut-off function is introduced to make sure that the bispectrum is computed in the perturbative vacuum (in this context, see, for example, Refs. [52, 53]). Numerically, the cut-off helps us to regulate the rapid oscillations of the mode functions that occur when they are evolving in the sub-Hubble regime. The cut-off parameter κ is chosen such that the integrals converge when $\eta_{\rm i}$ is set sufficiently inside the Hubble radius [56]. In a later chapter, we shall discuss about the significance of the choice of the cut-off parameter in inflationary scenarios with kinetic dominated initial conditions. After performing the integrals with the cut-off function, the different contributions are summed, along with those arising due to the boundary terms, to arrive at the complete bispectrum.

The non-Gaussianity parameter $f_{_{\rm NL}}(\boldsymbol{k}_1, \boldsymbol{k}_2, \boldsymbol{k}_3)$ associated with the scalar bispectrum $G(\boldsymbol{k}_1, \boldsymbol{k}_2, \boldsymbol{k}_3)$ is expressed as a suitable dimensionless ratio of the bispectrum to a sum of products of the power spectrum $\mathcal{P}_{_{\rm S}}(k)$ as follows (see, for instance, Refs. [56, 60])

$$\begin{aligned} f_{_{\rm NL}}(\boldsymbol{k}_1, \boldsymbol{k}_2, \boldsymbol{k}_3) &= -\frac{10}{3}\,\frac{1}{(2\,\pi)^4}\,k_1^3\,k_2^3\,k_3^3\,G(\boldsymbol{k}_1, \boldsymbol{k}_2, \boldsymbol{k}_3) \\ &\quad\times\left[k_1^3\,\mathcal{P}_{_{\rm S}}(k_2)\,\mathcal{P}_{_{\rm S}}(k_3) + \text{two permutations}\right]^{-1}. \end{aligned} \tag{1.28}$$

In a later chapter, we shall explicitly derive this equation from the definition of scalar perturbation and discuss the associated caveats. In slow roll inflationary scenarios, we can utilize the expressions (1.17a) and (1.27) for the scalar power and bi-spectra to arrive at the corresponding non-Gaussianity parameter. In such cases, the quantity $f_{_{\rm NL}}(\boldsymbol{k}_1, \boldsymbol{k}_2, \boldsymbol{k}_3)$ is given by

$$\begin{aligned} f_{_{\rm NL}}(\boldsymbol{k}_1, \boldsymbol{k}_2, \boldsymbol{k}_3) &= -\frac{5}{12}\,\biggl\{\epsilon_2 + \epsilon_1\,\biggl[-k_1^4 - k_2^4 - k_3^4 + 10\,\left(k_1^2\,k_2^2 + k_1^2\,k_3^2 + k_1^2\,k_3^2\right) \\ &\quad + 2\,k_1\,k_2\,k_3\,(k_1 + k_2 + k_3)\biggr]\,\left[(k_1 + k_2 + k_3)(k_1^3 + k_2^3 + k_3^3)\right]^{-1}\biggr\}. \end{aligned} \tag{1.29}$$

Note that, in the so-called equilateral and squeezed limits, *i.e.* when $k_1 = k_2 = k_3$ and $k_1 \to 0$, $k_2 \simeq k_3 = k$, the values of the above non-Gaussianity parameter simplifies to $f_{_{\rm NL}} = -5\,(11\,\epsilon_1 + 3\,\epsilon_2)/36$ and $f_{_{\rm NL}} = -5\,(2\epsilon_1 + \epsilon_2)/12$, respectively.

Let us now make a few clarifying remarks regarding the numerical setup used to compute the bispectrum and the associated non-Gaussianity parameter $f_{_{\rm NL}}$. The code is an extension of the Fortran package used to compute the power spectra. It uses the Boole's rule to perform the integrals involved in the contributions to the scalar bispectrum and estimate the complete $f_{_{\rm NL}}$ as a function of the three

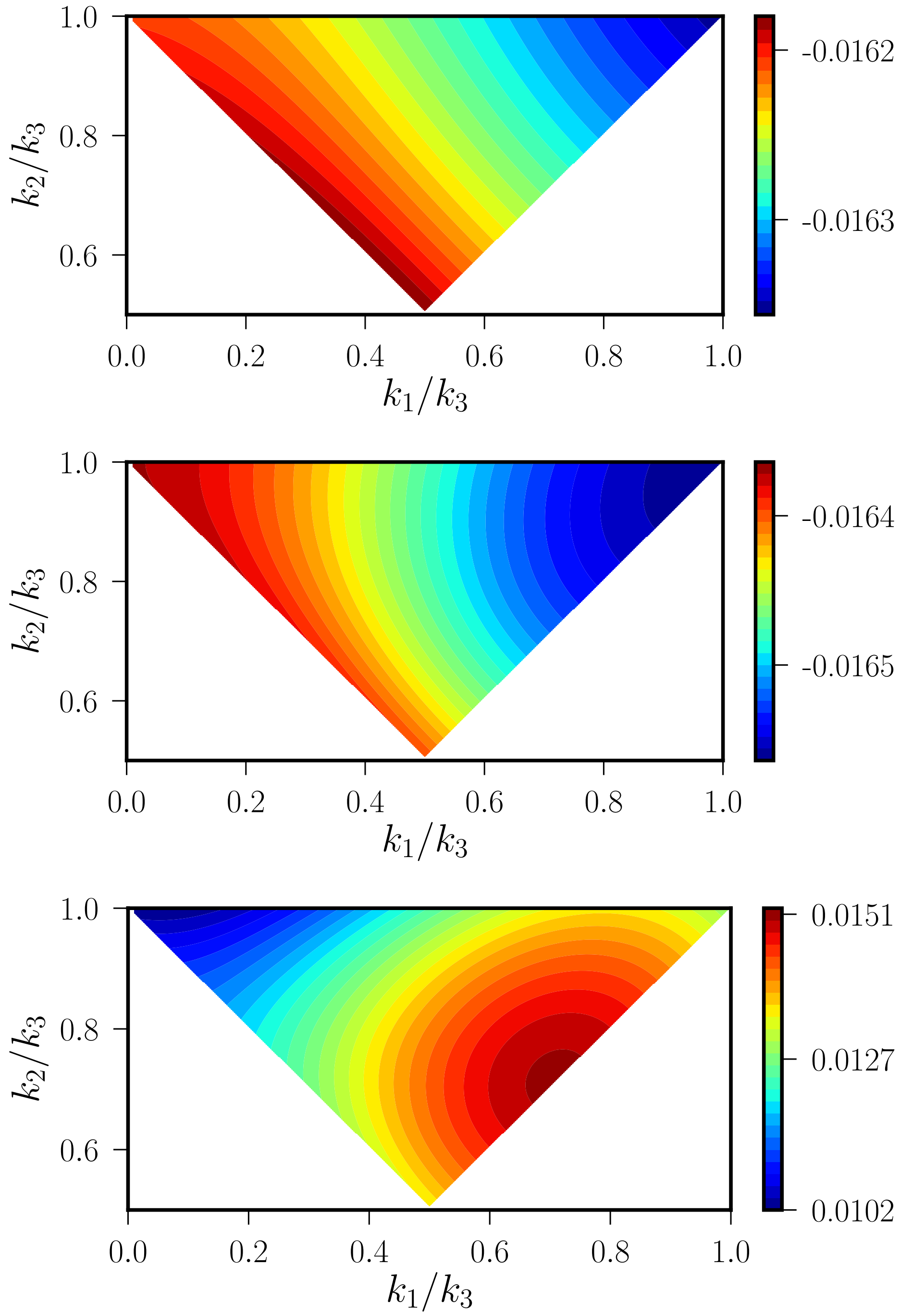

Figure 1.4: The density plots of the non-Gaussianity parameter $f_{\rm NL}$ arising in the Starobinsky model obtained numerically (on top) and analytically using the slow roll approximation (in the middle) have been plotted in the k_1/k_3-k_2/k_3-plane. The ranges of the axes have been chosen so that all the possible shapes of the triangles formed by the wave vectors $\boldsymbol{k}_1$, $\boldsymbol{k}_2$ and $\boldsymbol{k}_3$ are covered. We have also illustrated the relative difference between analytical and numerical estimates (at the bottom). As we can see, the error is of the order of $1\,\%$ and it can be attributed to the slow roll approximation used in arriving at the analytical form for $f_{\rm NL}$.

constituent wave vectors [51]. (As in the case of the inflationary power spectra, we have made the numerical code to arrive at the scalar bispectrum available at the URL: https://gitlab.com/ragavendrahv/pbs.git.) In Fig. 1.4, we have presented the $f_{_{\rm NL}}(\boldsymbol{k}_1, \boldsymbol{k}_2, \boldsymbol{k}_3)$ computed numerically using this setup for the Starobinsky model. We have also illustrated the corresponding analytical estimate, which is arrived at using the slow roll approximation. The shapes and amplitudes of the numerical and analytical estimates match closely and, in the figure, we have quantified the extent of matching by plotting the relative difference over the same range of wave numbers. We find that the code computes $f_{_{\rm NL}}$ to an accuracy of order 1%. We should mention that the code is also optimized to run in multi-threaded setups and can be modified to compute $f_{_{\rm NL}}$ not just for creating density plots (as in Fig. 1.4), but also focus on certain limits of the configuration of wave numbers, such as the equilateral and squeezed limits. We have utilized this package for examining non-Gaussianities in models that involve non-trivial evolution of the modes and hence are not readily solvable by the analytical methods. We shall discuss these models in subsequent chapters.

1.2 OBSERVATIONAL PROBES

Having understood the computation of the predictions of inflationary models at the level of two-point and three-point correlations, we shall now turn to a discussion on comparing them against observations. In this section, we shall describe the observational probes and datasets that help us constrain the models and the relevant parameters. We shall discuss three such probes that we have used in this thesis, *viz.* anisotropies in the CMB, constraints on population of PBHs, and the current and future constraints on the amplitude of GWs. As we shall see, the CMB provides the strongest constraint on the amplitudes and shapes of the primordial power spectra on large scales, whereas PBHs and GWs provide relatively weaker bounds on them.

1.2.1 Anisotropies in the CMB and constraints on the large scales

First, let us consider the data of the anisotropies in the CMB. The measurements of the anisotropies in the temperature and polarization of the CMB by the Planck mission has been the most efficient dataset thus far in constraining the inflationary models [6]. We have used the 2018 release of the Planck mission containing the likelihoods of anisotropies in temperature and E-mode polarization (*i.e.* TT, TE and EE) to arrive at bounds on the inflationary models of interest [62]. The exact likelihoods we have used are Plik-TTTEEE (plik_rd12_HM_v22b_TTTEEE) for correlations over the higher multipoles ℓ, lowT (commander_dx12_v3_2_29) for low-ℓ TT correlations, and lowE (simall_100×143_offlike5_EE_Aplanck_B) for low-ℓ EE correlations. We have also included the lensing likelihood (smicadx12_Dec5_ftl_mv2_ndclpp_p_teb_consext8) that captures the effect of gravitational lensing on the above correlations particularly over the high multipoles. We have used the setup of CosmoMC, a widely used package, to compare our models of interest against this dataset [63]. We have coupled the Fortran code we have developed to compute power spectra, with the part of CosmoMC, called CAMB, that computes the angular power spectra of the CMB [64]. We have modified CAMB with our code such that the primordial power scalar and tensor spectra are no longer the default power law functions but numerically computed as per the predictions of the models of interest. Such a setup allows us to compare models with features over larger scales against the CMB data and arrive at constraints on the relevant parameters that describe the inflationary models of interest. We should mention that, when we compare the predictions of the inflationary models with the CMB data, we shall assume that the background cosmology is described by the standard Λ-cold dark matter (ΛCDM) model.

Often, when comparing against the cosmological data, the primordial scalar and tensor power spectra are assumed to be of the power law form. The power spectra are usually written as

$$\mathcal{P}_{\rm S}(k) = A_{\rm S}\left(\frac{k}{k_*}\right)^{n_{\rm S}-1}, \tag{1.30a}$$
$$\mathcal{P}_{\rm T}(k) = r\,\mathcal{P}_{\rm S}(k_*), \tag{1.30b}$$

where $A_{\rm S}$, $n_{\rm S}$ and r are three parameters that describe the shape and amplitudes of the spectra. The parameter $A_{\rm S}$ is the amplitude of the scalar power at the pivot scale, which is typically taken to be $k_* = 5\times 10^{-2}\,{\rm Mpc}^{-1}$ (or, in some instances, to be $k_* = 2\times 10^{-3}\,{\rm Mpc}^{-1}$). The parameter $n_{\rm S}$ is called the scalar spectral index, which quantifies the tilt of the spectrum at the pivot scale. It is generally defined as

$$n_{\rm S} - 1 = \frac{{\rm d}\ln\mathcal{P}_{\rm S}}{{\rm d}\ln k}, \tag{1.31}$$

which for the case of the spectrum in power law form reduces to a constant. The parameter r is known as the tensor-to-scalar ratio, which characterizes the amplitude of the tensor power with respect to the scalar power. We have compared the above spectra with the Planck CMB data and have reproduced the constraints on these parameters as arrived at by Planck team [6]. In Fig. 1.5, we have presented the 1-σ and 2-σ contours of the posterior distributions on the parameters $A_{\rm S}$, $n_{\rm S}$ and r. The plots in the figure have been obtained using a python package called GetDist [65]. We have obtained the best fit and 1-σ bounds on the scalar amplitude to be $A_{\mathrm{s}} = (2.10 \pm 0.29) \times 10^{-9}$. We have also reproduced the well known result of $n_{\mathrm{s}} = 0.9659 \pm 0.0042$, which strongly implies a deviation from strictly scale invariant behavior and a small red tilt of the scalar power spectrum. Besides, we obtain the upper bound on the tensor-to-scalar ratio to be $r < 0.055$. We shall remark further about the constraint on r later in the section. It is worth noting at this point that, in the case of slow roll inflation, one can utilize the expressions of the scalar and tensor power spectra arrived at using slow roll approximation [*cf.* Eq. (1.17)], to estimate the predictions on the parameters n_{s} and r. On using the expression of scalar power spectrum given in Eq. (1.17a) and the definition of n_{s} in Eq. (1.31), one can show that the spectral index in slow roll approximation can be written in terms of the slow roll parameters as $n_{\mathrm{s}} = 1 - 2\,\epsilon_1 - \epsilon_2$. Similarly, upon utilizing the expressions of the scalar and tensor power spectra [*cf.* Eq. (1.17)], we can express the tensor-to-scalar ratio in slow roll approximation to be $r = 16\,\epsilon_1$. These expressions, along with the constraints on these parameters, help us gain an idea of the typical values of slow roll parameters favored by the data, *i.e.* $\epsilon_n \lesssim \mathcal{O}(10^{-2})$.

Let us now turn to the comparison of Starobinsky model (1.5) with the Planck data at the level of the power spectra. To perform such an exercise, we have replaced the default power law forms in CosmoMC for the primordial scalar and tensor power spectra with the corresponding numerical power spectra arising from the Starobinsky model. There is only one parameter describing the model, *viz.* V_0, which sets the energy scale of the potential and hence determines the amplitudes of the power spectra. We have constrained the parameter using the above mentioned likelihoods and illustrated the bounds on the various parameters in Fig. 1.6. The contours in Fig. 1.6 are the 1-σ and 2-σ regions of the marginalized posterior distribution for the standard background cosmological parameters and V_0. We can infer that the inflationary parameter of our interest V_0 is well constrained with the best fit value and 1-σ bounds being $V_0 = (1.10 \pm 0.05) \times 10^{-9}$. In Fig. 1.7, we have presented CMB angular power spectrum C_ℓ corresponding to these best-fit values.

Apart from constraints on the primordial power spectra, the Planck CMB data

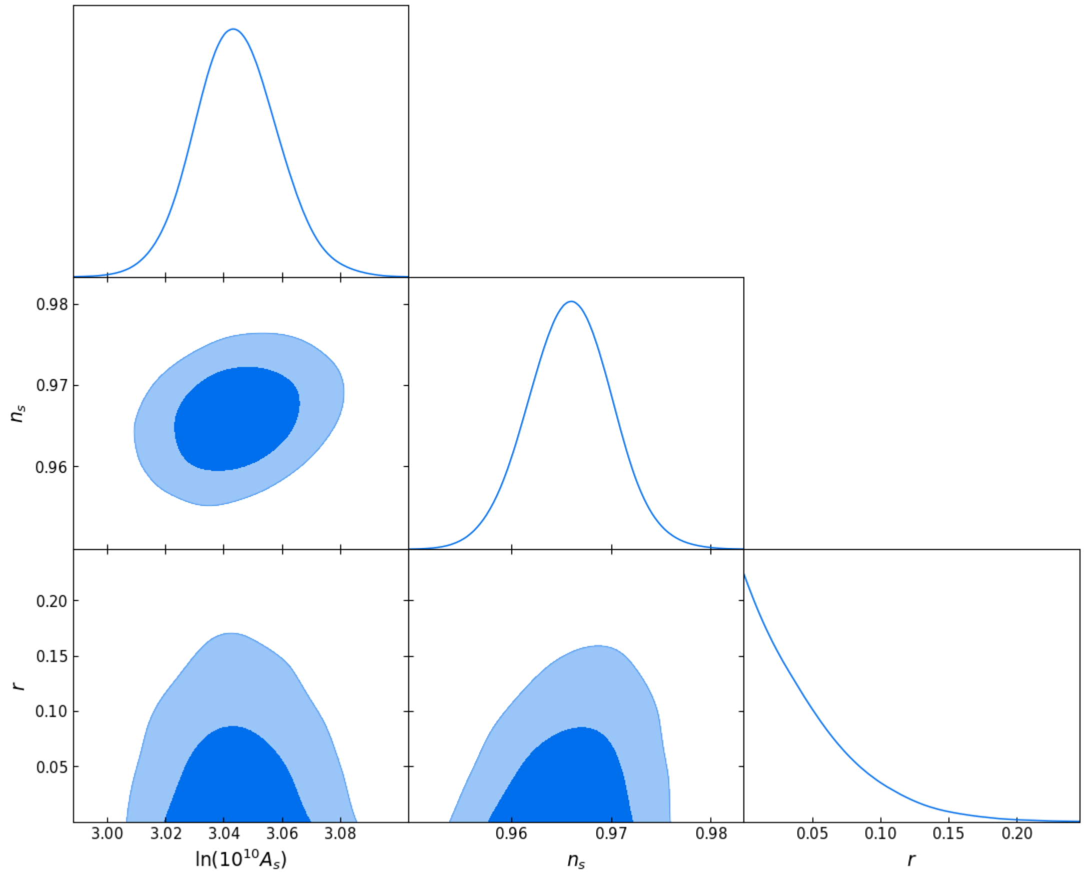

Figure 1.5: We have presented the constraints on the parameters describing the power law primordial scalar and tensor power spectra, *viz.* the primordial scalar amplitude A_{s}, the scalar spectral index n_{s} and the tensor-to-scalar ratio r, arrived at from the recent Planck CMB data. Note that the two contours (in dark and light blue) correspond to the 1-σ and 2-σ posterior distributions, obtained after having marginalized over the other parameters involved.

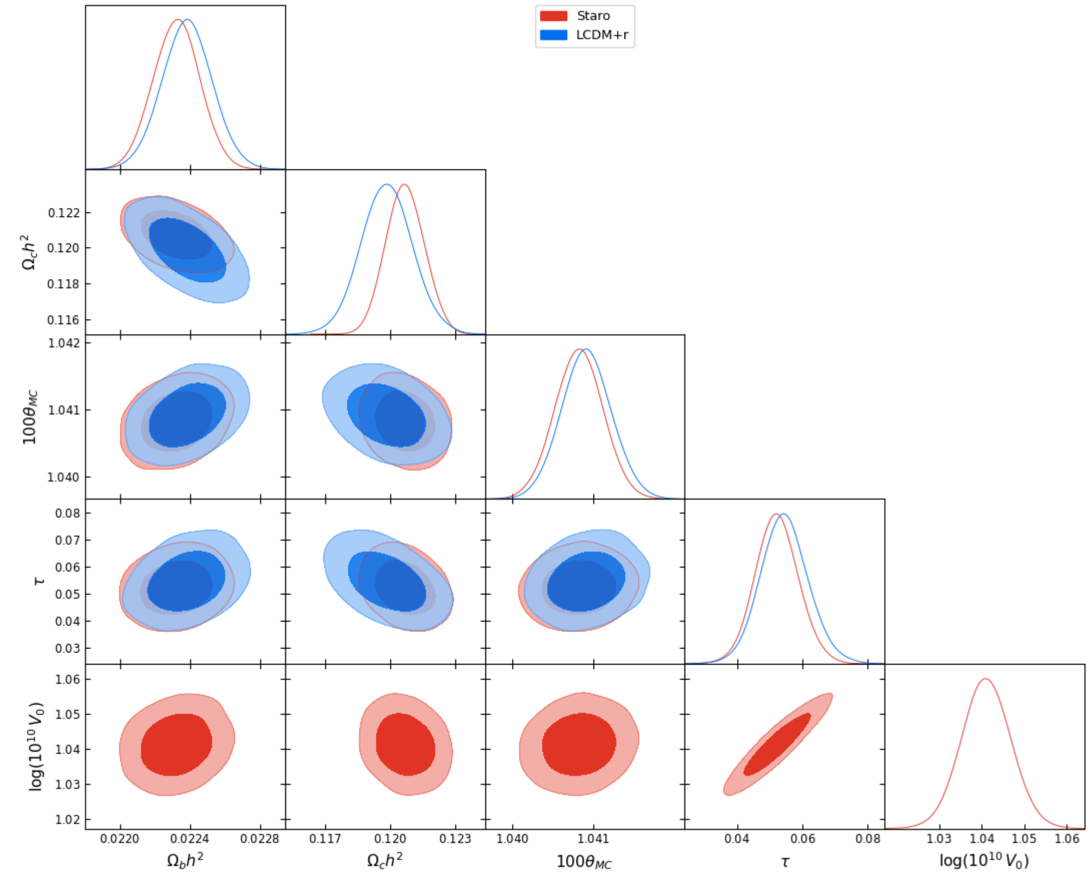

Figure 1.6: We have presented the contours of the marginalized posterior distribution of the background cosmological parameters, with inflation described by the Starobinsky model (in red), as constrained by the recent CMB data from Planck. For comparison, we have also included the constraints arrived at upon assuming the primordial spectra to be of the power law form [*cf.* Eqs. (1.30)]. In both the cases, we have assumed that the background cosmology is described by the standard ΛCDM model.

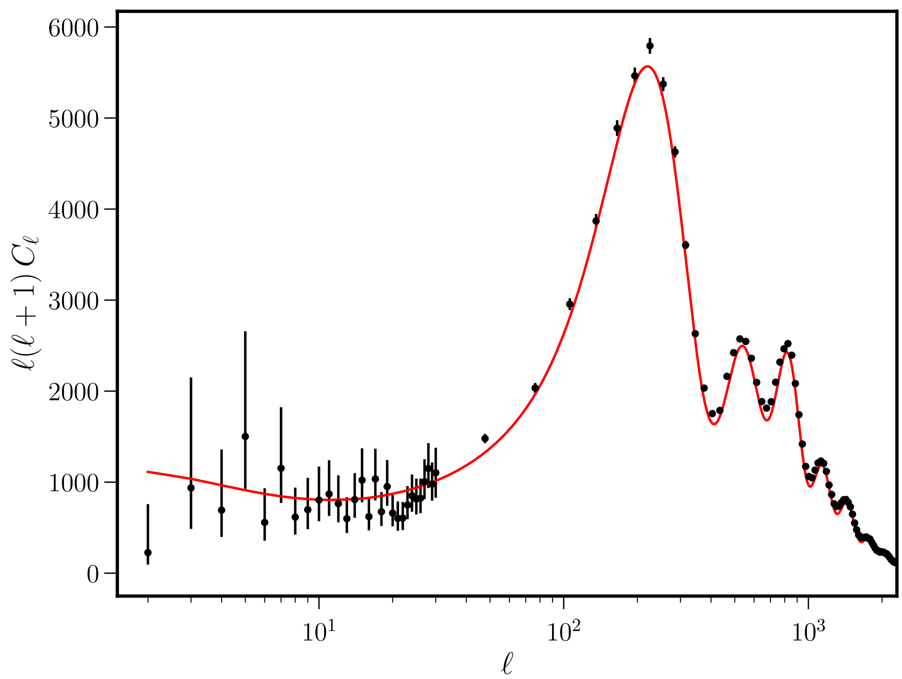

Figure 1.7: The angular power spectrum $\ell\,(\ell+1)\,C_\ell$ of the TT anisotropies of the CMB as predicted by the Starobinsky model has been plotted (in red) along with the binned data points from the Planck 2018 dataset (in black). We have compared the Starobinsky model against the Planck data and have used the best-fit values of the model parameters to arrive at the angular power spectrum.

allows us to arrive at constraints on the scalar non-Gaussianity parameter $f_{_{\rm NL}}$ as well. However, there are no strict constraints on $f_{_{\rm NL}}$, but rather relatively weaker bounds on its amplitude [58]. We should also point out that unlike the power spectra, the constraints on $f_{_{\rm NL}}$ are not specific to models, but rather arrived at using templates that are suggestive of the shapes of $f_{_{\rm NL}}$ expected from typical models of inflation. Hence, we should be careful in interpreting these constraints for the predictions of specific inflationary models.

To constrain the primordial non-Gaussianities using the CMB data, the standard templates for the scalar bispectrum that are often used in the literature are as follows [66–68]:

$$G^{\rm local}(k_1,k_2,k_3) = -\frac{3}{10}\,(2\,\pi)^4\, f_{_{\rm NL}}^{\rm local}\left[\frac{\mathcal{P}_{_{\rm S}}(k_1)\,\mathcal{P}_{_{\rm S}}(k_2)}{k_1^3\,k_2^3} + \text{two permutations}\right], \tag{1.32a}$$

$$\begin{aligned} G^{\rm equil}(k_1,k_2,k_3) &= \frac{9}{10}\,(2\,\pi)^4\, f_{_{\rm NL}}^{\rm equil}\biggl\{\frac{\mathcal{P}_{_{\rm S}}(k_1)\,\mathcal{P}_{_{\rm S}}(k_2)}{k_1^3\,k_2^3} + \frac{\mathcal{P}_{_{\rm S}}(k_2)\,\mathcal{P}_{_{\rm S}}(k_3)}{k_2^3\,k_3^3}] \\ &\quad + \frac{\mathcal{P}_{_{\rm S}}(k_1)\,\mathcal{P}_{_{\rm S}}(k_3)}{k_1^3\,k_3^3} + \frac{[\mathcal{P}_{_{\rm S}}(k_1)\,\mathcal{P}_{_{\rm S}}(k_2)\,\mathcal{P}_{_{\rm S}}(k_3)]^{2/3}}{k_1^2\,k_2^2\,k_3^2} \\ &\quad - \left[\frac{\mathcal{P}_{_{\rm S}}^{1/3}(k_1)\,\mathcal{P}_{_{\rm S}}^{2/3}(k_2)\,\mathcal{P}_{_{\rm S}}(k_3)}{k_1\,k_2^2\,k_3^3} + \text{five permutations}\right]\biggr\}, \end{aligned} \tag{1.32b}$$

$$\begin{aligned} G^{\rm ortho}(k_1,k_2,k_3) &= \frac{27}{10}\,(2\,\pi)^4\, f_{_{\rm NL}}^{\rm ortho}\biggl\{\frac{\mathcal{P}_{_{\rm S}}(k_1)\,\mathcal{P}_{_{\rm S}}(k_2)}{k_1^3\,k_2^3} + \frac{\mathcal{P}_{_{\rm S}}(k_2)\,\mathcal{P}_{_{\rm S}}(k_3)}{k_2^3\,k_3^3}] \\ &\quad + \frac{\mathcal{P}_{_{\rm S}}(k_1)\,\mathcal{P}_{_{\rm S}}(k_3)}{k_1^3\,k_3^3} + \frac{8\,[\mathcal{P}_{_{\rm S}}(k_1)\,\mathcal{P}_{_{\rm S}}(k_2)\,\mathcal{P}_{_{\rm S}}(k_3)]^{2/3}}{3\,k_1^2\,k_2^2\,k_3^2} \\ &\quad - \left[\frac{\mathcal{P}_{_{\rm S}}(k_1)^{1/3}\mathcal{P}_{_{\rm S}}(k_2)^{2/3}\mathcal{P}_{_{\rm S}}(k_3)}{k_1\,k_2^2\,k_3^3} + \text{five permutations}\right]\biggr\}. \end{aligned} \tag{1.32c}$$

Note that the bispectra in these templates are expressed as functions of power spectra with the non-Gaussianity parameter $f_{_{\rm NL}}$ retained as a number, independent of wave numbers. The constraints on the parameters $(f_{_{\rm NL}}^{\rm local}, f_{_{\rm NL}}^{\rm equil}, f_{_{\rm NL}}^{\rm ortho})$ appearing in the above mentioned templates are found to be [58]

$$f_{_{\rm NL}}^{\rm local} = -0.9 \pm 5.1, \tag{1.33a}$$

$$f_{_{\rm NL}}^{\rm equil} = -26 \pm 47, \tag{1.33b}$$

$$f_{_{\rm NL}}^{\rm ortho} = -38 \pm 24. \tag{1.33c}$$

We should clarify that these constraints have been arrived at by comparing each of the above templates *separately* with the CMB data. It should be evident from Fig. 1.4 that, in the Starobinsky model, the quantity $f_{\rm NL}$ has an equilateral shape, *i.e.* its value peaks when $k_1 = k_2 = k_3$. The above constraints then suggest that the Starobinsky model is also consistent with the CMB data at the level of non-Gaussianities. In later chapters, we shall discuss scalar bispectra arising in models that do not necessarily fit any of these templates and have a more complicated dependence on wave numbers. We shall also discuss a different definition of $f_{\rm NL}$ that enables us to account for such non-trivial behavior in calculations without resorting to specific templates.

Let us now discuss the constraints on the primordial tensor power spectrum from the CMB data. The direct imprints of the tensor perturbations on the CMB — the so-called B-mode — remains the holy grail in cosmology. Since they are yet to be detected, as of now, we only have an upper bound on the amplitude of the primary GWs. As we mentioned earlier, the bound is usually expressed in terms of the tensor-to-scalar ratio r [*cf.* Eq. (1.30b)]. In fact, the quantity r is constrained at a specific wave number, often chosen to be the pivot scale k_* at which the scalar amplitude is well known. As we mentioned earlier, for power law primordial spectra, we have obtained the constraint $r < 0.055$, which is consistent with the latest bound by Planck [6]. We should point out that the most recent data from the BICEP/Keck observations together with the Planck data constrains the tensor-to-scalar ratio to be $r < 0.036$ at $k_* = 0.05\,{\rm Mpc}^{-1}$ [69]. This implies that the tensor power has to be lower than the scalar power by at least by an order of magnitude over the CMB scales. Since, the scalar amplitude is tightly constrained to be $A_{\rm S} = 2.10 \times 10^{-9}$, as mentioned earlier, the tensor amplitude has to be less than 10^{-10}. For the Starobinsky model, we do not have this explicit parameter to constrain. However, the amplitude of tensor power predicted for the best fit value of the parameter V_0 is $\mathcal{O}(10^2)$ less than that of the scalar power, as can be seen in Fig. 1.3. These bounds suggest that the strength of the primary GWs over the CMB scales is constrained to be highly suppressed at the level of current observational precision.

1.2.2 Production of PBHs

Another probe that helps us constrain models indirectly over scales much smaller than the CMB scales are PBHs. These are black holes that are hypothesized to have formed by direct collapse of energy density due to scalar perturbations of large amplitudes (see, for instance, Refs. [8, 70–72]). Such PBHs are also regarded as candidates for dark matter in the current universe (for a review, see Ref. [9]). There are several indirect constraints on the amount of such PBHs that could constitute the dark matter density today (see Refs. [12, 73] and references therein). Hence, any model of inflation that generates scalar power of large amplitudes over small scales are bound to be constrained by this phenomenon.

To understand the basics of this phenomenon, let us begin by recalling a few essentials. Scales with wave numbers greater than $k \simeq 10^{-2}\,\mathrm{Mpc}^{-1}$ renter the Hubble radius during the radiation dominated epoch. When these modes reenter the Hubble radius, the perturbations in the matter density at the corresponding scales collapse to form structures. We shall assume that the density contrast in matter characterized by the quantity δ is a Gaussian random variable described by the probability density

$$\mathcal{P}(\delta) = \frac{1}{\sqrt{2\,\pi\,\sigma^2}}\,\exp\left(-\frac{\delta^2}{2\,\sigma^2}\right), \tag{1.34}$$

where σ^2 is the variance of the spatial density fluctuations. Let us assume that perturbations with a density contrast beyond a certain threshold, say, δ_{c}, are responsible for the formation of PBHs. In such a case, the fraction, say, β, of the density fluctuations that collapse to form PBHs is described by the integral (in this context, see the reviews [9, 74–76])

$$\beta = \int_{\delta_{\mathrm{c}}}^{1} \mathrm{d}\delta\,\mathcal{P}(\delta) \simeq \frac{1}{2}\left[1 - \mathrm{erf}\left(\frac{\delta_{\mathrm{c}}}{\sqrt{2\,\sigma^2}}\right)\right], \tag{1.35}$$

where $\mathrm{erf}(z)$ denotes the error function. Note that the lower limit of the above integral is the threshold value of the density contrast beyond which matter is expected to collapse to form PBHs. We should clarify here that the value of δ_{c} is not unique and it is expected to depend on the amplitude of the perturbation at a given scale (see Refs. [77, 78]; in this context, also see the recent discussions [75, 79–83]). The choice of δ_{c} becomes important for the reason that the extent of PBHs formed is exponentially sensitive to its value. In order to calculate the extent of PBHs formed, we shall work with the following values of δ_{c}: $1/3$, 0.35 and 0.4.

During the radiation dominated epoch, the matter power spectrum $P_\delta(k)$ and the inflationary scalar power spectrum $\mathcal{P}_{_{\mathrm{S}}}(k)$ are related through the expression

$$P_\delta(k) = \frac{16}{81}\left(\frac{k}{aH}\right)^4 \mathcal{P}_{_{\mathrm{S}}}(k). \tag{1.36}$$

The variance in the spatial density fluctuations σ^2, which determines the fraction β of PBHs formed [*cf.* Eq. (1.35)], can be expressed as an integral over the matter power spectrum $P_\delta(k)$. In order to introduce a length scale, say, R, the variance is smoothened over the scale with the aid of a window function $W(k\,R)$. The variance $\sigma^2(R)$ can then be written as

$$\sigma^2(R) = \int_0^\infty \frac{\mathrm{d}k}{k}\, P_\delta(k)\, W^2(k\,R), \tag{1.37}$$

and we shall work with a Gaussian window function of the form $W(k\,R) = \mathrm{e}^{-(k^2\,R^2)/2}$.

There remains the task of relating the scale R to the mass, say, M, of the PBHs formed. Let M_{H} denote the mass within the Hubble radius H^{-1} at a given time. It is reasonable to suppose that a certain fraction of the total mass within the Hubble radius, say, $M = \gamma_*\,M_{\mathrm{H}}$, goes on to form PBHs when a mode with wave number k reenters the Hubble radius. The quantity γ_* that has been introduced reflects the efficiency of the collapse. In the absence of any other scale, it seems natural to choose $k = R^{-1}$, and make use of the fact that $k = a\,H$ when the modes reenter the Hubble radius, to finally obtain the relation between R and M. One can show that R and M are related as follows:

$$R = \frac{2^{1/4}}{\gamma_*^{1/2}} \left(\frac{g_{*,k}}{g_{*,\mathrm{eq}}}\right)^{1/12} \left(\frac{1}{k_{\mathrm{eq}}}\right) \left(\frac{M}{M_{\mathrm{eq}}}\right)^{1/2}, \tag{1.38}$$

where k_{eq} is the wave number that reenters the Hubble radius at the epoch of radiation-matter equality, and M_{eq} denotes the mass within the Hubble radius at equality. Also, the quantities $g_{*,k}$ and $g_{*,\mathrm{eq}}$ represent the number of relativistic degrees of freedom at the times of PBH formation and radiation-matter equality, respectively. It can be easily determined that $M_{\mathrm{eq}} = 5.83\times 10^{47}$ kg, so that we can express the above relation between R and M in terms of the solar mass $M_\odot$ as follows:

$$R = 4.72 \times 10^{-7} \left(\frac{\gamma_*}{0.2}\right)^{-1/2} \left(\frac{g_{*,k}}{g_{*,\mathrm{eq}}}\right)^{1/12} \left(\frac{M}{M_\odot}\right)^{1/2} \mathrm{Mpc}. \tag{1.39}$$

On using the above arguments, we can arrive at the fraction of PBHs, say, f_{PBH}, that contribute to the dark matter density today. The quantity $f_{\mathrm{PBH}}(M)$ can be expressed as

$$f_{\mathrm{PBH}}(M) = 2^{1/4}\,\gamma_*^{3/2}\,\beta(M) \left(\frac{\Omega_{\mathrm{m}}\,h^2}{\Omega_{\mathrm{c}}\,h^2}\right) \left(\frac{g_{*,k}}{g_{*,\mathrm{eq}}}\right)^{-1/4} \left(\frac{M}{M_{\mathrm{eq}}}\right)^{-1/2}, \tag{1.40}$$

where Ω_{m} and Ω_{c} are the dimensionless parameters describing the matter and dark cold matter densities, with the Hubble parameter, as usual, expressed as $H_0 = 100\,h\,\mathrm{km}\,\mathrm{sec}^{-1}\,\mathrm{Mpc}^{-1}$. In our calculations, we shall choose $\gamma_* = 0.2$, $g_{*,k} = 106.75$ and $g_{*,\mathrm{eq}} = 3.36$ and set $\Omega_{\mathrm{m}}\,h^2 = 0.14$, $\Omega_{\mathrm{c}}\,h^2 = 0.12$, with the last two being the best fit values from the recent Planck data [38, 84]. On substituting these values, one can arrive at the following expression for $f_{\rm PBH}(M)$:

$$f_{\rm PBH}(M) = \left(\frac{\gamma}{0.2}\right)^{3/2} \left(\frac{\beta(M)}{1.46 \times 10^{-8}}\right) \left(\frac{g_{*,k}}{g_{*,\rm eq}}\right)^{-1/4} \left(\frac{M}{M_\odot}\right)^{-1/2}. \tag{1.41}$$

Given a primordial power spectrum $\mathcal{P}_{\rm S}(k)$, we can utilize the relations (1.36) and (1.37) to arrive at the quantity $\sigma^2(R)$. Then, using the relation (1.38), we can determine σ^2 as a function of M and utilize the result (1.35) to obtain $\beta(M)$. With $\beta(M)$ at hand, we can use the relation (1.41) to finally arrive at $f_{\rm PBH}(M)$ for a given inflationary scalar power spectrum.

In later chapters, we shall discuss the predictions for $f_{\rm PBH}$ arising in certain classes of inflationary models and examine them against the constraints on the quantity.

1.2.3 Generation of secondary GWs

Yet another observation that helps us constrain inflationary models is that of GWs. We had earlier discussed the power spectrum of the primary tensor perturbations arising during inflation and had also described the constraints on the tensor-to-scalar ratio r over the CMB scales. However, on small scales, there are relatively weaker constraints on the strength of the primordial tensor perturbations that could be detected as GWs today (see, for instance, Refs. [85–87]; for a review see, Ref. [14] and references therein). Moreover, in models that predict high amplitudes of scalar perturbations at small scales, the tensor perturbations sourced by the scalars at the second order may get amplified enough to have detectable strengths. These are known as secondary GWs (for early discussions in this context, see for instance, Refs. [88–91]; for recent reviews, see for example, Refs. [11, 92]). In this subsection, we shall outline the details of computing the spectral density of secondary GWs in a given model of inflation.

Earlier, we had described the scalar and tensor perturbations at the first order in terms of the curvature perturbation $\mathcal{R}$ and the quantity γ_{ij}. It is well known that, at the linear order, the scalar and tensor perturbations evolve independently, with their evolution being governed by the corresponding equations of motion, *viz.* Eqs. (1.11). However, one finds that, at the second order, the tensor perturbations are sourced by quadratic terms involving the first order scalar perturbations. These contributions due to the scalar perturbations become important particularly when the amplitude of the scalar power spectrum is boosted over small scales such as in the situations leading to enhanced formation of PBHs. In this subsection, we shall describe the calculation of the dimensionless spectral density parameter associated with the GWs, say, $\Omega_{\rm GW}$, generated due to the scalar perturbations.

Let us begin by outlining the primary steps towards the calculation of $\Omega_{\rm GW}(f)$, where f is the frequency associated with the wave number k. We shall start with the following perturbed metric:

$$\mathrm{d}s^2 = a^2(\eta)\left\{-(1+2\,\Phi)\,\mathrm{d}\eta^2 + \left[(1-2\,\Psi)\,\delta_{ij} + \frac{1}{2}\,h_{ij}\right]\,\mathrm{d}x^i\mathrm{d}x^j\right\}, \tag{1.42}$$

where Φ and Ψ are the Bardeen potentials describing the scalar perturbations at the first order, while the quantity h_{ij} represents the second order tensor perturbations. We should clarify that we have denoted the second order tensor perturbations as h_{ij} in order to distinguish them from the first order tensor perturbations γ_{ij} which we had introduced earlier. The transverse and traceless nature of the tensor perturbations implies that $\partial^i\,h_{ij} = 0$ and $h^i_i = 0$. In our discussion below, we shall assume that anisotropic stresses are absent so that $\Phi = \Psi$.

The tensor perturbations h_{ij} can be decomposed in terms of the Fourier modes, say, $h_{\boldsymbol{k}}$, as

$$h_{ij}(\eta,\boldsymbol{x}) = \int \frac{\mathrm{d}^3\boldsymbol{k}}{(2\,\pi)^{3/2}}\,\left[e^+_{ij}(\boldsymbol{k})\,h^+_{\boldsymbol{k}}(\eta) + e^\times_{ij}(\boldsymbol{k})\,h^\times_{\boldsymbol{k}}(\eta)\right]\,\mathrm{e}^{i\,\boldsymbol{k}\cdot\boldsymbol{x}}, \tag{1.43}$$

where $e^+_{ij}(\boldsymbol{k})$ and $e^\times_{ij}(\boldsymbol{k})$ denote the polarization tensors which have non-zero components in the plane perpendicular to the direction of propagation, *viz.* $\hat{\boldsymbol{k}}$. The polarization tensors $e^+_{ij}(\boldsymbol{k})$ and $e^\times_{ij}(\boldsymbol{k})$ can be expressed in terms of the set of orthogonal unit vectors $(e(\boldsymbol{k}), \bar{e}(\boldsymbol{k}), \hat{\boldsymbol{k}})$ in the following manner (see, for instance, the review [10]):

$$e^+_{ij}(\boldsymbol{k}) = \frac{1}{\sqrt{2}}\,\left[e_i(\boldsymbol{k})\,e_j(\boldsymbol{k}) - \bar{e}_i(\boldsymbol{k})\,\bar{e}_j(\boldsymbol{k})\right], \tag{1.44a}$$

$$e^\times_{ij}(\boldsymbol{k}) = \frac{1}{\sqrt{2}}\,\left[e_i(\boldsymbol{k})\,\bar{e}_j(\boldsymbol{k}) + \bar{e}_i(\boldsymbol{k})\,e_j(\boldsymbol{k})\right]. \tag{1.44b}$$

The orthonormal nature of the vectors $e(\boldsymbol{k})$ and $\bar{e}(\boldsymbol{k})$ lead to the normalization condition: $e^\lambda_{ij}(\boldsymbol{k})\,e^{\lambda',ij}(\boldsymbol{k}) = \delta^{\lambda\lambda'}$, where λ and λ' can be either $+$ or $\times$.

The equation of motion governing the Fourier modes $h_{\boldsymbol{k}}$ can be arrived at using the second order Einstein equations describing the tensor perturbation h_{ij} and the Bardeen equation describing the scalar perturbation Ψ at the first order (see, for example, Refs. [88, 89]; for recent discussions, see Refs. [87, 93–95]). One finds that the equation governing $h_{\boldsymbol{k}}$ can be written as

$$h_{\boldsymbol{k}}^{\lambda\,\prime\prime} + 2\,\mathcal{H}\,h_{\boldsymbol{k}}^{\lambda\,\prime} + k^2\,h_{\boldsymbol{k}}^{\lambda} = S_{\boldsymbol{k}}^{\lambda} \tag{1.45}$$

with the source term $S_{\boldsymbol{k}}^{\lambda}$ being given by

$$\begin{aligned} S_{\boldsymbol{k}}^{\lambda}(\eta) \;=\; & 4\int \frac{\mathrm{d}^3\boldsymbol{p}}{(2\,\pi)^{3/2}}\,e^{\lambda}(\boldsymbol{k},\boldsymbol{p})\,\biggl\{2\,\Psi_{\boldsymbol{p}}(\eta)\,\Psi_{\boldsymbol{k}-\boldsymbol{p}}(\eta) \\ & + \frac{4}{3\,(1+w)\,\mathcal{H}^2}\,\left[\Psi_{\boldsymbol{p}}'(\eta) + \mathcal{H}\,\Psi_{\boldsymbol{p}}(\eta)\right]\,\left[\Psi_{\boldsymbol{k}-\boldsymbol{p}}'(\eta) + \mathcal{H}\,\Psi_{\boldsymbol{k}-\boldsymbol{p}}(\eta)\right]\biggr\}, \end{aligned} \tag{1.46}$$

where, evidently, $\Psi_{\boldsymbol{k}}$ represents the Fourier modes of the Bardeen potential, while $\mathcal{H}$ and w denote the conformal Hubble parameter and the equation of state parameter describing the universe at the conformal time η. Also, for convenience, we have defined the quantity $e^{\lambda}(\boldsymbol{k},\boldsymbol{p}) = e_{ij}^{\lambda}(\boldsymbol{k})\,p^i\,p^j$. While discussing the formation of PBHs earlier, we had assumed that the scales of our interest reenter the Hubble radius during the epoch of radiation domination. In such a case, we have $w = 1/3$ and $\mathcal{H} = 1/\eta$. Moreover, during radiation domination, it is well known that we can express the Fourier modes $\Psi_{\boldsymbol{k}}$ of the Bardeen potential in terms of the inflationary Fourier modes $\mathcal{R}_{\boldsymbol{k}}$ of the curvature perturbations generated during inflation through the relation

$$\Psi_{\boldsymbol{k}}(\eta) = \frac{2}{3}\,\mathcal{T}(k\,\eta)\,\mathcal{R}_{\boldsymbol{k}}, \tag{1.47}$$

where $\mathcal{T}(k\,\eta)$ is the transfer function given by

$$\mathcal{T}(k\,\eta) = \frac{9}{(k\,\eta)^2}\left[\frac{\sin\left(k\,\eta/\sqrt{3}\right)}{k\,\eta/\sqrt{3}} - \cos\left(k\,\eta/\sqrt{3}\right)\right]. \tag{1.48}$$

Utilizing the Green's function corresponding to the tensor modes during radiation domination, we can express the inhomogeneous contribution to $h_{\boldsymbol{k}}^{\lambda}$ as [95]

$$\begin{aligned} h_{\boldsymbol{k}}^{\lambda}(\eta) \;=\; & \frac{4}{9\,k^3\,\eta}\int \frac{\mathrm{d}^3\boldsymbol{p}}{(2\,\pi)^{3/2}}\,e^{\lambda}(\boldsymbol{k},\boldsymbol{p})\,\mathcal{R}_{\boldsymbol{p}}\,\mathcal{R}_{\boldsymbol{k}-\boldsymbol{p}} \\ & \times \left[\mathcal{I}_c\left(\frac{p}{k},\frac{|\boldsymbol{k}-\boldsymbol{p}|}{k}\right)\,\cos\left(k\,\eta\right) + \mathcal{I}_s\left(\frac{p}{k},\frac{|\boldsymbol{k}-\boldsymbol{p}|}{k}\right)\,\sin\left(k\,\eta\right)\right], \end{aligned} \tag{1.49}$$

where the quantities $\mathcal{I}_c(v,u)$ and $\mathcal{I}_s(v,u)$ are described by the integrals

$$\mathcal{I}_c(v,u) \;=\; -4\int_0^{\infty}\mathrm{d}\tau\,\tau\,\sin\tau\,\biggl\{2\,\mathcal{T}(v\,\tau)\,\mathcal{T}(u\,\tau)$$

$$
+ \left[\mathcal{T}(v\,\tau) + v\,\tau\,\mathcal{T}_{v\tau}(v\,\tau)\right]\,\left[\mathcal{T}(u\,\tau) + u\,\tau\,\mathcal{T}_{u\tau}(u\,\tau)\right]\Big\}, \quad (1.50a)
$$

$$
\mathcal{I}_s(v,u) = 4\int_0^\infty \mathrm{d}\tau\,\tau\,\cos\tau\,\Big\{2\,\mathcal{T}(v\,\tau)\,\mathcal{T}(u\,\tau)
+ \left[\mathcal{T}(v\,\tau) + v\,\tau\,\mathcal{T}_{v\tau}(v\,\tau)\right]\,\left[\mathcal{T}(u\,\tau) + u\,\tau\,\mathcal{T}_{u\tau}(u\,\tau)\right]\Big\}, \quad (1.50b)
$$

with $\mathcal{T}_z = \mathrm{d}\mathcal{T}/\mathrm{d}z$. The above integrals can be carried out analytically and they are given by

$$
\mathcal{I}_c(v,u) = -\frac{27\,\pi}{4\,v^3\,u^3}\,\Theta\left(v+u-\sqrt{3}\right)\,(v^2+u^2-3)^2, \quad (1.51a)
$$

$$
\mathcal{I}_s(v,u) = -\frac{27}{4\,v^3\,u^3}\,(v^2+u^2-3)\,\left[4\,v\,u + (v^2+u^2-3)\,\log\left|\frac{3-(v-u)^2}{3-(v+u)^2}\right|\right], \quad (1.51b)
$$

where $\Theta(z)$ denotes the theta function. It is useful to note that $\mathcal{I}_{c,s}(v,u) = \mathcal{I}_{c,s}(u,v)$.

The power spectrum of the secondary GWs, say, $\mathcal{P}_h(k,\eta)$, generated due to the second order scalar perturbations can be defined as follows:

$$
\langle h_{\boldsymbol{k}}^\lambda(\eta)\,h_{\boldsymbol{k}'}^{\lambda'}(\eta)\rangle = \frac{2\,\pi^2}{k^3}\,\mathcal{P}_h(k,\eta)\,\delta^{(3)}(\boldsymbol{k}+\boldsymbol{k}')\,\delta^{\lambda\lambda'}. \quad (1.52)
$$

Note that $h_{\boldsymbol{k}}^\lambda$ involves products of the Fourier modes $\mathcal{R}_{\boldsymbol{k}}$ and $\mathcal{R}_{\boldsymbol{k}-\boldsymbol{p}}$ of the curvature perturbations generated during inflation [*cf.* Eq. (1.49)]. Evidently, the power spectrum $\mathcal{P}_h(k)$ of the secondary GWs will involve products of four such variables. Since, the quantity $\mathcal{R}_{\boldsymbol{k}}$ is a Gaussian random variable, we can express the four-point function in terms of the two-point functions or, equivalently, the inflationary scalar power spectrum $\mathcal{P}_{\mathrm{S}}(k)$ [*cf.* Eq. (1.12a)] as

$$
\mathcal{P}_h(k,\eta) = \frac{4}{81\,k^2\,\eta^2}\int_0^\infty \mathrm{d}v\int_{|1-v|}^{1+v}\mathrm{d}u\,\left[\frac{4\,v^2-(1+v^2-u^2)^2}{4\,u\,v}\right]^2\,\mathcal{P}_{\mathrm{S}}(k\,v)\,\mathcal{P}_{\mathrm{S}}(k\,u)
\times\left[\mathcal{I}_c(u,v)\cos(k\,\eta) + \mathcal{I}_s(u,v)\sin(k\,\eta)\right]^2. \quad (1.53)
$$

We shall now choose to average $\mathcal{P}_h(k,\eta)$ over small time scales so that the trigonometric functions in the above expressions are replaced by their average over a time period. In such a case, only the overall time dependence remains, leading to [95, 96]

$$
\overline{\mathcal{P}_h(k,\eta)} = \frac{2}{81\,k^2\,\eta^2}\int_0^\infty \mathrm{d}v\int_{|1-v|}^{1+v}\mathrm{d}u\,\left[\frac{4\,v^2-(1+v^2-u^2)^2}{4\,u\,v}\right]^2\,\mathcal{P}_{\mathrm{S}}(k\,v)\,\mathcal{P}_{\mathrm{S}}(k\,u)
\times\left[\mathcal{I}_c^2(u,v) + \mathcal{I}_s^2(u,v)\right], \quad (1.54)
$$

where the bar over $\mathcal{P}_h(k,\eta)$ implies that we have averaged over small time scales. The energy density of GWs associated with a Fourier mode corresponding to the wave number k at a time η is given by [10]

$$\rho_{\mathrm{GW}}(k,\eta) = \frac{M_{\mathrm{Pl}}^2}{8}\left(\frac{k}{a}\right)^2 \overline{\mathcal{P}_h(k,\eta)}. \tag{1.55}$$

The corresponding dimensionless spectral density parameter $\Omega_{\mathrm{GW}}(k,\eta)$ can be defined in terms of the critical density $\rho_{\mathrm{cr}}(\eta)$ as [95]

$$\Omega_{\mathrm{GW}}(k,\eta) = \frac{\rho_{\mathrm{GW}}(k,\eta)}{\rho_{\mathrm{cr}}(\eta)} = \frac{1}{24}\left(\frac{k}{\mathcal{H}}\right)^2 \overline{\mathcal{P}_h(k,\eta)}. \tag{1.56}$$

Note that the dimensionless density parameter $\Omega_{\mathrm{GW}}(k,\eta)$ above has been evaluated during the radiation dominated epoch. Once the modes are inside the Hubble radius, the energy density of GWs decrease with the expansion of the universe just as the energy density of radiation does. Upon utilizing this point, we can express $\Omega_{\mathrm{GW}}(k)$ today in terms of the above $\Omega_{\mathrm{GW}}(k,\eta)$ as follows:

$$\begin{aligned} h^2\,\Omega_{\mathrm{GW}}(k) &= \left(\frac{g_{*,k}}{g_{*,0}}\right)^{-1/3} \Omega_{\mathrm{r}}\,h^2\,\Omega_{\mathrm{GW}}(k,\eta) \\ &\simeq 1.38\times 10^{-5}\left(\frac{g_{*,k}}{106.75}\right)^{-1/3}\left(\frac{\Omega_r\,h^2}{4.16\times 10^{-5}}\right)\Omega_{\mathrm{GW}}(k,\eta), \end{aligned} \tag{1.57}$$

where Ω_{r} and $g_{*,0}$ denote the dimensionless energy density of radiation and the number of relativistic degrees of freedom today. We should point out here that, since $\mathcal{H} \propto \eta^{-1}$ during radiation domination and $\mathcal{P}_h(k,\eta) \propto \eta^{-2}$, the quantity $\Omega_{\mathrm{GW}}(k,\eta)$ in the expression (1.56) is actually independent of time. Moreover, the observable parameter today is usually expressed as a function of the frequency, say, f, which is related to the wave number k as

$$f = \frac{k}{2\,\pi} = 1.55\times 10^{-15}\left(\frac{k}{1\,\mathrm{Mpc}^{-1}}\right)\,\mathrm{Hz}. \tag{1.58}$$

The parameter Ω_{GW} can be compared and constrained against the sensitivity curves of various current and upcoming GW missions (for a review of the sensitivity curves of various missions, see Ref. [14] and the associated web-page.). In later chapters, we shall examine inflationary models that lead to twin predictions of significant amount of f_{PBH} and secondary Ω_{GW}. We shall also compare the spectra of Ω_{GW} predicted by the different models against the sensitivity curves of various observational missions. Further, we shall discuss how the computation of the bispectrum associated with the secondary tensor perturbations lends more insights about such models.

1.3 ORGANIZATION OF THE THESIS

We shall conclude this introductory chapter with an outline of the thesis. The thesis comprises of four pieces of work that analyze features in the primordial correlations which were considered because of their unique observational imprints over various ranges of scales in the current universe.

In Chap. 2, we shall present the analysis of the suppression of scalar power over the largest observable scales and the associated bispectra. We shall discuss how the scalar non-Gaussianity parameter $f_{\rm NL}$ breaks the degeneracy among the models that lead to similar features at the level of power spectrum.

In Chap. 3, we shall describe a work wherein we consider models which generate enhanced scalar power over small scales. These correspond to scales which can be constrained using PBHs and GWs. We shall also discuss the bispectra of scalar and secondary tensor perturbations in these models.

In Chap. 4, we shall consider the generation of features through an alternative mechanism of evolving perturbations from excited initial states. We shall describe the relative ease of modeling in this alternative scenario and present the possibility of generating extremely large values of $f_{\rm NL}$. We shall also discuss the serious drawback due to backreaction that plagues this mechanism.

In Chap. 5, we shall discuss a method to account for the scalar bispectrum in the predictions of the spectral density of GWs $\Omega_{\rm GW}$ from a given model of inflation. We shall reconsider the standard definition of the non-Gaussianity parameter $f_{\rm NL}$ and extend it to account for arbitrary scale dependence. Such a generalization allows us to calculate the non-Gaussian corrections to the scalar power spectrum when $f_{\rm NL}$ is scale dependent. Further, it enables us to compute the non-Gaussian contributions to $\Omega_{\rm GW}$ arising due to $f_{\rm NL}$ with non-trivial scale dependence. This opens up the possibility of constraining $f_{\rm NL}$ on small scales through its imprints on the behavior of $\Omega_{\rm GW}$.

Finally, we shall conclude in Chap. 6 with a brief summary and outlook.

We shall relegate some of the discussions to Apps. A–H.

CHAPTER 2

SUPPRESSION OF SCALAR POWER ON LARGE SCALES AND ASSOCIATED BISPECTRA

2.1 INTRODUCTION

Ever since the advent of the three-year data from the Wilkinson Microwave Anisotropy Probe (WMAP), it has been repeatedly found that a sharp drop in power at large scales roughly corresponding to the Hubble radius today improves the fit to the anisotropies in the CMB at the low multipoles (for an early analysis, see, for instance, Ref. [97]; for later discussions in this context, see Refs. [98–101]). A variety of inflationary scenarios have been constructed to generate such a drop in power on large scales (for a short list of possibilities, see Refs. [102–116]).

One of the scenarios that generates a scalar spectrum with suppressed power on large scales corresponds to a situation wherein the scalar field driving inflation starts rolling down the potential with a high velocity (for the original discussion, see Ref. [103]; for more recent discussions, see Refs. [117–121]). While the very early kinetically dominated phase does not permit accelerated expansion, the friction arising due to the expansion of the universe slows down the field, initially leading to a brief period of fast roll inflation and eventually to the standard phase of slow roll inflation. If one chooses the beginning of inflation to occur at an appropriately early time, the inflationary power spectra exhibit lower power at suitably large scales, improving the fit to the CMB data at the low multipoles [121]. However, it should be emphasized that, in such scenarios, a range of large scale modes are never inside the Hubble radius and the spectra with a suppression of power arise provided the standard Bunch-Davies initial conditions are imposed on super-Hubble scales [103, 121].

A competing inflationary scenario that, in fact, leads to sharper drop in power over large scales corresponds to a short phase of fast roll sandwiched between two epochs of slow roll inflation. Such scenarios can be further sub-divided into two categories: one wherein inflation is sustained even during the phase of fast roll and another wherein the epoch of fast roll leads to a brief departure from inflation. While the first type of scenario can be achieved in a model originally due to Starobinsky involving a linear potential with an abrupt change in slope [122], the second type of scenario — dubbed punctuated inflation — is known to arise due to inflationary potentials containing a point of inflection [110, 111]. The advantage of such scenarios is that the initial epoch of slow roll inflation permits one to impose the standard Bunch-Davies initial conditions in the sub-Hubble domain for *all* the modes of cosmological interest.

As we shall see, these alternative scenarios lead to scalar power spectra which have almost the same shape. Moreover, as we shall illustrate, these power spectra also lead to a slightly improved fit to the CMB data than the nearly scale invariant power spectra. One can expect that non-Gaussianities, specifically, the scalar bispectrum, would help us discriminate between these models. In this chapter, we shall evaluate the scalar bispectrum numerically using the procedure we have described earlier (*cf.* Subsec. 1.1.3) in models with kinetically dominated initial conditions. We shall discuss in detail the various contributions to the scalar bispectrum in these cases and arrive at the corresponding non-Gaussianity parameter $f_{_{\rm NL}}$. Interestingly, as we shall illustrate, in such models, the contributions due to the boundary terms in the third order action governing the scalar perturbations dominate the contributions due to the bulk terms [16]. We shall also compare the bispectrum that arises in these models with those that occur in the Starobinsky model and punctuated inflation. Moreover, apart from the above mentioned scenarios, we shall also examine two other situations involving inflation of a finite duration, which can be considered to be variations of the model with kinetically dominated initial conditions. We shall consider a case wherein the background scalar field begins on the inflationary attractor (a scenario which we shall call as the hard cut-off model) and another wherein the field starts with a small velocity and evolves towards the attractor (a scenario which we shall refer to as the dual to kinetic domination). As in the model with an early kinetically dominated phase, these cases too lead to a sharp drop in power on large scales when the initial conditions on the perturbations are imposed on super-Hubble scales for a range of modes. Further, since the trajectory always remains on the attractor in the hard cut-off model, it leads to slow roll, permitting us to evaluate the scalar power and bispectra analytically. We find that, in the equilateral limit, the amplitude of the scalar non-Gaussianity parameter $f_{_{\rm NL}}$ proves to be very large [with $f_{_{\rm NL}} \simeq \mathcal{O}(10^2\text{–}10^6)$] in the scenario of dual to kinetic domination and the hard cut-off model. We also find that $f_{_{\rm NL}}$ is relatively larger in the model with kinetically dominated initial conditions [with $f_{_{\rm NL}} \simeq \mathcal{O}(1\text{–}10)$] as well as in the Starobinsky model (with $f_{_{\rm NL}} \simeq 10$). Moreover, as expected, in the models wherein the Bunch-Davies initial conditions are imposed on super-Hubble scales, the consistency relation governing the scalar bispectrum is violated for the large scale modes, whereas the relation is satisfied for all the modes in the other scenarios (*viz.* the Starobinsky model and punctuated inflation). These differences in the behavior of the scalar bispectrum can hopefully help us observationally discriminate between the various models.

The remainder of this chapter is organized as follows. In the next section, we shall discuss the power spectra that arise in the different inflationary scenarios of interest, *viz.* inflation with kinetically dominated initial conditions, the Starobinsky model, punctuated inflation, the hard cut-off model and the model which is dual to kinetic domination. We shall also compare the scalar power spectra with the CMB data. In Sec. 2.3, we shall numerically evaluate the scalar bispectra that arise in all these models. We shall also present the analytical calculation of the scalar bispectrum in the hard cut-off model. In Sec. 2.4, we shall describe the amplitude and the shape of the scalar non-Gaussianity parameter $f_{_{\rm NL}}$ that arise in all the cases. In Sec. 2.5, we shall examine the consistency relation governing the scalar bispectrum in the squeezed limit. We shall conclude in Sec. 2.6 with a summary of the results obtained. In App. A, we shall illustrate the imprints of the initial kinetically dominated epoch on the scalar power spectrum across different inflationary models.

2.2 SUPPRESSING THE SCALAR POWER ON LARGE SCALES

In this section, we shall describe the models of our interest and discuss the scalar and tensor power spectra that arise in these cases. We shall solve for the evolution of the background and evaluate the scalar and tensor power spectra numerically in the manner described in Subsecs. 1.1.1 and 1.1.2.

2.2.1 The models of interest

Let us now describe the different inflationary models that we shall consider and discuss the power spectra arising in these models.

Models with kinetically dominated initial conditions

The scenario of our primary interest is the one with kinetically dominated initial conditions, *i.e.* the situation wherein the kinetic energy of the inflaton completely dominates its potential energy during the initial stages of evolution [103, 120, 121, 123–125]. We shall examine the scenario in the quadratic potential (which we shall refer to as QP)

$$V(\phi) = \frac{1}{2}\, m^2\, \phi^2, \tag{2.1}$$

and the Starobinsky model described by the potential (1.5). As we shall also be considering a different model due to Starobinsky, we shall refer to the model described by the potential (1.5) as Starobinsky model I (or, simply, SMI, hereafter).

In these potentials, to achieve kinetic domination, we shall set the initial value of the first slow roll parameter to be $\epsilon_{1\mathrm{i}} = 2.99$. Evidently, this value determines the initial velocity of the field. The expansion of the universe slows down the field and one finds that inflation sets in (*i.e.* ϵ_1 becomes less than unity) after about an e-fold or two (say, at N_1) counted from, say, $N = 0$, when we begin evolving the background. Moreover, slow roll inflation (say, when $\epsilon_1 \lesssim 10^{-2}$) is actually achieved only after a few e-folds. We shall choose the initial value of the field so as to lead to adequate number of e-folds (say, about 60 or so) before inflation is terminated at late times. We shall assume that the pivot scale of $k_* = 5 \times 10^{-2}\,\mathrm{Mpc}^{-1}$ leaves the Hubble radius at, say, N_* number of e-folds *prior to the end of inflation*. As we shall discuss later, we shall be comparing the scalar power spectra from the different inflationary models with the CMB data. When doing so, we shall vary N_*, along with the inflationary parameters, to arrive at the best-fit values for N_* as well as the other parameters.

Recall that, in the inflationary scenario, the standard practice is to impose the initial conditions on the perturbations in the sub-Hubble limit. However, due to the initial kinetic domination, in the scenarios of our interest, a range of large scale modes are always outside the Hubble radius. As is illustrated in Fig. 2.1, for the initial conditions for the background and the best-fit values of the parameters that we shall work with (when the scalar power spectra are compared with the CMB data, see our discussion below as well as Subsec. 2.2.2), we find that a certain range of large scale modes never satisfy the condition $k > \sqrt{|z''/z|}$ required for imposing the Bunch-Davies initial conditions. We shall evolve the perturbations when the initial conditions are imposed at two instances in the quadratic potential (2.1) and the Starobinsky model (1.5). We shall choose to impose the Bunch-Davies conditions on the perturbations at the time when we begin to evolve the background (*i.e.* at $N = 0$) and at the onset of inflation (*i.e.* at N_1). For convenience, we shall refer to these cases as (QPa, QPb) and (SMIa, SMIb), respectively. In Fig. 2.2, to illustrate the differences in the behavior of the various modes, we have plotted the evolution of the curvature perturbation for three different modes of cosmological interest in the case of QPa.

In the case of QP, we choose the initial value of the scalar field to be $\phi_{\mathrm{i}} = 18.85\,M_{_{\mathrm{Pl}}}$. As we mentioned, the initial velocity of the field is determined by the choice $\epsilon_{1\mathrm{i}} = 2.99$. Under these conditions, the best-fit values for the mass m of the scalar field prove to be $6.41 \times 10^{-6}\,M_{_{\mathrm{Pl}}}$ and $6.17 \times 10^{-6}\,M_{_{\mathrm{Pl}}}$ in the cases of QPa and

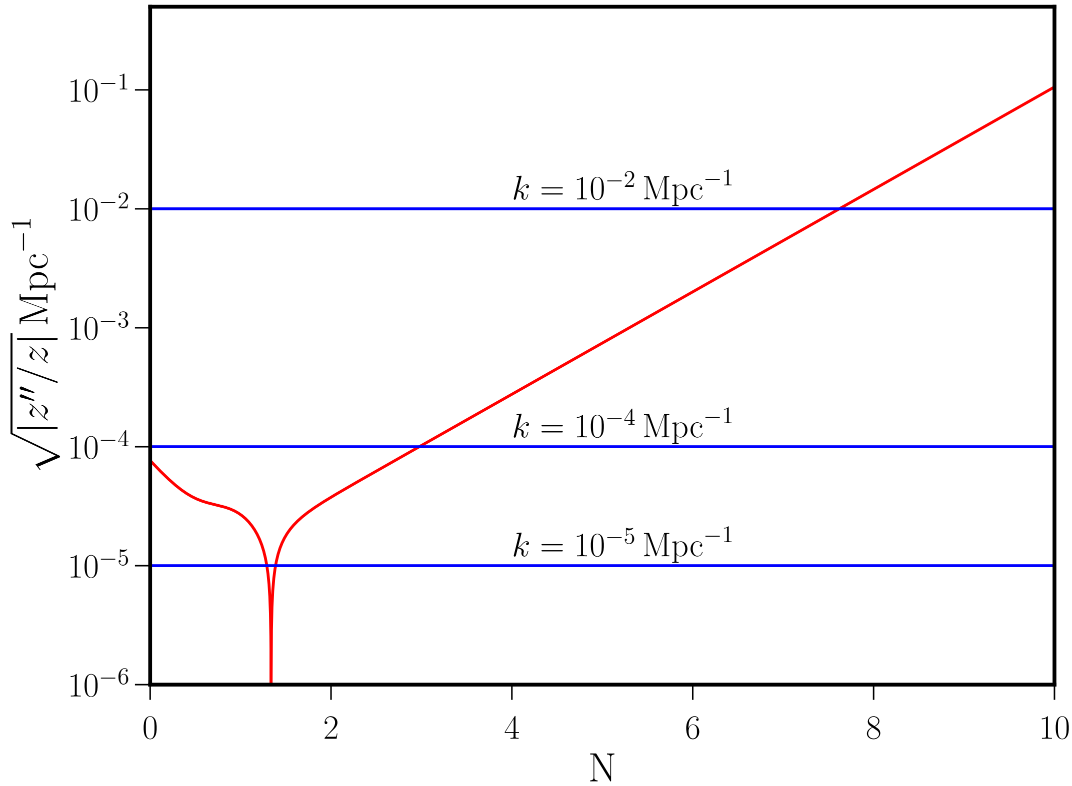

Figure 2.1: The behavior of the quantity $\sqrt{|z''/z|}$ has been plotted (in red) as a function of e-folds N in an inflationary scenario of finite duration achieved due to an initial epoch of kinetic domination in the model which we refer to as QPa. Note that $\sqrt{|z''/z|}$ decreases from its initial value until inflation sets in, after which it begins to rise. (Actually, the quantity z''/z is negative during the initially kinetic dominated regime and turns positive during the transition to the inflationary epoch. Hence, we have plotted the quantity $\sqrt{|z''/z|}$.) It is well known that $\sqrt{z''/z} \simeq a\,H$ in slow roll inflation, as is reflected in the linear growth of $\sqrt{z''/z}$ (in the log-linear plot) at later times. Interestingly, we find that $\sqrt{|z''/z|} = \mathcal{O}(a\,H)$ even in the initial fast roll phase. The wave numbers of three modes, *viz.* $k = 10^{-5}\,\mathrm{Mpc}^{-1}$, $10^{-4}\,\mathrm{Mpc}^{-1}$ and $10^{-2}\,\mathrm{Mpc}^{-1}$, have also been indicated (in blue) to highlight the differences in their evolution. While the first mode always remains in the super-Hubble domain (*i.e.* $k < \sqrt{|z''/z|}$), the second and the third modes spend a certain amount of time in the sub-Hubble regime (*i.e.* $k > \sqrt{|z''/z|}$) before they cross over to the super-Hubble regime.

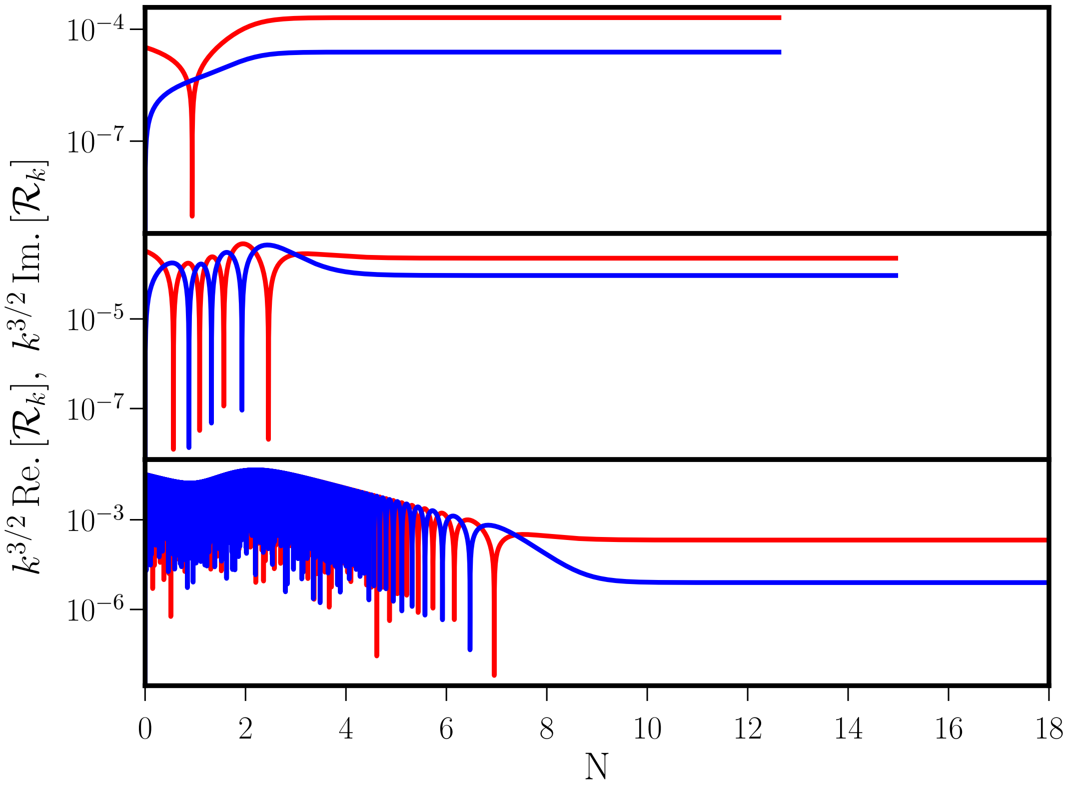

Figure 2.2: The evolution of the Fourier modes f_k of the curvature perturbation have been plotted as a function of e-folds N in a typical inflationary scenario with an initial epoch of kinetic domination. In order to illustrate the oscillations, we have plotted the evolution of the amplitudes of the real (in red) and imaginary (in blue) parts of the Fourier modes for three different wave numbers of cosmological interest that we had considered in the previous figure, *viz.* $k = 10^{-5}\,\mathrm{Mpc}^{-1}, 10^{-4}\,\mathrm{Mpc}^{-1}$ and $10^{-2}\,\mathrm{Mpc}^{-1}$ (in the top, middle and bottom panels, respectively). Note that these plots correspond to the case of QPa wherein the modes have been evolved from $N = 0$ (when the initial conditions are imposed on the background scalar field) up to a point in the super-Hubble regime, when they satisfy the condition $k = 10^{-5}\,\sqrt{|z''/z|} \simeq 10^{-5}\,(a\,H)$. Evidently, the large scale mode with wave number $10^{-5}\,\mathrm{Mpc}^{-1}$, which is always in the super-Hubble regime, barely oscillates and its amplitude almost remains constant (*cf.* top panel). The intermediate scale mode with wave number $10^{-4}\,\mathrm{Mpc}^{-1}$ spends a limited amount of time in the sub-Hubble regime. It oscillates a few times before its amplitude freezes soon after leaving the Hubble radius (*cf.* middle panel). The small scale mode with wave number $10^{-2}\,\mathrm{Mpc}^{-1}$ spends an adequate amount of time in the sub-Hubble regime, and it reflects the behavior of modes in standard slow roll inflation (*cf.* bottom panel). It oscillates repeatedly in the sub-Hubble regime and settles to a constant amplitude on super-Hubble scales. These differences in the behavior of the different modes of cosmological interest lead to different amplitudes at late times and hence to features in the scalar power and bispectra.

QPb, respectively (*cf.* Tab. 2.3). Moreover, in these cases, the best-fit values of N_* turn out to be 55.06 and 57.32. For the above parameter values and initial conditions, the scalar field rolls down the potential for about 65 e-folds (counted from $N = 0$ when the scalar field is at $\phi_{\rm i}$), before inflation is terminated close to the minimum of the quadratic potential.

In the case of SMI, we choose the initial value of the scalar field to be $\phi_{\rm i} = 8.37\, M_{_{\rm Pl}}$, with $\epsilon_{1{\rm i}} = 2.99$. We find that the best-fit values for the parameter V_0 in the cases of SMIa and SMIb prove to be $9.66\times 10^{-10}\, M_{_{\rm Pl}}^4$ and $8.99\times 10^{-10}\, M_{_{\rm Pl}}^4$, respectively (*cf.* Tab. 2.3). Also, the corresponding best-fit values for N_* turn out to be 53.22 and 55.19. For the above initial conditions and parameter values, we find that inflation ends after approximately 64 e-folds.

Having evolved the background and the perturbations, we evaluate the scalar and tensor power spectra at a suitably late time when *all* the modes of cosmological interest (say, $10^{-5} < k < 1\,{\rm Mpc}^{-1}$) are sufficiently outside the Hubble radius. One finds that, all the scalar and tensor power spectra, generically, exhibit a drop in power on large scales, as illustrated in Fig. 2.3. In fact, the suppression in power occurs when the Bunch-Davies initial conditions are imposed over modes that never satisfy the sub-Hubble condition $k > \sqrt{z''/z}$ (in the case of scalars) or $k > \sqrt{a''/a}$ (in the case of tensors). Further, as is expected in any transition, the power spectra exhibit a burst of oscillations before they turn nearly scale invariant on smaller scales. However, there is a minor difference in the scale at which the suppression of the tensor power occurs in the cases wherein the modes are evolved from N_1 and $N = 0$. If we choose the parameters of a model such that the onset of suppression in the scalar power is matched when evolved from N_1 and $N = 0$, then, we find that, the corresponding suppression in the tensor power occurs at slightly different scales. This can be attributed to the difference in the behavior of the quantities z''/z and a''/a that govern the evolution of the scalar and tensor modes. In Fig. 2.4, we have plotted the scalar power spectra that arise in these models for the best-fit values of the parameters involved.

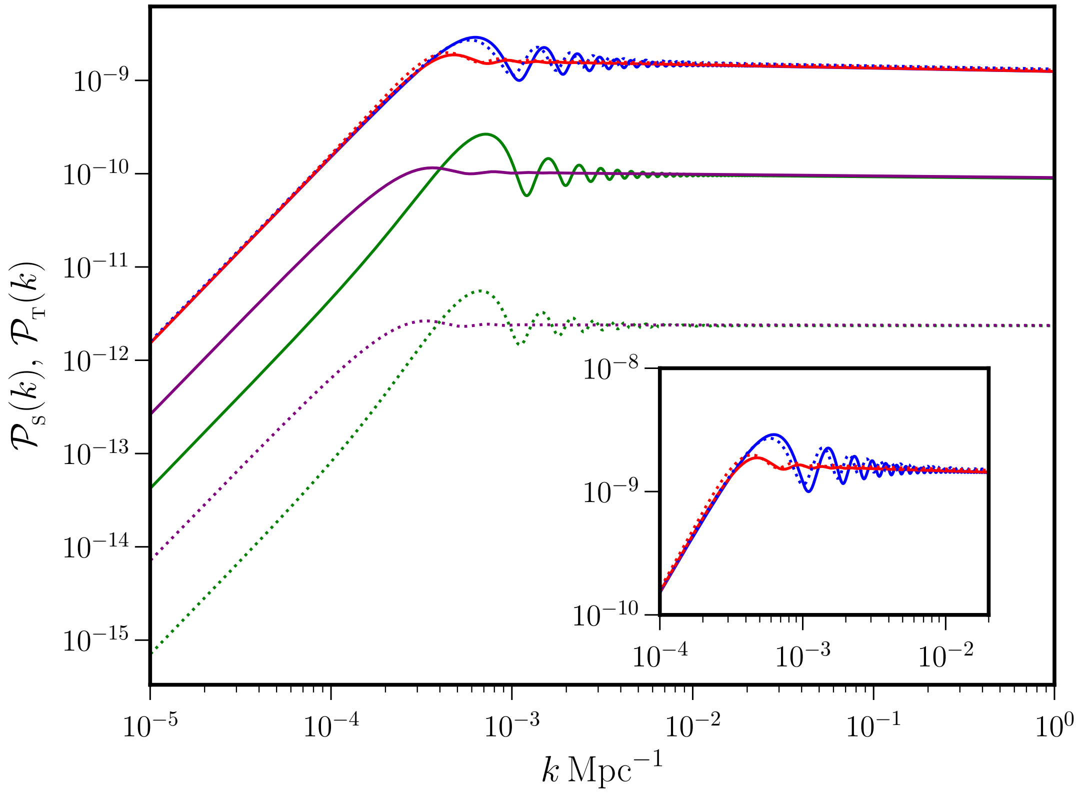

Figure 2.3: The scalar (in red and blue) and tensor (in purple and green) power spectra generated in the quadratic potential (as solid curves) and the Starobinsky model (as dotted curves) with kinetically dominated initial conditions have been plotted for the two cases wherein the perturbations are evolved from N_1 (in red and purple) and $N = 0$ (in blue and green). We have evolved the field from $\phi_{\rm i} = 18.85\, M_{_{\rm Pl}}$ and $8.3752\, M_{_{\rm Pl}}$ in the quadratic potential and the Starobinsky model respectively, and have set $\epsilon_{1{\rm i}} = 2.99$. The parameters m and V_0 have been chosen suitably so that the scalar spectra match over the range of modes wherein a suppression in power arises (say, for $k < k_{\rm i}$) and in the nearly scale invariant regime (which occurs for $k \gg k_{\rm i}$). We find that this is possible if we set $m/M_{_{\rm Pl}} = (5.0 \times 10^{-6}, 4.9 \times 10^{-6})$ and $V_0/M_{_{\rm Pl}}^4 = (5.8 \times 10^{-10}, 5.7 \times 10^{-10})$ in the cases evolved from N_1 and $N = 0$, respectively. In these four instances, the pivot scale $k_\ast = 5 \times 10^{-2}\,{\rm Mpc}^{-1}$ leaves the Hubble radius at $(57.48, 58.50)$ and $(57.07, 58.08)$ e-folds *before the end of inflation*. Also, in these cases, we find that, $k_{\rm i}/{\rm Mpc}^{-1} = (2.38 \times 10^{-4}, 2.32 \times 10^{-3})$ and $(2.38 \times 10^{-4}, 1.92 \times 10^{-3})$. Note that the two sets of scalar spectra differ only in the amplitude and range of the oscillations that arise near $k_{\rm i}$ (highlighted in the inset). As far as the tensor spectra are concerned, the Starobinsky model predicts lower tensor power overall, when compared to the quadratic potential. Moreover, the tensor spectra too exhibit a suppression in power on large scales as the scalar spectra. However, there is a small difference in the scale at which the onset of the suppression in the tensor power occurs when the modes are evolved from N_1 and $N = 0$.

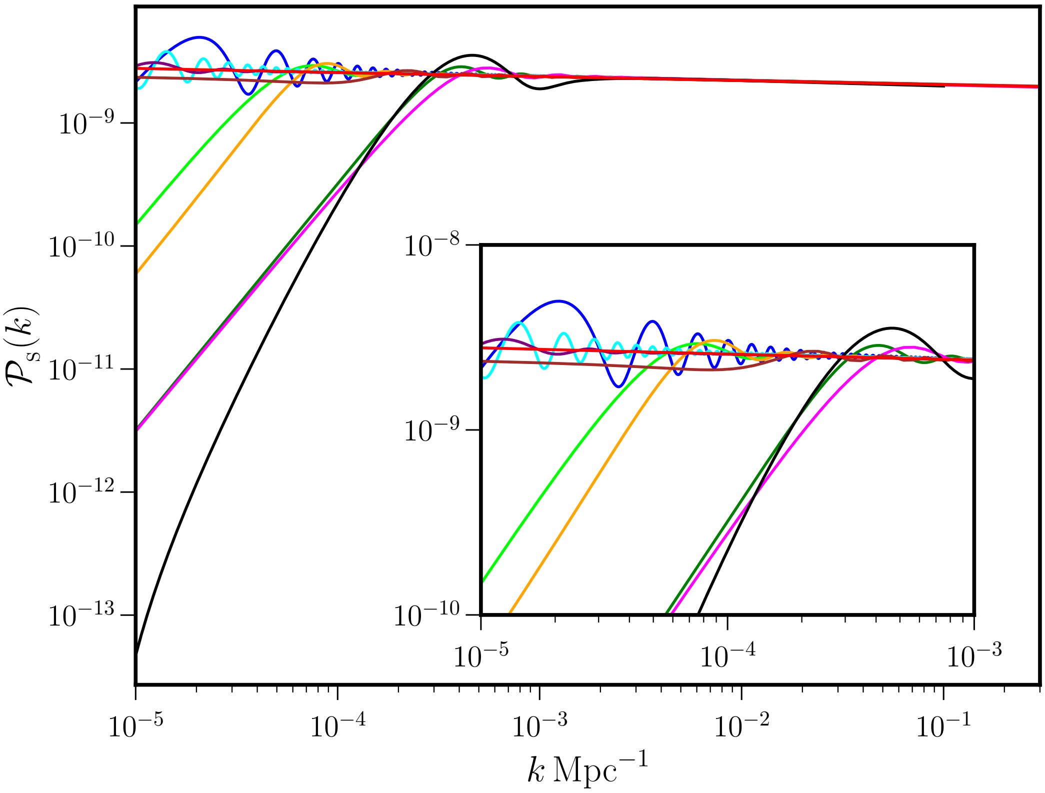

Figure 2.4: The scalar power spectra evaluated either analytically or numerically have been plotted in the various scenarios of our interest. We have plotted the best-fit power spectra in all the different models we have considered: *viz.* the cases of the quadratic potential (QPa, QPb and QPc, in blue, green and lime) and the first Starobinsky model (SMIa, SMIb and SMIc, in cyan, orange and purple) with kinetically dominated initial conditions and their duals, the second Starobinsky model (SMII, in brown), punctuated inflation (PI, in black) and the hard cut-off model (HCO, in magenta). For comparison we have also included the best-fit, featureless, nearly scale invariant power law spectrum (in red). While most models exhibit a cut-off on large scales, the drop in scalar power is the sharpest in PI than in the other cases. As we shall see, the scalar power spectrum in PI leads to the largest level of improvement in the fit to the CMB data. Moreover, all the models lead to oscillations before the spectra turn nearly scale invariant and, understandably, the amplitude of the oscillations is the smallest in the case of HCO, since it involves only slow roll.

Another model due to Starobinsky

The second scenario we shall consider is another model due to Starobinsky which is described by the following linear potential with an abrupt change in its slope [60, 122, 126]:

$$V(\phi) = \begin{cases} V_0 + A_+\,(\phi - \phi_0) & \text{for } \phi > \phi_0, \\ V_0 + A_-\,(\phi - \phi_0) & \text{for } \phi < \phi_0, \end{cases} \tag{2.2}$$

where $A_- \neq A_+$. In order to distinguish from the first Starobinsky model, we shall refer to the scenario described by this potential as Starobinsky model II (SMII, hereafter). We should mention here that, to permit numerical analysis, one often works with a smoothened form of the above potential given by [127]

$$V(\phi) = V_0 + \frac{1}{2}\,(A_+ + A_-)\,(\phi - \phi_0) + \frac{1}{2}\,(A_+ - A_-)\,(\phi - \phi_0)\,\tanh\left(\frac{\phi - \phi_0}{\Delta\phi}\right). \tag{2.3}$$

It is useful here to briefly describe the dynamics that arises in the model. If we work with parameters such that the constant term V_0 in the potential dominates, then the first slow roll parameter ϵ_1 always remains fairly small through most of the evolution. One also finds that, in such a case, there arise two stages of slow roll inflation with a brief period of departure from slow roll. The deviation from slow roll is reflected in the large values of the second and the third slow roll parameters, *viz.* ϵ_2 and ϵ_3 [with $\epsilon_{n+1} = \mathrm{d}\ln\epsilon_n/\mathrm{d}N$, for $n > 1$, *cf.* Eq. (1.7)], which occur briefly when the scalar field crosses ϕ_0. In fact, the small value for ϵ_1 permits one to express the scalar modes in terms of the de Sitter modes and thereby evaluate the power spectrum even analytically. It can be shown that the power spectrum in the model can be expressed as [60, 122, 126]

$$\begin{aligned}\mathcal{P}_{_{\mathrm{S}}}(k) \simeq\ & A_{_{\mathrm{S}}}\left\{1 - \frac{3\,\Delta A}{A_+}\,\frac{k_0}{k}\left[\left(1 - \frac{k_0^2}{k^2}\right)\sin\left(\frac{2\,k}{k_0}\right) + \frac{2\,k_0}{k}\cos\left(\frac{2\,k}{k_0}\right)\right]\right.\\ & + \frac{9\,\Delta A^2}{2\,A_+^2}\,\frac{k_0^2}{k^2}\left(1 + \frac{k_0^2}{k^2}\right)\left[1 + \frac{k_0^2}{k^2} - \frac{2\,k_0}{k}\sin\left(\frac{2\,k}{k_0}\right)\right.\\ & \left.\left. + \left(1 - \frac{k_0^2}{k^2}\right)\cos\left(\frac{2\,k}{k_0}\right)\right]\right\},\end{aligned} \tag{2.4}$$

where we have set $A_{_{\mathrm{S}}} = \left[3\,H_{_{\mathrm{I}}}^3/(2\,\pi\,A_-)\right]^2$, while $\Delta A = A_- - A_+$ and $H_{_{\mathrm{I}}}^2 \simeq V_0/(3\,M_{_{\mathrm{Pl}}}^2)$. Note that, since the above analytical result for the scalar power spectrum has been arrived at using the de Sitter modes, the spectrum is strictly scale invariant on small scales. In order to account for a tilt, while comparing the with the CMB data, we multiply the above power spectrum by $(k/k_*)^{n_{\rm S}-1}$. The tensor power spectrum is computed through the parameter r, which is defined as $\mathcal{P}_{\rm T} = r\,\mathcal{P}_{\rm S}(k_*)$. It is thus parameterized to be of constant amplitude throughout the range of wave numbers as the features in the model occur only in the scalar power spectrum. As we shall discuss later, upon comparing such spectra with the CMB data, we obtain the following best-fit values for the parameters involved: $A_{\rm S} = 2.11 \times 10^{-9}$, $n_{\rm S} = 0.97$, $k_0 = 6.32 \times 10^{-5}\,{\rm Mpc}^{-1}$, $\Delta\,A/A_+ = -0.074$ and $r = 0.017$. We have illustrated the best-fit scalar power spectrum in Fig. 2.4. As should be clear from the figure, the scalar power spectrum exhibits a step-like feature on large scales and is nearly invariant at small scales. It should be pointed out that the height of the step in the power spectrum is essentially determined by the difference in the slopes A_+ and A_-.

The punctuated inflationary scenario

The third scenario we shall consider is the so-called punctuated inflationary scenario (referred to hereafter as PI) achieved with the aid of the potential [110, 111]

$$V(\phi) = \frac{1}{2}\,m^2\,\phi^2 - \frac{2}{3}\,m^2\,\phi_0^2\,\left(\frac{\phi}{\phi_0}\right)^3 + \frac{1}{4}\,m^2\,\phi_0^2\,\left(\frac{\phi}{\phi_0}\right)^4. \tag{2.5}$$

The potential contains a point of inflection at $\phi = \phi_0$. If one starts with a suitably large initial value of the scalar field such that $\phi \gg \phi_0$, the potential admits two stages of slow roll inflation separated by a brief departure (for less than an e-fold) from inflation. We shall choose to work with $\phi_{\rm i} = 12\,M_{_{\rm Pl}}$ and $\epsilon_{1{\rm i}} = 2 \times 10^{-3}$. On setting $\phi_0 = 1.9654\,M_{_{\rm Pl}}$, we obtain the best-fit value for the parameter m to be $7.16 \times 10^{-8}\,M_{_{\rm Pl}}$. We have plotted the resulting scalar power spectrum in Fig. 2.4. Clearly, the power spectrum exhibits a sharp drop in power on large scales. However, the model has a major drawback. One finds that, in order for the drop in power to occur at wave numbers roughly corresponding to the Hubble scale today, the largest scale has to leave the Hubble radius during inflation considerably (about 30–35 e-folds) earlier than the nominally accepted upper bound of about 65 e-folds, when counted from the end of inflation (for a discussion on this upper bound, see Refs. [128, 129]). For the above values of the parameters, we find that inflation lasts for about 110 e-folds and the pivot scale itself exits the Hubble radius at 90.61 e-folds before the end of inflation. Despite the drawback, we believe the model is interesting for the reason that, among the different models we consider, it leads to the largest improvement in the fit to the CMB data. We shall briefly comment about the model further in concluding section.

The hard cut-off model

It would be interesting to analytically describe the model with kinetically dominated initial conditions and evaluate the corresponding observable quantities of interest. However, it proves to be a bit cumbersome to do so. A simpler model, which permits complete analytical evaluation of the scalar power and bi-spectra corresponds to a situation wherein the scalar field starts *on* the inflationary attractor at some given conformal time, say, $\eta_{\rm i}$. We shall refer to such a scenario as the hard cut-off model (or, simply, HCO). The attractive aspect of the initially kinetically dominated model is that inflation begins naturally at a specific time when the velocity of the scalar field decreases below a threshold value as it rolls down the potential. In contrast, in the hard cut-off model, we have to *a priori* assume that inflation begins at a specific time with the scalar field being on the attractor.

Since the model involves only slow roll, it is straightforward to arrive at the Fourier modes f_k describing the curvature perturbation. As is well known, during slow roll, the scalar mode f_k, in general, can be expressed in terms of the de Sitter solutions as

$$f_k(\eta) = \frac{i\, H_{_{\rm I}}}{M_{_{\rm Pl}}\,\sqrt{4\,k^3\,\epsilon_1}}\,\left[\alpha(k)\,(1+i\,k\,\eta)\,{\rm e}^{-i\,k\,\eta} - \beta(k)\,(1-i\,k\,\eta)\,{\rm e}^{i\,k\,\eta}\right], \tag{2.6}$$

where $H_{_{\rm I}}$ represents the Hubble scale during inflation and ϵ_1 denotes the first slow roll parameter. The quantities $\alpha(k)$ and $\beta(k)$ are the so-called Bogoliubov coefficients. If one imposes the standard Bunch-Davies initial conditions in the sub-Hubble limit, then one will have $\alpha(k)=1$ and $\beta(k)=0$. In our case, we shall impose the initial conditions at the time $\eta_{\rm i}$ irrespective of whether the modes are inside or outside the Hubble radius. In such a case, we obtain the Bogoliubov coefficients $\alpha(k)$ and $\beta(k)$ to be

$$\alpha(k) = 1+\frac{i}{k\,\eta_{\rm i}} - \frac{1}{2\,k^2\,\eta_{\rm i}^2} = 1 - \frac{i\,k_{\rm i}}{k} - \frac{k_{\rm i}^2}{2\,k^2}, \tag{2.7a}$$

$$\beta(k) = -\frac{1}{2\,k^2\,\eta_{\rm i}^2}\,{\rm e}^{-2\,i\,k\,\eta_{\rm i}} = -\frac{k_{\rm i}^2}{2\,k^2}\,{\rm e}^{2\,i\,k/k_{\rm i}}, \tag{2.7b}$$

where we have set $k_{\rm i} = -1/\eta_{\rm i}$. Note that, as $\eta_{\rm i}\to-\infty$ (*i.e.* as $k_{\rm i}\to 0$), $\alpha(k)\to 1$ and $\beta(k)\to 0$, which corresponds to the conventional sub-Hubble, Bunch-Davies initial conditions often imposed on all the modes.

With the modes f_k at hand, it is now straightforward to evaluate the resulting power spectrum by substituting the modes in the expression (1.13a) and taking the late time (*i.e.* $\eta \to 0$) limit. One can easily show that the power spectrum can be written as

$$\begin{aligned}
\mathcal{P}_{\rm S}(k) &= A_{\rm S}\,|\alpha(k)-\beta(k)|^2 \\
&= A_{\rm S}\left[1+\frac{k_{\rm i}^4}{2\,k^4}-\frac{k_{\rm i}^3}{k^3}\,\sin\left(\frac{2\,k}{k_{\rm i}}\right)+\left(\frac{k_{\rm i}^2}{k^2}-\frac{k_{\rm i}^4}{2\,k^4}\right)\,\cos\left(\frac{2\,k}{k_{\rm i}}\right)\right], \qquad (2.8)
\end{aligned}$$

where we have set $A_{\rm S} = H_{\rm I}^2/(8\,\pi^2\,\epsilon_1)$. We find that this analytical expression matches the corresponding numerical result very well, say, in QP or SMI, modulo at small scales where the de Sitter modes are not adequate to capture the spectral tilt that arises in a realistic model. Therefore, when comparing the HCO model with the CMB data, to allow for the spectral tilt at small scales, we have multiplied the above scalar power spectrum by $(k/k_*)^{n_{\rm S}-1}$ as in the case of SMII. Moreover, we define the tensor power spectrum to be $\mathcal{P}_{\rm T}(k) = r\,\mathcal{P}_{\rm S}(k)$. Such a scale-dependent definition (in contrast to the SMII case, where the tensor power spectrum was scale invariant) is important because the model predicts features in the tensor power spectrum similar to that in the scalar power spectrum [*cf.* Fig. 2.3], and we have consistently accounted for it in the analysis. We obtain the following best-fit values for the parameters involved: $A_{\rm S} = 2.09 \times 10^{-9}$, $n_{\rm S} = 0.96$, $k_{\rm i} = 2.03 \times 10^{-4}\,{\rm Mpc}^{-1}$, and $r = 0.043$. In Fig. 2.4, we have plotted the analytical scalar power spectrum, with the $(k/k_*)^{n_{\rm S}-1}$ term included, corresponding to the above mentioned best-fit values. Clearly, the scalar power spectrum exhibits a suppression of power on large scales as in the case of the other models. As we shall discuss later, the HCO model allows us to evaluate the scalar bispectrum too analytically. The analytical calculations prove to be handy as they permit us to test the numerical results against the analytical results in a situation wherein the Bunch-Davies initial conditions are imposed on super-Hubble scales.

A dual to initial kinetic domination

We shall now discuss a situation which we shall refer to as the dual to the scenario with kinetically dominated initial conditions. Recall that, in the model with initial kinetic domination, the scalar field starts with a large velocity. Evidently, this corresponds to a situation wherein the field begins from a point away from the inflationary attractor. It is interesting to examine the effects on the power spectrum in a scenario with a finite duration of inflation where the field starts with a small velocity (than its value on the attractor) rather than a large velocity. As in the hard cut-off model, there is no natural way of terminating inflation (when one goes back in time) in such a case. Therefore, we shall assume that inflation begins at a specific time and that the Bunch-Davies initial conditions are imposed on super-Hubble scales for a range of modes. A version of such a scenario has been considered previously in the literature and we find that they are referred to as non-attractor models of inflation (in this context, see, for instance, Refs. [130, 131]). Under these conditions, we find that, as the field evolves towards the attractor, there occurs a sharp drop in power on large scales and a regime of oscillations arises over intermediate scales before the spectrum turns nearly scale invariant on small scales. We shall refer to this case as QPc and SMIc when implemented in the quadratic potential (2.1) and Starobinsky model (1.5), respectively. In the case of QPc, we choose $\phi_{\rm i} = 16.00\, M_{_{\rm Pl}}$ and $\epsilon_{1{\rm i}} = 10^{-4}$, which leads to inflation of about 65 e-folds. In the case of SMIc, we work with $\phi_{\rm i} = 5.52\, M_{_{\rm Pl}}$ and $\epsilon_{1{\rm i}} = 10^{-4}$, which too results in inflation lasting for about 65 e-folds. We find that the best-fit values for the parameter in these models prove to be $m = 6.15 \times 10^{-6}\, M_{_{\rm Pl}}$ and $V_0 = 8.75 \times 10^{-10}\, M_{_{\rm Pl}}^4$. The pivot scale exits the Hubble radius at 57.32 and 55.87 e-folds before the end of inflation in the cases of QPc and SMIc, respectively. In Fig. 2.4, we have illustrated the scalar power spectra (that lead to the best-fit to the CMB data) in the dual scenario, *viz.* QPc and SMIc, along with the spectra arising in the cases with initial kinetic domination, *i.e.* QPa, SMIa, QPb and SMIb (as well as the other models of interest). Clearly, the kinetically dominated model and its dual generate spectra with roughly similar features. We find that the drop in power at large scales have the same shape in both the scenarios and is mostly independent of the initial velocity of the field.

2.2.2 Performance against the CMB data

We have compared all the models we have described in the previous subsection against the recent Planck data [62]. In this subsection, we shall discuss the assumptions we have made while comparing the models with the CMB data, the priors on the parameters we have worked with and present the final results for the CMB angular power spectrum.

We have taken into account both the scalar and tensor power spectra arising in the models of interest when comparing against the CMB data. We have modified the CAMB package suitably to include the power spectra from the different models [64]. We have made use of CosmoMC to carry out the comparison of the models with the CMB data and have arrived at the respective likelihoods [63]. We have worked with the 2018 release of Planck data, which comprises of the likelihoods of the TT, TE and EE correlations along with the lensing likelihood [62]. We have included nonlinear lensing in the calculation of the CMB angular power spectra which has a significant effect over small scales. For models with spectra calculated numerically, we have evaluated the power spectra at 2000 points over the following range of wave numbers: $10^{-6} \leq k \leq$

Parameter	Lower limit	Upper limit
$\Omega_{\mathrm{b}}\, h^2$	0.005	0.1
$\Omega_{\mathrm{c}}\, h^2$	0.001	0.99
θ_{MC}	0.5	10
τ	0.01	0.8

Table 2.1: The background cosmological parameters which we have varied and the priors that we have worked with. These are the standard set of background parameters that are often considered while comparing with the CMB data [38].

Model	$\ln\left(A_{\mathrm{S}} \times 10^{10}\right)$	n_{S}	r	$\log_{10}(k_{\mathrm{i}}/\mathrm{Mpc}^{-1})$ or $\log_{10}(k_0/\mathrm{Mpc}^{-1})$	$\Delta A/A_{+}$
PL	$[1.61, 3.91]$	$[0.8, 1.2]$	$[0, 2]$	-	-
HCO	$[1.61, 3.91]$	$[0.8, 1.2]$	$[0, 2]$	$[-4, -2]$	-
SMII	$[1.61, 3.91]$	$[0.8, 1.2]$	$[0, 2]$	$[-5, -3]$	$[-0.999, 0.700]$

Model	N_{*}	$\log_{10}(10^{10}\, m^2/M_{_{\mathrm{Pl}}}^2)$	$\log_{10}(10^{10}\, V_0/M_{_{\mathrm{Pl}}}^4)$
QPa, QPb, QPc	$[50, 60]$	$[-0.55, -0.25]$	-
SMIa, SMIb, SMIc	$[50, 60]$	-	$[0.8, 1.2]$
PI	$[87, 93]$	$[-5.20, -3.47]$	-

Table 2.2: The parameters associated with the different inflationary models of our interest and the priors that we have worked with. The first set (on top) corresponds to models wherein we have made use of the analytical results for the power spectra and the second set (at the bottom) corresponds to models wherein we have evaluated the spectra numerically.

$10\,\mathrm{Mpc}^{-1}$. We should mention that, in CAMB, the maximum value of the multipole ℓ is set to be 2700 to compute the CMB angular power spectrum C_ℓ. We perform an MCMC sampling of the posterior distribution of the parameter space using CosmoMC for each model and arrive at the best-fit χ^2 and the corresponding set of parameter values using the in-built package called GetDist.

In Tab. 2.1, we have listed the priors on the four background cosmological parameters that we have worked with. In Tab. 2.2, we have listed the priors on the parameters describing the various inflationary models of our interest. Earlier experience suggests that the drop in power leading to an improved fit to the CMB data is expected to occur around the wave number $k \simeq 10^{-4}\,\mathrm{Mpc}^{-1}$. Hence, while choosing the range of priors for the model parameters which determine the location of the drop in the scalar

Model	$\ln(A_{\rm s} \times 10^{10})$	$n_{\rm s}$	r	$\log_{10}(k_{\rm i}/{\rm Mpc}^{-1})$ or $\log_{10}(k_0/{\rm Mpc}^{-1})$	$\Delta A/A_+$	$\Delta\chi^2$
PL	3.042	0.967	0.011	-	-	-
HCO	3.039	0.962	0.043	-3.692	-	-0.096
SMII	3.048	0.969	0.017	-4.199	-0.074	-0.672

Model	N_*	$\log_{10}(10^{10}m^2/M_{\rm Pl}^2)$	$\log_{10}(10^{10}V_0/M_{\rm Pl}^4)$	$\Delta\chi^2$
QPa	55.06	-0.386	-	2.494
QPb	57.32	-0.419	-	-0.384
QPc	57.32	-0.422	-	-0.014
SMIa	53.22	-	0.985	-0.896
SMIb	55.19	-	0.954	-0.880
SMIc	55.87	-	0.942	-1.170
PI	90.61	-4.290	-	-1.746

Table 2.3: The best-fit values of the inflationary parameters and the extent of improvement in χ^2 with respect to the standard power law case, arrived at by comparing the models with the recent CMB data. As in the previous table, the first set (on top) corresponds to models with analytical forms for the scalar power spectra and the second set (at the bottom) corresponds to those cases wherein the spectra have been evaluated numerically. We have defined $\Delta\chi^2 = (\chi^2_{\rm model} - \chi^2_{\rm PL})$ so that a negative value for $\Delta\chi^2$ implies an improvement in the fit with respect to the power law case. Note that PI leads to the largest improvement in the fit to the data. The dataset we have used is the following combination of likelihoods: TT + TE + EE + low ℓ + low E + lensing from Planck 2018 data release. The models were compared while accounting for tensors as well as non-linear lensing. We should mention that the best-fit value for χ^2 in the power law case we have obtained is $\chi^2 = 2\,(1390.928) = 2781.856$. The corresponding value quoted by Planck team is $\chi^2 = 2\,(1391.104) = 2782.208$, which is close to the value we obtain [38].

power (such as N_*), we have made sure that the feature occurs over the wave numbers $10^{-5} \lesssim k \lesssim 10^{-3}\,{\rm Mpc}^{-1}$.

In Tab. 2.3, we have listed the improvement in the χ^2 and the best-fit values for the inflationary parameters for the different models we have considered. Recall that the power law (PL) case corresponds to the simplest situation wherein the scalar power spectrum is expressed as $\mathcal{P}_{\rm S}(k) = A_{\rm s}\,(k/k_*)^{n_{\rm s}-1}$ [*cf.* Eq. (1.30a)]. For the PL case, the χ^2 we obtain from the GetDist package is 2781.856, while the value quoted by the Planck team is 2782.208[1]. Note that the quantity $\Delta\chi^2$ is the difference in χ^2

[1]See the Planck Legacy Archive located at the following URL: http://pla.esac.esa.int/pla/#cosmology.

between a given inflationary model and the PL case, with a negative value indicating an improvement in the fit to the data. Evidently, PI leads to the largest improvement in the fit to the data. Earlier, in Fig. 2.4 we had plotted the inflationary scalar power spectra for parameter values of the various models that lead to the best fit to the CMB data. In Fig. 2.5, we have plotted the corresponding CMB angular power spectra for three of the models which lead to reasonable levels of improvement ($\Delta\chi^2 \simeq 0.6$–1.7) in their fit to the data.

Having described the alternative scenarios resulting in scalar spectra with a sharp drop in power on large scales, let us now turn to the evaluation of the scalar non-Gaussianities in these models.

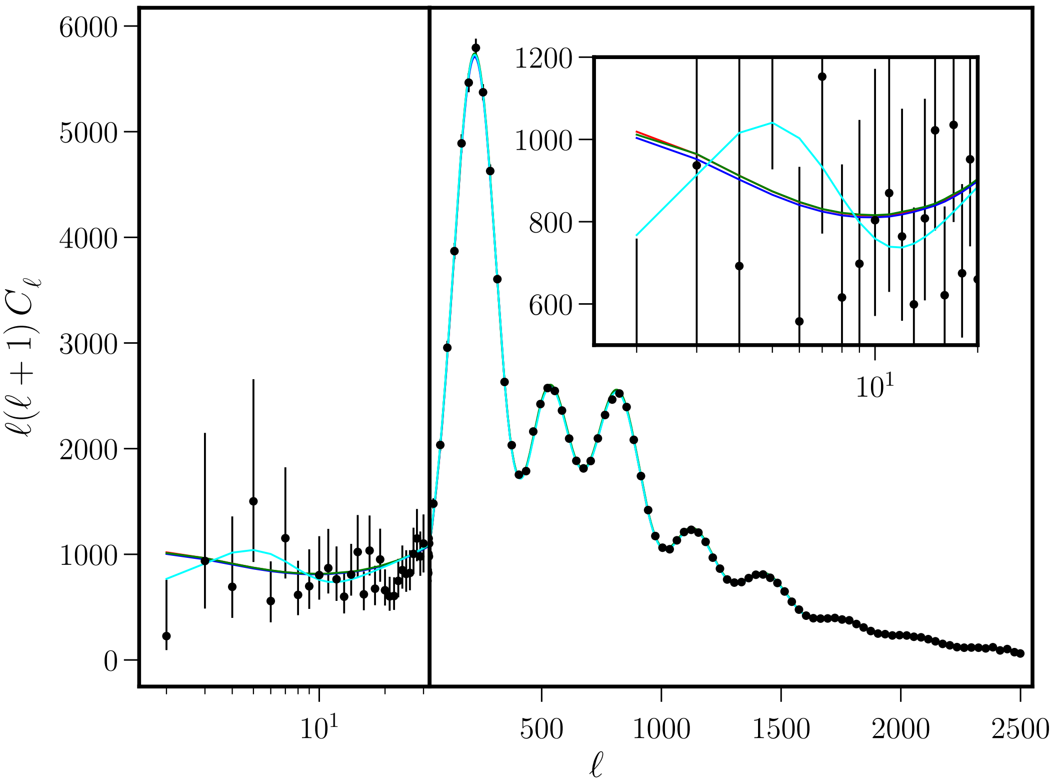

Figure 2.5: The best-fit CMB angular power spectra have been plotted for the three models SMIc (in blue), SMII (in green) and PI (in cyan) which lead to an improvement in $\Delta\chi^2$ of 0.6–1.7 in the fit to the recent Planck data. In order to highlight the differences, we have also plotted the best-fit angular power spectrum for the power law case (in red). We have also included the Planck 2018 data points along with their error bars (in black). Note that the multipoles ℓ appear on a log scale until $\ell = 32$ (indicated by the vertical line) and on a linear scale for $\ell > 32$. We should point out the fact that the CMB angular spectrum in the case of PI exhibits an oscillation over the lower multipoles before it merges with, say, the result for the power law case, at the higher multipoles. The angular spectra for the models of SMIc and SMII are suppressed to a far less extent when compared to the spectrum of PI over the low multipoles (as highlighted in the inset).

2.3 EVALUATING THE SCALAR BISPECTRUM

In this section, we shall describe the numerical evaluation of the scalar bispectrum and the corresponding non-Gaussianity parameter $f_{_{\rm NL}}$ in the different models of our interest. In fact, these quantities have been calculated earlier in the cases of the second Starobinsky model and punctuated inflation (in this context, see, for example, Refs. [56, 60, 132]). Besides, the scalar bispectrum in models with kinetic dominated initial conditions have been briefly presented earlier [16]. The models wherein the initial conditions are imposed on super-Hubble scales pose certain challenges and it is instructive to compare the numerical procedure for the computation of the bispectrum and the non-Gaussianity parameter $f_{_{\rm NL}}$ in the different cases.

2.3.1 Numerical computation of the scalar bispectrum

In Subsec. 1.1.3, we had discussed the various contributions to the scalar bispectrum arising from the bulk and the boundary terms in the action describing the curvature perturbation at the third order. We had also outlined the numerical procedure to evaluate the scalar bispectrum. As we had pointed out, once the background evolution has been determined, it is a matter of arriving at the solution for the modes f_k and then using them to compute the integrals $\mathcal{G}_{_C}(\boldsymbol{k}_1, \boldsymbol{k}_2, \boldsymbol{k}_3)$ [*cf.* Eqs. (1.24)] and the corresponding contributions to the bispectrum. Evidently, evaluating the contributions due to the boundary terms $G_7(\boldsymbol{k}_1, \boldsymbol{k}_2, \boldsymbol{k}_3)$, $G_8(\boldsymbol{k}_1, \boldsymbol{k}_2, \boldsymbol{k}_3)$ and $G_9(\boldsymbol{k}_1, \boldsymbol{k}_2, \boldsymbol{k}_3)$ [*cf.* Eqs. (1.25) and (1.26)] is relatively straightforward as it involves no integrals and can be arrived at from the background quantities and the modes f_k.

As we had discussed earlier, in the standard slow roll scenario or in situations involving brief intermediate departures from slow roll [such as in the second Starobinsky model (SMII) and punctuated inflation (PI)], to arrive at the scalar power spectrum, the modes f_k are evolved from the time when $k = 10^2\,\sqrt{z''/z}$ to the time when $k = 10^{-5}\,\sqrt{z''/z}$. It has been established that it is often adequate to consider the evolution of modes over this domain to arrive at the bispectra as well (see Refs. [55, 56, 132]; in this context, also see Refs. [133, 134]). Since the amplitude of curvature perturbation freezes on super-Hubble scales, one finds that the contribution over the domain $k < 10^{-5}\,\sqrt{z''/z}$ proves to be insignificant. However, as the bispectrum involves three modes, one has to evolve the modes and carry out the integrals from a domain when the smallest of the three wave numbers (k_1, k_2, k_3) satisfies the sub-Hubble condition $k = 10^2\,\sqrt{z''/z}$ until the time when the largest of the three satisfy the super-Hubble condition $k = 10^{-5}\,\sqrt{z''/z}$.

As we had pointed out in Subsec. 1.1.3, there is yet another point one needs to take into account when computing the integrals. Since the modes oscillate in the sub-Hubble domain, one actually needs to introduce a cut-off in order to regulate the integrals involved. Theoretically, such a cut-off is necessary to identify the correct perturbative vacuum (see, for instance, Refs. [52, 53]). Numerically, the cut-off helps us to efficiently compute the integrals. For an arbitrary triangular configuration of the wave vectors, one often works with a democratic cut-off of the form $\exp-[\kappa\,(k_1+k_2+k_3)/(3\,\sqrt{z''/z})]$, where κ is a suitably chosen constant. The value of κ is determined by calculating the integrals starting from different times inside the Hubble radius and examining the dependence of the results for the integrals on the initial time and the value of κ. It is found that, in most of the cases, if one chooses to integrate from $k = 10^2\,\sqrt{z''/z}$, the value of $\kappa \simeq 0.3$ proves to be optimal [56, 132–134]. In other words, for $\kappa = 0.3$, the values of the integrals prove to be independent of how deep inside the Hubble radius the integrals are carried out from. We use this procedure to calculate the integrals $\mathcal{G}_{_C}(\boldsymbol{k}_1, \boldsymbol{k}_2, \boldsymbol{k}_3)$ [*cf.* Eqs. (1.24)], the resulting bispectrum $G(\boldsymbol{k}_1, \boldsymbol{k}_2, \boldsymbol{k}_3)$ and the corresponding non-Gaussianity parameter $f_{_{\rm NL}}(\boldsymbol{k}_1, \boldsymbol{k}_2, \boldsymbol{k}_3)$ in the cases of SMII and PI [56].

But, the scenario with kinetically dominated initial conditions and variations of it such as its dual and the hard cut-off model pose a peculiar problem. Recall that, in these cases, modes over a certain range of wave numbers are never inside the Hubble radius (in this context, see Fig. 2.1). Therefore, the integrals involving modes over this range do not actually require a cut-off. For these modes, we evaluate the integrals from $N = 0$ or $N = N_1$ when we begin to evolve the perturbations. When we do so, we find that, the contributions to the scalar bispectrum for this range of modes are completely insensitive to the value of the cut-off parameter κ. This point is illustrated in Fig. 2.6 wherein we have plotted the contributions to the bispectrum in the equilateral limit (*i.e.* when $k_1 = k_2 = k_3 = k$) due to the bulk and the boundary terms as a function of κ in the case of QPa. Also, in QPa and similar scenarios, for the initial conditions and the best-fit values of the parameters we have worked with, we find that we can impose the Bunch-Davies initial condition at $k = 10^2\,\sqrt{z''/z}$ for modes with $k \gtrsim 8\times 10^{-3}\,\mathrm{Mpc}^{-1}$. As one would have expected, for these modes, the choice of $\kappa = 0.3$ turns out to be ideal as in the cases of SMII and PI (see Fig. 2.6). However, since the modes over the range $8\times 10^{-5} \lesssim k \lesssim 8\times 10^{-3}\,\mathrm{Mpc}^{-1}$ do not spend an adequate amount of time in the sub-Hubble domain, we are unable to carry out the exercise described above for identifying an apt value of κ over this set of wave numbers. We choose to be democratic,

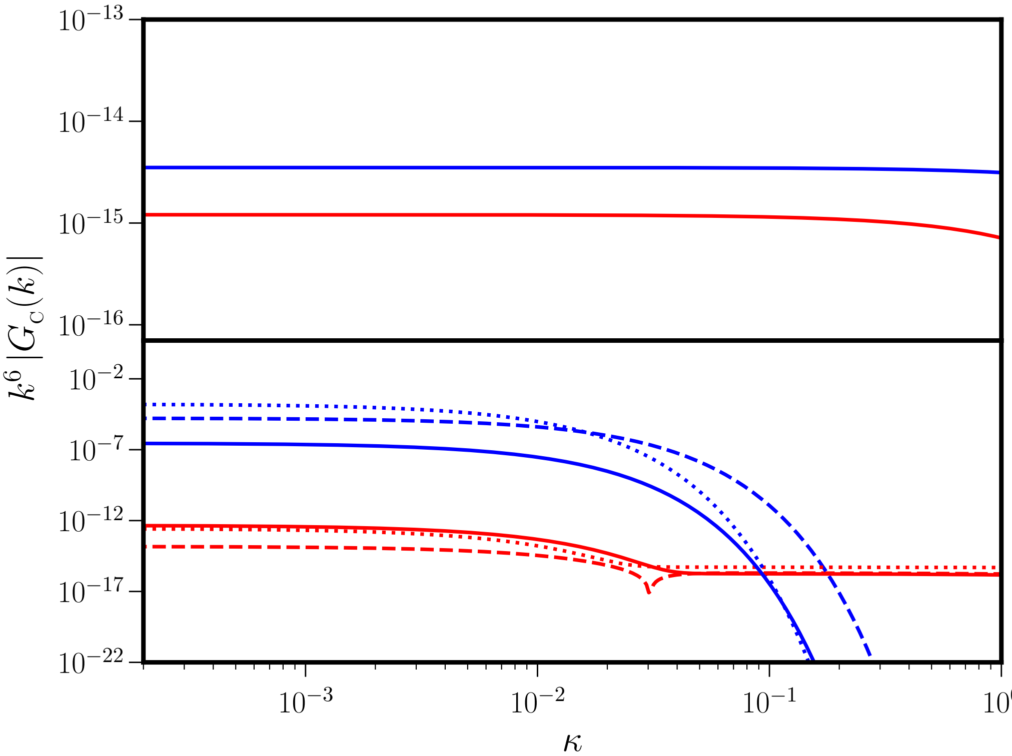

Figure 2.6: The bulk and the boundary contributions to the scalar bispectrum evaluated numerically in the equilateral limit for the case of the quadratic potential with kinetically dominated initial conditions have been plotted as functions of the cut-off parameter κ. For highlighting the points we wish to make, we have grouped the six standard bulk terms, along with the seventh term, *viz.* $G_{_C}(k)$ with $C = \{1, 2, \ldots, 7\}$ (in red) and the boundary terms, *viz.* $G_8(k)$ and $G_9(k)$ (in blue). We have plotted these quantities for two modes with the wave numbers $k = 5 \times 10^{-5}\,\mathrm{Mpc}^{-1}$ (in the top panel) and $k = 0.1\,\mathrm{Mpc}^{-1}$ (in the bottom panel) in the case of the model QPa. The first of these wave numbers is representative of the modes with suppressed power and is always outside the Hubble radius, whereas the second corresponds to a typical mode in the nearly scale invariant regime that emerges from sufficiently deep inside the sub-Hubble domain (*cf.* Fig. 2.1). We have plotted the quantities when the integrals involved have been evaluated from $N = 0$ (as solid curves) and from the e-folds satisfying the conditions $k = 100\sqrt{z''/z}$ and $k = 200\sqrt{z''/z}$ (as dashed and dotted curves, respectively), with the latter two being, evidently, possible only for the mode with the larger wave number. Note that, while the quantities are completely insensitive to κ for the first mode, the plots suggest the optimal value of the cut-off parameter to be $\kappa = 0.3$ for the second mode. Also, we should point out that the boundary terms dominate the bulk terms for the mode with the smaller wave number (*cf.* top panel). Moreover, in the case of the mode with the larger wave number, for $\kappa = 0.3$, the boundary terms cease to be important and the contributions to the bispectrum are dominated by the bulk terms, as is expected for a mode that emerges from sufficiently deep inside the Hubble radius.

and we work with $\kappa = 0.3$ over this range of modes as well. Also, we carry out the integrals from $N = 0$ or $N = N_1$ for all the modes (*viz.* for $10^{-5} < k < 1\,\mathrm{Mpc}^{-1}$) until the time when the largest of the three wave numbers involved satisfies the condition $k = 10^{-5}\,\sqrt{z''/z}$.

In Fig. 2.7, we have plotted the various bulk and boundary contributions to the bispectrum for QPa, SMII and PI. One finds that, in the equilateral limit, the contributions due to the first and the third terms and the contributions due to the fifth and the sixth terms have the same form. Therefore, in the figure, we have plotted the combinations $G_1(k)+G_3(k)$, $G_2(k)$, $G_4(k)+G_7(k)$[2], $G_5(k)+G_6(k)$, $G_8(k)$ and $G_9(k)$. In the cases of SMII and PI, the boundary terms do not contribute due to the fact that all the modes of interest emerge from well within the Hubble radius. Also, in these two models, as is well known, it is the contribution due to the term $G_4(k) + G_7(k)$ that dominates [56, 132]. This is easy to understand as the term $G_4(k)$ depends on ϵ_2' which grows large for a brief period of time in these scenarios [*cf.* Eq. (1.24d)]. In complete contrast, in QPa, one finds that all the contributions to the bispectrum are roughly of the same order over a wide range of wave numbers. Moreover, in SMII and PI, all the contributions to the bispectrum are enhanced over wave numbers that leave the Hubble radius during the period of departure from slow roll inflation. However, in the case of QPa, the contributions to the scalar bispectrum due to the boundary terms dominate the contributions due to the bulk terms over a range of large scale modes. This is a novel result that does not seem to have been noticed earlier in the literature [16].

2.3.2 Analytical calculation in the hard cut-off model

Since it involves only slow roll, the hard cut-off model (HCO) provides a simple situation to evaluate the scalar bispectrum analytically. In this subsection, we shall compare the analytical results in this case with the corresponding numerical results to highlight the accuracy of our numerical computations in situations wherein the initial conditions for a range of modes are imposed on super-Hubble scales.

It is well known that, in slow roll, it is the first, second and the third bulk terms, *viz.* $G_{_C}(\boldsymbol{k}_1, \boldsymbol{k}_2, \boldsymbol{k}_3)$ with $C = \{1, 2, 3\}$, that contribute significantly to the bispectrum.

[2] Note that $G_7(k)$ is not a bulk term but is actually a boundary term. Earlier, we had mentioned that the integrals describing the bulk terms do not contribute when the modes are on super-Hubble scales at late times. For the term $G_4(k)$, this proves to be true only when the boundary term $G_7(k)$ is added. For this reason, often one considers the combination $G_4(k) + G_7(k)$ [56].

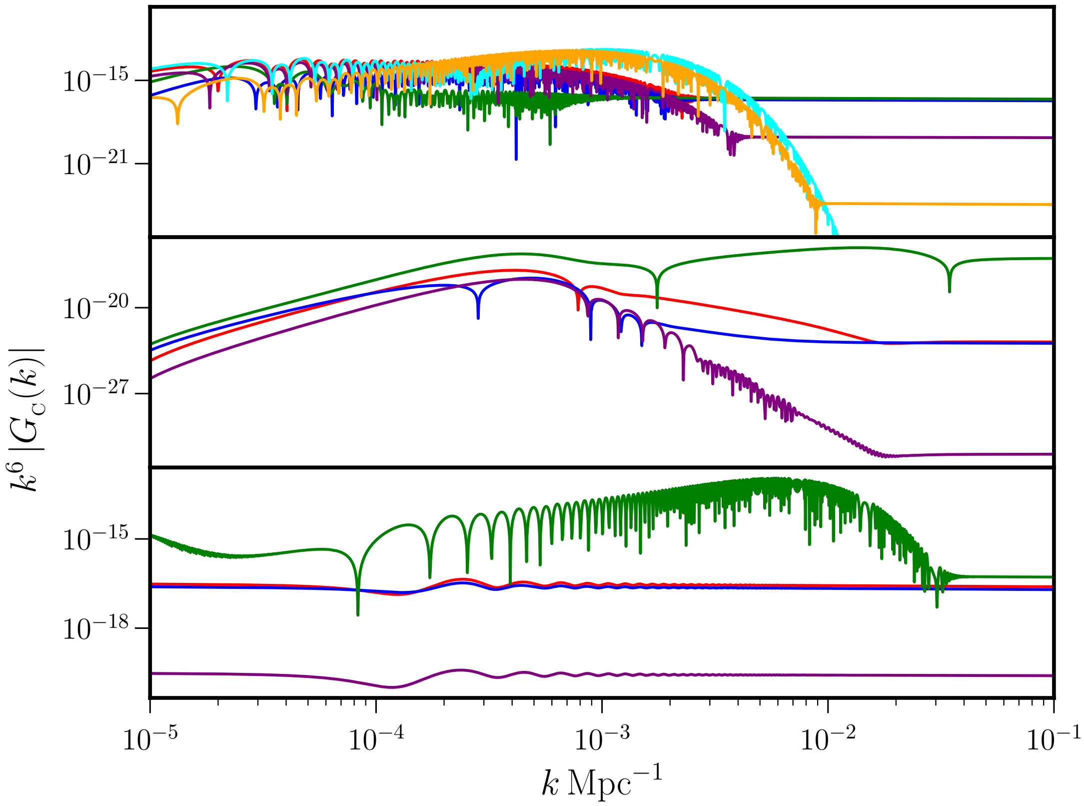

Figure 2.7: The different contributions to the scalar bispectrum in the equilateral limit, *viz.* the bulk terms $G_1(k) + G_3(k)$ (in red), $G_2(k)$ (in blue), $G_4(k) + G_7(k)$ (in green), $G_5(k) + G_6(k)$ (in purple) and the boundary terms $G_8(k)$ (in cyan) and $G_9(k)$ (in orange), evaluated numerically, have been plotted for three models of our interest, *viz.* QPa (on top), PI (in the middle) and SMII (at the bottom). We should mention that we have made use of the smoothened potential (2.3) to evaluate the results numerically in the case of SMII. Note that, since all the modes of cosmological interest emerge from sufficiently inside the Hubble radius in SMII and PI, there arise no contributions from the boundary terms in these cases. However, in the case of QPa, it should be clear that the boundary terms dominate at small wave numbers. We should also point out the linear growth in $G_4(k) + G_7(k)$ at large k in SMII. The growth is known to be become indefinite in the limit when the quantity $\Delta\phi$ in the potential (2.3) vanishes, *i.e.* when the change in the slope of the potential ceases to be smooth and is infinitely abrupt as in the original potential (2.2) [126, 127].

These bulk terms are characterized by integrals of the form [*cf.* Eqs. (1.24)]

$$I_1 = \int_{\eta_{\rm i}}^{\eta_{\rm e}} {\rm d}\eta\, f_{k_1}(\eta)\, f_{k_2}'(\eta)\, f_{k_3}'(\eta)\, {\rm e}^{\kappa\,(k_1+k_2+k_3)\,\eta/3} + \text{two permutations}, \tag{2.9a}$$

$$I_2 = \int_{\eta_{\rm i}}^{\eta_{\rm e}} {\rm d}\eta\, f_{k_1}(\eta)\, f_{k_2}(\eta)\, f_{k_3}(\eta)\, {\rm e}^{\kappa\,(k_1+k_2+k_3)\,\eta/3}, \tag{2.9b}$$

with the modes f_k given by Eq. (2.6) in the case of HCO. Since the initial conditions are imposed on super-Hubble scales for a range of modes, apart from these bulk terms, we also need to evaluate the contributions due to the boundary terms, *viz.* $G_{_C}(\boldsymbol{k}_1, \boldsymbol{k}_2, \boldsymbol{k}_3)$ with $C = \{7, 8, 9\}$. While the boundary terms are straightforward to evaluate as they involve no integrals, one finds that the above-mentioned integrals are easy to calculate as well.

Note that, in the above integrals, we have introduced the cut-off in the democratic (in k_1, k_2, k_3) manner that we had discussed earlier. In Fig. 2.8, we have compared the analytical results for the different contributions to the bispectrum with the corresponding numerical results in the equilateral limit. To arrive at the numerical results, we have worked with the quadratic potential (2.1) and have started the evolution on the inflationary attractor, as we had described in Subsec. 2.2.1 wherein we had discussed the scalar power spectrum arising in the model. It is clear that the analytical results match well with the numerical results indicating the extent of accuracy of the numerical procedures we have adopted. As in the cases of QP and SMI, we find that the boundary terms, in particular $G_8(k)$, dominate at suitably small wave numbers.

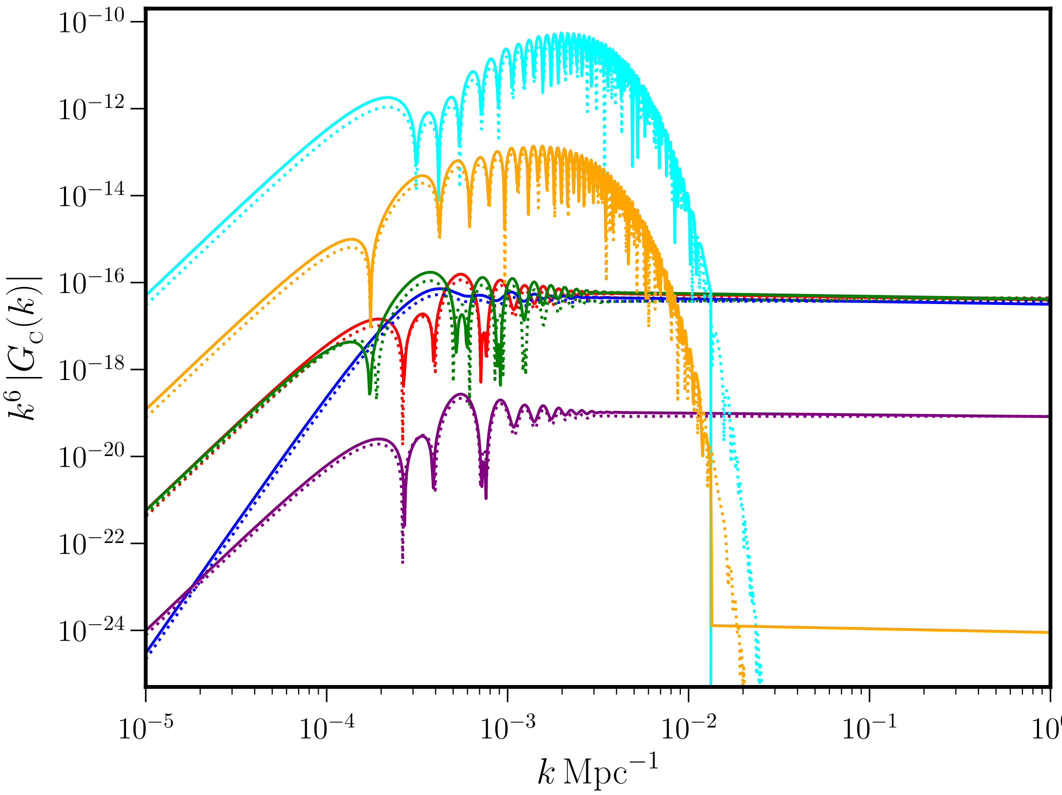

Figure 2.8: The different bulk and boundary contributions to the scalar bispectrum, evaluated in the equilateral limit, have been plotted for the hard cut-off model (HCO) with the same choices of colors as in the previous figure. We have plotted the quantities arrived at analytically (as dotted curves) as well as numerically (as solid curves). Clearly, the analytical results match the numerical results quite well. Moreover, as in the case of QPa plotted in the previous figure, the contributions from the boundary terms dominate those due to the bulk terms on large scales.

2.4 AMPLITUDE AND SHAPE OF THE NON-GAUSSIANITY PARAMETER

Having obtained the scalar bispectrum, let us now turn to understand the amplitude and shape of the corresponding non-Gaussianity parameter $f_{\rm NL}$. In the next section, we shall discuss the behavior of the parameter in the so-called squeezed limit wherein it is expected to be expressed completely in terms of the scalar spectral index. In this section, we shall discuss the behavior in the equilateral limit as well as the complete shape, which is often illustrated in the form of density plots.

Let us first consider the equilateral limit. In Fig. 2.9, we have illustrated the behavior of the parameter $f_{\rm NL}$ in the equilateral limit in the different models of our interest. Recall that, according to the most recent constraints from Planck: $f_{\rm NL}^{\rm local} = -0.9 \pm 5.1$, $f_{\rm NL}^{\rm equil} = -26 \pm 47$ and $f_{\rm NL}^{\rm ortho} = -38 \pm 24$ [*cf.* Eqs. (1.33); in this context, also see Ref. [58]]. Amongst the models we have considered, we find that the parameter $f_{\rm NL}$ is very large in the cases of QPc, SMIc and HCO. In fact, these scenarios are likely to be inconsistent with the most recent constraints on the parameter. The models SMII and PI also lead to relatively large value of $f_{\rm NL}$, but this can attributed to the sharp drop in the scalar power spectra over the relevant scales rather than a rise in the amplitude of the bispectrum. As we shall discuss in the concluding section, it seems urgent to arrive at a template for the bispectrum in models such as PI in order to be able to compare it with the CMB data at the level of three-point functions.

In Fig. 2.10, we have illustrated the complete shape of the scalar non-Gaussianity parameter $f_{\rm NL}(\boldsymbol{k}_1, \boldsymbol{k}_2, \boldsymbol{k}_3)$ that arises in the various models of our interest in the form of density plots, as is usually done. We should mention that the density plots of $f_{\rm NL}$ have been computed with k_3 set to be the pivot scale. For the models QPa and QPb, we find that the non-Gaussianity parameter around the pivot scale is equilateral in shape corresponding to the slow roll value of $f_{\rm NL} \simeq 2 \times 10^{-2}$ in the equilateral limit. The suppression in the scalar power spectrum, which occurs roughly two decades in wave numbers away from the pivot scale does not affect the shape of $f_{\rm NL}$ around the pivot scale. In the cases of SMIa and SMIb, we see a roughly similar behavior with a slightly lesser amplitude of $f_{\rm NL}$ as expected in SMI models. In the case of SMII, we see small but persistent oscillations with $f_{\rm NL} \simeq 10^{-2}$ throughout the range of wave numbers around the pivot scale. This can be attributed to the behavior of the contribution $G_4(k) + G_7(k)$ in the model. In PI, the bispectrum is largely local in shape with a sharp increase in

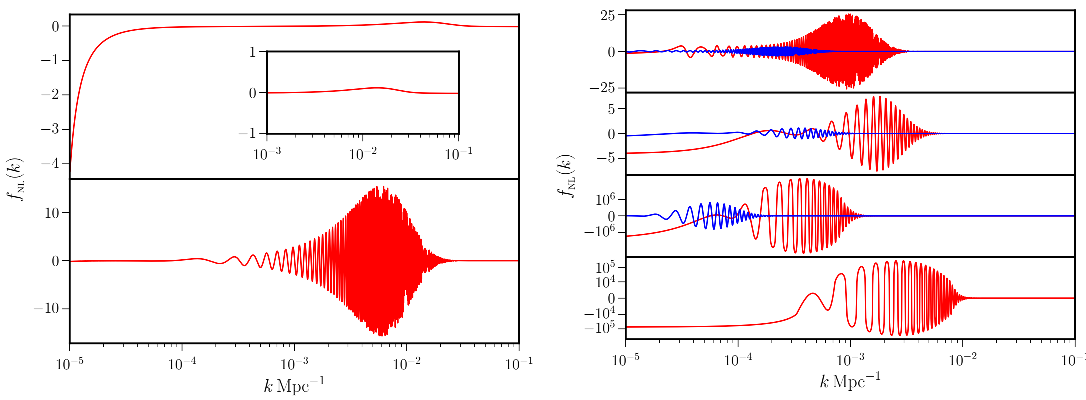

Figure 2.9: The scalar non-Gaussianity parameter $f_{\rm NL}$ computed in the equilateral limit has been plotted for all the models of our interest: PI and SMII (in the top and bottom panels on the left), QPa, QPb and QPc (in the top three panels on the right, respectively, as red curves), SMIa, SMIb and SMIc (in the top three panels on the right, in blue) and, lastly, HCO (in the bottom panel on the right). In the case of PI, $f_{\rm NL}$ has been plotted on a log scale to cover the wide range over which it varies. Note that the scalar power spectrum appears in the denominator in the definition of $f_{\rm NL}$ [*cf.* Eq. (1.28)]. The spike in the amplitude of $f_{\rm NL}$ in the case of PI arises due to the sharp drop in the power spectrum (in this context, see Fig. 2.4). The oscillations with increasing amplitude at larger wave numbers in the case of SMII is caused due to the contribution from $G_4(k) + G_7(k)$, which rises linearly before eventually dying down (*cf.* Fig. 2.7). Such a behavior occurs due to the sharp transition in the evolution of the field as it crosses the discontinuity in the potential. Also note that the maximum amplitude of $f_{\rm NL}$ is larger in QPa and SMIa when compared to QPb and SMIb (also see Ref. [16]). This can be partly attributed to the larger initial velocity of the background scalar field when the initial conditions are imposed on the perturbations. Moreover, interestingly, we find that the amplitude of $f_{\rm NL}$ is larger in the case of QP than SMI. Lastly, the amplitude of $f_{\rm NL}$ in the cases of QPc, SMIc and HCO are extremely large, indicating that these models are unlikely to be viable in the light of the constraints on $f_{\rm NL}$ from Planck.

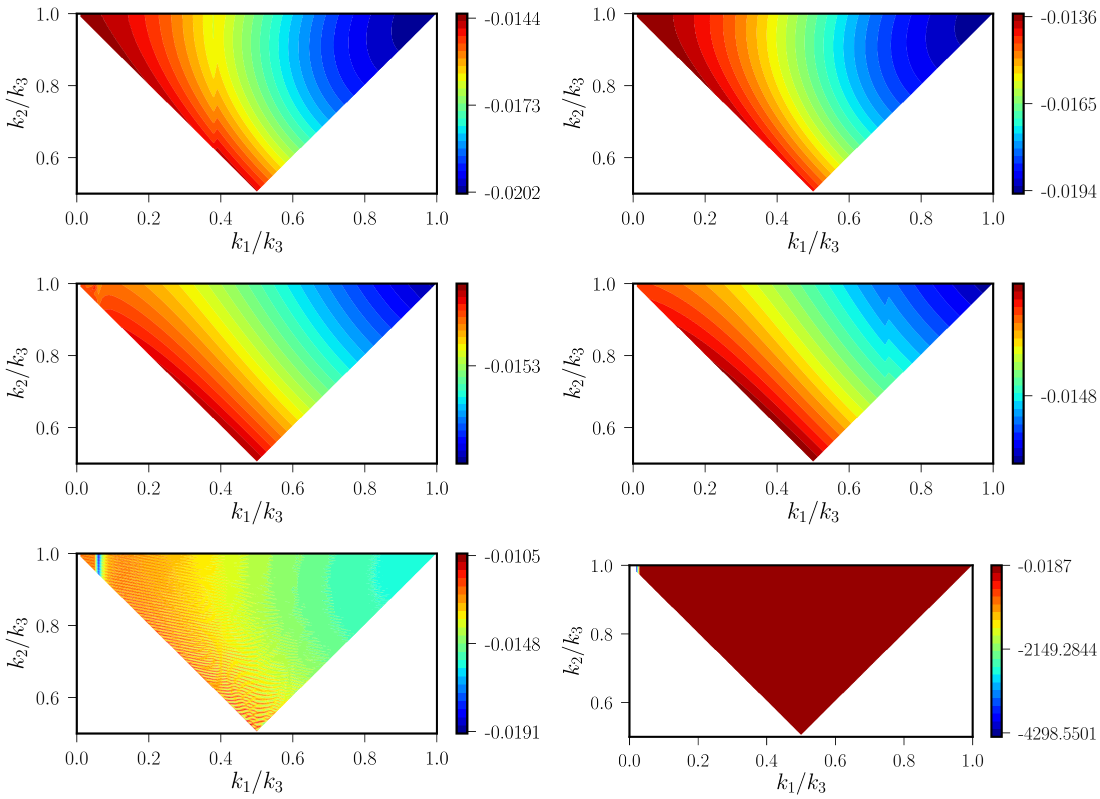

Figure 2.10: The amplitude and shape of the non-Gaussianity parameter $f_{\rm NL}(\boldsymbol{k}_1, \boldsymbol{k}_2, \boldsymbol{k}_3)$ has been illustrated as density plots for the various models of our interest (QPa, SMIa and SMII from top to bottom on the left, and QPb, SMIb and PI in the same order on the right) as a function of k_1/k_3 and k_2/k_3. Note that we have chosen k_3 to be the pivot scale in all the plots.

amplitude occurring at wave numbers around the location where the scalar spectrum exhibits a sharp drop in power.

2.5 VALIDITY OF THE CONSISTENCY RELATION

Let us now turn to the behavior of the three-point functions in the squeezed limit wherein one of the three wave numbers is much smaller than the other two [52, 132, 135, 136]. Since the amplitude of the long wavelength mode freezes on super-Hubble scales during inflation, it can be treated as part of the background. Consequently, one finds that, in such a limit, the three-point functions generated during inflation can be expressed entirely in terms of the two-point functions through the so-called consistency relation. In the squeezed limit, the scalar bispectrum is expected to reduce to the following form (see, for instance, Ref. [132]):

$$\lim_{k_1 \to 0} G(\boldsymbol{k}_1, \boldsymbol{k}, -\boldsymbol{k}) = -\frac{(2\,\pi)^4}{4\,k_1^3\,k^3}\,[n_{_\mathrm{S}}(k) - 1]\;\mathcal{P}_{_\mathrm{S}}(k_1)\,\mathcal{P}_{_\mathrm{S}}(k), \tag{2.10}$$

where $n_{_\mathrm{S}}(k) = 1 + [\mathrm{d}\ln\mathcal{P}_{_\mathrm{S}}(k)/\mathrm{d}\ln k]$ is the scalar spectral index [*cf.* Eq. (1.31)], and it should be clear that we have considered $\boldsymbol{k}_1$ to be the squeezed mode. Upon substituting the above expression in the definition (1.28) for the non-Gaussianity parameter $f_{_\mathrm{NL}}(\boldsymbol{k}_1, \boldsymbol{k}_2, \boldsymbol{k}_3)$, we find that we can express the consistency relation in the squeezed limit as follows:

$$\lim_{k_1 \to 0} f_{_\mathrm{NL}}(\boldsymbol{k}_1, \boldsymbol{k}, -\boldsymbol{k}) = \frac{5}{12}\,[n_{_\mathrm{S}}(k) - 1] \equiv f_{_\mathrm{NL}}^{\mathrm{CR}}(k). \tag{2.11}$$

With the results we have obtained, it is straightforward to examine if the above consistency relation is satisfied in the models of our interest. Actually, it has already been established that the consistency relation is satisfied in SMII and PI despite the strong departures from slow roll, as reflected in the sharp features in the power spectra and bispectra (see Fig. 2.11; in this context, also see Refs. [60, 132]). However, in the case of the scenarios with kinetically dominated initial conditions, we find that the consistency condition is violated on large scales where the scalar power spectrum exhibits a suppression. This should be clear from Fig. 2.11 wherein we have plotted the non-Gaussianity parameter $f_{_\mathrm{NL}}(k)$ in the squeezed limit as well as the quantity $f_{_\mathrm{NL}}^{\mathrm{CR}}(k)$ [*cf.* Eq. (2.11)] for most of the models we have been interested in. We find that the consistency relation begins to be satisfied in these cases only at small scales (for

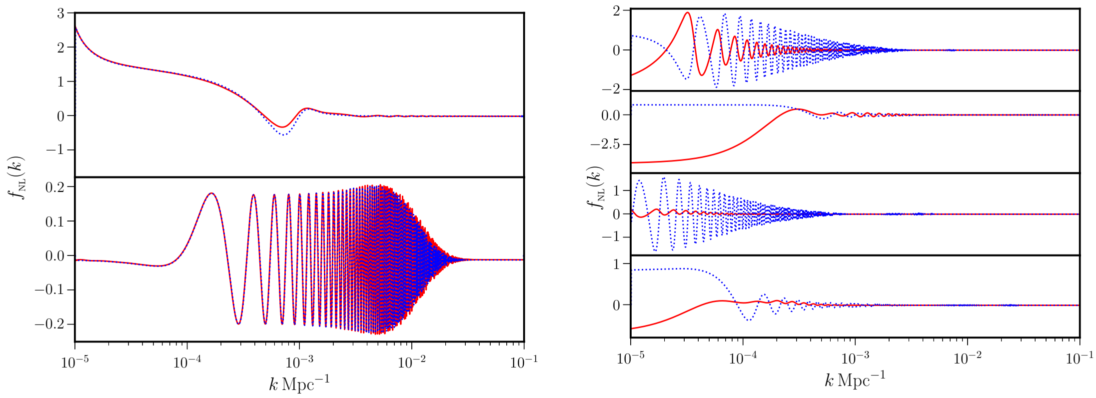

Figure 2.11: The non-Gaussianity parameter $f_{\rm NL}(k)$ in the squeezed limit has been plotted (in red) for the cases of PI, SMII (top and bottom panels, on the left), QPa, QPb, SMIa and SMIb (panels from top to bottom in that order, on the right). We have also plotted the quantity $f_{\rm NL}^{\rm CR}(k)$ [*cf.* Eq. (2.11)], determined completely by the scalar spectral index, for each of these models (as dotted blue curves). Clearly, the consistency condition (2.11) is satisfied in PI and SMII (as is evident from the figure on the left) even over wave numbers wherein there arise strong departures from near scale invariance in the power and bi-spectra. In complete contrast, in QPa, QPb, SMIa and SMIb, the consistency condition is violated at large scales (as should be clear from the figure on the right), but it is eventually restored at the small scales (in this context, also see our earlier work [16]). We find that the behavior of $f_{\rm NL}$ is similar in the cases of QPc, SMIc and HCO. Hence, we have not plotted them here. The difference arises only in the magnitude of $f_{\rm NL}$ over large scales where the consistency condition is violated.

$k \gtrsim 8 \times 10^{-3}\,\mathrm{Mpc}^{-1}$) which emerge from sufficiently deep inside the Hubble radius [say, from $k \simeq 10^2\,\sqrt{|z''/z|}$] after slow roll inflation has set in. Evidently, the violation of the consistency condition is associated with the fact that the Bunch-Davies initial condition on the large scale modes are imposed when they are outside the Hubble radius. We should mention here that the violation of the consistency condition at large scales that we encounter is somewhat similar to the violation of the condition noticed earlier in the case of non-attractor inflation [130, 131, 137–139].

2.6 SUMMARY AND SCOPE

At the level of the power spectrum, all the models we have considered here, *viz.* models with kinetically dominated initial conditions, their dual, the hard cut-off model, the second Starobinsky model and punctuated inflation, lead to a suppression of power on large scales. Naively, one would have expected that non-Gaussianities would help us discriminate between the different models, and we find that indeed they do. Though there arise some differences in the overall amplitude of the scalar bispectra in the various models, the crucial distinction seems to be their behavior in the squeezed limit. While the consistency condition is satisfied in PI and SMII over all modes of cosmological interest, in the models with initial kinetic domination, their dual and HCO, the consistency relation is found to be violated on large scales for the modes that always remain in the super-Hubble regime. However, as in the cases of PI and SMII, in QP, SMI and HCO, the consistency relation is satisfied for the small scale modes which evolve from the sub-Hubble regime.

Models such as punctuated inflation or the second Starobinsky model may be considered to be more appealing theoretically than the models with kinetically dominated initial conditions. However, the data can help us evaluate the performance of the models and rule in favor of one over the other. In order to compare with the CMB data at the level of the bispectrum, it will be useful to obtain an analytical template for the scalar bispectrum (in this context, see, for example, Refs. [140, 141]). While there have been efforts to reproduce the power spectra analytically in the case of models with kinetically dominated initial conditions (in this context, see Ref. [103]), these analytical calculations seem to underestimate the amplitude of the oscillations that arise as the spectrum turns scale invariant. In the context of PI, there seems to have been no effort at all to arrive at the power spectrum analytically. We are currently working on evaluating the spectra as well as the bispectra analytically in PI as well as in models with kinetically dominated initial conditions with the aim of eventually comparing these models with the CMB data at the level of bispectra [142].

CHAPTER 3

PBHs AND SECONDARY GWs FROM ULTRA SLOW ROLL AND PUNCTUATED INFLATION

3.1 INTRODUCTION

With the recent observations of GWs from merging binary black holes involving a few to tens of solar masses [143–154], there has been a considerable interest in examining whether such black holes could have a primordial origin [155–157]. The most popular mechanism to generate PBHs is the inflationary scenario (for earlier discussions, see, for example, Refs. [12, 77]; also see the recent reviews [9, 74–76]). PBHs are formed when the curvature perturbations generated during inflation reenter the Hubble radius during the radiation and matter dominated epochs. However, most inflationary models permit only slow roll inflation and, in such cases, the extent of PBHs produced proves to be considerably smaller than required for any astrophysical implications (see, for example, Ref. [70]). Recall that, on large scales, the primordial scalar power spectrum is strongly constrained by the increasingly precise observations of the anisotropies in the CMB (for recent constraints from Planck, see Refs. [6, 158]). In order to lead to a significant amount of PBHs, the scalar power spectrum on small scales should be considerably enhanced from the COBE normalized values over the CMB scales (for an early discussion in this context, see, for instance, Ref. [70]). In inflation, this is possible only when there are strong departures from slow roll. It boils down to identifying inflationary potentials that permit slow roll initially and then violating it for a certain period of time, before restoring it again until close to the termination of inflation.

In models of inflation driven by a single, canonical scalar field, the so-called ultra slow scenario has turned out to be the most popular mechanism in the literature to enhance scalar power on small scales. This scenario involves a period during inflation wherein the first slow roll parameter turns very small (for the initial discussions, see Refs. [71, 72, 159]; in this context, also see, for instance, Refs. [160, 161]). In fact, one finds that the scenario can be further divided into two types, those which admit a brief period of departure from inflation and another wherein no such departure arises. The scenario wherein inflation is interrupted briefly is referred to as punctuated inflation (for the original discussions, see Refs. [162–164]; for later and recent efforts, see Refs. [17, 109–111]; for a discussion in the context of PBHs, see Refs. [160, 165]). Interestingly, in such scenarios, the interruption of inflation is inevitably followed by an epoch of ultra slow roll which aids in boosting the power on small scales. While, in the case of punctuated inflation, all the slow roll parameters (including the first) turn large briefly, in ultra slow roll inflation, the first slow parameter remains small until the very end of inflation and slow roll is said to be violated due to the large values achieved by the second and higher slow roll parameters.

Often, the above-mentioned scenarios are achieved with the aid of potentials which contain a point of inflection [71, 72, 110, 111, 159, 161]. The inflection point seems to play a crucial role in these scenarios in inducing a period of ultra slow roll. The two stages of slow roll and ultra slow roll lead to either a step or a bump-like feature in the resulting inflationary scalar power spectrum, depending on the details of the dynamics involved. The lower level of the step is associated with the large scale modes that leave the Hubble radius during the first epoch of slow roll and the power is enhanced on small scales corresponding to modes that leave the Hubble radius during the later epoch of ultra slow roll. As we discussed in the last chapter, the punctuated inflationary scenario has been considered to explain the lower power observed at the small multipoles in the CMB data. If one chooses the drop in power to occur at scales roughly corresponding to the Hubble radius today, one finds that the resulting power spectrum can improve the fit to the CMB data to a certain extent (for an earlier analysis, see Ref. [110]; for a recent discussion, see Ref. [17]).

We mentioned above that both ultra slow roll inflation and punctuated inflation can lead to a sharp rise in power on small scales. Evidently, if one chooses the rise to occur at suitable scales, one can utilize these power spectra to lead to enhanced formation of PBHs. As has been established, such an enhanced amplitude for the scalar power spectrum can induce secondary GWs when these modes reenter the Hubble radius at later times during the radiation dominated epoch (for the original discussions, see, for example, Refs. [88–91]; for recent discussions in this context, see Refs. [95, 96, 166]). These secondary GWs with boosted amplitudes can, in principle, be detected by current and forthcoming observatories such as LIGO/Virgo [167], Pulsar Timing Arrays (PTA) [85, 168, 169], the Laser Interferometer Space Antenna (LISA) [170, 171], the Big Bang Observer (BBO) [172–174], the Deci-hertz Interferometer Gravitational wave Observatory (DECIGO) [175, 176] and the Einstein Telescope (ET) [177, 178]. Moreover, the deviations from slow roll inflation, even as they boost the scalar power spectrum on small scales, also lead to larger levels of scalar non-Gaussianities on these scales (in this context, see, for example, Refs. [55, 56, 60]). These non-Gaussianities can, in principle, further increase the extent of PBH formation (for early discussions, see, for example, Refs. [70, 179, 180]; for recent discussions, see Refs. [181–188]) as well as the strength of the secondary GWs (see Refs. [189–191]; for a recent discussion, also see Ref. [192]). In this chapter, we examine the enhanced formation of PBHs and the generation of secondary GWs in ultra slow roll and punctuated inflation. We also numerically evaluate the inflationary scalar bispectrum generated on small scales in these scenarios and utilize the results to discuss the corresponding imprints on the extent of PBHs formed and the amplitude of secondary GWs. In addition to considering specific potentials that lead to the scenarios of our interest, we choose functional forms for the first slow roll parameter leading to ultra slow roll and punctuated inflation, reverse engineer potentials and examine the observational implications (for other efforts in these directions, see, for instance, Refs. [70, 193–195]). Interestingly, such an exercise also confirms the understanding that, in models of inflation involving a single, canonical scalar field, a point of inflection in the potential seems essential to lead to ultra slow roll or punctuated inflation.

This chapter is organized as follows. In the following section, we shall introduce the different models of our interest which lead to ultra slow roll and punctuated inflation. In Sec. 3.3, we shall discuss the power spectra that arise in these models and illustrate how the intrinsic entropy perturbation associated with the scalar field proves to be responsible for enhancing the amplitude of the curvature perturbation. In this section, we shall also highlight some of the challenges that one encounters in constructing viable models of ultra slow roll and punctuated inflation. In Sec. 3.4, we shall consider specific forms for the first slow roll parameter leading to ultra slow roll and punctuated inflation, and reverse engineer the potentials that lead to such scenarios. We shall also discuss the power spectra that arise in these cases. In Secs. 3.5 and 3.6, we shall discuss extent of PBHs formed and calculate the dimensionless parameters characterizing the power as well as bispectra of secondary GWs generated in the models and scenarios of interest. We shall also compare our results with the constraints from observations. In Sec. 3.7, we shall calculate the dimensionless non-Gaussianity parameter $f_{_{\rm NL}}$ associated with the scalar bispectrum in all the different cases. We shall highlight some of the properties of the non-Gaussianity parameter $f_{_{\rm NL}}$ and then go on to discuss the imprints of the scalar non-Gaussianities on the formation of PBHs and the generation of secondary GWs. In Sec. 3.8, we shall conclude with a summary of the main results. We shall relegate some of the related discussions to the appendices.

3.2 MODELS OF ULTRA SLOW ROLL AND PUNCTUATED INFLATION

In this section, we shall briefly describe the specific models of interest that lead to ultra slow roll and punctuated inflation. We should mention that all the five models that we shall discuss in the following two subsections contain a point of inflection. Recall that, while the first slow roll parameter is defined as $\epsilon_1 = -\mathrm{d}\ln H/\mathrm{d}N$, the higher order slow roll parameters are defined in terms of the first slow roll parameter ϵ_1 through the relations $\epsilon_{n+1} = \mathrm{d}\ln\epsilon_n/\mathrm{d}N$, for $n \geq 1$ [*cf.* Eqs. (1.7)]. As it is the first three slow roll parameters, *viz.* ϵ_1, ϵ_2, and ϵ_3, that determine the amplitude and shape of the power spectrum as well as the bispectrum, we shall illustrate the behavior of these slow roll parameters in the models of interest.

3.2.1 Potentials leading to ultra slow roll inflation

We shall consider two specific models that permit ultra slow roll inflation. The first potential we shall consider which leads to a period of ultra slow roll inflation is often written in the following form (see, for instance, Ref. [71]):

$$V(\phi) = V_0\, \frac{6\,x^2 - 4\,\alpha\,x^3 + 3\,x^4}{(1+\beta\,x^2)^2}, \tag{3.1}$$

where $x = \phi/v$, with v being a constant rescaling factor. We shall work with the following choices of the parameters involved: $V_0/M_{_{\rm Pl}}^4 = 4\times 10^{-10}$, $v/M_{_{\rm Pl}} = \sqrt{0.108}$, $\alpha = 1$ and $\beta = 1.4349$. For these choices of parameters, the inflection point, say, ϕ_0, is located at $0.39\,M_{_{\rm Pl}}$. We find that, if we choose the initial value of the field to be $\phi_{\rm i} = 3.614\,M_{_{\rm Pl}}$, then inflation lasts for about 63 e-folds in the model. For convenience, we shall hereafter refer to the potential (3.1), along with the above-mentioned set of parameters, as USR1.

The second potential that we shall consider is given by [160]

$$V(\phi) = V_0\left\{\tanh\left(\frac{\phi}{\sqrt{6}\,M_{_{\rm Pl}}}\right) + A\,\sin\left[\frac{\tanh\left[\phi/\left(\sqrt{6}\,M_{_{\rm Pl}}\right)\right]}{f_\phi}\right]\right\}^2, \tag{3.2}$$

and we shall work with the following values of the parameters involved: $V_0/M_{_{\rm Pl}}^4 = 2\times 10^{-10}$, $A = 0.130383$ and $f_\phi = 0.129576$. We find that, for these values of the parameters, the inflection point occurs at $\phi_0 = 1.05\,M_{_{\rm Pl}}$. For the initial value of the field $\phi_{\rm i} = 6.1\,M_{_{\rm Pl}}$, we obtain about 66 e-folds of inflation in the model. We shall refer to the potential (3.2) and the above set of parameters as USR2.

As we mentioned, the background dynamics driven by these potentials can be well captured by the behavior of the first three slow roll parameters ϵ_1, ϵ_2 and ϵ_3. We have plotted the evolution of these quantities as a function of e-folds N in Fig. 3.1. It is clear from the behavior of ϵ_1 that these models permit two different regimes of slow roll, separated by a short phase of departure from slow roll. Note that the value of ϵ_1 during

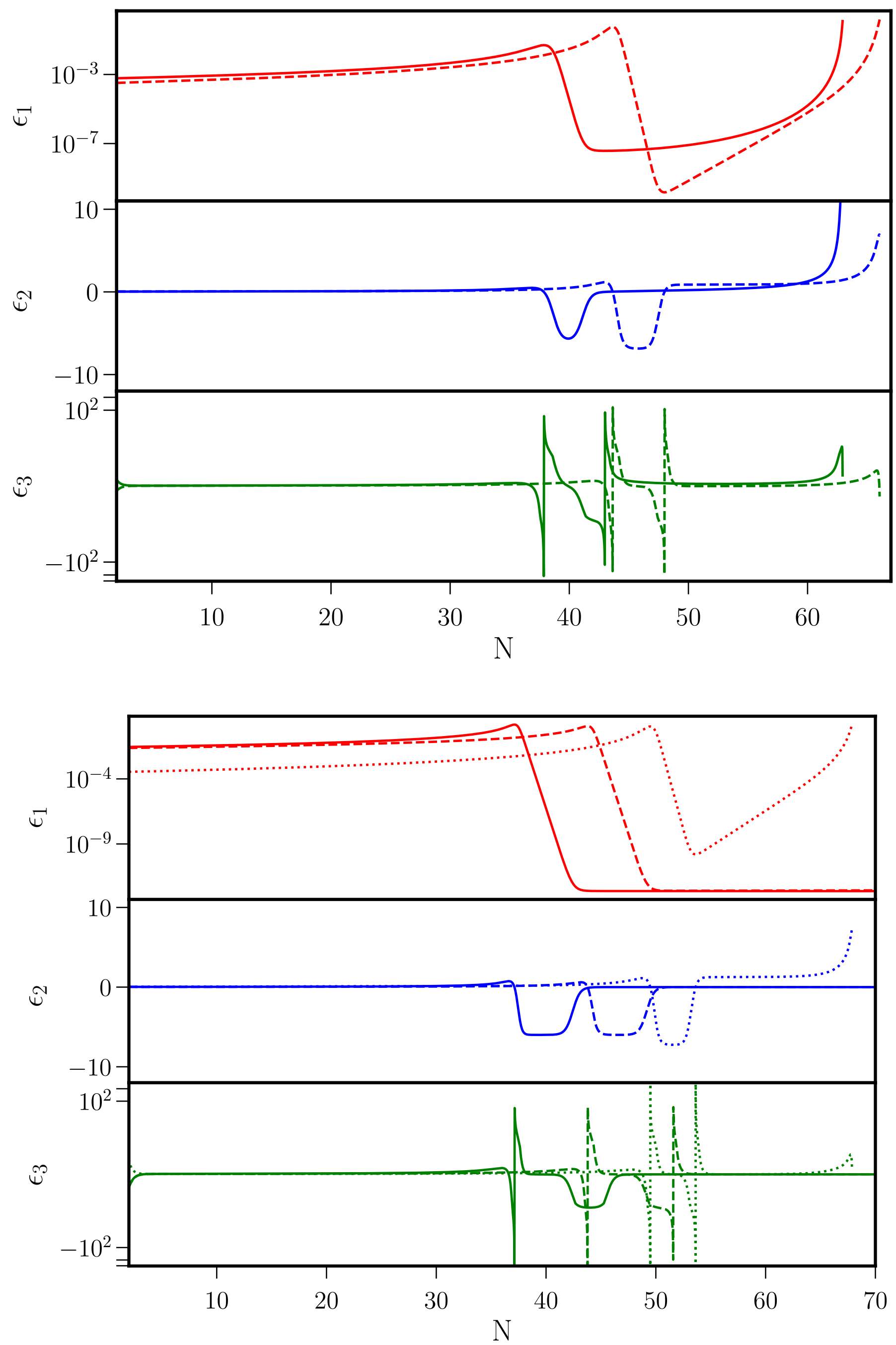

Figure 3.1: The behavior of the first three slow roll parameters ϵ_1, ϵ_2 and ϵ_3 have been plotted in the models of interest which lead to ultra slow roll and punctuated inflation. We have plotted the behavior for all the five models we have discussed, *viz.* USR1 and USR2 (as solid and dashed curves, on top) as well as PI1, PI2 and PI3 (as solid, dashed and dotted curves, at the bottom). Note that all the models consist of two distinct regimes of slow roll and ultra slow roll inflation, while the punctuated inflationary models also contain a short period of departure from inflation.

the second regime of slow roll is a few orders of magnitude smaller than its value during the initial regime, thereby leading to the nomenclature of ultra slow roll inflation. We should point out that there is no deviation from inflation in these models, as the first slow roll parameter always remains smaller than unity until the very end of inflation. The transition from slow roll to ultra slow roll is rather rapid and this aspect is reflected by the sharp rise and fall in the amplitude of the second and third slow roll parameters within a short period. It should also be highlighted that the second slow roll parameter ϵ_2 is large and negative (about -6 and -7 in USR1 and USR2) during the ultra slow phase when the first slow roll parameter ϵ_1 is rapidly decreasing. The parameter ϵ_2 changes sign when ϵ_1 begins to rise as the field crosses the point of inflection and rolls down towards the minimum of the potential. But, ϵ_2 continues to remain relatively large (it is about 0.2 and 0.9 in the cases of USR1 and USR2) even during this latter phase, when compared to the typical slow roll values encountered, say, at early times before the transition to the epoch of ultra slow roll.

To gain a better understanding of the dynamics involved, in Fig. 3.2, we have also plotted the evolution of the scalar field in phase space for the case of USR2. Evidently, trajectories from different initial conditions eventually merge with the primary trajectory of interest. The transition to the ultra slow roll regime corresponds to the sharp upward turn in the phase space trajectory when the velocity of the field decreases as it nears the point of inflection. It is interesting to note that the solution obtained in the slow roll approximation closely follows the primary trajectory even during the ultra slow roll regime. The field crosses the point of inflection, eventually emerging from the ultra slow regime, and inflation ends as the field approaches the minimum of the potential.

3.2.2 Potentials permitting punctuated inflation

As we have discussed, punctuated inflation corresponds to a scenario wherein a short period of departure from inflation is sandwiched between two epochs of slow roll. With the help of specific examples, we shall illustrate that the period of departure from inflation is inevitably followed by an epoch of ultra slow roll inflation.

A simple model that has been examined in the early literature which permits interrupted inflation is described by the potential (see Ref. [162]; also see Refs. [163,

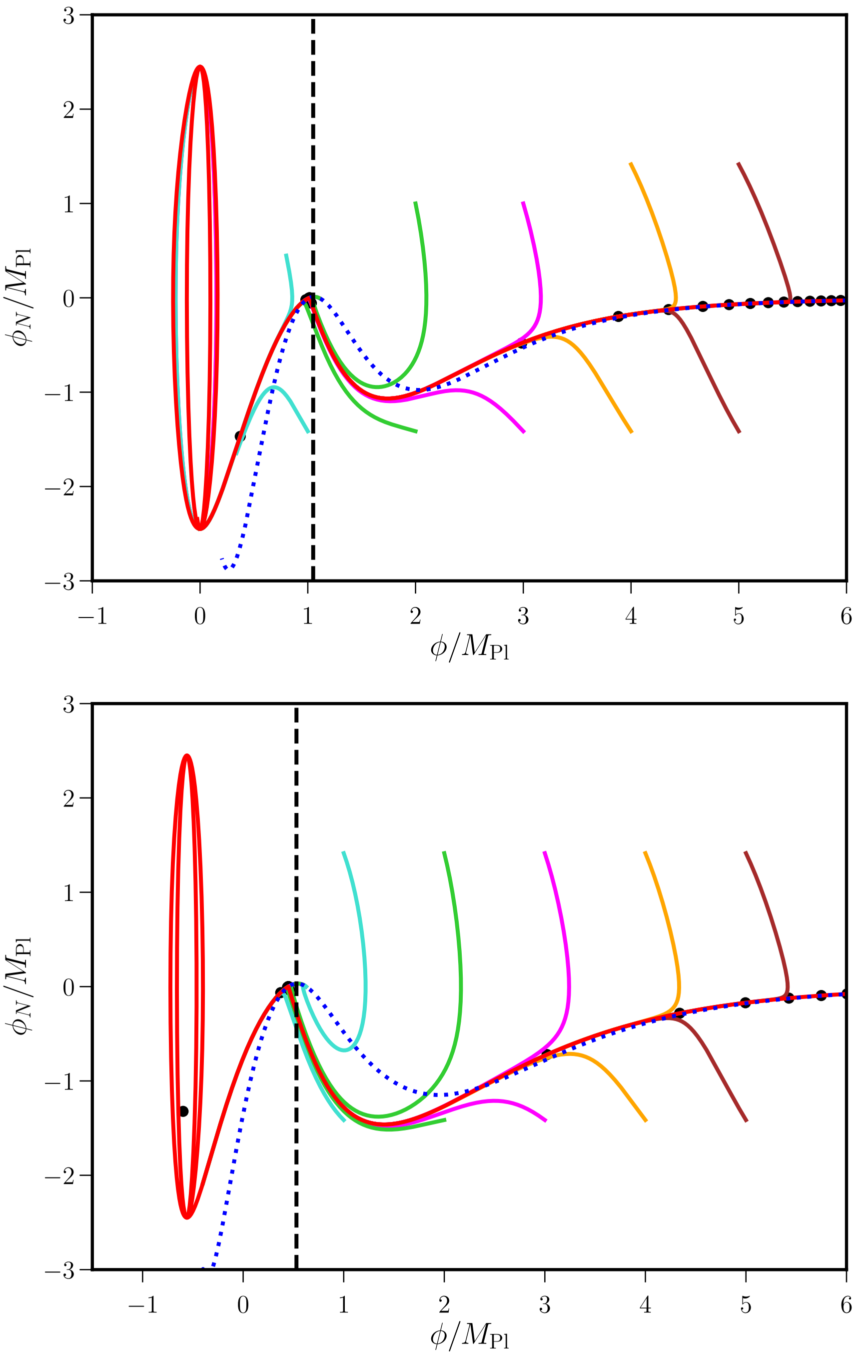

Figure 3.2: The dynamics of the scalar field in the phase space ϕ-ϕ_N, where $\phi_N = \mathrm{d}\phi/\mathrm{d}N$, has been illustrated for the models USR2 (on top) and PI3 (at the bottom). Apart from the trajectory for the specific initial conditions we shall be working with (plotted in red), we have also plotted the evolution for a few other initial conditions (as solid curves in different colors). Moreover, in the case of the primary trajectory, we have indicated the lapse in time every 3 e-folds (as black dots on the red curves). Further, we have highlighted the evolution arrived at using the standard slow roll approximation (as dotted blue curves). Note that the vertical lines (in dashed black) identify the point of inflection.

164])

$$V(\phi) = V_0 \left(1 + B\,\phi^4\right). \tag{3.3}$$

It should be evident that the inflection point for this model is located at $\phi = 0$. For $B/M_{_{\rm Pl}}^4 = 0.5520$, one finds that the model leads to two epochs of inflation separated by a brief interruption of inflation. In fact, around the interruption, the first slow roll parameter rises above unity and quickly falls to very small values, resulting in a period of ultra slow roll. It is easy to argue that such a behavior arises due to the constant term V_0 in the potential [162]. But, the presence of the constant term simultaneously leads to an important drawback of the model. Once inflation is restored after the interruption, it is found that the eventual slow roll regime lasts forever. There is no conventional termination of inflation as the constant term V_0 sustains slow roll evolution even when the field has reached the bottom of the potential. So, one is either forced to terminate inflation by hand or invoke an additional source to end inflation. Despite these drawbacks, we shall nevertheless briefly discuss the model due to its simplicity. We shall work with the above-mentioned value for the parameter B and choose $V_0/M_{_{\rm Pl}}^4 = 8 \times 10^{-13}$. We shall set the initial value of the field to be $\phi_{\rm i} = 17\, M_{_{\rm Pl}}$, and we shall assume that inflation ends after 70 e-folds. We shall hereafter refer to this model as PI1.

The second potential that we shall consider can be expressed as (see, for instance, Refs. [110, 111, 196])

$$V(\phi) = \frac{m^2}{2}\,\phi^2 - \left(\frac{\sqrt{2\,\lambda\,(n-1)}\,m}{n}\right)\,\phi^n + \frac{\lambda}{4}\,\phi^{2\,(n-1)}, \tag{3.4}$$

where n is an integer. These potentials contain a point of inflection at

$$\phi_0 = \left[\frac{2\,m^2}{\lambda\,(n-1)}\right]^{1/[2\,(n-2)]}. \tag{3.5}$$

We shall focus on the case $n = 3$, wherein the potential above reduces to

$$V(\phi) = \frac{m^2}{2}\,\phi^2 - \frac{2\,m^2}{3\,\phi_0}\,\phi^3 + \frac{m^2}{4\,\phi_0^2}\,\phi^4, \tag{3.6}$$

which is the same as the potential (2.5) we had discussed in the last chapter. We shall work with the following values of the parameters: $m/M_{_{\rm Pl}} = 1.8 \times 10^{-6}$ and $\phi_0/M_{_{\rm Pl}} = 1.9777$. As we shall soon discuss, these choice of parameters indeed admit punctuated inflation. However, one finds, as in the case of PI1, the above potential (for the parameters mentioned) does not naturally result in an end of inflation after the desired duration. Despite this limitation, we shall discuss the model, since, it should be clear that, modulo the denominator, the potential describing USR1 [*cf.* Eq. (3.1)] is essentially the same as the potential (3.4). We shall choose the initial value of the field to be $\phi_{\mathrm{i}} = 20\, M_{_{\mathrm{Pl}}}$, and we shall again assume that inflation ends after 70 e-folds. We shall refer to this model as PI2.

Another model we shall consider that permits punctuated inflation is motivated by supergravity. It is described by the potential (see Ref. [160]; for a recent discussion, also see Ref. [197])

$$V(\phi) = V_0\, \left[c_0 + c_1\, \tanh\left(\frac{\phi}{\sqrt{6\,\alpha}}\right) + c_2\, \tanh^2\left(\frac{\phi}{\sqrt{6\,\alpha}}\right) + c_3\, \tanh^3\left(\frac{\phi}{\sqrt{6\,\alpha}}\right)\right]^2, \tag{3.7}$$

and we shall work with the following values for the parameters involved: $V_0/M_{_{\mathrm{Pl}}}^4 = 2.1 \times 10^{-10}$, $c_0 = 0.16401$, $c_1 = 0.3$, $c_2 = -1.426$, $c_3 = 2.20313$ and $\alpha = 1$. This model too contains a point of inflection and, for the above values for the parameters, the point of inflection is located at $\phi_0 = 0.53\, M_{_{\mathrm{Pl}}}$. If we choose the initial value of the field to be $\phi_{\mathrm{i}} = 7.4\, M_{_{\mathrm{Pl}}}$, we find that inflation ends after about 68 e-folds. We shall refer to this model as PI3. For the above choice of the parameters, apart from a plateau for large field values, the potential admits a second plateau at smaller values of the field. As we shall see soon, it is these aspects of the potential that permits punctuated inflation and thereby aids in boosting the scalar power spectrum at small scales.

As in the case of the ultra slow roll models we had discussed in the previous subsection, we have plotted the first three slow roll parameters ϵ_1, ϵ_2 and ϵ_3 for the models PI1, PI2 and PI3 in Fig. 3.1. It is easy to see from the plots that the behavior of the three slow roll parameters are very similar across the models and they differ only in their location of the departures from slow roll. Evidently, after an initial slow roll regime, a brief departure from inflation occurs with ϵ_1 growing above unity. The interruption of inflation is immediately followed by a period of ultra slow roll with ϵ_1 falling to a value that is considerably smaller than its value during the initial slow roll regime. Moreover, other than PI3, the models have no definite end of inflation since ϵ_1 does not rise to unity once the ultra slow roll regime has begun. Further, note that, when the epoch of ultra slow roll sets in, as in USR1 and USR2, the second slow roll parameter ϵ_2 turns large and negative in all the cases of PI1, PI2 and PI3. The parameter ϵ_2 eventually approaches zero in the cases of PI1 and PI2, since the first slow roll parameter never rises from its very low values in these models. However, in PI3, since ϵ_1 rises ultimately leading to the end of inflation, the second slow roll parameter ϵ_2 eventually turns positive (from nearly -7) and attains a large value (around 1.2), in very much the same manner it had in USR2. As with USR2, we have plotted the behavior of the field in phase space for the case of PI3 in Fig. 3.2. It should be clear from the figure that the velocity of the field reaches larger values in the case of PI3 than in the case of USR2 prior to entering the ultra slow roll regime. Evidently, it is this behavior that is responsible for the brief interruption of inflation.

3.3 EVOLUTION OF THE CURVATURE PERTURBATION AND POWER SPECTRA

In this section, we shall discuss the scalar and tensor power spectra that arise in the models permitting ultra slow roll and punctuated inflation we had introduced in the previous section. However, before we go on to discuss the power spectra, we shall illustrate the behavior of the curvature perturbations during the period of deviation from slow roll. Specifically, we shall highlight the role played by the intrinsic entropy perturbations in the enhancement of the amplitude of the curvature perturbations over wave numbers that leave the Hubble radius either immediately prior to or during the departure from slow roll.

3.3.1 Role of the intrinsic entropy perturbation

Often the evolution of the curvature perturbations in non-trivial scenarios involving departures from slow roll inflation are examined in terms of the behavior of the quantity z (see, for instance, Refs. [160, 198, 199]). We find that it proves to be instructive to understand this aspect from the behavior of the intrinsic entropy perturbation [109, 163]. It is well known that, in contrast to perfect fluids, scalar fields, in general, possess non-vanishing non-adiabatic pressure perturbation $\delta p_{_{\rm NA}}$ or, equivalently, the intrinsic entropy perturbation $\mathcal{S}$, which are related through the expression (in this context, see, for example, Refs. [200, 201])

$$\delta p_{_{\rm NA}} = \frac{p'}{\mathcal{H}}\,\mathcal{S}, \tag{3.8}$$

where p denotes the pressure associated with the background and, as we have indicated earlier, $\mathcal{H} = a\,H$ is the conformal Hubble parameter. In the case of inflation driven by a single, canonical scalar field, one can show that the intrinsic entropy perturbation $\mathcal{S}_k$ associated with a given mode of the field can be expressed in terms of the corresponding curvature perturbation, say, $\mathcal{R}_k$, as follows [109, 163]:

$$\mathcal{R}_k' = -\left[\frac{2\,a^2\,p'}{M_{_{\rm Pl}}^2\,(\mathcal{H}' - \mathcal{H}^2)}\right]\,\left(\frac{1}{1-c_{_{\rm A}}^2}\right)\,\mathcal{S}_k, \tag{3.9}$$

where $c_{_{\rm A}} = \sqrt{p'/\rho'}$ is adiabatic speed of the scalar perturbations, with ρ being the background energy density. It is easy to show using the equation of motion (1.11a) describing the curvature perturbation that, in the super Hubble limit, the intrinsic entropy perturbation $\mathcal{S}_k$ decays as ${\rm e}^{-2\,N}$. However, it is found that, during deviations from slow roll, for modes which are either about to leave or have just left the Hubble radius, the amplitude of the intrinsic entropy perturbation briefly increases, sourcing the curvature perturbation [109, 164]. This, in turn, alters the amplitude of the curvature perturbation for modes which cross the Hubble radius just before or during the departure from slow roll.

To demonstrate these effects, in Fig. 3.3, we have plotted the evolution of the curvature and the intrinsic entropy perturbations in the inflationary models USR2 and PI3. In order to highlight the differences in the behavior of the modes, we have plotted the evolution of the amplitudes for three modes which leave the Hubble radius just prior to the start of the departure from slow roll inflation, immediately after start of the period of transition, and during the middle of the transition. We should point out that we have plotted the imaginary parts of $\mathcal{R}_k$ and $\mathcal{S}_k$ since they dominate at late times. Moreover, they allow us to highlight the oscillations in the sub-Hubble regime. The time when these oscillations cease is an indication that the modes have crossed the Hubble radius. Evidently, there is a sharp rise in the amplitude of the intrinsic entropy perturbation for all the modes during the departure from slow roll inflation. We should add here that the corresponding real parts of $\mathcal{R}_k$ and $\mathcal{S}_k$ behave in a roughly similar manner. It is the sharp rise in $\mathcal{S}_k$ that is responsible for either an enhancement or a suppression in the asymptotic (*i.e.* late time) amplitude of the curvature perturbation, thereby leading to features in the power spectrum (for related discussions in this context, also see, for instance, Refs. [160, 202]). In contrast, we find that there is relatively little effect of the deviation from slow roll on the evolution of the amplitude of the tensor perturbations. Due to this reason, the tensor power spectrum exhibits far less sharper features than the scalar power spectrum.

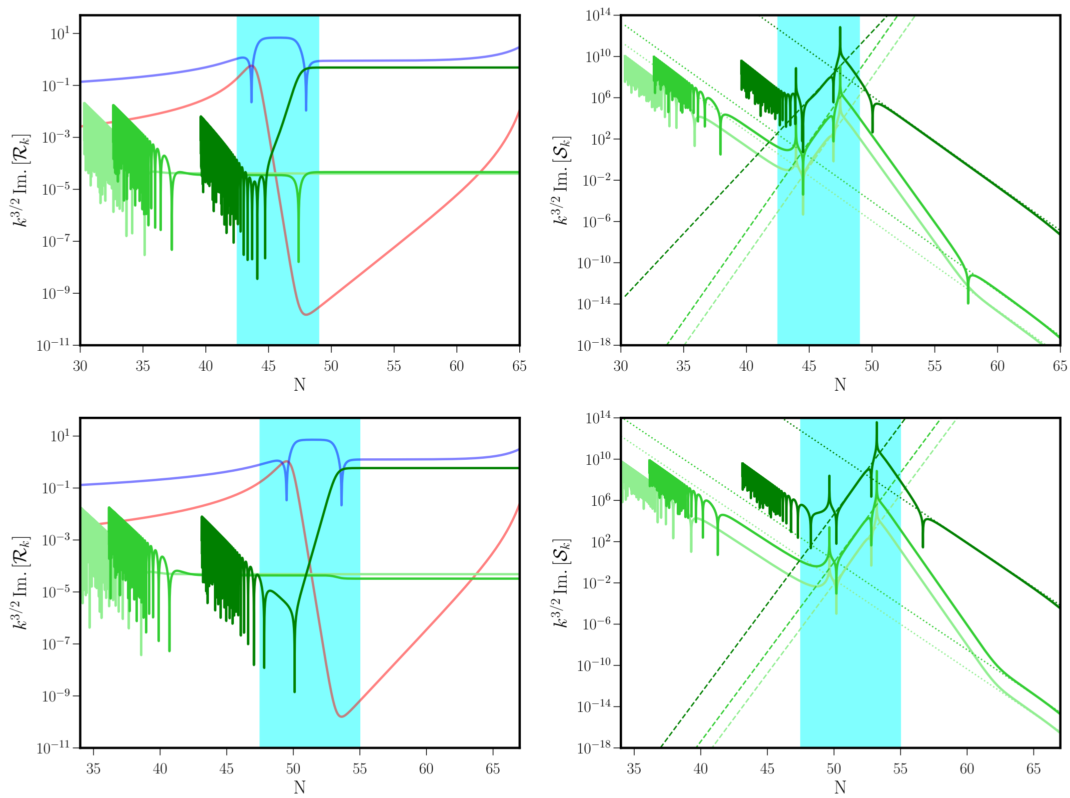

Figure 3.3: The evolution of the amplitudes of the imaginary parts of the curvature perturbation $\mathcal{R}_k$ (on the left) and the corresponding intrinsic entropy perturbation $\mathcal{S}_k$ (on the right) have been plotted for the three wave numbers $k = 10^{10}\,\mathrm{Mpc}^{-1}, 10^{11}\,\mathrm{Mpc}^{-1}$ and $10^{14}\,\mathrm{Mpc}^{-1}$ (in light, lime and dark green, respectively) in the two models USR2 (on top) and PI3 (at the bottom) as a function of e-folds. We have also included the behavior of the first two slow roll parameters ϵ_1 and $|\epsilon_2|$ (in red and blue, respectively, on the left) in these models to indicate the regime (demarcated by the cyan band) over which the transition from slow roll to ultra slow roll occurs. The first mode with the smallest wave number is already in the super-Hubble regime when the departure from slow roll sets in, and the amplitude of the corresponding curvature perturbation is hardly affected by the transition. The second mode is barely in the super-Hubble regime when the transition from slow roll begins. The amplitude of its curvature perturbation is slightly attenuated as it emerges from the departure from slow roll. Whereas, the amplitude of the curvature perturbation associated with the third mode, which leaves the Hubble radius right in the middle of the transition, exhibits a considerable enhancement due to the transition. These changes in the curvature perturbations can be attributed to the rapid growth in the corresponding entropy perturbations (plotted on the right) during the transition. We find that $\mathcal{S}_k$ grows as either $\mathrm{e}^{3\,N}$ or $\mathrm{e}^{4\,N}$ (indicated as dashed lines) during the transition. We also find that the entropy perturbations eventually die down as $\mathrm{e}^{-2\,N}$ in the super-Hubble limit (indicated by dotted lines) as expected. It is these behavior that lead to features in the inflationary scalar power spectra.

3.3.2 Scalar and tensor power spectra

We shall now turn to the scalar and tensor power spectra that arise in the ultra slow roll and punctuated inflationary scenarios we had discussed in the last section. Barring the brief rise of ϵ_1 above unity in the models of punctuated inflation and the location of the deviations from slow roll inflation, we had seen that the behavior of the first three slow roll parameters were very similar in the different models of our interest (*cf.* Fig. 3.1). We can expect these features to be reflected in the corresponding power spectra. In Fig. 3.4, we have plotted the power spectra arising in all the five models, *viz.* USR1, USR2, PI1, PI2 and PI3.

We shall first point out the features in the scalar power spectra that are common to all the models. All the models exhibit a rise in scalar power on small scales corresponding to modes that leave the Hubble radius during the second stage of slow roll. Moreover, the location of the rise in power is determined by the time when the deviation from slow roll occurs. This is due to the fact that, as we discussed in the previous subsection, it is the amplitude of the modes which exit the Hubble radius during the phase of departure from slow roll that are enhanced compared to the amplitudes of modes which leave during the initial phase of slow roll. Further, the modes that exit the Hubble radius during the epoch of ultra slow roll carry the imprints of the extremely small values of the first slow roll parameter and hence exhibit higher amplitudes.

Let us now consider the power spectra in the models USR1 and USR2. The location of features in the spectra is determined by the finely tuned values of parameters of the potential and the time when the modes leave the Hubble radius. Note that both USR1 and USR2 have a definite end of inflation. Let us say that the pivot scale $k_* = 0.05\,\mathrm{Mpc}^{-1}$ leaves the Hubble radius N_* number of e-folds prior to the end of inflation. For USR1 and USR2, to arrive at the power spectra plotted in Fig. 3.4, we have assumed that $N_* = (50.0, 56.2)$. The occurrence of a peak in the scalar power spectra at small scales in these models can be easily understood if we recall the behavior of the slow roll parameters in these cases. Recall that, in slow roll inflation, the scalar spectral index n_{S} is given in terms of the first two slow roll parameters as $n_{\mathrm{S}} = 1 - 2\,\epsilon_1 - \epsilon_2$. Though the regime of our interest does not strictly correspond to slow roll dynamics, we can utilize this relation to roughly understand the rise and fall of the scalar power spectra. We had earlier mentioned that, as ϵ_1 decreases rapidly during the epoch of ultra slow roll and eventually rises from its very small values, ϵ_2 changes from relatively large

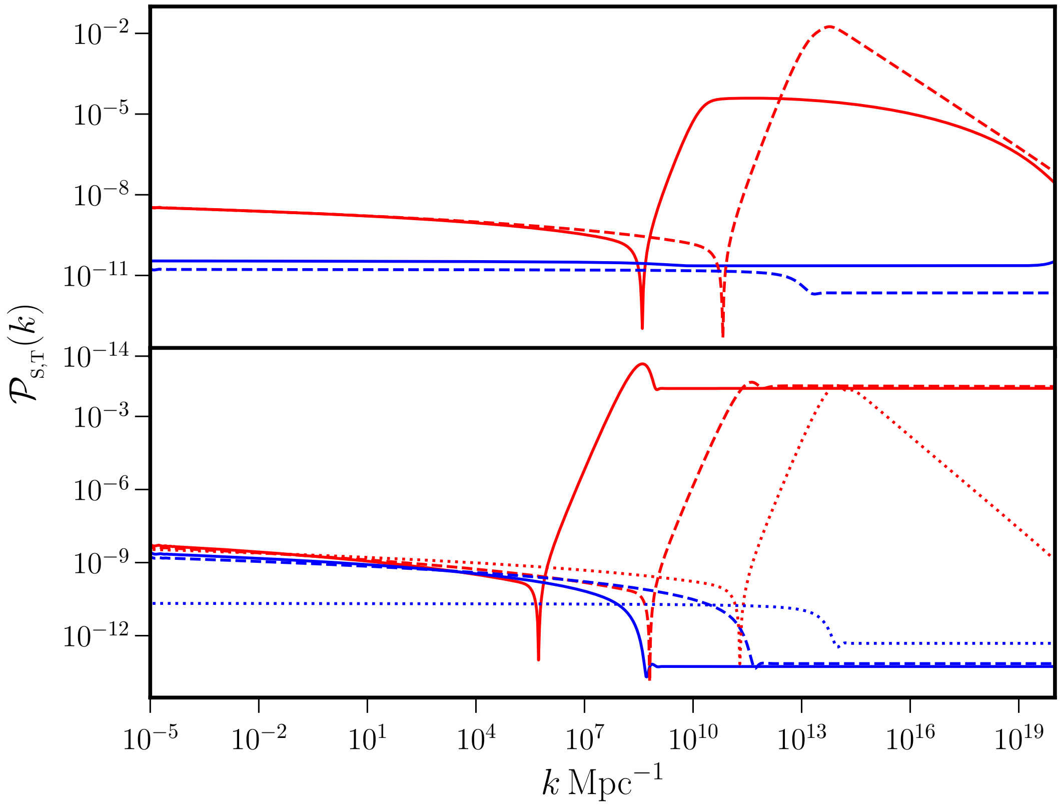

Figure 3.4: The scalar (in red) and tensor power spectra (in blue) have been plotted in the various ultra slow roll and punctuated inflationary models of our interest — USR1 and USR2 (as solid and dashed curves, on top) and PI1, PI2, and PI3 (as solid, dashed and dotted curves, at the bottom) — over a wide range of scales. Note that the enhancement of power on small scales is more in the case of USR2 than USR1. Moreover, in the case of the punctuated inflationary models, the scalar power in PI1 and PI2 do not eventually come down at very small scales due to the fact that inflation does not terminate in these models. We should also point out that, in contrast to the scalar power spectra, the tensor power spectra have lower power at small scales when compared to the large scales.

negative values to positive values in USR1 and USR2. Since ϵ_1 is very small during the ultra slow roll regime, for modes which leave around this epoch, the spectral index $n_{\rm S}$ mimics the behavior of $-\epsilon_2$, changing from large positive values (corresponding to an initially blue spectrum) to negative values (corresponding to a red spectrum on smaller scales), leading to a peak in the power spectra. Clearly, we also require that the power spectra at large scales are consistent with the current constraints on the scalar spectral index $n_{\rm S}$ and the tensor-to-scalar ratio r from the CMB data [6, 158]. We find that the models USR1 and USR2 lead to $(n_{\rm S}, r) = (0.945, 0.015)$ and $(0.946, 0.007)$ at the pivot scale. We should add a word of caution in this regard. The above values for $n_{\rm S}$ and r lie barely within the 2-σ limits on the respective parameters according to the latest constraints from Planck [6]. Importantly, if one were to even slightly change the values of the model parameters, the features in the power spectra get considerably altered. In other words, there is a severe fine tuning involved in arriving at the desired power spectra, an aspect which is well known and has been highlighted earlier (in this regard, see, for instance, Ref. [72]).

Let us now turn to the power spectra arising in the punctuated inflationary models. Once again, we can understand the behavior of the spectra at small scales in these cases from the relation between the scalar spectral index and the slow roll parameters. Recall that, while PI3 has a finite duration of inflation, there exists the problem of termination of inflation in the models PI1 and PI2. Due to this reason, as should be evident from the power spectra plotted in Fig. 3.4, the power never comes down in PI1 and PI2 because the eventual slow roll regime lasts for a long duration. However, since the evolution of the slow roll parameters in PI3 mimic their behavior in USR1 and USR2, the resulting scalar power spectrum exhibits a peak for the same reason that we discussed above, *viz.* the relatively large values and the change in the sign of the second slow roll parameter ϵ_2. For the three models of PI1, PI2 and PI3, we have set $N_* = (60.0, 60.0, 54.5)$ to arrive at their respective spectra presented in Fig. 3.4. We find that, for the choice of parameters that lead to COBE normalized scalar amplitude on large scales, the scalar spectral index and the tensor-to-scalar ratio at the pivot scale prove to be $(n_{\rm S}, r) = (0.885, 0.580)$, $(0.909, 0.461)$ and $(0.944, 0.009)$ in PI1, PI2 and PI3, respectively. Evidently, PI1 and PI2 are ruled out due to the large tensor-to-scalar ratio (beyond the upper limits from Planck, see our discussion in Subsec. 1.2.1) generated on the CMB scales in these models. In contrast, PI3 leads to a rather small tensor-to-scalar ratio that is consistent with the bounds from the Planck data and also comes close to satisfying the constraints on $n_{\rm S}$ [6, 158]. As far as the extent of boosting the power on small scales and the tunability of the model parameters are concerned, PI3 seems to require the same extent of fine-tuning as USR1 and USR2. In contrast to PI3, we find that it is easier to achieve sustained amplification of power over a wider range of scales in PI1 and PI2. But, obviously, it is achieved at the high cost that inflation does not end within the desired duration, essentially making them unviable. Nevertheless, we believe that there are lessons to be learnt from the simpler models PI1 and PI2 and we will exploit the main features of these models to reverse engineer desired potentials in the following section.

Lastly, let us make a few remarks on the tensor power spectra that we obtain in the various models. Note that the tensor power spectra also exhibit a step-like feature in all the models, but the step is in the opposite direction as compared to the scalars, with the amplitude of tensors at small scales being a few orders of magnitude smaller than their amplitude over large scales [110, 111, 203]. This can be attributed to the fact that after the period of deviation from slow roll, the inflaton evolves over smaller values of the field and hence smaller values of the potential.

3.3.3 Challenges in constructing viable models

With the experience of examining a handful of inflationary models, let us briefly summarize the challenges in constructing viable and well motivated models that lead to enhanced power on small scales.

To begin with, we need to ensure that the scalar spectral index $n_{\rm s}$ and the tensor-to-scalar ratio r are consistent with the cosmological data over the CMB scales. Moreover, in order to boost the extent of PBHs formed and the amplitude of the secondary GWs, we require enhanced power on small scales. Simultaneously, we need to make sure that inflation ends in a reasonable number of (say, about 65) e-folds. It is found that, as one attempts to resolve one issue, say, reduce the level of fine tuning or permit room to shift the location of the features in the scalar power spectrum, another difficulty, such as the prolonged duration of inflation, creeps in.

We should point out here that, a given potential which admits ultra slow roll inflation for a set of values of the parameters involved may permit punctuated inflation for another set (in this context, see App. B). For that reason, we should stress that the potentials themselves cannot always be classified as ultra slow roll or punctuated inflationary models. Hence, the dichotomy of ultra slow roll and punctuated inflationary scenarios that we have created may be considered somewhat artificial. However, we find it intriguing that whenever a potential admits restoration of inflation after a brief interruption, it seems to naturally result in a regime of ultra slow roll inflation. We believe that this aspect ought to be exploited to construct well motivated and viable canonical, single field inflationary models that also lead to enhanced PBH formation and generate secondary GWs of significant amplitudes.

With the eventual aim of overcoming these difficulties in single, canonical scalar field models of inflation, we shall now attempt to reconstruct potentials that possess the desired features.

3.4 REVERSE ENGINEERING POTENTIALS ADMITTING ULTRA SLOW ROLL AND PUNCTUATED INFLATION

In this section, we shall assume specific time-dependence for the first slow roll parameter ϵ_1 so that it leads to ultra slow roll or punctuated inflation. With the functional form of $\epsilon_1(N)$ at hand, we shall reconstruct the potentials using the equations of motion for the background and evaluate the resulting scalar and tensor power spectra that arise in the different scenarios [193–195].

3.4.1 Choices of $\epsilon_1(N)$

We shall consider the following two forms for $\epsilon_1(N)$ which lead to ultra slow roll or punctuated inflation for suitable choice of the parameters involved:

$$\epsilon_1^{\mathrm{I}}(N) = [\epsilon_{1a}\,(1+\epsilon_{2a}\,N)]\left[1-\tanh\left(\frac{N-N_1}{\Delta N_1}\right)\right]+\epsilon_{1b}+\exp\left(\frac{N-N_2}{\Delta N_2}\right), \tag{3.10a}$$

$$\epsilon_1^{\mathrm{II}}(N) = \epsilon_1^{\mathrm{I}}(N)+\cosh^{-2}\left(\frac{N-N_1}{\Delta N_1}\right). \tag{3.10b}$$

We find that considering a parametrization of the first slow roll parameter rather than the quantity z or the scale factor a proves to be much more convenient and easy to model the scenarios of our interest (in this context, see the recent efforts [204, 205]). The approach we adopt also allows us to easily ensure that the CMB constraints on large scales are satisfied. The above forms of $\epsilon_1(N)$ are supposed to represent the ultra slow roll and the punctuated inflationary scenarios we had discussed earlier. For convenience, we shall hereafter refer to the reconstructed inflationary scenarios arising from the forms of $\epsilon_1(N)$ in Eqs. (3.10a) and (3.10b) as RS1 and RS2, respectively. We shall now highlight a few points concerning the above constructions before proceeding to calculate the resulting power spectra.

Consider RS1 described by $\epsilon_1(N)$ in Eq. (3.10a). Note that the functional form contains seven parameters, *viz.* ϵ_{1a}, ϵ_{1b}, ϵ_{2a}, N_1, N_2, ΔN_1 and ΔN_2. For suitable choices of these parameters, this form of $\epsilon_1(N)$ leads to a period of slow roll followed by an epoch of ultra slow roll, before inflation eventually ends, as encountered in the ultra slow models USR1 and USR2 we had discussed in the last section. While ϵ_{1a} and ϵ_{1b} determine the values of the first slow roll parameter during slow roll and ultra slow roll, the parameters N_1 and N_2 determine the duration of these two phases. Note that the first term in the functional form (3.10a) is expressed as a product of two parts. The first part involving the parameter ϵ_{2a} induces a small time dependence during the early stages. Such a time dependence is necessary to achieve slow roll inflation which leads to scalar and tensor power spectra that are consistent with the CMB data. Recall that, in slow roll inflation, the scalar spectral index and the tensor-to-scalar ratio are given by $n_{\mathrm{S}} = 1 - 2\,\epsilon_1 - \epsilon_2$ and $r = 16\,\epsilon_1$, with the slow roll parameters evaluated at the time when the modes cross the Hubble radius. For suitable choices of ϵ_{1a} and ϵ_{2a}, we find that we can arrive at spectra that are consistent with the constraints on n_{S} and r from CMB, *viz.* $n_{\mathrm{S}} = 0.9649 \pm 0.0042$ and $r < 0.056$ at the pivot scale (see Refs. [6, 158]; also see Subsec. 1.2.1). The second part of the first term containing the hyperbolic tangent function aids in the transition from the slow roll to the ultra slow roll phase around the e-fold N_1. We need to set N_1 so that all the large scale modes leave the Hubble radius during the first slow roll phase.

The second term ϵ_{1b} in Eq. (3.10a) essentially prevents the first slow parameter ϵ_1 from reducing to zero beyond N_1. Since ϵ_{1b} defines the ultra slow roll phase of the model, we shall choose the parameter to be much smaller than ϵ_{1a}. The last term involving the exponential factor has been included to essentially ensure that ϵ_1 rapidly rises at later times, crossing unity at N_2, resulting in the termination of inflation. Lastly, the rapidity of the transitions from slow roll to ultra slow roll and from ultra slow roll to the end of inflation are determined by the parameters ΔN_1 and ΔN_2, respectively. In summary, since ϵ_{1a} and ϵ_{2a} are constrained by the CMB data on large scales, we have five free parameters, *viz.* ϵ_{1b}, N_1, N_2, ΔN_1 and ΔN_2, to construct the features we desire in the scalar power spectra over small scales.

Let us now turn to RS2 with $\epsilon_1(N)$ described by Eq. (3.10b). In this case, evidently, the term involving the hyperbolic cosine function has been added to the form of $\epsilon_1(N)$ in RS1. This additional terms leads to a brief interruption of inflation around the e-fold N_1, as is encountered in the punctuated inflationary models PI1, PI2, and PI3 discussed earlier.

Both the constructions of ϵ_1 above have been motivated to simplify the study of models containing an epoch of ultra slow roll with or without punctuation and thus producing inflationary spectra with either extended or localized features on small scales. The advantage of these constructions is that the parameters are easy to tune, which allows us to directly infer the corresponding effects on the background dynamics and importantly on the power spectra, unlike the specific inflationary models examined earlier. Of course, this has been possible due to the fact the reconstructions involve more parameters than the potentials we have considered.

3.4.2 Reconstructed potentials and the corresponding scalar and tensor power spectra

Using the Friedmann equations and the equation of motion governing the inflaton, it is straightforward to show that the time evolution of the scalar field $\phi(N)$ and the Hubble parameter $H(N)$ can be expressed in terms of the slow roll parameter $\epsilon_1(N)$ as follows:

$$\phi(N) = \phi_{\mathrm{i}} - M_{_{\mathrm{Pl}}} \int_{N_{\mathrm{i}}}^{N} \mathrm{d}N \sqrt{2\,\epsilon_1(N)}, \tag{3.11a}$$

$$H(N) = H_{\mathrm{i}} \exp\left[-\int_{N_{\mathrm{i}}}^{N} \mathrm{d}N\, \epsilon_1(N)\right], \tag{3.11b}$$

where ϕ_{i} and H_{i} are the values of the scalar field and the Hubble parameter at some initial e-fold N_{i}. We can use the above relations to arrive at the required background quantities given a functional form for $\epsilon_1(N)$. These background quantities can then be utilized to evaluate the resulting scalar and tensor power spectra. It is useful to note that the potential $V(N)$ can be expressed in terms of the Hubble parameter and the first slow roll parameter as

$$V(N) = M_{_{\mathrm{Pl}}}^2\, H^2(N)\, [3 - \epsilon_1(N)]\,. \tag{3.12}$$

Having obtained $\phi(N)$ and $V(N)$, clearly, we can construct $V(\phi)$ parametrically.

In Fig. 3.5, we have plotted the two choices (3.10) for $\epsilon_1(N)$ and the corresponding potentials for a small range of the parameter ΔN_1 that determines the duration of the transition from slow roll to ultra slow roll. The parameters we have worked with in the case of the reconstructed scenario RS1 are as follows: $\epsilon_{1a} = 10^{-4}$, $\epsilon_{2a} = 5 \times 10^{-2}$, $\epsilon_{1b} = 10^{-10}$, $N_1 = 42$, $N_2 = 72$ and $\Delta N_2 = 1.1$. We have varied the parameter ΔN_1 over the range $(0.3345, 0.7)$ to obtain the bands of ϵ_1 and the corresponding potential in

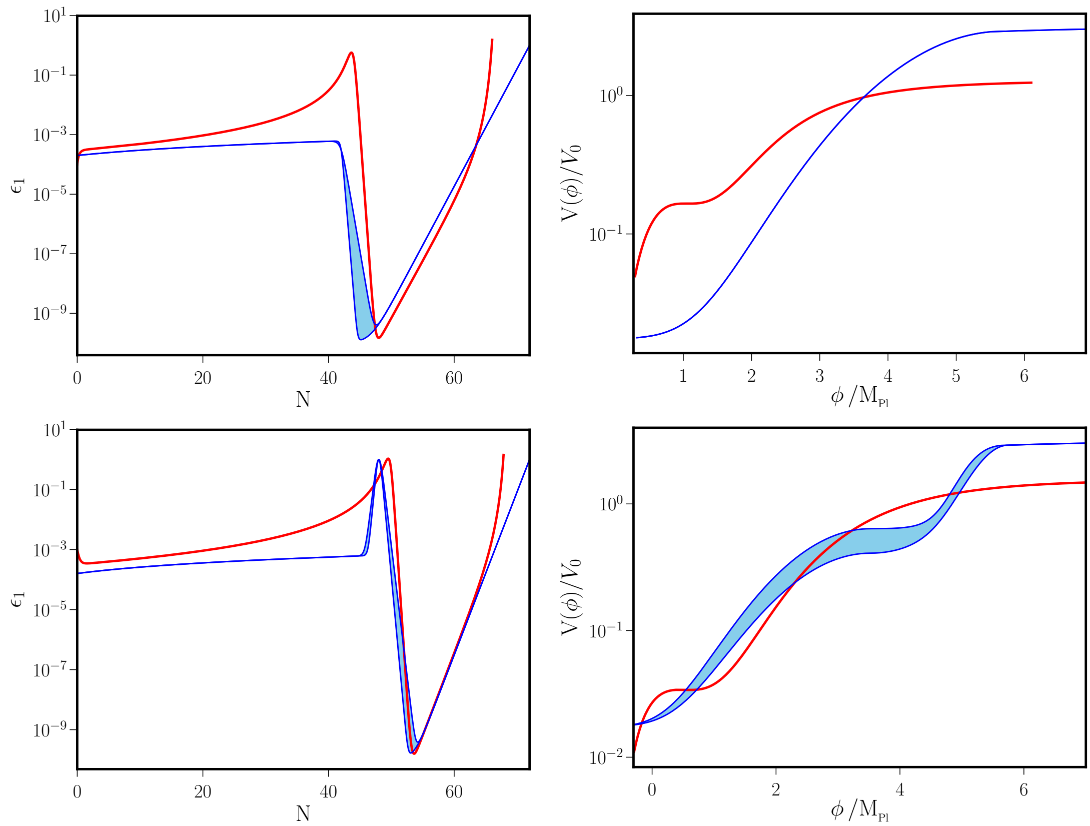

Figure 3.5: We have plotted the functional forms of $\epsilon_1(N)$ (in blue, on the left) as well as the corresponding forms of the reconstructed potentials (in blue, on the right) in the cases of RS1 (on top) and RS2 (at the bottom) for suitable values of the parameters involved. In fact, we have plotted the behavior in RS1 and RS2 as bands corresponding to a small range of the parameter ΔN_1 which determines the duration of the transition from slow roll to ultra slow roll. For comparison, we have also plotted the behavior of ϵ_1 (in red, on the left) and illustrated the potentials (in red, on the right) in the models USR2 (on top) and PI3 (at the bottom). We have chosen the parameters in the cases of RS1 and RS2 so that they closely resemble the behavior of ϵ_1 in the models USR2 and PI3. Interestingly, we find that the reconstructed potentials always contain a point of inflection. Note that, in the cases of RS1 and RS2, we have set $V_0 = H_{\rm i}^2\, M_{_{\rm Pl}}^2$, which corresponds to $V_0 = 5.625 \times 10^{-9}\, M_{_{\rm Pl}}^4$.

the figure. Similarly, in the case of RS2, the parameters we have chosen to work with are as follows: $\epsilon_{1a} = 8 \times 10^{-5}$, $\epsilon_{2a} = 6.25 \times 10^{-2}$, $\epsilon_{1b} = 10^{-10}$, $N_1 = 48$, $N_2 = 72$ and $\Delta N_2 = 0.8$. The parameter ΔN_1 has been varied over the range $(0.3847, 0.5)$ to arrive at the bands of ϵ_1 and the corresponding potential. We should note that the band describing the potential is more pronounced in the case of RS2 than in RS1. The choices for ϵ_{1a} and ϵ_{2a} have been made so that the resulting power spectra are consistent with the Planck constraints on the scalar spectral index $n_{\rm s}$ and the tensor-to-scalar ratio r at the pivot scale that we mentioned earlier. For comparison, in the figure, we have also included the behavior of the first slow parameter as well as the form of the potential in the models USR2 and PI3. It should be clear that, for suitable values of the parameters, our functional forms for $\epsilon_1(N)$ closely mimic the corresponding behavior in these models. Moreover, from the parametric forms of $V(\phi)$ constructed numerically, we have been able to determine if the reconstructed potentials in the cases of RS1 and RS2 contain a point of inflection. At an accuracy of 0.1%, we find that the reconstructed potentials indeed contain an inflection point.

With the background quantities at hand, it is straightforward to compute the power spectra by integrating the differential equations (1.11) for the curvature and the tensor perturbations. In Fig. 3.6, we have plotted the power spectra that arise in the scenarios RS1 and RS2. We have also compared the power spectra in these cases with the spectra in USR2 and PI3. It is clear that, while the scalar power spectra from the reconstructed potentials are indeed very similar to the power spectra from USR2 and PI3, the corresponding tensor power spectra exhibit some differences. Since we shall be focusing on the observational imprints of the scalar perturbations generated during inflation, we shall ignore these differences for now. We shall make a few clarifying remarks regarding this point in the concluding section.

Earlier, we had emphasized the point that the models USR2 and PI3 are highly fine-tuned and that it is difficult to move the locations of the peaks in the scalar power spectra substantially without either considerably affecting the duration of inflation or the spectra over the CMB scales. In contrast, because of the presence of the additional parameters, the scenarios RS1 and RS2 are easier to tune and, as a result, we find that we can shift the location of the peak as well as broaden its width. In Fig. 3.6, apart from the spectra in RS1 and RS2 which closely mimic the scalar spectra that arise in USR2 and PI3, we have plotted the power spectra for two other sets of parameters which lead to peaks at different locations and also exhibit a broader peak. These spectra have

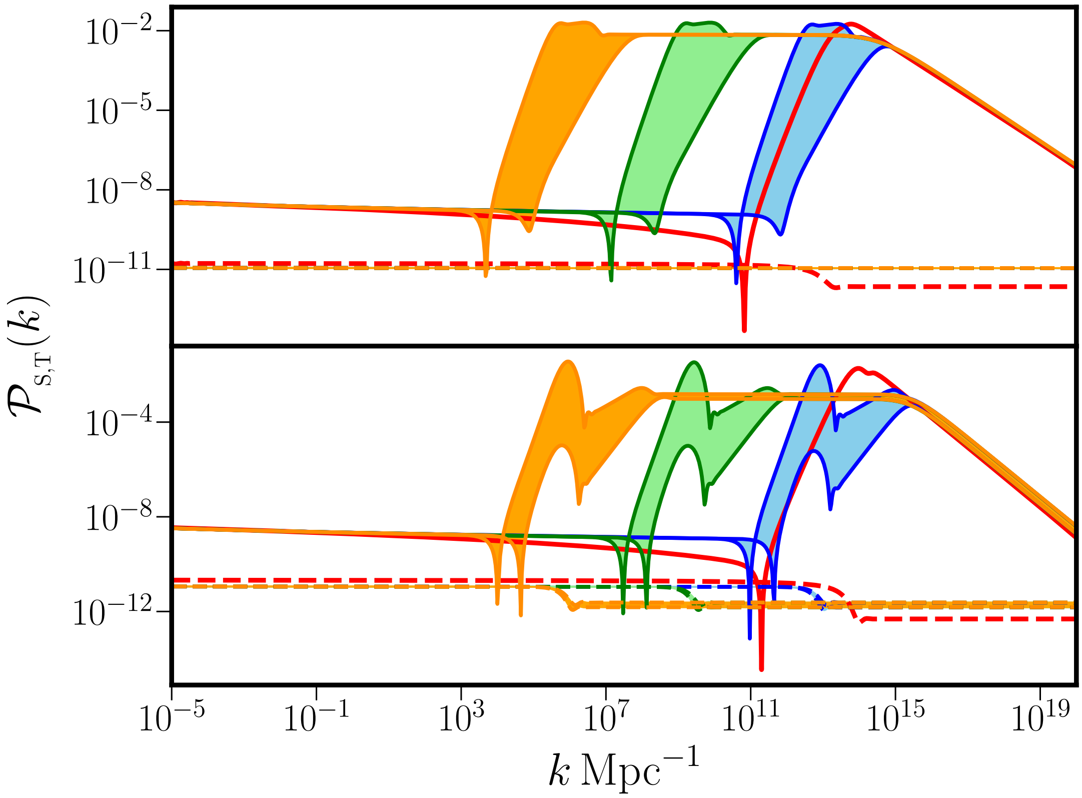

Figure 3.6: The scalar (in solid blue) and tensor power spectra (in dashed blue) resulting from the scenarios RS1 (on top) and RS2 (at the bottom) have been plotted over a wide range of wave numbers. For comparison, we have also plotted the scalar (in solid red) and tensor (in dashed red) power spectra that arise in the cases of USR2 (on top) and in PI3 (at the bottom). In the cases of RS1 and RS2 (plotted in blue), we have chosen the parameters so that the peak in the scalar power spectra roughly coincides with the peaks in the models of USR2 and PI3 (plotted in red), respectively. In addition, we have plotted the spectra arising in RS1 and RS2 for two other values of the parameter N_1 to produce peaks in the scalar power at smaller wave numbers (in green and orange). Actually, we have plotted the spectra in RS1 and RS2 as bands (in blue, green and orange) corresponding to a small range of the parameter ΔN_1 [*cf.* Eqs. (3.10)].

been achieved by choosing different values for the parameter N_1, while keeping the other parameters fixed at the values mentioned earlier. To arrive at the spectra with the broader peaks in Fig. 3.6, we have set $N_1 = 34$ and 26 in the case of RS1 and $N_1 = 40$ and 32 in the case of RS2. We should mention that a smaller choice of N_1 leads to a peak at a smaller wave number. Moreover, the bands associated with these two spectra correspond to the variation of the parameter ΔN_1 over the domain we had mentioned before.

In the next two sections, we shall study the imprints of the various power spectra on the formation of PBHs and the generation of secondary GWs.

3.5 FORMATION OF PBHS

Earlier, in Subsec. 1.2.2, we had described the calculation of the quantity f_{PBH}, *i.e.* the fraction of PBHs that constitute the cold dark matter density today, in a given inflationary model. Using the method outlined, we have calculated the quantity $f_{\mathrm{PBH}}(M)$ in the models USR2, PI3, RS1, and RS2, and have plotted the results in Fig. 3.7. In the figure, we have also indicated the constraints from the various observations such as constraints from gravitational lensing [206, 207], constraints due to the limits on extragalactic background photons from PBH evaporation [12], constraints from microlensing searches by Kepler [208], MACHO [209], EROS [210] and OGLE [211], constraints from the large scale structure [12], constraints from the CMB anisotropies due to accretion onto PBHs (FIRAS and WMAP3) [212] and, finally, constraints from the dynamics of ultra-faint dwarf galaxies [213]. (For the latest and comprehensive list of these constraints and a detailed discussion, see Refs. [13, 214]. For related discussions in these contexts, also see Refs. [215–218].) We find that, in the cases of USR2 and RS1, where the location of the peaks in the scalar power spectra approximately match, the maximum values of f_{PBH} achieved are 1.5×10^{-2} and 0.10, respectively. For the models PI3 and RS2, when the peaks are located at roughly the same wave number, we similarly obtain f_{PBH} to be 3×10^{-3} and 0.11 at their respective maxima. In these cases, the maxmima in $f_{\mathrm{PBH}}(M)$ are located over the domain $M \simeq 10^{-16}$–$10^{-12}\, M_{\odot}$. For peaks in the scalar power spectra that occur at smaller wave numbers in the cases of RS1 and RS2, as expected, the locations of the maxima in $f_{\mathrm{PBH}}(M)$ shift towards larger masses of PBHs. Interestingly, for the power spectra in RS1 and RS2 which exhibit a broad peak beginning at $k \simeq 10^6\,\mathrm{Mpc}^{-1}$, there arise maxima in f_{PBH} at tens of solar masses. However, the corresponding

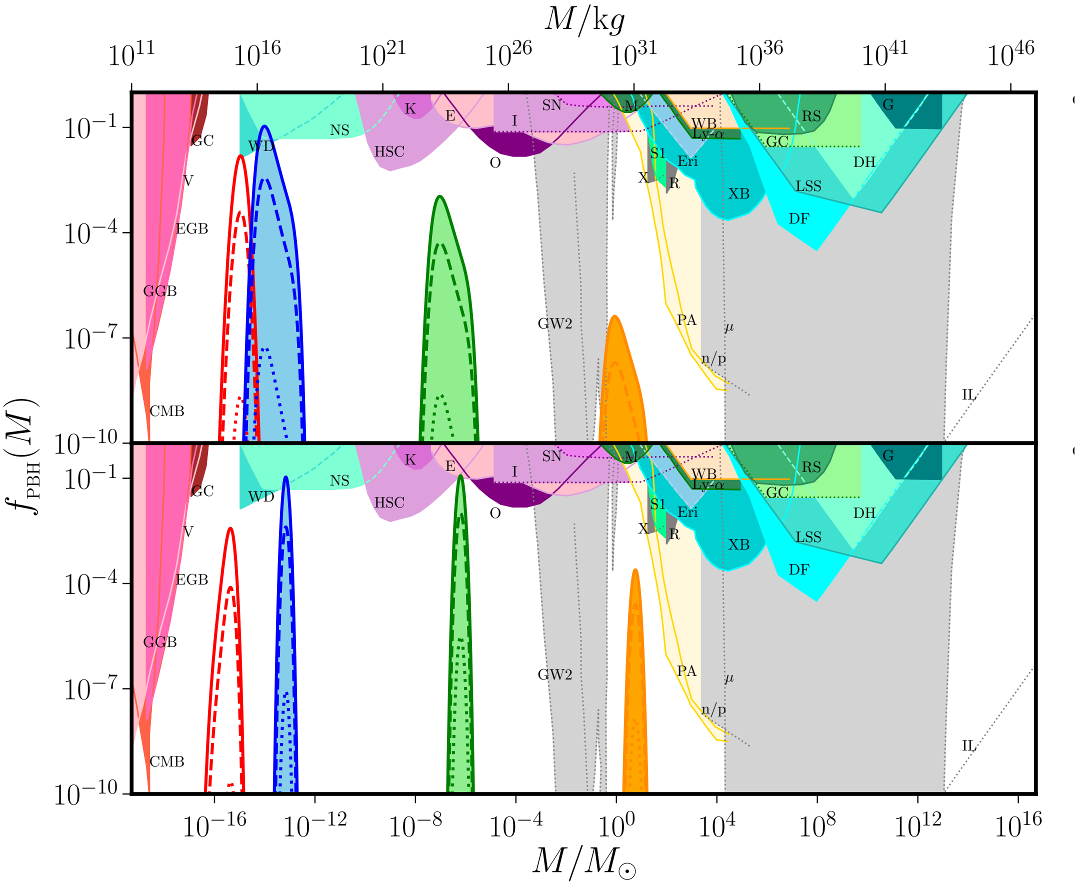

Figure 3.7: The fraction of PBHs contributing to the dark matter density today f_{PBH} has been plotted for the various models and scenarios of interest, *viz.* USR2 and RS1 (on top, in red and blue) and PI3 and RS2 (at the bottom, in red and blue). We have plotted the quantity f_{PBH} for the following three values of δ_{c}: $1/3$ (as solid curves) and 0.35 (as dashed curves) and 0.4 (as dotted curves). In the cases of RS1 and RS2, apart from the original choices of parameters that led to scalar spectra that closely matched the spectra in USR2 and PI3, we have plotted the quantity f_{PBH} for spectra which had exhibited broader peaks starting at smaller wave numbers (*cf.* Fig. 3.6). As in the previous figure, in the cases of RS1 and RS2, we have plotted bands corresponding to a range of the parameter ΔN_1. We have also indicated the latest direct (in different colors) and indirect (in gray) constraints on f_{PBH} from a variety of observations. We should mention here that the indirect constraints depend on additional assumptions. Evidently, for the parameters of the potentials we have been working with, USR2 leads to a larger formation of PBHs than PI3. Moreover, note that the existing observational constraints already limit the parameter ΔN_1 in the reconstructions RS1 and RS2.

maximum value of $f_{_{\rm PBH}}$ at $M \simeq 10\,M_\odot$ is a few orders of magnitude smaller than the maximum values we discussed above at smaller masses. This arises despite the fact the amplitude of the scalar power spectra at their peak is the same in all these cases. We believe that this result can be attributed to the dependence of $f_{_{\rm PBH}}$ on M as $M^{-1/2}$ [*cf.* Eq. (1.41)]. We should point out here that the shaded bands corresponding to RS1 and RS2 in Fig. 3.7 indicate the range of $f_{_{\rm PBH}}$ that can be generated by varying the parameter ΔN_1 in the functional forms of $\epsilon_1(N)$ [*cf.* Eqs. (3.10)]. The intersection of the shaded bands with the constraints readily translate to the limits on this parameter in our reconstructions RS1 and RS2. We find that a smaller ΔN_1 leads to a steeper growth of power and hence to a higher fraction of PBHs. Therefore, for a fixed set of values for the other parameters, the constraints essentially restrict the rapidity of the transition of inflation from slow roll to ultra slow roll epoch in our reconstructions.

3.6 POWER AND BI-SPECTRA OF SECONDARY GWS

In Subsec. 1.2.3, we had described the calculation of the dimensionless spectral energy density of secondary GWs induced by the scalar perturbations at the second order over wave numbers that reenter the Hubble radius during the radiation domination epoch. Using the method, in this section, we shall calculate the power spectra of secondary GWs generated in the inflationary models and scenarios of our interest. We shall also calculate the bispectrum associated with the secondary GWs.

3.6.1 The spectrum of secondary GWs

In Fig. 3.8, we have plotted the quantity $\Omega_{_{\rm GW}}(f)$ arising in the models USR2 and PI3 as well as the reconstructed scenarios RS1 and RS2. In the figure, we have also included the sensitivity curves associated with the various current and forthcoming observatories, *viz.* PTA and the Square Kilometre Array (SKA) [14], LISA [87], MAGIS-100 [95, 219], BBO [172–174], DECIGO [175, 176], ET [178], advanced LIGO + Virgo [167, 220] and CE [221]. (For a summary of the sensitivity curves and their updated versions, see Ref. [14] and the associated web-page.) We should mention here that the estimated sensitivity curves have been arrived at assuming a power law spectrum (the so-called 'power-law integrated curves') over the bands of interest. These sensitivities are expected to be achieved by integrating over frequency in addition

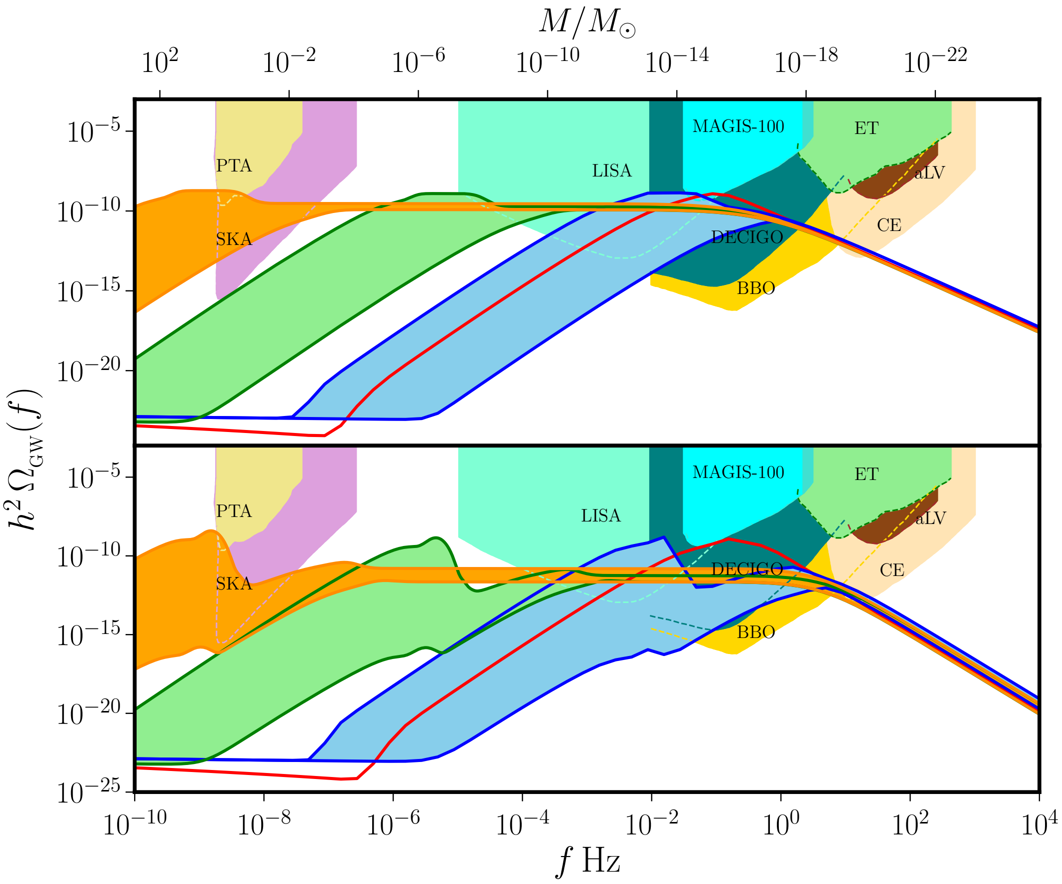

Figure 3.8: The dimensionless density parameter $\Omega_{\rm GW}$ associated with the secondary GWs generated in the models and reconstructed scenarios of USR2 and RS1 (in red and blue, on top) as well as PI3 and RS2 (in red and blue, at the bottom) have been plotted as a function of the frequency f. We have also plotted the $\Omega_{\rm GW}$ produced by the scenarios RS1 and RS2 with broader peaks beginning at smaller wave numbers (in green and orange). The bands of spectra, as with the previous figures, correspond to variation of the parameter ΔN_1 for a given N_1. Moreover, we have included the sensitivity curves of various existing and upcoming observational probes of GWs (as shaded regions, in the top part of the panels). Clearly, it should be possible to detect the GWs generated in the models and scenarios of our interest by some of the forthcoming observatories.

to integrating over time [222, 223]. It should be evident from the figure that the strength of the GWs generated in the models and scenarios we have examined here is significant enough to be detectable by one or more of these observatories. Recall that, spectra arising in the scenarios RS1 and RS2 with broad peaks starting from a wave number of about $10^6\,\mathrm{Mpc}^{-1}$ had led to PBHs with tens of solar masses. It should be clear from Fig. 3.8 that the constraints from PTA on $\Omega_{_{\mathrm{GW}}}$ already rule out such spectra for certain values of ΔN_1.

3.6.2 The secondary tensor bispectrum

In this subsection, we shall evaluate the secondary tensor bispectrum generated in the inflationary models and scenarios of our interest. The secondary tensor bispectrum, say, $\mathcal{B}_h^{\lambda_1\lambda_2\lambda_3}(\boldsymbol{k}_1, \boldsymbol{k}_2, \boldsymbol{k}_3)$ is defined as

$$\left\langle h_{\boldsymbol{k}_1}^{\lambda_1}(\eta)\, h_{\boldsymbol{k}_2}^{\lambda_2}(\eta)\, h_{\boldsymbol{k}_3}^{\lambda_3}(\eta)\right\rangle = (2\,\pi)^3\, \mathcal{B}_h^{\lambda_1\lambda_2\lambda_3}(\boldsymbol{k}_1, \boldsymbol{k}_2, \boldsymbol{k}_3, \eta)\, \delta^{(3)}(\boldsymbol{k}_1 + \boldsymbol{k}_2 + \boldsymbol{k}_3). \tag{3.13}$$

We can evaluate the tensor bispectrum during the radiation dominated era by using the expression (1.49) for $h_{\boldsymbol{k}}^{\lambda}(\eta)$. As we had discussed, $h_{\boldsymbol{k}}^{\lambda}(\eta)$ is quadratic in the Gaussian variables $\mathcal{R}_{\boldsymbol{k}}$. Therefore, obviously, the bispectrum $\mathcal{B}_h^{\lambda_1\lambda_2\lambda_3}(\boldsymbol{k}_1, \boldsymbol{k}_2, \boldsymbol{k}_3, \eta)$ will involve six of these variables. Upon utilizing Wick's theorem applicable to Gaussian random variables, one can show that the tensor bispectrum consists of eight terms all of which lead to the same contribution [94, 95]. For convenience, we shall define

$$G_h^{\lambda_1\lambda_2\lambda_3}(\boldsymbol{k}_1, \boldsymbol{k}_2, \boldsymbol{k}_3, \eta) = (2\,\pi)^{-9/2}\, \mathcal{B}_h^{\lambda_1\lambda_2\lambda_3}(\boldsymbol{k}_1, \boldsymbol{k}_2, \boldsymbol{k}_3, \eta) \tag{3.14}$$

and hereafter refer to $G_h^{\lambda_1\lambda_2\lambda_3}(\boldsymbol{k}_1, \boldsymbol{k}_2, \boldsymbol{k}_3, \eta)$ as the secondary tensor bispectrum. We find that the secondary tensor bispectrum can be expressed as

$$\begin{aligned} G_h^{\lambda_1\lambda_2\lambda_3}(\boldsymbol{k}_1, \boldsymbol{k}_2, \boldsymbol{k}_3, \eta) &= \left(\frac{8\,\pi}{9}\right)^3 \frac{1}{(k_1\, k_2\, k_3\, \eta)^3} \\ &\quad \times \int \mathrm{d}^3\boldsymbol{p}_1\, e^{\lambda_1}(\boldsymbol{k}_1, \boldsymbol{p}_1)\, e^{\lambda_2}(\boldsymbol{k}_2, \boldsymbol{p}_2)\, e^{\lambda_3}(\boldsymbol{k}_3, \boldsymbol{p}_3) \\ &\quad \times \frac{\mathcal{P}_{_{\mathrm{S}}}(p_1)}{p_1^3}\, \frac{\mathcal{P}_{_{\mathrm{S}}}(p_2)}{p_2^3}\, \frac{\mathcal{P}_{_{\mathrm{S}}}(p_3)}{p_3^3} \\ &\quad \times J\left(\frac{p_1}{k_1}, \frac{p_2}{k_1}, \eta\right)\, J\left(\frac{p_2}{k_2}, \frac{p_3}{k_2}, \eta\right)\, J\left(\frac{p_3}{k_3}, \frac{p_1}{k_3}, \eta\right), \end{aligned} \tag{3.15}$$

where $\boldsymbol{p}_2 = \boldsymbol{p}_1 - \boldsymbol{k}_1$, $\boldsymbol{p}_3 = \boldsymbol{p}_1 + \boldsymbol{k}_3$ and, for convenience, we have set

$$J\left(\frac{p_1}{k_1}, \frac{p_2}{k_1}, \eta\right) = \mathcal{I}_c\left(\frac{p_1}{k_1}, \frac{p_2}{k_1}\right) \cos\left(k_1\,\eta\right) + \mathcal{I}_s\left(\frac{p_1}{k_1}, \frac{p_2}{k_1}\right) \sin\left(k_1\,\eta\right), \tag{3.16}$$

with $\mathcal{I}_c(v,u)$ and $\mathcal{I}_s(v,u)$ given by Eqs. (1.51). In a manner partly similar to the case of the secondary tensor power spectrum, we shall replace the trigonometric functions by their averages so that the function $J(x,y,\eta)$ is instead given by

$$\bar{J}(v,u) = \frac{1}{\sqrt{2}}\left[\mathcal{I}_c^2(v,u) + \mathcal{I}_s^2(v,u)\right]^{1/2}. \tag{3.17}$$

Our aim in this work is to understand the amplitude of the secondary tensor bispectrum generated due to the scalar perturbations for modes that reenter the Hubble radius during the radiation dominated era. For simplicity, we shall restrict our analysis to the equilateral limit of the bispectrum so that $k_1 = k_2 = k_3 = k$. In order to determine the integrals involved in the expression (3.15), we shall choose a specific configuration for the vectors $\boldsymbol{k}_1$, $\boldsymbol{k}_2$ and $\boldsymbol{k}_3$. We shall assume that the vectors lie in the x-y-plane with $\boldsymbol{k}_3$ oriented along the negative x-direction. In such a case, we find that the vectors $(\boldsymbol{k}_1, \boldsymbol{k}_2, \boldsymbol{k}_3)$ in the equilateral limit are given by

$$\boldsymbol{k}_1 = \left(k/2, \sqrt{3}\,k/2, 0\right), \quad \boldsymbol{k}_2 = \left(k/2, -\sqrt{3}\,k/2, 0\right), \quad \boldsymbol{k}_3 = (-k, 0, 0). \tag{3.18}$$

We shall choose $\boldsymbol{p}_1 = (p_{1x}, p_{1y}, p_{1z})$ so that, since $\boldsymbol{p}_2 = \boldsymbol{p}_1 - \boldsymbol{k}_1$ and $\boldsymbol{p}_3 = \boldsymbol{p}_1 + \boldsymbol{k}_3$, we have

$$\boldsymbol{p}_2 = \left(p_{1x} - k/2, p_{1y} - \sqrt{3}\,k/2, p_{1z}\right), \quad \boldsymbol{p}_3 = (p_{1x} - k, p_{1y}, p_{1z}). \tag{3.19}$$

We find that such a choice of Cartesian coordinates proves to be convenient to carry out the integrals involved than the cylindrical polar coordinates that have been adopted earlier [94, 95]. Therefore, the tensor bispectrum in the equilateral limit $G_h^{\lambda_1\lambda_2\lambda_3}(k)$ can be written as

$$\begin{aligned} k^6\, G_h^{\lambda_1\lambda_2\lambda_3}(k,\eta) \;=\; & \left(\frac{8\,\pi}{9\sqrt{2}}\right)^3 \frac{1}{(k\,\eta)^3} \\ & \times \int_{-\infty}^{\infty} \mathrm{d}p_{1x} \int_{-\infty}^{\infty} \mathrm{d}p_{1y} \int_{-\infty}^{\infty} \mathrm{d}p_{1z}\, e^{\lambda_1}(\boldsymbol{k}_1, \boldsymbol{p}_1)\, e^{\lambda_2}(\boldsymbol{k}_2, \boldsymbol{p}_2) \\ & \times e^{\lambda_3}(\boldsymbol{k}_3, \boldsymbol{p}_3)\, \frac{\mathcal{P}_{\mathrm{S}}(p_1)}{p_1^3}\, \frac{\mathcal{P}_{\mathrm{S}}(p_2)}{p_2^3}\, \frac{\mathcal{P}_{\mathrm{S}}(p_3)}{p_3^3} \\ & \times \bar{J}\left(\frac{p_1}{k}, \frac{p_2}{k}\right)\, \bar{J}\left(\frac{p_2}{k}, \frac{p_3}{k}\right)\, \bar{J}\left(\frac{p_3}{k}, \frac{p_1}{k}\right). \end{aligned} \tag{3.20}$$

The factors $e^{\lambda}(\boldsymbol{k},\boldsymbol{p})$ involving the polarization tensor can be readily evaluated for our configurations of $(\boldsymbol{k}_1,\boldsymbol{k}_2,\boldsymbol{k}_3)$ and $(\boldsymbol{p}_1,\boldsymbol{p}_2,\boldsymbol{p}_3)$ (for details, see App. C). Since λ can be $+$ or $\times$, clearly, the tensor bispectrum $G_h^{\lambda_1\lambda_2\lambda_3}(k,\eta)$ has eight components. However, we find that $e^{\times}(\boldsymbol{k},\boldsymbol{p})$ is odd in p_{1z} [*cf.* Eqs. (C.1)]. As a result, the tensor bispectrum proves to be non-zero only for the following combinations of $(\lambda_1\lambda_2\lambda_3)$: $(+\,+\,+)$, $(+\times\times)$, $(\times+\times)$ and $(\times\times+)$. Also, note that the integral above describing the tensor bispectrum in the equilateral limit is symmetric under the simultaneous interchange of $\lambda_1 \leftrightarrow \lambda_2$, $\boldsymbol{k}_1 \leftrightarrow \boldsymbol{k}_2$ and $\boldsymbol{p}_1 \leftrightarrow \boldsymbol{p}_2$. This implies that, in the equilateral limit of interest, the tensor bispectrum for the three components $(+\times\times)$, $(\times+\times)$ and $(\times\times+)$ are equal. Hence, we are left with only $G_h^{+++}(k,\eta)$ and, say, $G_h^{+\times\times}(k,\eta)$ to evaluate.

We proceed to numerically evaluate $G_h^{+++}(k)$ and $G_h^{+\times\times}(k)$ in the models and scenarios of our interest, *viz.* USR2, PI3, RS1, and RS2. Because the scalar power spectra in these cases exhibit a localized maxima, we restrict our evaluation of the tensor spectrum to the range of wave numbers around the peak. We find that the integrand in Eq. (3.20) exhibits a maximum around $|\boldsymbol{p}_1| \simeq k$ and, beyond that, it quickly decreases in all the three directions of integration. In fact, the contributions to the integral prove to be negligible for $|\boldsymbol{p}_1| \gtrsim 100\,k$. So, we choose the limits for our integrals over p_{1x}, p_{1y} and p_{1z} to be $(-10^3\,k, 10^3\,k)$.

In order to understand the behavior of the tensor bispectrum, we shall calculate the dimensionless quantity referred to as the shape function, say, $\mathcal{S}_h(k)$, which is defined as [94, 95]

$$S_h^{\lambda_1\lambda_2\lambda_3}(k) = \frac{k^6\, G_h^{\lambda_1\lambda_2\lambda_3}(k,\eta)}{\sqrt{\mathcal{P}_h^3(k,\eta)}}. \tag{3.21}$$

Note that, in this expression, both the quantities $k^6\, G_h^{\lambda_1\lambda_2\lambda_3}(k)$ and $\mathcal{P}_h(k)$ are dimensionless. Moreover, the overall dependence on time cancels out leading to a shape function that is time-independent. In Fig. 3.9, we have plotted the shape functions $S_h^{+++}(k)$ and $S_h^{+\times\times}(k)$ for the four cases of interest, *viz.* USR2, PI3, RS1 and RS2. We find that the amplitude of $S_h(k)$ for a given model or scenario is maximum around the wave number where the scalar power spectrum exhibits a peak. This is true for both the cases of $S_h^{+++}(k)$ and $S_h^{+\times\times}(k)$ though there is a certain asymmetry in the behavior of the functions about the peak. We should point out that, while the amplitude of $S_h(k)$ remains large over large wave numbers, it quickly reduces to small values at smaller wave numbers. In fact, this behavior should not come as a surprise since such a behavior was also encountered in the case of $\Omega_{\mathrm{GW}}(f)$ (*cf.* Fig. 3.8). It is interesting to note that

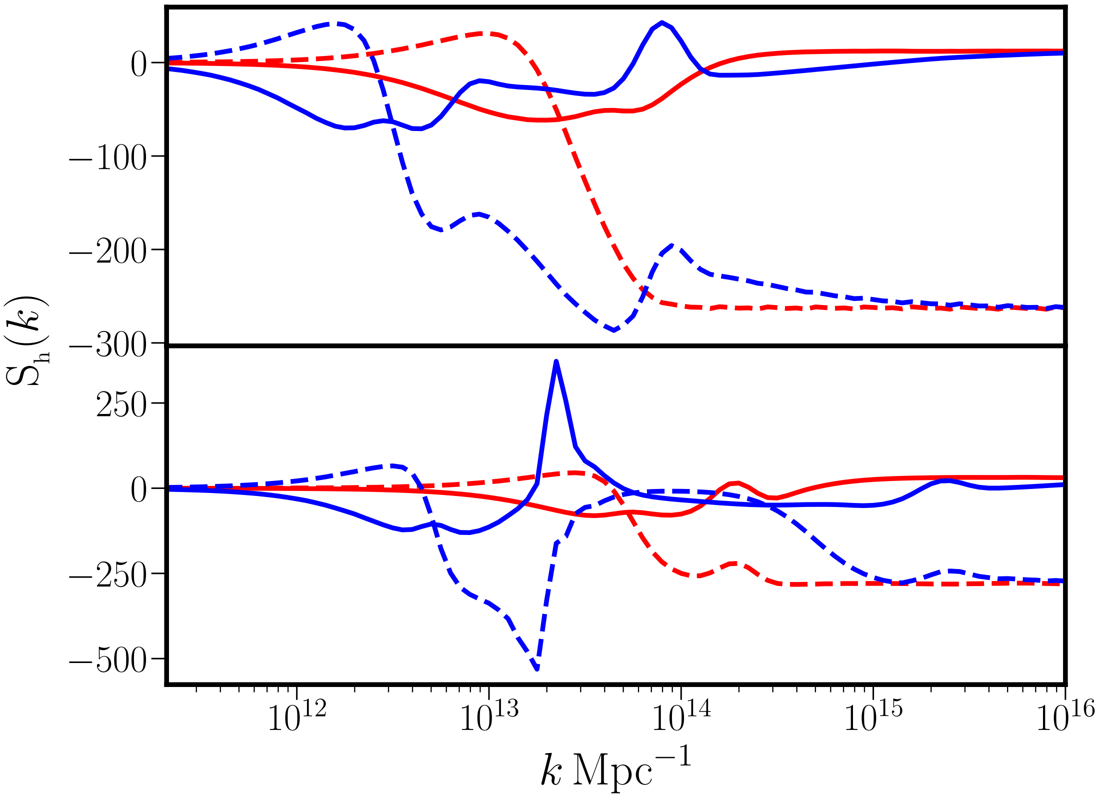

Figure 3.9: The dimensionless shape function $S_h(k)$ characterizing the tensor bispectrum has been plotted in the equilateral limit for the models and scenarios of interest, *viz.* USR2 and RS1 (in red and blue, in the top panel) as well as PI3 and RS2 (in red and blue, in the bottom panel). We have plotted both the non-zero components $S_h^{+++}(k)$ (as solid curves) and $S_h^{+\times\times}(k)$ (as dashed curves) for all the cases. In plotting the results for RS1 and RS2, we have set $N_1 = 42$ and 48 and chosen ΔN_1 to be the lowest value within our windows, *viz.* 0.3345 and 0.3847. We find that, at large wave numbers [when compared to the location of the peak in the scalar power spectra (*cf.* Figs. 3.4 and 3.6)], the amplitudes of $S_h^{+++}(k)$ and $S_h^{+\times\times}(k)$ settle down to around 10 and -250, respectively. Also, at wave numbers smaller than the location of the peak, the amplitudes of both the components prove to be of order unity or less in all the cases.

$S_h^{+++}(k)$ and $S_h^{+\times\times}(k)$ settle down to about 10 and -250, respectively, at large wave numbers. Recall that the secondary tensor bispectra and hence the shape functions we have illustrated in Fig. 3.9 have been evaluated during the radiation dominated epoch, when the modes are well inside the Hubble radius. They will have to be evolved until today to examine the corresponding observational imprints which may possibly be detected by upcoming missions such as, say, LISA and PTA (in this context, see Ref. [94]; also see Refs. [224–226]).

3.7 CONTRIBUTIONS TO PBH FORMATION AND SECONDARY GWS FROM SCALAR NON-GAUSSIANITIES

Until now, we have focused on the imprints of the scalar power spectrum on the extent of PBHs formed and the generation of secondary GWs. Clearly, if the scalar non-Gaussianities prove to be large in a given inflationary model, it seems plausible that they would significantly alter the observables $f_{_{\rm PBH}}$, $\Omega_{_{\rm GW}}$ and S_h [70, 179–190]. To understand the possible effects of non-Gaussianities on $f_{_{\rm PBH}}$, $\Omega_{_{\rm GW}}$ as well as S_h, in this section, we shall first calculate the scalar bispectrum and thereby the corresponding non-Gaussianity parameter $f_{_{\rm NL}}$ in the two inflationary models USR2 and PI3 and the reconstructed scenarios RS1 and RS2. We shall then discuss the corresponding contributions from the scalar bispectrum to $f_{_{\rm PBH}}$, $\Omega_{_{\rm GW}}$ and S_h.

3.7.1 Amplitude and shape of the bispectrum and the scalar non-Gaussianity parameter $f_{_{\rm NL}}$

Recall that the non-Gaussianity parameter $f_{_{\rm NL}}(\boldsymbol{k}_1, \boldsymbol{k}_2, \boldsymbol{k}_3)$ associated with the scalar bispectrum is defined in Eq. (1.28) (see, for instance, Refs. [56, 60]). As in the case of the scalar power spectrum, due to the deviation from slow roll, it proves to be difficult to evaluate the scalar bispectrum analytically in the inflationary models introduced earlier in this chapter. In Sec. 1.1.3, we had outlined the procedure to numerically compute the scalar bispectrum in inflationary models involving a single, canonical scalar field [55, 56]. In this subsection, using the method, we shall compute the scalar bispectrum in the different inflationary models of our interest. With the scalar power and bi-spectra at hand, evidently, it is straightforward to arrive the non-Gaussianity parameter $f_{_{\rm NL}}$ for a given model.

Based on prior experience, we would like to emphasize a few points concerning the expected shape and amplitude of the scalar bispectrum before we go on to present the results for $f_{\rm NL}$ in the different models and scenarios we have considered earlier in this chapter. As is well known, in slow roll inflationary models involving a single, canonical scalar field, the scalar non-Gaussianity parameter $f_{\rm NL}$ proves to be of the order of the first slow roll parameter ϵ_1 [52, 53, 59]. In other words, the parameter $f_{\rm NL}$ is typically of the order of 10^{-2} or smaller in such situations (see our discussion in Subsec. 1.1.3). Moreover, the bispectrum is found to have an equilateral shape, with the $f_{\rm NL}$ parameter slightly peaking when $k_1 = k_2 = k_3$ (see Fig. 1.4; in this context, also see Ref. [56]). However, when departures from slow roll occur, the non-Gaussianity parameter $f_{\rm NL}$ can be expected to be of the order of unity or larger, depending on the details of the background dynamics. Further, in contrast to the slow roll case, wherein there is only a weak dependence of the parameter $f_{\rm NL}$ on scale, when departures from slow roll occur, the parameter turns out to be strongly scale dependent. Needless to say, we can expect that the non-Gaussianity parameter $f_{\rm NL}$ to be relatively large as well as strongly scale dependent in the situations of our interest.

Let us now discuss the results we obtain in the different models we have introduced. In order to illustrate the complete shape of the bispectrum, the non-Gaussianity parameter $f_{\rm NL}$ is usually presented as a density plot in, say, the (k_1/k_3)-(k_2/k_3)-plane (see Fig. 1.4; in this context, also see Refs. [56, 68]). It proves to be a bit of a numerical challenge to compute the complete shape of the bispectrum across the wide range of wave numbers over which we have evaluated the power spectra. As a result, we shall focus on the amplitude of $f_{\rm NL}$ in the equilateral and the squeezed limits, *i.e.* when $k_1 = k_2 = k_3 = k$ and when $k_1 \to 0$, $k_2 \simeq k_3 = k$, respectively. It is easier to calculate the scalar bispectrum in the equilateral limit as we just need to follow the evolution of one mode at a time. To arrive at the scalar bispectrum in the squeezed limit, we shall set $k_2 = k_3 = k$ and choose $k_1 = 10^{-3}\, k$. We have confirmed that our results are robust against choosing a smaller value of k_1. Before we go to illustrate the amplitude and shape of the non-Gaussianity parameter $f_{\rm NL}$, let us understand the behavior of the scalar bispectrum $G(\boldsymbol{k}_1, \boldsymbol{k}_2, \boldsymbol{k}_3)$ itself. In Fig. 3.10, we have plotted the scalar bispectra that arise in the equilateral and squeezed limits in the models of USR2 and PI3. We would like to highlight a few aspects regarding the amplitude and shape of the bispectra. Note that the scalar bispectra have roughly the same shape in the equilateral and squeezed limits. Also, they closely resemble the corresponding scalar power spectra and, in particular, they exhibit a dip and a peak around the same locations (*cf.* Fig. 3.4). Moreover, at small scales, the scalar bispectra have a larger amplitude in the equilateral limit than in the squeezed limit. Further, in the equilateral limit, the

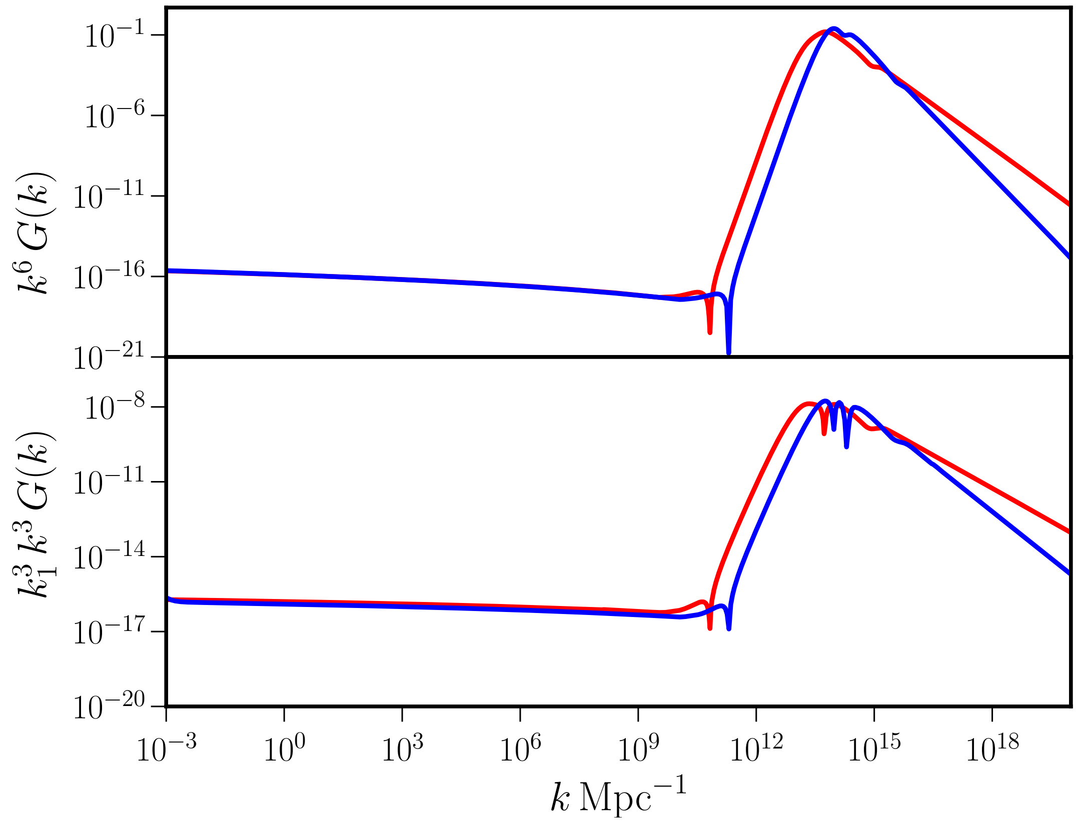

Figure 3.10: The amplitude of the dimensionless scalar bispectra has been plotted in the equilateral (on top) and squeezed limits (at the bottom) for the models USR2 (in red) and PI3 (in blue). Clearly, the bispectra have approximately the same shape as the corresponding power spectra (*cf.* Fig. 3.4). Note that, at small scales, the dimensionless bispectra have considerably lower amplitudes in the squeezed limit when compared to their values in the equilateral limit, whereas they have roughly the same amplitude over the CMB scales.

scalar bispectra have almost the same amplitude as the power spectra near the peak.

Let us now understand the behavior of the non-Gaussianity parameter $f_{\rm NL}$. In Figs. 3.11 and 3.12, we have plotted the behavior of the $f_{\rm NL}$ parameter in the equilateral and squeezed limits over a wide range of wave numbers in the models USR2 and PI3 as well as the scenarios RS1 and RS2. The following points are evident from the two figures. Firstly, in the equilateral limit, the non-Gaussianity parameter $f_{\rm NL}$ proves to be fairly large (of the order of 10^1–10^4) over a small range of wave numbers. In fact, the $f_{\rm NL}$ exhibit an upward spike in their amplitude around exactly the same wave numbers wherein the scalar power spectra exhibit a downward spike (*cf.* Figs. 3.4 and 3.6). Since the definition of the parameter $f_{\rm NL}$ [*cf.* Eq. (1.28)] contains the scalar power spectrum in the denominator, the upward spike can be partly attributed to the downward spike in the power spectrum. If we ignore the large spike, we find that $f_{\rm NL} \simeq 1$–10 around these wave numbers. It is worth noting that these wave numbers correspond to those modes which leave the Hubble radius just prior to or during the transition from the slow roll to the ultra slow roll regime. In contrast, the non-Gaussianity parameter $f_{\rm NL}$ proves to be relatively small (at most of order unity) over wave numbers where the scalar power spectra exhibit their peak. However, we should clarify that, though the value of $f_{\rm NL}$ is smaller than unity around this domain, it is considerably larger than its typical value in slow roll inflation (of about 10^{-2}, such as over the CMB scales in our models). For instance, in USR2 and PI3, we find that, in the equilateral limit, $f_{\rm NL}$ is about -0.37 and -0.44, respectively, near the locations of the peak in the power spectra. This can be attributed to the large value of ϵ_2 during the ultra slow roll regime. Secondly, in the squeezed limit, the scalar bispectrum is expected to satisfy the so-called consistency condition wherein it can be completely expressed in terms of the scalar power spectrum [see Refs. [52, 135]; also see Eq. (2.10)]. In Figs. 3.11 and 3.12, apart from plotting $f_{\rm NL}$ in the squeezed limit, we have also plotted the quantity $f_{\rm NL}^{\rm CR}$ [*cf.* Eq. (2.11)] obtained from the scalar spectral index. We should add that we have also examined the validity of the consistency relation more closely by working with a smaller k_1. We find that the consistency condition is indeed satisfied even when there arise strong features in the scalar power spectrum in all the scenarios of our interest (in this context, however, see App. D). Therefore, in the squeezed limit, we find that $f_{\rm NL}$ is at most of order unity around the peaks of the scalar power spectra.

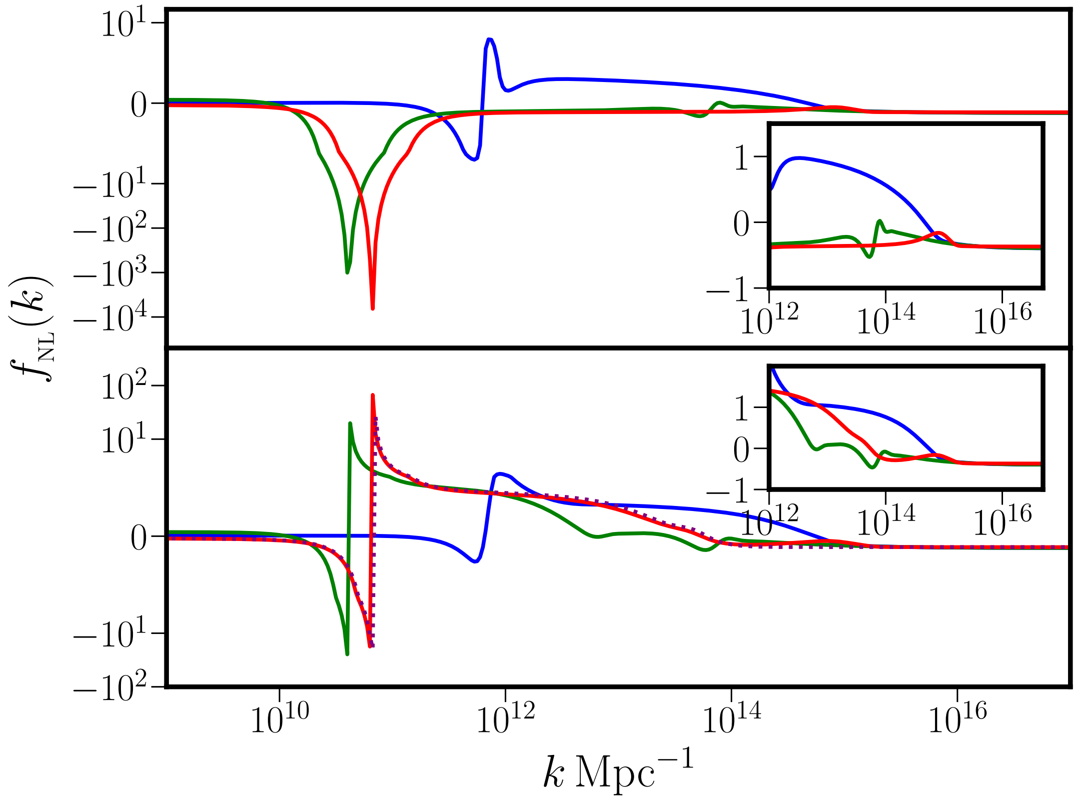

Figure 3.11: The scalar non-Gaussianity parameter $f_{\rm NL}$ has been plotted in the equilateral (on top) and the squeezed (at the bottom) limits for the model of USR2 (in red) and the reconstructed scenario RS1 (in blue and green). Note that, in the case of RS1, we have worked with our original choice of $N_1 = 42$ and plotted the lower (in blue) and the upper (in green) bounds of $f_{\rm NL}$ corresponding to the range over which the parameter ΔN_1 is varied. In the case of USR2, we have also plotted the consistency condition $f_{\rm NL}^{\rm CR}(k) = (5/12)\,[n_{\rm S}(k) - 1]$ (as purple dots) along with the results in the squeezed limit. Despite the deviations from slow roll leading to strong features in the scalar power and bi-spectra, we find that the consistency condition is always satisfied. The insets highlight the $f_{\rm NL}$ around the wave numbers where the scalar power spectra exhibit their peaks. It is clear that the parameter $f_{\rm NL}$ attains larger values in the equilateral (where $f_{\rm NL} \simeq 10^1$–10^4 at its maximum) than the squeezed (where $f_{\rm NL} \simeq 1$–10) limit. Importantly, we find that $f_{\rm NL}$ is at most of order unity near the peaks of the scalar power spectra.

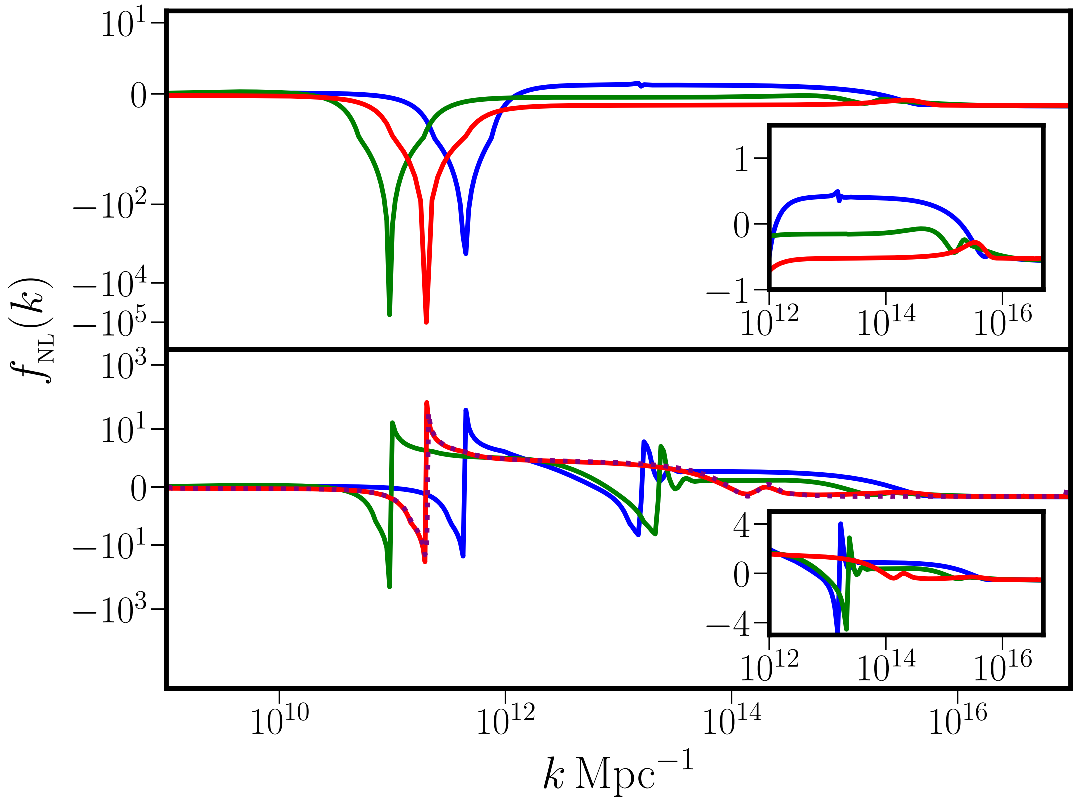

Figure 3.12: The scalar non-Gaussianity parameter $f_{\rm NL}$ has been plotted in the equilateral and the squeezed limits for the model PI3 and the reconstructed scenario RS2 in the same manner (and the same choices of colors) as in the cases of USR2 and RS1 in the previous figure. In the case of RS2, we have worked with our initial choice of $N_1 = 48$ and plotted the lower (in blue) and the upper (in green) bounds of $f_{\rm NL}$ corresponding to the range over which the parameter ΔN_1 is varied. It should be evident that our earlier comments regarding the results for USR2 and RS1 apply to the cases of PI3 and RS2 as well.

It seems important that we clarify a point regarding the validity of the consistency condition at this stage of our discussion. One may be concerned if the period of ultra slow roll, with its large value of ϵ_2, could lead to a violation of the consistency condition over wave numbers that leave the Hubble radius during this epoch (in this context, see Refs. [137, 138, 227]). Recall that the amplitude of scalar modes over a certain range of wave numbers are modified to some extent during the transition from slow roll to ultra slow roll (*cf.* Fig. 3.3). However, since, in the cases of our interest, the epoch of ultra slow roll ends leading to the eventual termination of inflation, the amplitude of the scalar modes asymptotically freeze at sufficiently late times (for further details, see App. E; in this context, also see Refs. [132, 187]). Due to this asymptotic behavior of the scalar modes, it should not come as a surprise that the consistency condition is satisfied in the models and scenarios of our interest despite the phase of ultra slow roll (for very recent discussions in this context, see Refs. [228, 229]).

3.7.2 Imprints of $f_{\rm NL}$ on $f_{\rm PBH}$ and $\Omega_{\rm GW}$

Recall that the observationally relevant dimensionless, scalar non-Gaussianity parameter $f_{\rm NL}$ is usually introduced through the following relation (see Ref. [230]; also see Refs. [56, 60]):

$$\mathcal{R}(\eta, \boldsymbol{x}) = \mathcal{R}^{\rm G}(\eta, \boldsymbol{x}) - \frac{3}{5}\, f_{\rm NL}\, \left[\mathcal{R}^{\rm G}(\eta, \boldsymbol{x})\right]^2 \tag{3.22}$$

where $\mathcal{R}^{\rm G}$ denotes the Gaussian contribution. In Fourier space, this relation can be written as (see, for instance, Ref. [60])

$$\mathcal{R}_{\boldsymbol{k}} = \mathcal{R}^{\rm G}_{\boldsymbol{k}} - \frac{3}{5}\, f_{\rm NL} \int \frac{{\rm d}^3\boldsymbol{p}}{(2\,\pi)^{3/2}}\, \mathcal{R}^{\rm G}_{\boldsymbol{p}}\, \mathcal{R}^{\rm G}_{\boldsymbol{k}-\boldsymbol{p}}. \tag{3.23}$$

If one uses this expression for $\mathcal{R}_{\boldsymbol{k}}$ and evaluates the corresponding two-point correlation function in Fourier space, one obtains that [189, 190]

$$\langle \hat{\mathcal{R}}_{\boldsymbol{k}}\, \hat{\mathcal{R}}_{\boldsymbol{k}'} \rangle = \frac{2\,\pi^2}{k^3}\, \delta^{(3)}(\boldsymbol{k}+\boldsymbol{k}')\, \left[\mathcal{P}_{\rm S}(k) + \left(\frac{3}{5}\right)^2\, \frac{k^3}{2\,\pi}\, f_{\rm NL}^2 \int {\rm d}^3\boldsymbol{p}\, \frac{\mathcal{P}_{\rm S}(p)}{p^3}\, \frac{\mathcal{P}_{\rm S}\left(\vert\boldsymbol{k}-\boldsymbol{p}\vert\right)}{\vert\boldsymbol{k}-\boldsymbol{p}\vert^3}\right], \tag{3.24}$$

where $\mathcal{P}_{\rm S}(k)$ is the original scalar power spectrum defined in the Gaussian limit [*cf.* Eq. (1.12a)], while the second term represents the leading non-Gaussian correction. We find that we can write the non-Gaussian correction to the scalar power spectrum, say, $\mathcal{P}_{\rm C}(k)$, as follows:

$$\begin{aligned}\mathcal{P}_{\rm C}(k) &= \left(\frac{3}{5}\right)^2 f_{\rm NL}^2 \int_0^\infty {\rm d}v \int_{|1-v|}^{1+v} \frac{{\rm d}u}{v^2\, u^2}\, \mathcal{P}_{\rm S}(k\, v)\, \mathcal{P}_{\rm S}(k\, u) \\ &= \left(\frac{12}{5}\right)^2 f_{\rm NL}^2 \int_0^\infty {\rm d}s \int_0^1 \frac{{\rm d}d}{(s^2-d^2)^2}\, \mathcal{P}_{\rm S}[k\,(s+d)/2]\, \mathcal{P}_{\rm S}[k\,(s-d)/2].\end{aligned} \tag{3.25}$$

Since we have evaluated the scalar non-Gaussianity parameter in the inflationary models of our interest, we can now calculate the non-Gaussian corrections $\mathcal{P}_{\rm C}(k)$ to the scalar power spectrum and the corresponding modifications to $f_{\rm PBH}$, $\Omega_{\rm GW}$ and S_h. However, before we do so, we need to clarify an important point. In introducing the scalar non-Gaussianity parameter through the relation (3.22), it has been assumed that $f_{\rm NL}$ is local, *i.e.* it is independent of the wave number [230]. In contrast, the parameter $f_{\rm NL}$ proves to be strongly scale dependent in all the situations we have considered. In order to be consistent with the fact that the $f_{\rm NL}$ in Eq. (3.22) is local, we shall consider the squeezed limit of the parameter (in this context, also see the discussions in Ref. [181]). Moreover, in the expression (3.25) for $\mathcal{P}_{\rm C}(k)$, we shall assume that $f_{\rm NL}$ is dependent on the wave number k, with $k_2 = k_3 \simeq k$ and $k_1 \ll k$ to be consistent with the squeezed limit. In Fig. 3.13, we have plotted the original Gaussian power spectrum as well the modified power spectrum including the non-Gaussian corrections $\mathcal{P}_{\rm C}(k)$. Recall that the non-Gaussianity parameter $f_{\rm NL}$ had contained sharp spikes around the wave numbers where the Gaussian scalar power spectra had exhibited a downward spike (*cf.* Figs. 3.11 and 3.12). While evaluating the modified power spectra, we have regulated the maximum value of these spikes to be $|f_{\rm NL}| \simeq 100$. Evidently, the non-Gaussian corrections to the scalar power spectrum are insignificant. This can be attributed to the fact that the peaks in the original power spectrum $\mathcal{P}_{\rm S}(k)$ and the non-Gaussianity parameter $f_{\rm NL}$ are located at different wave numbers. Therefore, we find the corresponding modifications to $f_{\rm PBH}$, $\Omega_{\rm GW}$ and S_h are insignificant as well. This conclusion can also be understood from the fact the amplitude of the dimensionless bispectrum in the squeezed limit is considerably smaller than the amplitude of the scalar power spectrum around its peak (*cf.* Fig. 3.10).

We should clarify a particular point regarding the non-Gaussian corrections we have calculated in this section. Note that we have calculated the cubic order non-Gaussian corrections to the power spectrum. In fact, as we shall discuss in Chap. 5,

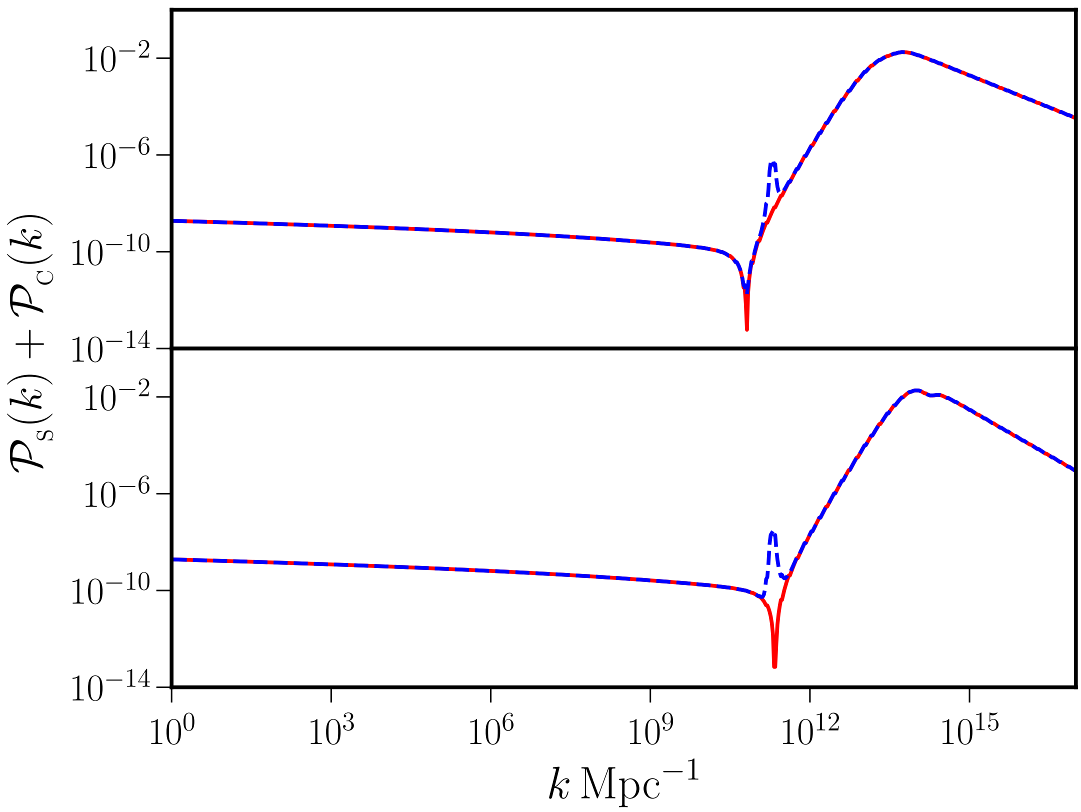

Figure 3.13: The original scalar power spectrum $\mathcal{P}_{\rm S}(k)$ (in solid red) and the modified spectrum $\mathcal{P}_{\rm S}(k) + \mathcal{P}_{\rm C}(k)$ (in dashed blue) arrived at upon including the leading non-Gaussian corrections, have been plotted for the models of USR2 (on top) and PI3 (at the bottom). In these models, the non-Gaussianity parameter $f_{\rm NL}$ had exhibited sharp spikes in its amplitude around wave numbers where the Gaussian scalar power spectrum had contained downward spikes. We should clarify here that, in order to arrive at the modified power spectra, we have regulated the spikes in the $f_{\rm NL}$ parameter so that its maximum value around these wave numbers is 10^2. Clearly, the modifications to the scalar spectra, particularly at their peak, is hardly significant.

this method does not take into account all the contributions due to the scalar bispectrum to the dimensionless spectral energy density $\Omega_{\rm GW}$ describing the secondary GWs. Similarly, the approach does not completely account for the effects of non-Gaussianities on the fraction $f_{\rm PBH}$ of PBHs produced (for an early discussion on the topic, see Ref. [231]; for recent discussions, see Refs. [232, 233]). In the context of PBHs, the non-Gaussianities also change the shape of the probability distribution characterizing the over-densities at the time of their formation, which we have assumed to be a Gaussian [*cf.* Eq. (1.34)]. These effects due to the non-Gaussianities are expected to be larger (than the corrections to the power spectrum we have calculated), and they need to be taken into account to arrive at the modified $f_{\rm PBH}$ [232].

3.8 DISCUSSION

In this chapter, we had considered models involving a single, canonical scalar field that lead to ultra slow roll or punctuated inflation. All these models had contained a point of inflection, which seems essential to achieve the epoch of ultra slow roll required to enhance scalar power on small scales. We had also examined the extent of PBHs formed and the secondary GWs generated in these models and had compared them with the constraints on the corresponding observables $f_{\rm PBH}$ and $\Omega_{\rm GW}$. These models require a considerable extent of fine tuning in order to lead to the desirable duration of inflation (of say, 60–70 e-folds), be consistent with the constraints from the CMB on large scales, and simultaneously exhibit higher scalar power on small scales.

In order to explore the possibilities in single field models further, we had also considered scenarios wherein the functional forms for the first slow roll parameter closely mimic the typical behavior in ultra slow roll and punctuated inflation. We had reconstructed the potentials associated with these scenarios, evaluated the resulting scalar and tensor power spectra as well as the corresponding imprints on $f_{\rm PBH}$, $\Omega_{\rm GW}$ and S_h. The presence of extra parameters in the choices for $\epsilon_1(N)$ had allowed us to construct the required scenarios rather easily. Interestingly, we had found that the reconstructed potentials too contain a point of inflection as the original models do. This lends further credence to the notion that a point of inflection is essential to achieve ultra slow roll or punctuated inflation. However, we should add a note of caution that, while we were able to broadly capture the expected shape of the scalar power spectra in the reconstructed scenarios, there were some differences in the tensor power spectra in these scenarios and the original models. Moreover, we find that these reconstructed scenarios allow us to easily examine the rate of growth of the scalar power from the CMB scales to small scales (for a discussion in this context, see Refs. [194, 199]).

While the steepest growth possible in the reconstructed scenario RS1 has $n_{\mathrm{S}} - 1 \simeq 4$, we find that the growth is non-uniform but faster in RS2 with $n_{\mathrm{S}} - 1$ between 4 and 6 over the relevant range of wave numbers (for details, see App. F). Further, though we have been able to reconstruct the potentials numerically in the scenarios RS1 and RS2, it would be worthwhile to arrive at analytical forms of these potentials [193–195].

We had also computed the scalar bispectrum and the associated non-Gaussianity parameter f_{NL} is these models and scenarios. We had found that the parameter f_{NL} is strongly scale dependent in all the cases. Also, the non-Gaussianities had turned out to be fairly large (with, say, $f_{\mathrm{NL}} > 10$ over a range of wave numbers) in the equilateral limit. Moreover, we had found that the consistency condition governing the non-Gaussianity parameter is always satisfied, despite the period of sharp departure from slow roll, implying that the non-Gaussianity parameter in the squeezed limit is at most of order unity around the domain where the scalar power spectra exhibit their peak. Due to this reason, we had found that the non-Gaussian corrections to power spectra were negligible leading to insignificant modifications to the observables f_{PBH}, Ω_{GW} and S_h on small scales. However, we should point out that the effects of non-Gaussianities on f_{PBH} and Ω_{GW} have been included in a simple fashion and a more detailed approach seems required to account for the complicated scale dependence of f_{NL} [182–187]. It has recently been argued that, in the squeezed limit of the bispectrum, the part satisfying the consistency relation should be subtracted away as it cannot be observed (in this context, see Refs. [234, 235]; however also see Ref. [236]). If this is indeed so, since the scalar bispectrum satisfies the consistency condition in the squeezed limit in the models and scenarios we have examined, the cubic order non-Gaussian corrections to the power spectrum would then identically vanish.

Moreover, we had calculated the secondary tensor bispectrum generated in the different inflationary models of interest during the radiation dominated epoch. Interestingly, we had found that the shape function characterizing the tensor bispectrum has an amplitude of about 10–250 at small wave numbers in all the models and scenarios of interest. It seems important to evolve the shape function until today and examine the possibility of observing its imprints in ongoing efforts such as PTA [224] and forthcoming missions such as LISA [94, 225, 226]. We are currently investigating these issues in a variety of single and two field models of inflation [237–245].

CHAPTER 4
COULD PBHs AND SECONDARY GWs HAVE ORIGINATED FROM SQUEEZED INITIAL STATES?

4.1 INTRODUCTION

It is now almost half-a-century since it was originally argued that black holes could have formed due to over-densities in the primordial universe [8, 77]. The investigations of such primordial black holes (PBHs) have gained traction over the last few years with the observations of gravitational waves (GWs) from the mergers of binary black holes [147–149, 246]. Several current and upcoming observational efforts promise to provide constraints on the fraction of the PBHs constituting the bulk of cold dark matter density in the current universe, a quantity usually referred to as f_{PBH} [13]. Motivated by these observational efforts, there has been several attempts to build models of inflation that could generate considerable population of PBHs over certain mass ranges (see, for example, Refs. [71, 72, 159, 160, 247]).

It is well known that scales smaller than those associated with the cosmic microwave background (CMB), say, with wave numbers $k > 1\,\mathrm{Mpc}^{-1}$, reenter the Hubble radius during the radiation dominated epoch. If the scalar power over these small scales have enhanced amplitudes (when compared to their COBE normalized values over the CMB scales), they could, in principle, induce instantaneous collapses of energy densities of corresponding sizes, thereby forming PBHs [70, 248, 249]. To achieve a higher amplitude in the inflationary scalar perturbation spectrum (say, of the order of 10^{-2}) at larger wave numbers, one has to suitably model the background dynamics so that a departure from slow roll inflation arises at late times. As we have discussed in Chap. 3, in single field models, inflationary potentials containing a point of inflection can generate the required boost in the scalar power (see, for instance, Refs. [18, 72, 161, 250]). The inflection point in the potential leads to a transient epoch of ultra slow roll inflation, which turns out to be responsible for the rise in the scalar power over small scales. Other features, such as a bump or dip artificially added to the potential are also known to boost the scalar power at larger wave numbers [237, 251]. There have also been attempts to generate PBHs using other mechanisms such as models involving non-canonical scalar fields [252, 253], inflation driven by multiple fields [243–245, 254, 255], inducing a non-trivial speed of sound during inflation [256–258], or a modified history of reheating and radiation dominated era following inflation [259, 260].

Moreover, as we have discussed, when the scalar power is boosted to large amplitudes, the second order tensor perturbations that are sourced by the quadratic terms involving the first order scalar perturbations can dominate the contributions due to the original, inflationary, first order tensor perturbations [88, 89]. In other words, the enhanced scalar power, apart from producing a significant amount of PBHs, also leads to considerable amplification of the secondary GWs at small scales or, equivalently, at large frequencies [15]. These GWs induced by the scalar perturbations are expected to be stochastic and isotropic. There are several experiments and observational surveys that constrain the dimensionless energy density of such a stochastic gravitational wave background, say, Ω_{GW}, observable today [14].

As we mentioned above, the enhancement in the scalar power over small scales can be achieved with the aid of a brief period of departure from slow roll inflation. We should point out here that such scenarios would also produce a strongly scale dependent bispectrum. However, it has been shown that, in single field models of inflation wherein the deviation from slow roll is brief, the consistency condition relating the bispectrum and the power spectrum in the squeezed limit is indeed satisfied (in this context, see Refs. [18, 132, 228]). This implies that the magnitude of the scalar non-Gaussianity parameter f_{NL} is at the most of order unity over the range of wave numbers which contains enhanced power. As a result, any corrections due to the bispectrum that has to be accounted for in the power spectrum proves to be negligible in these models [18].

However, the aforementioned methods of modifying slow roll inflation to achieve sufficient enhancement in the scalar power, and hence produce significant amount of PBHs and secondary GWs, are known to pose certain challenges. They typically require extreme fine-tuning of the parameters involved. Else, they may either prolong the duration of inflation beyond reasonable number of e-folds or alter the scalar spectral index n_{S} and the tensor-to-scalar ratio r over the CMB scales thereby leading to a tension with the constraints from Planck data (see, for instance, Refs. [18, 72]). There exists another approach to achieve power spectra with the desired shape at small scales. The alternative method is to work with non-vacuum, specifically, squeezed, initial states for the perturbations during inflation. This method of evolving the perturbations with initial states other than the standard Bunch-Davies vacuum is well known in the literature and has been discussed in various contexts (see, for example, Refs. [261–273]). These excited initial states for the perturbations can be expressed in terms of the so-called Bogoliubov coefficients. As we shall see, the Bogoliubov coefficients essentially provide us an independent function to introduce the desired features in the power spectrum. However, while it is technically straightforward to arrive at the required power spectrum with a suitable choice of the Bogoliubov coefficients, we encounter two drawbacks with the proposed approach. On the one hand, it seems challenging to design a mechanism that leaves the curvature perturbations in such an excited initial state. On the other hand, we find that squeezed initial states lead to significant backreaction during the early stages of inflation unless the state is remarkably close to the Bunch-Davies vacuum.

To illustrate these points, in this chapter, we shall focus on the popular lognormal shape of amplification in the scalar power spectrum [15, 166]. In the following section, we shall briefly describe the modes corresponding to squeezed initial states and discuss the corresponding scalar power and bispectra. We shall consider suitable functional forms for the Bogoliubov coefficients to produce the lognormal feature in the power spectrum and calculate the corresponding scalar bispectrum analytically. We shall show that the bispectrum is significantly enhanced in the squeezed limit and that the consistency condition is strongly violated over the range of wave numbers containing the lognormal feature. In other words, we find that the cubic order non-Gaussian modifications to the scalar power spectrum can possibly dominate the amplitude of the original scalar power around the feature for certain values of the parameter that characterizes the deviations from the Bunch-Davies vacuum. In Sec. 4.3, we shall compute the observable quantities of interest, *viz.* $f_{\rm PBH}$ and $\Omega_{\rm GW}$, generated from such an enhanced scalar power spectrum. In Sec. 4.4, we shall first discuss possible mechanisms that can lead to the squeezed initial states for the curvature perturbation at early times. Thereafter, we shall describe the issue of backreaction wherein we compute the energy density associated with the perturbations evolved from squeezed initial states and compare it against the background energy density. We argue that it is rather challenging to achieve such specific initial states by invoking mechanisms operating prior to inflation. Moreover, we find that backreaction severely restricts the extent of deviation of the initial state from the Bunch-Davies vacuum, particularly on small scales. This, in turn, implies that the desired amplification in the power spectrum and the larger levels of non-Gaussianities *cannot* be achieved in this approach unless the choice of the specific initial state is satisfactorily justified and the issue of backreaction is overcome. We shall finally conclude in Sec. 4.5 with a brief summary and outlook.

4.2 SQUEEZED INITIAL STATES, SCALAR POWER AND BI-SPECTRA

In this section, we shall construct scalar power spectra with a lognormal peak from squeezed initial states. We shall also calculate the associated scalar bispectra and utilize the result to arrive at the corresponding non-Gaussian modifications to the power spectrum.

As far as the background dynamics is concerned, we shall have in mind the scenario of slow roll inflation. Recall that, in such a case, while it is the combination of the nearly constant Hubble parameter $H_{\rm I}$ and the first slow parameter ϵ_1 that determine the amplitude of the scalar power spectrum, the first two slow roll parameters ϵ_1 and ϵ_2 determine the scalar spectral index $n_{\rm s}$. Moreover, the tensor-to-scalar ratio r is determined by the first slow roll parameter ϵ_1 (in these contexts, see Subsecs. 1.1.2 and 1.2.1). The values of these parameters can be chosen so that we achieve nearly scale invariant scalar and tensor power spectra that are consistent with the recent constraints from Planck over the CMB scales [6]. However, for convenience, in our calculations below, we shall work with the de Sitter modes to describe the scalar perturbations. The modes, say, $f_k(\eta)$, describing the scalar perturbations that emerge from initial conditions corresponding to squeezed states can be expressed as [261–271, 273]

$$f_k(\eta) = \frac{i\,H_{\rm I}}{2\,M_{_{\rm Pl}}\,\sqrt{k^3\,\epsilon_1}}\,\left[\alpha(k)\,\left(1+i\,k\,\eta\right)\,{\rm e}^{-i\,k\,\eta} - \beta(k)\,\left(1-i\,k\,\eta\right)\,{\rm e}^{i\,k\,\eta}\right], \tag{4.1}$$

where $\alpha(k)$ and $\beta(k)$ are the so-called Bogoliubov coefficients. Note that we have encountered such an expression for the mode function earlier in a particular scenario leading to a suppression of power over large scales and we have repeated the expression here for convenience [*cf.* Subsec. 2.2.1, Eq. (2.6)]. As we had pointed out earlier, the standard Bunch-Davies initial conditions correspond to setting $\alpha(k) = 1$ and $\beta(k) = 0$. The above modes correspond to squeezed initial states that are excited states above the Bunch-Davies vacuum. We should also mention that the Bogoliubov coefficients $\alpha(k)$ and $\beta(k)$ are not completely independent functions, but satisfy the following constraint:

$$|\alpha(k)|^2 - |\beta(k)|^2 = 1. \tag{4.2}$$

This constraint arises due to the fact that the Wronskian associated with the differential equation governing the scalar perturbations is a constant, which is determined by the initial conditions imposed on the modes.

4.2.1 Power spectrum from squeezed initial states

The power spectrum of the scalar perturbations evolving from squeezed initial states can be evaluated towards the end of inflation (*i.e.* as $\eta \to 0$). Upon using the modes (4.1), the resulting power spectrum can be expressed in terms of the Bogoliubov coefficients $\alpha(k)$ and $\beta(k)$ as follows:

$$\mathcal{P}_{_{\rm S}}(k) = \frac{k^3}{2\,\pi^2}\,|f_k(\eta\to 0)|^2 = \mathcal{P}_{_{\rm S}}^0(k)\,|\alpha(k)-\beta(k)|^2, \tag{4.3}$$

where $\mathcal{P}_{\rm S}^{0}(k)$ denotes the COBE normalized, nearly scale invariant spectrum with a small red tilt given by Eq. (1.17a). Since we are interested in the small scale features of the spectrum, for simplicity, we shall assume that $\mathcal{P}_{\rm S}^{0}(k)$ is strictly scale invariant with a COBE normalized amplitude over all the wave numbers of our interest. We should hasten to add that introducing a small red tilt does not affect our conclusions in the remainder of our discussion. We shall choose to work with the following values of the primary slow roll inflationary parameters: $H_{\rm I} = 4.16 \times 10^{-5}\, M_{\rm Pl}$, $\epsilon_1 = 10^{-2}$ and $\epsilon_2 = 2\,\epsilon_1$. Also, note that the power spectrum is independent of an overall phase factor and depends only on the relative phase factor between $\alpha(k)$ and $\beta(k)$.

Let us now define $\delta(k) = \beta(k)/\alpha(k)$. Then, upon using the constraint (4.2), the power spectrum (4.3) can be written in terms of the function $\delta(k)$ as

$$\mathcal{P}_{\rm S}(k) = \mathcal{P}_{\rm S}^{0}(k)\, \left[\frac{|1-\delta(k)|^2}{1-|\delta(k)|^2}\right]. \tag{4.4}$$

For ease of modeling, we shall assume the relative phase factor between $\alpha(k)$ and $\beta(k)$ to be zero. We should clarify that this assumption is made just to simplify our calculations. It can be relaxed, if needed, to model the spectrum with the phase factor taken into account. Setting the relative phase factor to be zero essentially implies that $\delta(k)$ is real so that the above expression for the scalar power spectrum reduces to

$$\mathcal{P}_{\rm S}(k) = \mathcal{P}_{\rm S}^{0}(k)\, \left\{\frac{[1-\delta(k)]^2}{1-\delta^2(k)}\right\}. \tag{4.5}$$

With the above form of the spectrum arising from squeezed initial states, we shall now proceed to model the feature of our interest. Let us assume that the power spectrum has a localized feature over a certain range of wave numbers, say, $g(k)$, so that $\mathcal{P}_{\rm S}(k)$ is given by

$$\mathcal{P}_{\rm S}(k) = \mathcal{P}_{\rm S}^{0}(k)\, [1+g(k)]. \tag{4.6}$$

Upon comparing the above two equations, it is evident that the feature $g(k)$ is related to $\delta(k)$ as follows:

$$\delta(k) = \frac{-g(k)}{2+g(k)}. \tag{4.7}$$

It should be clear that we have essentially traded off the function $g(k)$ for $\delta(k)$. In other words, we can choose an initial squeezed state described by $\delta(k)$ to lead to the desired feature $g(k)$ in the power spectrum. In this chapter, we shall assume $g(k)$ to be a lognormal function of the wave number k. Such a form for the feature in the spectrum is often considered because of the fact that, when departures from slow roll arise, many single field and two field models lead to scalar power spectra whose shape near the peak can be roughly approximated by such a function (see, for instance, Refs. [166, 245, 274]). Also, it simplifies the calculations involved and hence allows an easier comparison of the quantities $f_{_{\mathrm{PBH}}}$ and $\Omega_{_{\mathrm{GW}}}$ against the observational constraints [166, 275]. We shall assume that the function $g(k)$ takes the form

$$g(k) = \frac{\gamma}{\sqrt{2\,\pi\,\Delta_k^2}} \exp\left[-\frac{\ln^2(k/k_{\mathrm{f}})}{2\,\Delta_k^2}\right], \tag{4.8}$$

where γ represents the strength of the feature in the spectrum, Δ_k determines the width of the Gaussian and k_{f} denotes the location of the peak of the lognormal distribution. It is useful to note here that, given $g(k)$, the Bogoliubov coefficients $\alpha(k)$ and $\beta(k)$ can be obtained to be

$$\alpha(k) = \frac{2 + g(k)}{2\,\sqrt{1+g(k)}}, \quad \beta(k) = \frac{-g(k)}{2\,\sqrt{1+g(k)}}. \tag{4.9}$$

We should stress again that these expressions for $\alpha(k)$ and $\beta(k)$ have been arrived at under the assumption that their relative phase factor is zero. We should also point out that setting $\gamma = 0$ leads to $g(k) = 0$, $\delta(k) = 0$, $\alpha(k) = 1$ and $\beta(k) = 0$. This recovers the standard Bunch-Davies vacuum state and the scale invariant spectrum. Moreover, note that, for modes far away from k_{f}, *i.e.* for $k \gg k_{\mathrm{f}}$ or $k \ll k_{\mathrm{f}}$, $g(k) \to 0$, and we again recover the standard Bunch-Davies vacuum state. Therefore, it should be clear that, in our scenario, it is only modes around k_{f} which evolve from non-vacuum initial states. Further, the strength of their deviation from the vacuum state is proportional to the parameter γ.

In Fig. 4.1, we have plotted the scalar power spectra $\mathcal{P}_{_{\mathrm{S}}}(k)$ containing a lognormal feature with peaks located at four different wave numbers k_{f} with suitable values for the parameter γ. In the figure, we have also plotted the modified power spectra, *i.e.* $\mathcal{P}_{_{\mathrm{S}}}(k)+\mathcal{P}_{_{\mathrm{C}}}(k)$ [*cf.* Eqs. (3.24) and (3.25)], that have been arrived at when the non-Gaussian modifications are taken into account. The reason behind the specific choice of the values for the parameter γ will become clear when we discuss the non-Gaussian modifications to spectra in a subsequent subsection.

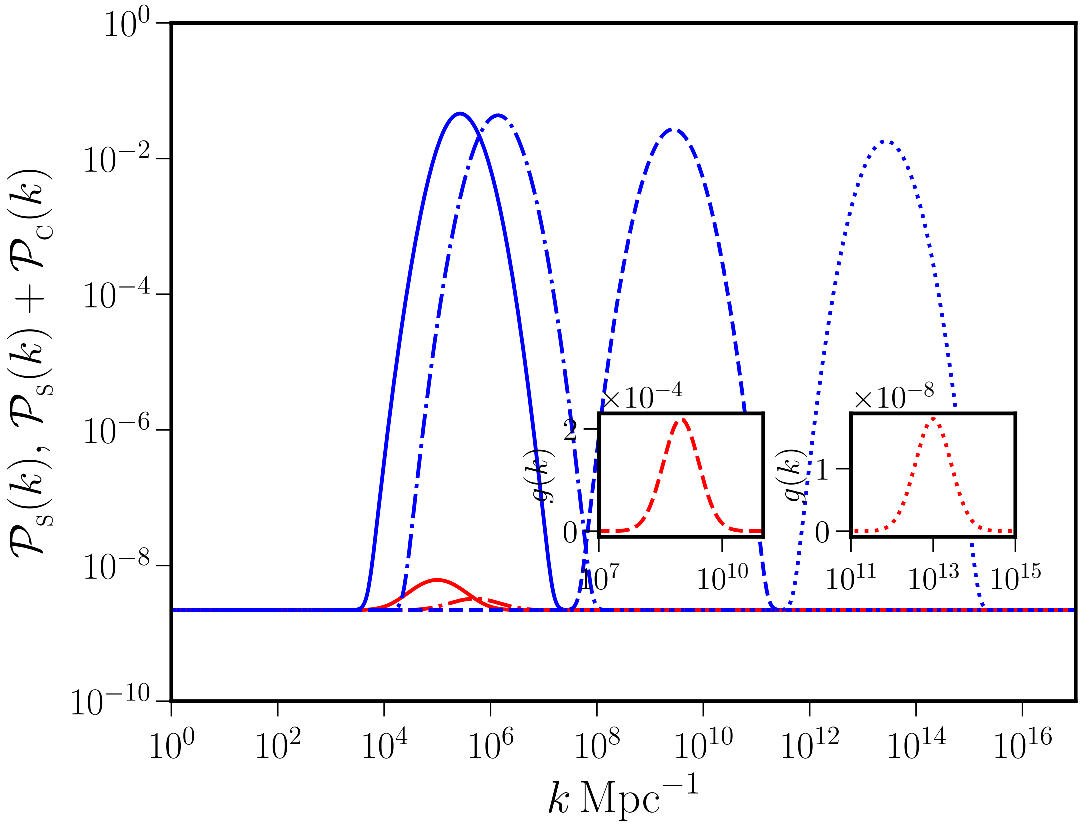

Figure 4.1: The scalar power spectra with a lognormal shape obtained from suitably chosen squeezed initial states have been plotted for different sets of the parameters γ and $k_{\rm f}$ that determine the strength and the location of the peaks. Note that, we have plotted the original spectra $\mathcal{P}_{\rm S}(k)$ (in red) as well as the modified spectra $\mathcal{P}_{\rm S}(k)+\mathcal{P}_{\rm C}(k)$ (in blue), where $\mathcal{P}_{\rm C}(k)$ denotes the non-Gaussian modifications to the power spectrum [*cf.* Eqs. (3.24) and (3.25)]. We have illustrated the spectra for the following four values of $k_{\rm f}$: $10^5\,{\rm Mpc}^{-1}$ (as solid curves), $5\times10^5\,{\rm Mpc}^{-1}$ (as dashed-dotted curves), $10^9\,{\rm Mpc}^{-1}$ (as dashed curves) and $10^{13}\,{\rm Mpc}^{-1}$ (as dotted curves). We have chosen the corresponding values of γ to be 4.5, 1.2, 5.5×10^{-4} and 4.5×10^{-8}, respectively. We have set the width Δ_k of the lognormal distribution to be unity in all the cases. The features in the original spectra $\mathcal{P}_{\rm S}(k)$ with peaks around $10^9\,{\rm Mpc}^{-1}$ and $10^{13}\,{\rm Mpc}^{-1}$ are not as discernible as those at the two other locations due to the small values of γ. Hence, in these two cases, we have included insets to highlight the function $g(k)$ [*cf.* Eq. (4.8)] instead. The parameter γ has been chosen so that, when the non-Gaussian modifications are taken into account, all the power spectra have roughly the same amplitudes at their peaks.

4.2.2 The associated scalar bispectrum and the non-Gaussianity parameter

We shall now proceed to calculate the corresponding scalar bispectra to eventually take into account the non-Gaussian modifications to the power spectra. In scenarios involving slow roll inflation, the scalar bispectrum, say, $G(\boldsymbol{k}_1, \boldsymbol{k}_2, \boldsymbol{k}_3)$, is known to consist of seven contributions, which arise from the cubic order action governing the scalar perturbations (see Refs. [52, 53, 59]; also see our discussion in Subsec. 1.1.3). Of these seven contributions, six arise due to the bulk terms in the third order action, while the seventh arises due to a field redefinition carried out to absorb the boundary terms [60, 61]. Amongst these contributions, in the situation of interest, it is known that the first, second, third and the seventh terms, say, $G_1(\boldsymbol{k}_1, \boldsymbol{k}_2, \boldsymbol{k}_3)$, $G_2(\boldsymbol{k}_1, \boldsymbol{k}_2, \boldsymbol{k}_3)$, $G_3(\boldsymbol{k}_1, \boldsymbol{k}_2, \boldsymbol{k}_3)$ and $G_7(\boldsymbol{k}_1, \boldsymbol{k}_2, \boldsymbol{k}_3)$, dominate the contributions due to the remaining terms. Recall that the three vectors $\boldsymbol{k}_1$, $\boldsymbol{k}_2$ and $\boldsymbol{k}_3$ form the edges of a triangle [*cf.* Eq. (1.18)]. As we had discussed in Subsec. 3.7.2, it is the bispectrum evaluated in the so-called squeezed limit of the triangular configuration, *i.e.* when $k_1 \to 0$ and $k_2 \simeq k_3 \simeq k$, that is expected to contribute to the non-Gaussian modifications to the power spectrum (in this context, see, for instance, Refs. [181, 189, 190]).

The scalar bispectrum in slow roll inflation with squeezed initial states can be calculated easily using the de Sitter modes (4.1) describing the scalar perturbations (see, for example, Refs. [264, 266, 268–271]). Since the resulting expressions are somewhat lengthy, we relegate them to an appendix. We have listed the complete expressions for dominant contributions $G_1(\boldsymbol{k}_1, \boldsymbol{k}_2, \boldsymbol{k}_3)$, $G_2(\boldsymbol{k}_1, \boldsymbol{k}_2, \boldsymbol{k}_3)$, $G_3(\boldsymbol{k}_1, \boldsymbol{k}_2, \boldsymbol{k}_3)$ and $G_7(\boldsymbol{k}_1, \boldsymbol{k}_2, \boldsymbol{k}_3)$ in App. G. It is useful to note that, in the squeezed limit, the dominant contributions to the scalar bispectrum at the wave number k_{f}, corresponding to the location of the peak in the power spectrum $\mathcal{P}_{\mathrm{S}}(k)$, can be obtained to be

$$\begin{aligned}
\lim_{k_1 \ll k_{\mathrm{f}}} k_1^3\, k_{\mathrm{f}}^3\, \left[G_1(\boldsymbol{k}_1, \boldsymbol{k}_{\mathrm{f}}, -\boldsymbol{k}_{\mathrm{f}}) + G_3(\boldsymbol{k}_1, \boldsymbol{k}_{\mathrm{f}}, -\boldsymbol{k}_{\mathrm{f}})\right] &= k_1^3\, k_{\mathrm{f}}^3\, \left[G_1(k_{\mathrm{f}}) + G_3(k_{\mathrm{f}})\right] \\
&\simeq \frac{H_{\mathrm{I}}^4}{16\, M_{\mathrm{Pl}}^4\, \epsilon_1}\, \frac{k_{\mathrm{f}}}{k_1}\, \frac{\gamma}{\sqrt{2\,\pi\,\Delta_k^2}} \\
&\quad \times \left(2 + \frac{\gamma}{\sqrt{2\,\pi\,\Delta_k^2}}\right),
\end{aligned} \tag{4.10a}$$

$$\begin{aligned}
\lim_{k_1 \ll k_{\mathrm{f}}} k_1^3\, k_{\mathrm{f}}^3\, G_2(\boldsymbol{k}_1, \boldsymbol{k}_{\mathrm{f}}, -\boldsymbol{k}_{\mathrm{f}}) &= k_1^3\, k_{\mathrm{f}}^3\, G_2(k_{\mathrm{f}}) \\
&\simeq \frac{H_{\mathrm{I}}^4}{16\, M_{\mathrm{Pl}}^4\, \epsilon_1}\, \frac{k_{\mathrm{f}}}{k_1}\, \frac{\gamma}{\sqrt{2\,\pi\,\Delta_k^2}} \\
&\quad \times \left(2 + \frac{\gamma}{\sqrt{2\,\pi\,\Delta_k^2}}\right),
\end{aligned}$$

(4.10b)

$$\lim_{k_1 \ll k_{\rm f}} k_1^3\, k_{\rm f}^3\, G_7(\boldsymbol{k}_1, \boldsymbol{k}_{\rm f}, -\boldsymbol{k}_{\rm f}) = k_1^3\, k_{\rm f}^3\, G_7(k_{\rm f}) \simeq \frac{H_{_{\rm I}}^4\, \epsilon_2}{16\, M_{_{\rm Pl}}^4\, \epsilon_1^2} \left(1 + \frac{\gamma}{\sqrt{2\,\pi\,\Delta_k^2}}\right). \tag{4.10c}$$

In the above expressions, as is usually done in the context of slow roll inflation, we have combined the contributions $G_1(k_{\rm f})$ and $G_3(k_{\rm f})$, as they have a similar dependence on the wave numbers [see, for instance, Ref. [60]; in this context, also see Eqs. (1.27)]. We should clarify that the above expressions are the dominant contributions for the values of γ we have worked with. The striking property of the contributions $G_1(k_{\rm f}) + G_3(k_{\rm f})$ and $G_2(k_{\rm f})$ is their dependence on the squeezed mode as $1/k_1$. This property of the bispectrum in the case of squeezed initial states is well known [266, 268, 270]. On the other hand, note that, $G_7(k_{\rm f})$ is independent of k_1 in the limit $k_1 \ll k_{\rm f}$. Therefore, at the leading order, the bispectrum around $k_{\rm f}$ is inversely proportional to the squeezed mode k_1.

Consider an observational survey extending over a certain range of scales such as, say, the measurements of the anisotropies in the CMB, which spans a few decades in wave numbers. In such a case, we can calculate the squeezed limit of the bispectrum assuming k_1 to be the smallest wave number within the range. In practice, this implies that $1 \lesssim k/k_1 \lesssim 10^4$ over the CMB scales. Therefore, for squeezed initial states, the bispectrum in the squeezed limit will be proportionately large and, hence, the associated non-Gaussianity parameter can be expected to be of a similar order. Note that, in this chapter, we are interested in examining phenomena leading to formation of PBHs and generation of secondary GWs which occur at much smaller scales. For such observations spanning several decades in wave numbers, it seems reasonable again to choose k_1 to be the smallest observable wave number. Therefore, in our calculations, we shall set the value of squeezed mode to be $k_1 \simeq 10^{-4}\,{\rm Mpc}^{-1}$, which roughly corresponds to the Hubble scale today. Such a choice can clearly lead to a considerable enhancement in the amplitude of the scalar bispectrum and the corresponding non-Gaussianity parameter at the small scales of interest. Moreover, we should mention that, because of this boost in the amplitude, the consistency condition relating the scalar bispectrum to the power spectrum in the squeezed limit can be expected to be violated over these scales.

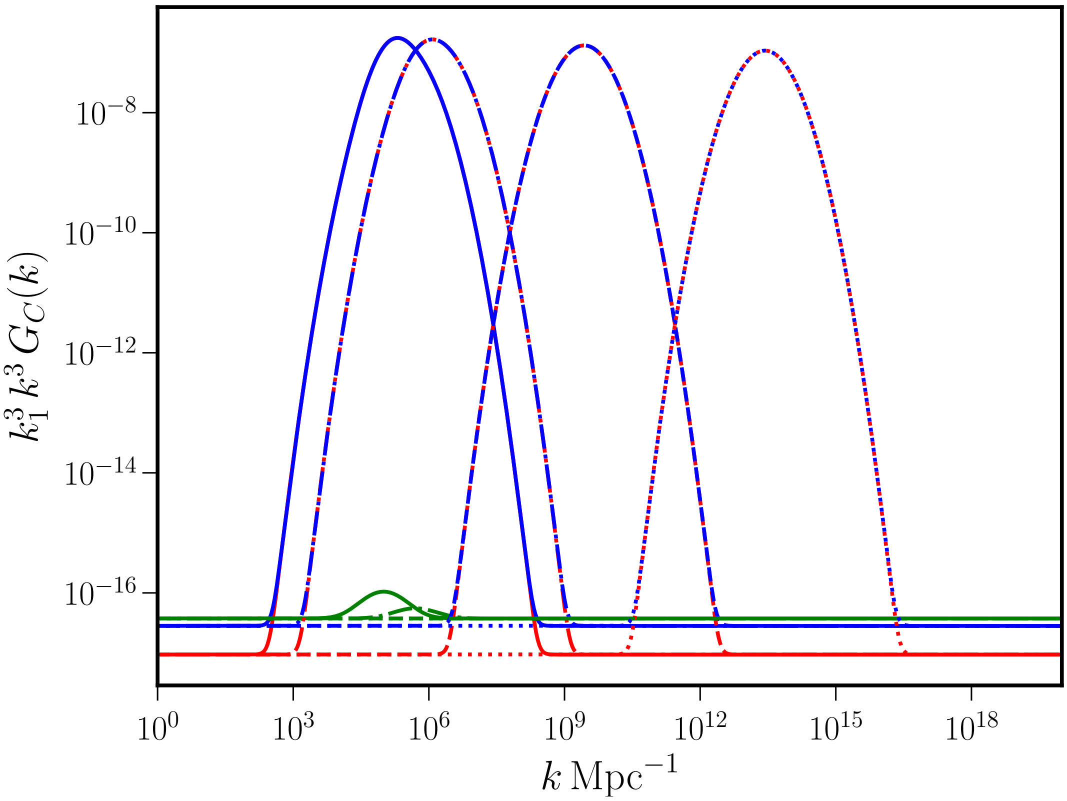

Figure 4.2: The dominant contributions to the dimensionless scalar bispectra in the squeezed limit, *viz.* $k_1^3\, k^3$ times $G_1(k) + G_3(k)$, $G_2(k)$ and $G_7(k)$, have been plotted (in red, blue and green, respectively) for non-vacuum initial states which lead to scalar power spectra with lognormal peaks. We have plotted the contributions to the dimensionless bispectra for the four sets of values for the parameters γ and $k_{\rm f}$ (as solid, dashed-dotted, dashed and dotted curves) we had considered in the previous figure. It is clear that the bulk terms $G_C(k)$ with $C = \{1, 2, 3\}$ dominate the contributions to the bispectrum. In contrast, as expected, the boundary term $G_7(k)$ has a much smaller amplitude and mimics the shape of the power spectrum.

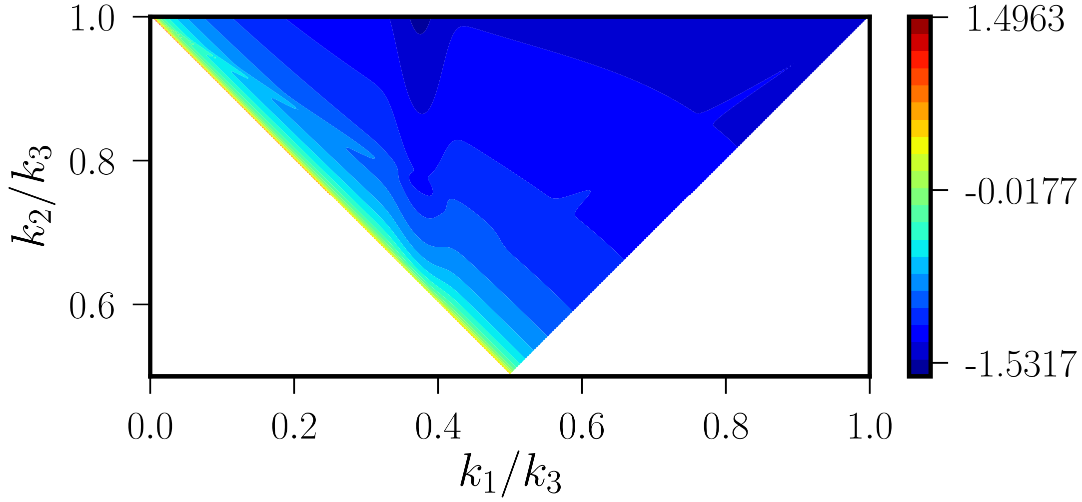

Figure 4.3: The non-Gaussianity parameter $\log|f_{_{\rm NL}}|$ has been plotted as a density plot in the k_1/k_3–k_2/k_3 plane, for the first of the four sets of parameters we had introduced in Fig. 4.1. We have set $k_3 = k_{\rm f}$ and varied k_1/k_3 over the range $[5 \times 10^{-4}, 1]$ in arriving at this figure. Note that the $f_{_{\rm NL}}$ parameter has a largely 'local' shape, with its maximum amplitude (in red) occurring in the so-called flattened limit corresponding to the left edge of the triangle.

In Fig. 4.2, we have plotted the behavior of the bispectrum in the squeezed limit for the four set of values for the parameters of γ and $k_{\rm f}$ we considered earlier. Notice that the amplitudes of the bispectra are significantly enhanced around the locations of the peaks in the power spectra. The amplitudes retain their slow roll values away from the peaks. The amplification of several orders of magnitude around $k_{\rm f}$ arises evidently due to the dependence of the bispectrum on the squeezed mode as $1/k_1$, as we discussed above. We should stress that this amplification occurs even for a relatively small value of the parameter γ, which quantifies the deviations from the Bunch-Davies vacuum. We find that, for a larger k, we require a smaller value of γ to achieve the same level of enhancement of the bispectrum. In other words, the bispectrum becomes increasingly sensitive to deviations from the standard vacuum state at smaller scales.

Recall that, we had introduced the non-Gaussianity parameter $f_{_{\rm NL}}(\boldsymbol{k}_1, \boldsymbol{k}_2, \boldsymbol{k}_3)$ associated with the scalar bispectrum $G(\boldsymbol{k}_1, \boldsymbol{k}_2, \boldsymbol{k}_3)$ in Eq. (1.28). The dimensionless parameter $f_{_{\rm NL}}(\boldsymbol{k}_1, \boldsymbol{k}_2, \boldsymbol{k}_3)$ can be calculated using the expressions (4.6), (4.8) and (G.1) for the power spectrum, the function $g(k)$ and the bispectrum. In order to understand the complete shape of the scalar bispectrum, in Fig. 4.3, we have illustrated the non-Gaussianity parameter as a density plot in the k_1/k_3–k_2/k_3 plane for the first of the four

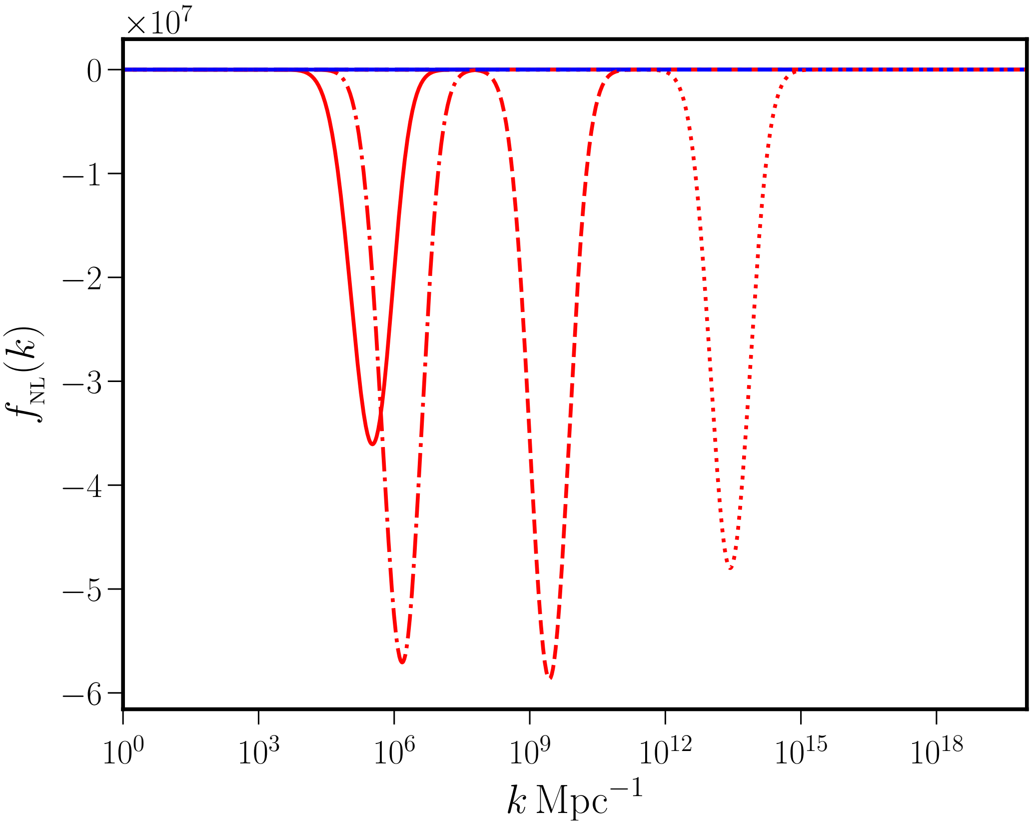

Figure 4.4: The non-Gaussianity parameter $f_{\rm NL}(k)$ in the squeezed limit has been plotted (in red) for the four set of parameters (as solid, dashed-dotted, dashed and dotted curves) leading to lognormal spectra we had considered in the first two figures. We have also plotted the quantity $f_{\rm NL}^{\rm CR}(k)$ (in blue) for all the cases to illustrate the fact that the consistency condition is strongly violated around the region of the peaks in the power spectra.

sets of parameters for γ and $k_{\rm f}$ we had introduced earlier (see the caption of Fig. 4.1). The figure clearly illustrates the fact that the non-Gaussianity parameter has a largely 'local' shape. As is well known, its amplitude is the largest in the flattened limit, *i.e.* along the line $k_2/k_3 = 1 - k_1/k_3$ which describes the left edge of the triangle in Fig. 4.3. This shape evidently depends on the choice of k_3, which in this illustration has been set to be the location of the peak $k_{\rm f}$.

Let us now turn to consider the behavior of the parameter $f_{\rm NL}$ in the squeezed limit. In such a limit, on utilizing the results (4.10), we obtain the value of $f_{\rm NL}$ at the location of the peak in the power spectrum $\mathcal{P}_{\rm S}(k)$ to be

$$\lim_{k_1\ll k_{\rm f}} f_{\rm NL}^{\rm SL}(\boldsymbol{k}_1, \boldsymbol{k}_{\rm f}, -\boldsymbol{k}_{\rm f}) = f_{\rm NL}^{\rm SL}(k_{\rm f}) \simeq -\frac{5\,\epsilon_1}{6}\,\frac{k_{\rm f}}{k_1}\,\frac{\gamma}{\sqrt{2\,\pi\,\Delta_k^2}}\,\left(\frac{2+\frac{\gamma}{\sqrt{2\,\pi\,\Delta_k^2}}}{1+\frac{\gamma}{\sqrt{2\,\pi\,\Delta_k^2}}}\right). \tag{4.11}$$

In Fig. 4.4, we have plotted the behavior of $f_{\rm NL}(k)$ in the squeezed limit for the four sets of parameters we have mentioned earlier. We find that, for these choices of the parameters, the value of $f_{\rm NL}$ is of order 10^7 around $k_{\rm f}$, while it has the slow roll value of 10^{-2} away from $k_{\rm f}$. Also, we find that the consistency condition — *viz.* that $f_{\rm NL}^{\rm CR}(k) = 5\,[n_{\rm S}(k)-1]\,/12$, where $n_{\rm S}(k) = 1 + {\rm d}\ln\mathcal{P}_{\rm S}(k)/{\rm d}\ln k$ is the scalar spectral index [*cf.* Eq. (2.11)] — is strongly violated around the lognormal peak as expected, while it is satisfied sufficiently far away from the peak. It has been argued that any calculation of $f_{\rm NL}$ has to account for the so-called local observer effect (in this context, see, for instance, Refs. [234, 235]). This essentially means that, to arrive at the observable value of the non-Gaussianity parameter in the squeezed limit, we need to subtract the part of $f_{\rm NL}$ satisfying the consistency relation from its total value. In the scenario of interest, around the peaks in the power spectra, the quantity $f_{\rm NL}^{\rm CR}(k)$ is negligible compared to the magnitude of $f_{\rm NL}$ obtained from the squeezed initial states. The main conclusions we can draw from the above considerations are twofold. Firstly, for perturbations evolved from non-vacuum initial states, the non-Gaussianity parameter $f_{\rm NL}$ is inversely proportional to the value of squeezed mode. Hence, it has a rather large amplitude over small scales for the values of the parameter γ we have considered. Secondly, the amplitude of $f_{\rm NL}$ is highly sensitive to even minor deviations from standard vacuum state. As we shall discuss in the following subsection, the large value for the non-Gaussianity parameter in the squeezed limit leads to substantial modifications to the original power spectrum. This should be contrasted with scenarios involving, say, ultra slow roll inflation, that we had considered in the previous chapter, wherein the consistency condition governing the scalar bispectrum is satisfied in the squeezed limit and hence the non-Gaussian corrections to the power spectrum prove to be either negligible or identically zero [18, 228].

4.2.3 Non-Gaussian modifications to the scalar power spectrum

Having arrived at the bispectrum and the corresponding non-Gaussianity parameter, let us now proceed to calculate the non-Gaussian modifications to the scalar power spectrum [18, 189, 190, 192, 276]. Recall that, we have earlier arrived at an expression for the non-Gaussian modifications to the power spectrum arising due to an $f_{\rm NL}$ that is assumed to be local in shape [*cf.* Subsec. 3.7.2]. Therefore, we shall work with the value $f_{\rm NL}$ in the squeezed limit when calculating the non-Gaussian modifications to the power spectrum. (Note that, around $k_{\rm f}$, the scalar bispectrum had a largely 'local' shape, as illustrated in Fig. 4.3.) Moreover, the parameter $f_{\rm NL}$ in the squeezed limit in our scenario is highly scale dependent in the sense that it is large around $k_{\rm f}$ (for the values of the parameter γ we have worked with), but is completely negligible away from it. Hence, when calculating the modifications to the spectrum, in Eq. (3.25), we have assumed $f_{\rm NL}$ to be a function of k. In Fig. 4.1, we have plotted the modified spectra, *viz.* $\mathcal{P}_{\rm S}(k) + \mathcal{P}_{\rm C}(k)$, as well as the spectra $\mathcal{P}_{\rm S}(k)$ we had originally constructed. Note that the non-Gaussian modifications $\mathcal{P}_{\rm C}(k)$ dominate at small scales around the peaks in the original power spectra. In fact, it is due to the dependence of the non-Gaussianity parameter $f_{\rm NL}$ on the squeezed mode as $1/k_1$ that we have been able to achieve the required boost in the power spectrum [of $\mathcal{O}(10^{-2})$] at small scales. Also, we should point out that, given a γ, the amplification due to the non-Gaussian modifications are larger at a higher $k_{\rm f}$. It is due to this reason that, for a larger $k_{\rm f}$, we have worked with a smaller value of γ. We have chosen these parameters so that, when the non-Gaussian modifications are taken into account, the modified power spectra have comparable amplitudes at their maxima despite the varying amplitudes of the peaks in their original spectra. We should clarify that the large, cubic order, non-Gaussian corrections do not lead to a breakdown of the perturbation theory since the scalar power spectra are of $\mathcal{O}(10^{-2})$ even when the modifications due to the scalar bispectra have been taken into account (*cf.* Fig. 4.1).

It is worthwhile to highlight another related point at this stage of our discussion. We find that the widths of the modified power spectra are larger than the widths of the original power spectra which were dictated by the parameter Δ_k that we have set to unity. This is because of the nature of the integrand involved that describes the non-Gaussian correction given in Eq. (3.25). The appearance of the integration variables s and d in the arguments of the original power spectrum as well as the limits of the integrals involved contribute to the widening of the peak and a slight shift of power towards larger wave numbers in the final modified spectra.

4.3 FORMATION OF PBHS AND GENERATION OF SECONDARY GWS

In this section, we shall compute the observable quantities at small scales, *viz.* the fraction of PBHs constituting the dark matter density today $f_{\rm PBH}$ and the dimensionless spectral energy density of secondary GWs $\Omega_{\rm GW}$, using the scalar power spectra with the non-Gaussian corrections taken into account. Recall that, we have described in detail the calculation of $f_{\rm PBH}(M)$ and $\Omega_{\rm GW}(f)$ arising from a given scalar power spectrum in

Subsecs. 1.2.2 and 1.2.3, respectively.

In Fig. 4.5, we have plotted the quantities $f_{\text{PBH}}(M)$ and $\Omega_{\text{GW}}(f)$ for the four power spectra we have obtained from squeezed initial states with the non-Gaussian modifications taken into account [*cf.* Eqs. (3.24) and (3.25)]. We have also included the constraints on $f_{\text{PBH}}(M)$ that are presently available from different datasets in the various mass ranges (see Refs. [9, 12]; for recent discussions of the constraints over specific mass ranges, see Refs. [217, 277]). Moreover, we have illustrated the sensitivity curves of the various GW observatories and missions (in this context, see Ref. [14]). As expected, the enhancements in the scalar power on small scales lead to proportional amplifications in $f_{\text{PBH}}(M)$ and $\Omega_{\text{GW}}(f)$ over the corresponding masses and frequencies. Also, due to the nature of the integrals that determine $\overline{\mathcal{P}_h(k,\eta)}$ [*cf.* Eq. (1.54)], the peaks of $\Omega_{\text{GW}}(f)$ are considerably wider when compared to the peaks of the scalar power spectra. As can be seen from the figure, the predicted $f_{\text{PBH}}(M)$ and $\Omega_{\text{GW}}(f)$ curves already intersect the various constraints and sensitivity curves. These constraints immediately translate to bounds on the parameter γ which determines the strength of the feature in the scalar power spectra. Recall that, the Bogoliubov coefficient $\beta(k)$ is proportional to γ [*cf.* Eq. (4.9)]. So, in our scenario of PBHs and secondary GWs produced from excited initial states, evidently, the limits on f_{PBH} and Ω_{GW} directly constrain the non-vacuum nature of the states from which the perturbations evolve.

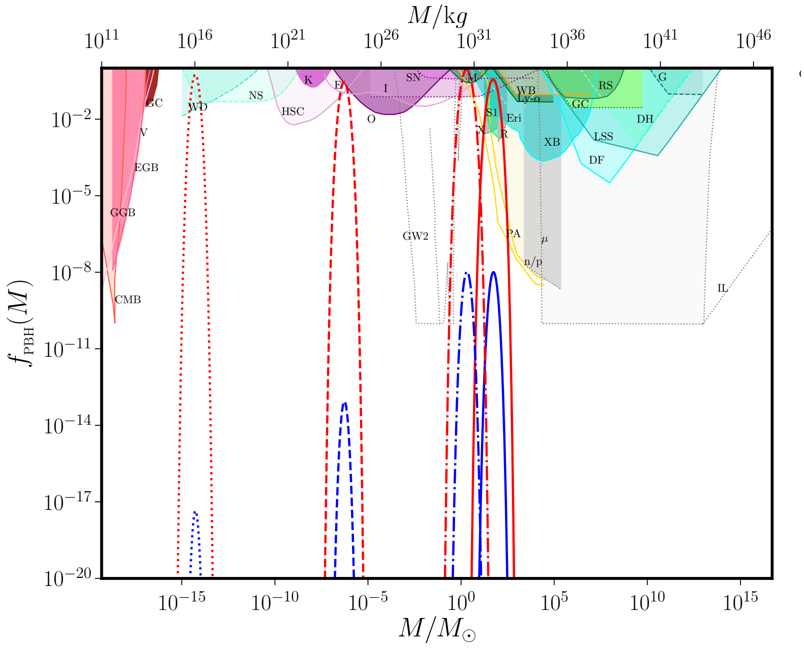

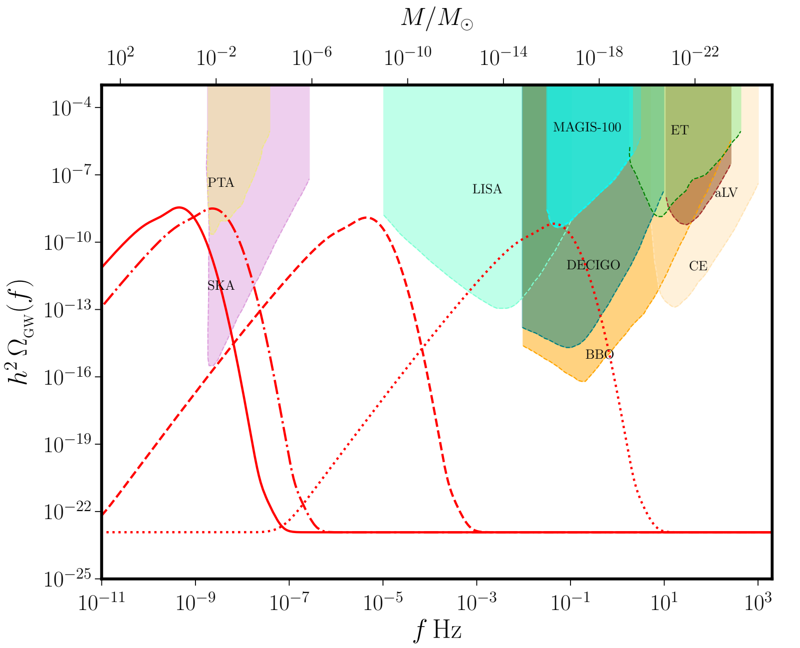

Figure 4.5: The quantity $f_{\rm PBH}(M)$ (on top, for $\delta_{\rm c} = 1/3$ and 0.5 in red and blue, respectively) and the dimensionless energy density of GWs $\Omega_{\rm GW}(f)$ (at the bottom) have been plotted for the cases of the four lognormal spectra with the non-Gaussian modifications to the power spectrum taken into account that were illustrated in Fig. 4.1. The various constraints on $f_{\rm PBH}(M)$ from different observations have also been indicated (in the top part of the figure on top) over the corresponding mass ranges. We have also included the sensitivity curves of the various ongoing and upcoming observational missions of GWs (as shaded regions in the top part of the figure at the bottom). The intersections of the curves with the shaded regions translate to constraints on the parameter γ which determines the extent of deviation of the initial state from the Bunch-Davies vacuum.

4.4 CHALLENGES ASSOCIATED WITH SQUEEZED INITIAL STATES

In the last two sections, we have illustrated that a specific choice for the Bogoliubov coefficient $\beta(k)$ can lead to the desired lognormal peak in the scalar power spectrum [*cf.* Eqs. (4.6), (4.8) and (4.9)]. We have also shown that, since the cubic order non-Gaussian corrections prove to be significant in the squeezed limit in the non-vacuum initial states, it is possible to choose a relatively small value for $\beta(k)$ to arrive at large peaks in the effective scalar power spectrum. We have also examined the possible imprints of such power spectra on the extent of PBHs produced and the secondary GWs generated on small scales. In this section, we shall discuss some of the challenges associated with squeezed initial states.

4.4.1 Possible mechanisms to generate squeezed states

The first task before us is to justify the choice of the squeezed initial states of our interest. In other words, we need to examine whether there exist mechanisms that can generate the specific form of $\beta(k)$ that we have considered. Note that, we have assumed that the curvature perturbation is in the non-vacuum initial state at some early time, say, η_{i}, when the smallest wave number of our interest, *viz.* $k_1 \simeq 10^{-4}\,\mathrm{Mpc}^{-1}$, is adequately inside the Hubble radius. In this subsection, we shall discuss mechanisms that can possibly excite the curvature perturbations to such an initial state and the challenges associated with them.

The first possibility would be to consider effects due to high energy physics. For instance, since the large scale modes emerge from sub-Planckian length scales during the initial stages of inflation, it has been argued that trans-Planckian physics may modify the dynamics of the perturbations during the early stages (for the original discussion, see Ref. [261]). But, in the absence of a viable model of quantum gravity to take into account the high energy effects, the equations describing the perturbations are often modified by hand. The modifications essentially introduce an energy scale into the equations of motion governing the perturbations, beyond which the new physics operates, while ensuring that the standard equations are satisfied at lower energies. One of the approaches that has been extensively examined in this context involves modifying the dispersion relation governing the perturbations (for example, see the review [270]). In this context, while the super-luminal dispersion relations are known to leave the primordial spectrum largely unaffected, the sub-luminal dispersion relations have been shown to lead to significant production of particles resulting in stronger features in the power spectrum [270]. However, the produced particles result in significant backreaction (a point which we shall discuss in the following subsection) making them unviable. We also find that, in some of the approaches, the power spectrum is modified on large scales, since they emerge from the sub-Planckian length scales at high energies (see, for instance, Ref. [278]). Another popular method that has been considered to take into account the high energy effects involves the imposition of non-trivial initial conditions on the standard modes as they emerge from the Planckian regime [279]. Such an approach is known to only result in oscillations in the power spectrum over a wide range of scales [280, 281].

Another possibility that can leave the curvature perturbation in an excited state during the early stages of inflation would be to consider an initial epoch of non-inflationary phase. Often, one either considers a radiation dominated phase or an initial period wherein the scalar field is rolling rapidly as we had discussed earlier in Chap. 2 (in this context, see, for instance, Refs. [103, 105]; for recent discussions, see Refs. [17, 121]). Again, in such cases, the power spectrum seems to be modified only on large scales and it often displays a sharp drop in power over these scales. Moreover, we should add that, in such scenarios, it is possible that a certain range of wave numbers would have never been inside the Hubble radius. Therefore, there can arise some ambiguity in the initial conditions that are to be imposed on these modes. Moreover, we should mention that, if such a pre-inflationary mechanism is to excite the state of the curvature perturbation at the small wave numbers $k_{\rm f}$ of interest, the mechanism should involve changes that occur as rapidly as $k_{\rm f}^{-1}$ (for a recent related discussion, see, for example, Ref. [282]). Yet another possibility would be to consider two stages of slow roll inflation with either a brief departure from slow roll or even a break from inflation sandwiched between them. But, these are exactly the scenarios of ultra slow roll and punctuated inflation that have been considered to generate increased power on small scales so as to lead to enhanced formation of PBHs and higher strengths of secondary GWs (see Refs. [18, 72, 161, 250]; also see our discussion in the previous chapter). Apart from single field models, as we had mentioned in the introductory section, there also exist inflationary scenarios involving two fields which can lead to a rapid rise in power on small scales [245, 255, 283]. Often, in this context, there arises a sharp turn in the trajectory of the fields, essentially giving rise to particle production and therefore a non-trivial form of $\beta(k)$ (in this context, see the discussion in Ref. [255]). However, these models involve a certain level of fine tuning of the field trajectory and the form of $\beta(k)$ will be dependent on the details of the model. Importantly, we should mention that, in such cases, the features are generated as the modes of interest leave the Hubble radius during the epochs of deviations from slow roll. Actually, this is true of any inflationary scenario. This implies that it is difficult to generate features on small scales as we desire by inducing or introducing transitions in or between inflationary phases at very early stages.

In fact, there exists one more possibility. One can treat the curvature perturbation that we are considering as associated with a test field in an inflationary regime driven by another source (for scenarios wherein the dominating background is driven by another scalar field, see, for instance, Refs. [284, 285]; for situations wherein the perturbations are dominated by, say, the Higgs field, see Refs. [95, 286]). The source that dominates the background dynamics either prior to inflation or in the early stages of the inflationary regime can excite the modes associated with the curvature perturbations leaving it in a squeezed state. Let us illustrate the points we wish to make in this regard by starting with the aid of an example. Consider a situation wherein the Fourier mode ψ_k of a quantum field satisfies an equation of motion of the following form:

$$\psi_k'' + \left(k^2 + \mu^2\, k_0^2\, \eta^2\right)\, \psi_k = 0, \tag{4.12}$$

where μ and k_0 denote scales associated with the system. The solution to such a differential equation can be expressed in terms of the parabolic cylinder functions and by comparing the asymptotic forms of the solutions at early and late times, one can immediately show that the number of particles produced in such a case is given by (in this context, see the discussions in the recent work [282])

$$|\beta(k)|^2 = \mathrm{e}^{-k^2/(\mu\, k_0)}. \tag{4.13}$$

In fact, such a result should not come as a surprise. One encounters an equation of motion of the above form when one considers a complex scalar field that is evolving in the background of a constant electric field in flat spacetime, leading to the well known Schwinger effect [287]. Note that the above Bogoliubov coefficient (to be precise, its modulus squared) is a Gaussian, which is close to the form that we desire. However, since it is not of the lognormal shape, it is peaked at $k = 0$ rather than at a non-zero k. Moreover, it has a maximum value of unity, whereas we require an additional parameter (such as γ) to be able to tune the amplitude of $\beta(k)$.

Let us now discuss mechanisms that can possibly help us achieve the desired $\beta(k)$ in a FLRW universe. A good starting point seems to be to construct situations in which the equation governing either the curvature perturbation or a test scalar field has the same form as Eq. (4.12) above so that we can at least arrive at a Gaussian form for $|\beta(k)|^2$. Recall that the Mukhanov-Sasaki variable v_k associated with the curvature perturbation satisfies Eq. (1.14a). Evidently, we require $z''/z = -\mu^2\, k_0^2\, \eta^2$ if we are to achieve the $|\beta(k)|^2$ mentioned above [*cf.* Eq. (4.13)]. In such a case, the generic solution to z can be immediately expressed in terms of a linear combination of the parabolic cylinder functions (as the modes v_k themselves can be). But, we find that the generic solution for z does not remain positive definite, which is unacceptable (due to the form of z quoted above). Therefore, the proposal does not seem viable. If we now instead consider a massive, test scalar field of mass μ in a radiation dominated universe, one arrives at an equation governing the modes exactly as in Eq. (4.12). Interestingly, one indeed obtains a spectrum of particles as in Eq. (4.13) when the evolution of massive scalar fields are examined in certain scenarios involving radiation dominated universes (in this context, see Ref. [288]). If such a scenario is acceptable, there still remains the task of converting the Gaussian distribution for $|\beta(k)|^2$ into a lognormal distribution. Remarkably, if we replace k^2 by $f^2(k)$ with $f(k) = \ln(k/k_{\mathrm{f}})$, we indeed arrive at a $|\beta(k)|^2$ which has a lognormal shape. However, the challenge is to justify the replacement of k^2 by a generic function $f^2(k)$. At first sight this seems possible if we modify the dispersion relation so that $\omega^2(k) = k^2$ is replaced by $\omega^2(k) = f^2(k)$. However, note that, since the field is evolving in a FLRW universe, such a modified dispersion relation would apply to the physical wave number k/a rather than to k itself (in this context, see the discussion in Ref. [270]). Clearly, such a choice modifies Eq. (4.12) and hence the solutions completely. More importantly, as we pointed out, it has been established that strong modifications to the dispersion relation will lead to a copious amount of particle production which backreacts significantly on the background (in this context, also see the following subsection on the issue of backreaction). The above set of arguments suggests that it is rather difficult to construct mechanisms that lead to the form of $\beta(k)$ that we have worked with.

4.4.2 Limits due to backreaction

In this subsection, we shall discuss another challenge that arises with the squeezed initial states we have worked with. When the perturbations are evolved from non-vacuum initial states, we must ensure that the energy density associated with the excited states is less than the energy density driving the inflationary background. If the densities become comparable, then, evidently, the perturbations can start affecting the background dynamics. This issue is often referred to as the backreaction problem (see, for instance, Refs. [263, 270, 272, 289–291]). We shall now arrive at constraints on the parameter γ that determines the strength of the squeezed states by demanding that the issue of backreaction is avoided in the situation we are considering.

The task ahead is to calculate the energy density associated with the curvature perturbations when they are assumed to be in a squeezed initial state. We find that the energy density associated with the curvature perturbations in the de Sitter limit that we are considering can be expressed as follows:

$$\begin{aligned}\rho_{\mathcal{R}} &= \rho_{\mathcal{R}}^{(1)} + \rho_{\mathcal{R}}^{(2)} \\ &\simeq \frac{1}{2\,\pi^2\,a^4}\int_{-\eta^{-1}}^{\infty} \mathrm{d}k\,k^3\,\vert\beta(k)\vert^2 \\ &\quad + \frac{H_{_{\mathrm{I}}}^2}{8\,\pi^2\,a^2}\int_{0}^{-\eta^{-1}} \mathrm{d}k\,k\,\biggl\{2\,\vert\beta(k)\vert^2 - [\alpha(k)\,\beta^\ast(k) + \alpha^\ast(k)\,\beta(k)]\biggr\}. \end{aligned} \tag{4.14}$$

where $\beta(k)$ is the Bogoliubov coefficient which indicates the extent of deviation from the Bunch-Davies vacuum. There are a couple of clarifying remarks we should make regarding this expression. Firstly, in arriving at the above expression, we have subtracted the contribution due to the Bunch-Davies vacuum, which, upon regularization, is known to correspond to (see, for example, Refs. [292, 293])

$$\rho_{\mathcal{R}}^{\mathrm{BD}} = \frac{61\,H_{_{\mathrm{I}}}^4}{960\,\pi^4}. \tag{4.15}$$

Clearly, this is sub-dominant to the background energy density which behaves as $\rho_{_{\mathrm{I}}} = 3\,H_{_{\mathrm{I}}}^2\,M_{_{\mathrm{Pl}}}^2$ (since $H_{_{\mathrm{I}}}/M_{_{\mathrm{Pl}}} < 10^{-5}$). Secondly, it should be evident that we have divided the total energy density $\rho_{\mathcal{R}}$ into two parts, with the first part $\rho_{\mathcal{R}}^{(1)}$ arising from the contributions due to the modes that are in the sub-Hubble domain at any instance, while the second part $\rho_{\mathcal{R}}^{(2)}$ corresponds to modes that are in the super-Hubble domain. At early times, when all the modes are well inside the Hubble radius, it is the first part that dominates (in this context, see, for instance, Refs. [263, 271]). This result can be easily understood in simple instances such as, say, power law inflation. In such cases, as is well known, the curvature perturbation behaves in a manner similar to that of a massless scalar field. The expression $\rho_{\mathcal{R}}^{(1)}$ is essentially the same as the energy density of a massless scalar field in the sub-Hubble limit. Note that the energy density $\rho_{\mathcal{R}}^{(1)}$ behaves as a^{-4}. In other words, the energy density is the largest at early times when the initial conditions are imposed on the modes of interest in the sub-Hubble regime. We shall soon see that this behavior severely restricts the amplitude of the parameter γ.

As we discussed above, it is the sub-Hubble contribution $\rho_{\mathcal{R}}^{(1)}$ that dominates in the expression (4.14) for $\rho_{\mathcal{R}}$ at early times. Recall that, in the scenario we are considering, $\beta(k)$ is determined by the lognormal function $g(k)$ [*cf.* Eqs. (4.8) and (4.9)] that describes the feature in the scalar power spectrum. Since $g(k)$ is a Gaussian with the strength γ at its maximum [*cf.* Eq. (4.8)], we have $g(k) \lesssim \gamma$ for all k. We have always worked with values such that $\gamma \lesssim \mathcal{O}(1)$. Therefore, we can approximate the expression for $\beta(k)$ that is to be used in the integral describing $\rho_{\mathcal{R}}^{(1)}$ [*cf.* Eq. (4.14)] as $\beta(k) \simeq -g(k)/2$. This simplifies the evaluation of $\rho_{\mathcal{R}}^{(1)}$, and we obtain the energy density of the perturbations in terms of the parameters γ, k_{f} and Δ_k to be

$$\rho_{\mathcal{R}} \simeq \rho_{\mathcal{R}}^{(1)} \simeq \frac{\gamma^2\, \mathrm{e}^{4\,\Delta_k^2}}{16\,\pi^{5/2}\,\Delta_k} \left(\frac{k_{\mathrm{f}}}{a}\right)^4. \tag{4.16}$$

We should stress again that we have subtracted the contribution due to the Bunch-Davies vacuum in arriving at this expression. Due to this reason, we should also add that no regularization is required to arrive at the above result. Hence, $\rho_{\mathcal{R}} \to 0$ when $\gamma \to 0$, as expected. We find that the relative difference between the above approximate estimate of $\rho_{\mathcal{R}}^{(1)}$ [obtained by assuming that $\beta(k) \simeq -g(k)/2$] and the exact estimate is at most of $\mathcal{O}(1)$. Therefore, for convenience, we shall use the approximate estimate to arrive at the bound on the parameter γ in our scenario.

For the backreaction to be negligible in our scenario, we require that $\rho_{\mathcal{R}} \ll \rho_{\mathrm{I}}$, where, as we mentioned, $\rho_{\mathrm{I}} = 3\,H_{\mathrm{I}}^2\,M_{\mathrm{Pl}}^2$ is the energy density of the background during inflation. This requirement leads to the condition

$$\frac{\gamma^2\, \mathrm{e}^{4\,\Delta_k^2}}{\Delta_k} \left(\frac{k_{\mathrm{f}}}{a\,H_{\mathrm{I}}}\right)^4 \ll 48\,\pi^{5/2} \left(\frac{M_{\mathrm{Pl}}}{H_{\mathrm{I}}}\right)^2. \tag{4.17}$$

During inflation, the value of the Hubble parameter H_{I} is related to the tensor-to-scalar ratio r through the relation $(H_{\mathrm{I}}/M_{\mathrm{Pl}})^2 \simeq r\,A_{\mathrm{S}}$, where $A_{\mathrm{S}} \simeq 2.11 \times 10^{-9}$ is the COBE normalized scalar amplitude over the CMB scales (in this context, see Subsec. 1.2.1). Since the energy density $\rho_{\mathcal{R}}$ is the largest at early times, let us evaluate it at the time when the smallest wave number of interest, say, k_{min}, leaves the Hubble radius, *i.e.* when $k_{\mathrm{min}} = a_{\mathrm{min}}\,H_{\mathrm{I}}$. At such a time, as we have set $\Delta_k = 1$, the above inequality reduces to (upon ignoring the constant coefficients)

$$\gamma \ll \frac{10^{9/2}}{\sqrt{r}} \left(\frac{k_{\mathrm{min}}}{k_{\mathrm{f}}}\right)^2. \tag{4.18}$$

It seems reasonable to set $k_{\mathrm{min}} = k_1/10 \simeq 10^{-5}\,\mathrm{Mpc}^{-1}$ (recall that we had earlier chosen $k_1 = 10^{-4}\,\mathrm{Mpc}^{-1}$). If we choose $k_{\mathrm{f}} = 10^5\,\mathrm{Mpc}^{-1}$, which is the smallest of the values for k_{f} that we had considered, then we arrive at $\gamma \ll 10^{-16.5}/\sqrt{r}$. In other words, for $r \simeq 10^{-3}$, we require $\gamma < 10^{-15}$. For a larger k_{f}, clearly, the limits on γ are even stronger. If $k_{\mathrm{f}} \simeq 10^{13}\,\mathrm{Mpc}^{-1}$ and $r \simeq 10^{-3}$, we require that $\gamma < 10^{-30}$. Evidently, γ can be larger if the tensor-to-scalar ratio is smaller, *i.e.* when the scale of inflation is lower. Nevertheless, even for an extreme value of $r \simeq 10^{-30}$ as suggested by the recent arguments based on the trans-Planckian censorship conjecture (in this context, see, for instance, Ref. [294]), we require $\gamma < 10^{-2}$ for $k_{\mathrm{f}} \simeq 10^5\,\mathrm{Mpc}^{-1}$ and $\gamma < 10^{-17}$ for $k_{\mathrm{f}} \simeq 10^{13}\,\mathrm{Mpc}^{-1}$. We have instead worked with $\gamma \simeq 1$ for $k_{\mathrm{f}} = 10^5\,\mathrm{Mpc}^{-1}$ and $\gamma \simeq 10^{-8}$ for $k_{\mathrm{f}} = 10^{13}\,\mathrm{Mpc}^{-1}$. Clearly, for a more reasonable r, the constraints on γ are considerably more severe. Under such conditions, $f_{_{\mathrm{NL}}}$ and hence the non-Gaussian modifications will prove to be small and we will not be able to achieve the desired level of amplification of the corrected power spectrum $\mathcal{P}_{_{\mathrm{S}}}(k) + \mathcal{P}_{_{\mathrm{C}}}(k)$. In fact, γ is so tightly constrained by the backreaction that we are essentially left with the slow roll results.

There are two related points we wish to make here. Firstly, one may wonder if the energy associated with the curvature perturbation $\rho_{_{\mathcal{R}}}$ itself may support accelerated expansion. Since $\rho_{_{\mathcal{R}}}^{(1)} \propto a^{-4}$, conservation of energy suggests that, at early times, the pressure associated with the excited states should be given by $p_{_{\mathcal{R}}}^{(1)} = \rho_{_{\mathcal{R}}}^{(1)}/3$. Upon explicit calculation, we find that this is indeed the case (in this context, also see Refs. [271, 272]). In other words, the pressure associated with the excited initial states does not possess the equation of state required to drive inflation. Secondly, since the energy density of the perturbations $\rho_{_{\mathcal{R}}}^{(1)}$ dies down as a^{-4}, one may imagine that it could decay rapidly enough permitting the background energy density to dominate. Given $\rho_{_{\mathcal{R}}}$ at $a = a_{\mathrm{min}}$, we find that the number of e-folds after which the energy density associated with the perturbations becomes sub-dominant to $\rho_{_{\mathrm{I}}}$ is given by

$$N \simeq \frac{1}{4} \ln\left(\frac{\gamma^2\, r}{10^9}\right) + \ln\left(\frac{k_{\mathrm{f}}}{k_{\mathrm{min}}}\right). \tag{4.19}$$

For the values of the various quantities we have worked with, say, $\gamma \simeq 1$, $k_{\mathrm{f}} = 10^5\,\mathrm{Mpc}^{-1}$ and $k_{\mathrm{min}} = 10^{-5}\,\mathrm{Mpc}^{-1}$, if we choose a tensor-to-scalar ratio of $r \simeq 10^{-3}$, we find that it will take as many as 16 e-folds before the background energy density begins to dominate. This duration will be more prolonged for larger values of k_{f}. Clearly, backreaction is a rather serious issue that needs to be accounted for.

4.5 DISCUSSION

In this chapter, we had explored a possible mechanism for the production of PBHs and GWs wherein the primordial scalar perturbations were evolved from squeezed initial states. The advantage of the mechanism is the fact that it is completely independent of the actual model that drives the background dynamics during inflation. All we require is typical slow roll inflation which leads to a power spectrum that is consistent with the recent CMB data on large scales. By choosing specific forms for the Bogoliubov coefficients that characterize the squeezed states, we had constructed scalar power spectra with a lognormal feature at small scales. It is well known that, in such cases, the scalar bispectra in the squeezed limit is inversely proportional to the value of the squeezed mode, a dependence which we expected to utilize so that we obtain significantly high values for the scalar non-Gaussianity parameter $f_{_{\rm NL}}$ at large wave numbers. We had hoped that this property can lead to large non-Gaussian modifications to the scalar power spectrum, which in turn can amplify the power considerably at small scales. While the proposal seemed feasible, there were two challenges that we had encountered. Mathematically, it was rather easy to construct squeezed initial states that led to a sharp rise in power on small scales, when the non-Gaussian modifications were taken into account. However, we had found that it can be a challenge to design scenarios that excite the curvature perturbation to such an initial state during the early stages of inflation. Moreover, we had found that the backreaction on the inflationary background due to the excited state of the perturbations strongly limits the extent of deviation from the Bunch-Davies vacuum. In fact, the bounds due to the backreaction are so strong that the slow roll results remain valid.

Let us make a few further clarifying remarks at this stage of our discussion. The consistency condition relating the bispectrum and the power spectrum is known to be violated for modes that evolve from the non-vacuum initial states (*i.e.* around the peaks in the original power spectra). As a result, we had expected that the contributions to the non-Gaussianity parameter due to the so-called local observer effect that has to be subtracted will be small when compared to the actual value $f_{_{\rm NL}}$ over these wave numbers (in this context, see Refs. [234, 235]). Motivated by the largely local form of the scalar bispectrum in the squeezed limit, we had utilized the corresponding $f_{_{\rm NL}}$ to calculate the non-Gaussian modifications to the power spectrum [18, 181, 189, 190]. We had hoped that the non-Gaussian modifications will dominate leading to enhanced power at small scales. However, we had found that the issue of backreaction put paid to the proposal.

Before we conclude, we would like to comment on four issues and their possible resolutions in the approach of generating PBHs and GWs from squeezed initial states.

1. Note that we have arrived at the scalar bispectrum by calculating the integrals involved over the domain $-\infty < \eta < 0$. In other words, we have assumed that the initial squeezed state was chosen in the infinite past, *i.e.* as $\eta \to -\infty$. It may be argued that if we choose to work with non-vacuum initial states, then the initial conditions need to be imposed at a finite initial time, say, $\eta_{\rm i}$. We believe that our results and conclusions will hold as long as $\eta_{\rm i} \ll -1/k_{\rm min}$, where, recall that, we have set $k_{\rm min} \simeq k_1/10$, with k_1 being the smallest wave number of observational interest, which we have assumed to be $10^{-4}\,{\rm Mpc}^{-1}$.

2. The method by which we have calculated modifications to the power spectrum due to the scalar non-Gaussianity parameter is strictly valid for an $f_{\rm NL}$ of the local type. In other words, $f_{\rm NL}$ ought to be a constant independent of scale. However, in our scenario, the $f_{\rm NL}$ we obtain is strongly scale dependent. There are two points that we believe support the method we have adopted. Firstly, in order to mimic the local behavior of $f_{\rm NL}$, we have chosen to work with its value in the squeezed limit (in this context, also see Ref. [181]). Secondly, and interestingly, we find that, near the wave numbers corresponding to the peaks of the power spectra, the non-Gaussianity parameter $f_{\rm NL}$ seems to have a strongly local shape. We should add here that a formal approach to arrive at the modifications to the power spectrum would be to calculate the loop corrections at the appropriate order. While such an effort seems worthwhile, we believe that, since the parameter $f_{\rm NL}$ is largely local around the maximum in the power spectrum, our calculations can be considered to be fairly suggestive (for further discussions in this context, see the following chapter).

3. In our approach, we have accounted for the cubic order non-Gaussianities by considering the corresponding modifications to the scalar power spectrum [189, 190, 276]. We should caution that this approach may not be adequate to account for the non-Gaussian modifications to the density parameter $\Omega_{\rm GW}$ describing the stochastic GW background (see Ref. [295] and also the discussions in the next chapter). Moreover, when calculating the density of PBHs formed, the non-Gaussianities are expected to also modify the probability distribution of the density contrast and hence the number of PBHs at the time of their formation [*cf.* Eq. (1.35)]. We should point out that this effect needs to be accounted for separately [80, 232].

4. Lastly, it may be interesting to explore if the contributions due to the higher order correlations such as the trispectrum may rescue our proposal and lead to large non-Gaussian modifications despite the strong constraints on γ due to the backreaction [192, 296]. For instance, we had seen that, in the squeezed limit, $f_{\rm NL}$ had behaved as $k_{\rm f}/k_1$. If the non-Gaussianity parameter, say, $\tau_{\rm NL}$, characterizing the trispectrum (in this context, see Ref. [297]) in a squeezed initial state behaves in a stronger fashion, it seems possible that the higher order terms may modify the power spectrum adequately to circumvent the limits on γ. However, even if this works out, one concern would remain. We had seen that, despite the large value of $f_{\rm NL}$, the amplitude of the modified power spectrum was of the order of 10^{-2} (for the original values of γ we had worked with). If the non-Gaussian modifications due to the trispectrum prove to be significant, it is possible that these higher order

contributions will also affect the validity of perturbation theory. One will have to ensure that the amplitude of the corrected power spectrum remains smaller than unity even when further contributions are taken into account. Probably, the conditions for the validity of the perturbation theory at higher orders would severely restrict the extent of deviations from the Bunch-Davies vacuum. We are currently exploring these issues.

We would like to close by pointing out that, the various arguments we have considered in this chapter suggest that the initial state of the curvature perturbations is likely to be remarkably close to the Bunch-Davies vacuum, in particular, on small scales.

CHAPTER 5
ACCOUNTING FOR SCALAR NON-GAUSSIANITY IN SECONDARY GWs

5.1 INTRODUCTION

Models of inflation leading to enhanced scalar power over small scales have recently been examined in the context of production of PBHs and the associated generation of secondary GWs. As we have discussed before, in these models, modes of scalar perturbations that have amplitudes large enough to form PBHs, also enhance the tensor perturbations by sourcing them at the second order. This leads to generation of secondary GWs of detectable strengths in the present universe (see, for instance, Refs. [13, 14, 88, 89, 94, 276] for discussions and constraints). Typical inflationary models considered in this context that are driven by a canonical scalar field, permit a brief epoch of ultra slow roll amidst an otherwise slow roll evolution of the inflaton field (see, for instance, Refs. [18, 71, 72, 160, 161] and our discussion in Chap. 3). This epoch is known to enhance the amplitude of curvature perturbations and lead to large amplitudes of scalar power over small scales. The production of PBHs is exponentially sensitive to the amplitude of scalar power and hence highly dependent on the behavior of the spectrum around the small range of wave numbers close to the peak. However, the spectrum of secondary GWs is proportional to the square of the scalar power spectrum sourcing it. Therefore, it can be expected to capture better any feature that may be present in the scalar power spectrum over a wider range of wave numbers.

Besides, there have been efforts to quantify the effect of the primordial scalar non-Gaussianity on the predicted signals of secondary GWs [19, 189, 190, 238, 295, 298]. The general approach is to account for corrections in the power spectrum arising due to the scalar bispectrum through the non-Gaussianity parameter $f_{\rm NL}$. There are usually well-motivated assumptions made about the shape of $f_{\rm NL}$ being local in such calculations. However, in realistic models of inflation, we find that, though $f_{\rm NL}$ is local close to the peak of the scalar power spectrum, it is highly scale dependent over a wide range of wave numbers. Moreover, it has been shown that the consistency condition relating the power spectrum and the bispectrum in the squeezed limit is satisfied in canonical, single field models considered in these scenarios [18, 299]. Therefore, it is important to take into account the complete form of the bispectrum in calculating the correction to the power spectrum and examining the imprints of scalar non-Gaussianity on the secondary GWs.

In this chapter, we present a method to account for a general, scale-dependent $f_{\rm NL}$ in such a calculation, by reconsidering the definition of the parameter. This method does not assume any shape or template for $f_{\rm NL}$ or the scalar bispectrum. Nevertheless it is consistent with the previous approaches when the assumptions are invoked, *i.e.* it reduces to earlier methods adopted if the $f_{\rm NL}$ is assumed to be of a certain shape, say, a local form. This allows us to capture the complete behavior of the bispectrum along with any non-trivial features that may be present therein and examine its imprints on the spectrum of GWs generated. We illustrate this method of accounting for scalar bispectrum using two models as examples. One is a toy model of inflation constructed by adding an artificial dip to a potential that otherwise admits slow roll inflation [237, 251]. The second is a model of inflation known as critical-Higgs inflation which is motivated by Higgs field driving inflation while containing an inflection point in the potential [300–302]. Both these models serve as interesting examples for a typical scenario of inflation where the field undergoes an interim epoch of ultra slow roll during its evolution. We calculate the scalar bispectrum in these models and compute the corresponding correction to the power spectrum. We further compute the non-Gaussian contributions to the dimensionless spectral energy density of secondary GWs, *i.e.* $\Omega_{\rm GW}$, generated in these models.

The structure of this chapter is as follows. In the next section, we shall present the extended definition of the non-Gaussianity parameter $f_{\rm NL}$ to include a generic scale dependence. In Sec. 5.3, we shall then arrive at the expression for the correction to the scalar power spectrum due to the bispectrum, *viz.* $\mathcal{P}_{\rm C}(k)$. In Sec. 5.4, we shall compute the non-Gaussian contributions to the $\Omega_{\rm GW}$ arising due to $f_{\rm NL}$. We shall point out that some of these contributions can be expressed in terms of $\mathcal{P}_{\rm C}(k)$. In Sec. 5.5, we shall present the models for illustration and compute the power and bi-spectra arising from them. We shall calculate the corrections to the power spectra using the respective bispectra and compare against the original spectra. Moreover, we shall obtain an analytical estimate of the correction and compare it against the exact numerical result. We shall finally evaluate the $\Omega_{\rm GW}$ generated from these models due to both Gaussian and non-Gaussian contributions and compare the amplitudes in each case. We shall conclude in Sec. 5.6 with a brief summary and outlook.

5.2 SCALE DEPENDENT $f_{\rm NL}(k_1, k_2, k_3)$ AND ITS RELATION TO THE BISPECTRUM

In this section, we shall reconsider the conventional definition of the scalar non-Gaussianity parameter $f_{\rm NL}$ and extend it to account for a generic scale dependence. Recall that the parameter $f_{\rm NL}$ is conventionally defined using the relation (3.22) we had introduced earlier [52, 60]. Evidently, this definition assumes $f_{\rm NL}$ to be local, *i.e.* independent of wave numbers. Nevertheless, this is often taken as the definition to calculate the bispectrum even in cases with non-trivial scale dependence. We shall extend this definition to explicitly account for the scale dependence in the parameter. Towards this end, we consider the relation (3.22) in Fourier space and redefine $f_{\rm NL}$ as a function in Fourier space with wave numbers as its arguments (for similar efforts in different contexts, see Refs. [303, 304]). We can write such a relation as

$$\mathcal{R}_{\boldsymbol{k}}(\eta) = \mathcal{R}^{\rm G}_{\boldsymbol{k}}(\eta) - \frac{3}{5}\int \frac{{\rm d}^3\boldsymbol{k}_1}{(2\,\pi)^{3/2}} \mathcal{R}^{\rm G}_{\boldsymbol{k}_1}(\eta)\, \mathcal{R}^{\rm G}_{\boldsymbol{k}-\boldsymbol{k}_1}(\eta)\, f_{\rm NL}[\boldsymbol{k}, (\boldsymbol{k}_1-\boldsymbol{k}), -\boldsymbol{k}_1], \tag{5.1}$$

where $\mathcal{R}_{\boldsymbol{k}}$ is the mode function corresponding to the curvature perturbation $\mathcal{R}$, and $\mathcal{R}^{\rm G}_{\boldsymbol{k}}$ denotes the Gaussian part of $\mathcal{R}_{\boldsymbol{k}}$. We should mention that the $f_{\rm NL}(\boldsymbol{k}_1, \boldsymbol{k}_2, \boldsymbol{k}_3)$ defined depends only on the magnitude of the three wave vectors in the argument. We have written the arguments in the integrand above as vectors to emphasize that by construction they form a triangular configuration in the space of wave vectors (*i.e.* sum of the three vectors vanishes identically), as is expected of the arguments of the bispectrum. We can also obtain the counterpart of this parameter in real space by considering the inverse Fourier transform of the above relation, *viz.*

$$\begin{aligned}\mathcal{R}(\eta, \boldsymbol{x}) &= \mathcal{R}^{\rm G}(\eta, \boldsymbol{x}) - \frac{3}{5}\int \frac{{\rm d}^3\boldsymbol{k}}{(2\pi)^3}\int {\rm d}^3\boldsymbol{k}_1 \mathcal{R}^{\rm G}_{\boldsymbol{k}_1}(\eta)\, \mathcal{R}^{\rm G}_{\boldsymbol{k}-\boldsymbol{k}_1}(\eta)\\ &\quad\times f_{\rm NL}[\boldsymbol{k}, (\boldsymbol{k}_1-\boldsymbol{k}), -\boldsymbol{k}_1]\, {\rm e}^{i\,\boldsymbol{k}\cdot\boldsymbol{x}}.\end{aligned} \tag{5.2}$$

We should mention that this equation reduces to the conventional definition of $f_{\rm NL}$, as given in Eq. (3.23), when $f_{\rm NL}(\boldsymbol{k}_1, \boldsymbol{k}_2, \boldsymbol{k}_3)$ turns out to be scale independent in a given model. Hence, our generalization is consistent with the existing approach to quantify the scalar non-Gaussianity.

Let us now proceed to establish the relation between the $f_{\rm NL}(\boldsymbol{k}_1, \boldsymbol{k}_2, \boldsymbol{k}_3)$ given above and the scalar bispectrum $G(\boldsymbol{k}_1, \boldsymbol{k}_2, \boldsymbol{k}_3)$. Recall that the scalar power spectrum $\mathcal{P}_{\rm S}(k)$ and the bispectrum $G(\boldsymbol{k}_1, \boldsymbol{k}_2, \boldsymbol{k}_3)$ are defined through the expressions (1.12a), (1.18) and (1.19). To express $f_{\rm NL}(\boldsymbol{k}_1, \boldsymbol{k}_2, \boldsymbol{k}_3)$ in terms of $G(\boldsymbol{k}_1, \boldsymbol{k}_2, \boldsymbol{k}_3)$ and $\mathcal{P}_{\rm S}(k)$, we compute the expectation value of the three point correlation of $\hat{\mathcal{R}}_k$. Using the relation given in Eq. (5.1), we obtain that

$$\begin{aligned}\langle \hat{\mathcal{R}}_{\boldsymbol{k}_1}\, \hat{\mathcal{R}}_{\boldsymbol{k}_2}\, \hat{\mathcal{R}}_{\boldsymbol{k}_3}\rangle &= -\frac{3}{5}\int \frac{{\rm d}^3\boldsymbol{k}_1'}{(2\,\pi)^{3/2}} \langle \hat{\mathcal{R}}^{\rm G}_{\boldsymbol{k}_1}\, \hat{\mathcal{R}}^{\rm G}_{\boldsymbol{k}_2}\, \hat{\mathcal{R}}^{\rm G}_{\boldsymbol{k}_3'}\, \hat{\mathcal{R}}^{\rm G}_{\boldsymbol{k}_3-\boldsymbol{k}_3'}\rangle\\ &\quad\times f_{\rm NL}[\boldsymbol{k}_3, (\boldsymbol{k}_3'-\boldsymbol{k}_3), -\boldsymbol{k}_3'] + \text{two permutations}.\end{aligned} \tag{5.3}$$

We should mention that the expectation values are evaluated in a specific initial state, which is assumed to be the Bunch-Davies vacuum. Also, note that the term in the right hand side of the above expression is the leading order term in the expansion assuming $\mathcal{R}^{\mathrm{G}}$ is perturbative. Using Wick's theorem, we can express the four point function in the above integral in terms of the power spectrum $\mathcal{P}_{\mathrm{S}}(k)$ and simplify it to obtain

$$\begin{aligned}\langle\hat{\mathcal{R}}_{\boldsymbol{k}_1}\hat{\mathcal{R}}_{\boldsymbol{k}_2}\hat{\mathcal{R}}_{\boldsymbol{k}_3}\rangle &= -\frac{3}{5}\frac{4\pi^4}{(2\pi)^{3/2}}\frac{\mathcal{P}_{\mathrm{S}}(k_1)}{k_1^3}\frac{\mathcal{P}_{\mathrm{S}}(k_2)}{k_2^3}\,\delta^{(3)}(\boldsymbol{k}_1+\boldsymbol{k}_2+\boldsymbol{k}_3)\\ &\quad\times\Big[f_{\mathrm{NL}}(\boldsymbol{k}_3,\boldsymbol{k}_2,\boldsymbol{k}_1)+f_{\mathrm{NL}}(\boldsymbol{k}_3,\boldsymbol{k}_1,\boldsymbol{k}_2)\Big]\ +\ \text{two permutations.}\end{aligned}\tag{5.4}$$

We again emphasize that the arguments of f_{NL} above satisfy the triangularity condition $(\boldsymbol{k}_1+\boldsymbol{k}_2+\boldsymbol{k}_3)=\boldsymbol{0}$. We then use the property of the bispectrum being symmetric in its arguments [*i.e.* $G(\boldsymbol{k}_1,\boldsymbol{k}_2,\boldsymbol{k}_3)=G(\boldsymbol{k}_1,\boldsymbol{k}_3,\boldsymbol{k}_2)$] to relate the $f_{\mathrm{NL}}(\boldsymbol{k}_1,\boldsymbol{k}_2,\boldsymbol{k}_3)$ constructed to the power and bi-spectra. Upon doing so, we obtain the relation

$$\begin{aligned}f_{\mathrm{NL}}(\boldsymbol{k}_1,\boldsymbol{k}_2,\boldsymbol{k}_3) &= -\frac{10}{3}\frac{(k_1\,k_2\,k_3)^3}{16\,\pi^4}\,G(\boldsymbol{k}_1,\boldsymbol{k}_2,\boldsymbol{k}_3)\\ &\quad\times\left[k_1^3\,\mathcal{P}_{\mathrm{S}}(k_2)\,\mathcal{P}_{\mathrm{S}}(k_3)+\text{two permutations}\right]^{-1}.\end{aligned}\tag{5.5}$$

This turns out to be the conventional relation used in the literature [*cf.* Eq. (3.22)] to express f_{NL} in terms $G(\boldsymbol{k}_1,\boldsymbol{k}_2,\boldsymbol{k}_3)$ and $\mathcal{P}_{\mathrm{S}}(k)$ [17, 56, 60, 132]. Thus, we infer that the $f_{\mathrm{NL}}(\boldsymbol{k}_1,\boldsymbol{k}_2,\boldsymbol{k}_3)$ defined in Eq. (5.1) is compatible with the conventional relation. The difference in this derivation is that we have explicitly accounted for the scale dependence of the bispectrum in the non-Gaussianity parameter $f_{\mathrm{NL}}(\boldsymbol{k}_1,\boldsymbol{k}_2,\boldsymbol{k}_3)$.

5.3 CORRECTION TO THE POWER SPECTRUM

Earlier, in Subsec. 1.1.3, we had outlined the numerical procedure to calculate the scalar bispectrum in a given model of inflation. Using the method, we shall evaluate the scalar bispectrum numerically and evaluate the corresponding non-Gaussianity parameter $f_{\mathrm{NL}}(\boldsymbol{k}_1,\boldsymbol{k}_2,\boldsymbol{k}_3)$ through the relation given in Eq. (5.5).

Having setup a method to account for a generic scale dependence in the non-Gaussianity parameter $f_{\mathrm{NL}}(\boldsymbol{k}_1,\boldsymbol{k}_2,\boldsymbol{k}_3)$, we shall now proceed to compute the non-Gaussian correction to the $\mathcal{P}_{\mathrm{S}}(k)$ arising due to the bispectrum. To compute the correction, which we shall call as $\mathcal{P}_{\mathrm{C}}(k)$, we calculate the two-point correlation of $\hat{\mathcal{R}}_k$ using the relation given in Eq. (5.1). We obtain the two-point correlation of $\hat{\mathcal{R}}_k$ to be

$$\langle\hat{\mathcal{R}}_{\boldsymbol{k}_1}\,\hat{\mathcal{R}}_{\boldsymbol{k}_2}\rangle = \langle\hat{\mathcal{R}}^{\mathrm{G}}_{\boldsymbol{k}_1}\,\hat{\mathcal{R}}^{\mathrm{G}}_{\boldsymbol{k}_2}\rangle+\frac{9}{25}\int\frac{\mathrm{d}^3\boldsymbol{k}_1'}{(2\,\pi)^3}\int\mathrm{d}^3\boldsymbol{k}_2'\,\langle\hat{\mathcal{R}}^{\mathrm{G}}_{\boldsymbol{k}_1'}\,\hat{\mathcal{R}}^{\mathrm{G}}_{\boldsymbol{k}_1-\boldsymbol{k}_1'}\,\hat{\mathcal{R}}^{\mathrm{G}}_{\boldsymbol{k}_2'}\,\hat{\mathcal{R}}^{\mathrm{G}}_{\boldsymbol{k}_2-\boldsymbol{k}_2'}\rangle$$

$$\times f_{_{\rm NL}}\left(\boldsymbol{k}_1,\boldsymbol{k}_1'-\boldsymbol{k}_1,\boldsymbol{k}_1'\right) f_{_{\rm NL}}\left(\boldsymbol{k}_2,\boldsymbol{k}_2'-\boldsymbol{k}_2,\boldsymbol{k}_2'\right). \tag{5.6}$$

On substituting the definition of scalar power spectrum [*cf.* Eq. (1.12a)] and expressing the four-point correlation in terms of the two-point correlations as before, the above equation leads to

$$\mathcal{P}_{_{\rm S}}^{_{\rm M}}(k) = \mathcal{P}_{_{\rm S}}(k) + \frac{9}{50\,\pi}\,k^3 \int {\rm d}^3\boldsymbol{k}_1\, \frac{\mathcal{P}_{_{\rm S}}(k_1)}{k_1^3}\, \frac{\mathcal{P}_{_{\rm S}}(\vert\boldsymbol{k}-\boldsymbol{k}_1\vert)}{\vert\boldsymbol{k}-\boldsymbol{k}_1\vert^3}\, f_{_{\rm NL}}^2(\boldsymbol{k},\boldsymbol{k}_1-\boldsymbol{k},\boldsymbol{k}_1), \tag{5.7}$$

where $\mathcal{P}_{_{\rm S}}(k)$ denotes the original power spectrum corresponding to the Gaussian perturbations $\mathcal{R}^{\rm G}$. Therefore, we can identify the correction $\mathcal{P}_{_{\rm C}}(k)$, that is to be added to the original spectrum $\mathcal{P}_{_{\rm S}}(k)$, as

$$\mathcal{P}_{_{\rm C}}(k) = \frac{9}{50\,\pi}\,k^3 \int {\rm d}^3\boldsymbol{k}_1\, \frac{\mathcal{P}_{_{\rm S}}(k_1)}{k_1^3}\, \frac{\mathcal{P}_{_{\rm S}}(\vert\boldsymbol{k}-\boldsymbol{k}_1\vert)}{\vert\boldsymbol{k}-\boldsymbol{k}_1\vert^3}\, f_{_{\rm NL}}^2(\boldsymbol{k},\boldsymbol{k}_1-\boldsymbol{k},\boldsymbol{k}_1). \tag{5.8}$$

We should note here that there can be additional terms to this correction which involve the irreducible part of the four point correlation, *viz.* the trispectrum of scalar perturbations [190, 238, 295]. Such terms shall receive contributions from higher order terms of the action and hence will be at higher order in perturbations than the terms we are working with. We believe those terms are beyond the scope of this work. In our analysis, we shall restrict ourselves to the terms of four-point correlations reduced in terms of the power spectra.

To simplify the above expression for $\mathcal{P}_{_{\rm C}}(k)$ we perform a suitable change of variables. Defining a variable $\boldsymbol{u} = \boldsymbol{k} - \boldsymbol{k}_1$, we get

$$\mathcal{P}_{_{\rm C}}(k) = \frac{9}{25}\,k^2 \int_0^\infty \frac{{\rm d}k_1}{k_1^2}\, \mathcal{P}_{_{\rm S}}(k_1) \int_{\vert\boldsymbol{k}-\boldsymbol{k}_1\vert}^{\vert\boldsymbol{k}+\boldsymbol{k}_1\vert} \frac{{\rm d}u}{u^2}\, \mathcal{P}_{_{\rm S}}(u)\, f_{_{\rm NL}}^2(\boldsymbol{k},\boldsymbol{u},\boldsymbol{k}_1). \tag{5.9}$$

Further, upon introducing the variables $x = k_1/k$ and $y = u/k$, we obtain that

$$\mathcal{P}_{_{\rm C}}(k) = \frac{9}{25} \int_0^\infty {\rm d}x \int_{\vert 1-x\vert}^{\vert 1+x\vert} {\rm d}y\, \frac{\mathcal{P}_{_{\rm S}}(kx)}{x^2}\, \frac{\mathcal{P}_{_{\rm S}}(ky)}{y^2}\, f_{_{\rm NL}}^2(\boldsymbol{k},x\,\boldsymbol{k},y\,\boldsymbol{k}). \tag{5.10}$$

Again, we can notice that if $f_{_{\rm NL}}(\boldsymbol{k}_1,\boldsymbol{k}_2,\boldsymbol{k}_3)$ turns out to be scale independent we recover the expression for $\mathcal{P}_{_{\rm C}}(k)$ that is used in case of a local $f_{_{\rm NL}}$ [see Refs. [19, 189, 190, 238]; also see Eq. (3.25)]. If we use the relation between $f_{_{\rm NL}}(\boldsymbol{k}_1,\boldsymbol{k}_2,\boldsymbol{k}_3)$ and the power and bi-spectra [*cf.* Eq. (5.5)], we can write down $\mathcal{P}_{_{\rm C}}(k)$ explicitly in terms of $G(\boldsymbol{k}_1,\boldsymbol{k}_2,\boldsymbol{k}_3)$

and $\mathcal{P}_{\mathrm{S}}(k)$ as follows:

$$\mathcal{P}_{\mathrm{C}}(k) = \frac{4}{(2\,\pi)^8}\,k^{12}\int_0^\infty \mathrm{d}x \int_{|1-x|}^{1+x}\mathrm{d}y\,\frac{x^4\,y^4}{\mathcal{P}_{\mathrm{S}}(kx)\,\mathcal{P}_{\mathrm{S}}(ky)}\,G^2(\boldsymbol{k}, x\,\boldsymbol{k}, y\,\boldsymbol{k}) \times \left[1 + x^3\,\frac{\mathcal{P}_{\mathrm{S}}(k)}{\mathcal{P}_{\mathrm{S}}(k\,x)} + y^3\,\frac{\mathcal{P}_{\mathrm{S}}(k)}{\mathcal{P}_{\mathrm{S}}(ky)}\right]^{-2}. \tag{5.11}$$

We should point out that, because of the well regulated nature of the integral involved, we shall use Eq. (5.10) as the working definition for computing $\mathcal{P}_{\mathrm{C}}(k)$.

5.4 COMPUTATION OF Ω_{GW} ACCOUNTING FOR f_{NL}

Having obtained the corrections to the power spectra, $\mathcal{P}_{\mathrm{C}}(k)$, we shall proceed to compute the corresponding Ω_{GW} for these models. During the computation of Ω_{GW} there may arise contributions from f_{NL} other than from $\mathcal{P}_{\mathrm{C}}(k)$. These are referred to as connected contributions in the literature [189, 190, 295]. We should note that there are arguments in the literature suggesting that these contributions vanish identically when integrated over azimuthal angles involved in the corresponding integrals [189, 238]. However, detailed calculations suggest that this may not be the case when accounted for exact dependence of the integrand over these angles appropriately [295]. In this work, we shall compute all the terms involved while consistently accounting for a scale dependent f_{NL} in them. We shall later compare the respective contributions against the contribution from the original power spectrum to the complete estimate of Ω_{GW}, when we consider specific models for illustration.

To begin with, let us recall the calculation of the secondary tensor power spectrum in terms of the scalar power spectrum (for some of the earlier discussions, see Refs. [88, 89]; for some of the recent efforts, see, Refs. [18, 94–96, 166, 276, 305]). The two-point correlation of the secondary tensor perturbation $h_{\boldsymbol{k}}^{\lambda}$ is related to the scalar perturbation $\mathcal{R}_{\boldsymbol{k}}$ as

$$\begin{aligned}\langle \hat{h}_{\boldsymbol{k}_1}^{\lambda}\,\hat{h}_{\boldsymbol{k}_2}^{\lambda'}\rangle = {} & \frac{16}{81}\frac{1}{k_1 k_2 \eta^2}\int \frac{\mathrm{d}^3\boldsymbol{p}}{(2\pi)^{3/2}}\int \frac{\mathrm{d}^3\boldsymbol{p}'}{(2\pi)^{3/2}}\,Q^{\lambda}(k_1,p)\,Q^{\lambda'}(k_2,p') \\ & \times \left[\mathcal{I}_c\left(\frac{p}{k_1}, \frac{|\boldsymbol{k}_1-\boldsymbol{p}|}{k_1}\right)\cos\left(k_1\,\eta\right) + \mathcal{I}_s\left(\frac{p}{k_1}, \frac{|\boldsymbol{k}_1-\boldsymbol{p}|}{k_1}\right)\sin\left(k_1\,\eta\right)\right] \\ & \times \left[\mathcal{I}_c\left(\frac{p'}{k_2}, \frac{|\boldsymbol{k}_2-\boldsymbol{p}'|}{k_2}\right)\cos\left(k_2\,\eta\right) + \mathcal{I}_s\left(\frac{p'}{k_2}, \frac{|\boldsymbol{k}_2-\boldsymbol{p}'|}{k_2}\right)\sin\left(k_2\,\eta\right)\right] \\ & \times \langle \hat{\mathcal{R}}_{\boldsymbol{p}}\,\hat{\mathcal{R}}_{\boldsymbol{k}_1-\boldsymbol{p}}\,\hat{\mathcal{R}}_{\boldsymbol{p}'}\,\hat{\mathcal{R}}_{\boldsymbol{k}_2-\boldsymbol{p}'}\rangle,\end{aligned} \tag{5.12}$$

where the functions $\mathcal{I}_{c,s}(u,v)$ arise due to the transfer function relating the Bardeen potential during the radiation dominated epoch to the primordial curvature perturbation [see Eqs. (1.51) in Subsec. 1.2.3]. The function $Q^\lambda(k,p)$ arises from the polarization tensor associated with the tensor modes [*cf.* App. C]. Upon using Wick's theorem, we can express the four-point correlation in the above integral in terms of the two-point correlations. This leads to the following expression for secondary tensor power spectrum in terms of the scalar power spectrum:

$$\begin{aligned}\mathcal{P}_h(k,\eta) &= 2\,\frac{16}{81}\,\frac{2\,\pi^2}{k^2\,\eta^2}\int\frac{\mathrm{d}^3\boldsymbol{k}'}{(2\,\pi)^3}\,Q^\lambda(k,k')\,Q_\lambda(k,k')\,\mathcal{I}^2(k,k')\\ &\quad\times\frac{k^3\,\mathcal{P}_{_\mathrm{S}}(k')\,\mathcal{P}_{_\mathrm{S}}(|\boldsymbol{k}-\boldsymbol{k}'|)}{k'^3\,|\boldsymbol{k}-\boldsymbol{k}'|^3},\end{aligned} \tag{5.13}$$

where the $\mathcal{P}_{_\mathrm{S}}(k)$ denotes the Gaussian part of the scalar power spectrum [*cf.* Subsec. 1.2.3]. We should note that the spectrum is averaged over the oscillations that occur on small time scales. Hence, the quantity $\mathcal{I}(k,k')$ can be expressed as

$$\mathcal{I}^2(k,k') = \left[\mathcal{I}_c^2\left(\frac{k'}{k},\frac{|\boldsymbol{k}-\boldsymbol{k}'|}{k}\right)+\mathcal{I}_s^2\left(\frac{k'}{k},\frac{|\boldsymbol{k}-\boldsymbol{k}'|}{k}\right)\right]. \tag{5.14}$$

Notice that the contraction of $Q(k,k')$ over λ implies summing over both polarizations. The quantity $Q^\lambda(k_1,k_2)$ is explicitly given by

$$Q^\lambda(k,k') = \begin{cases}\left(\frac{k'}{k}\right)^2\,\frac{\sin^2\theta}{\sqrt{2}}\,\cos{(2\phi)}, & \text{for } \lambda=+,\\ \left(\frac{k'}{k}\right)^2\,\frac{\sin^2\theta}{\sqrt{2}}\,\sin{(2\phi)}, & \text{for } \lambda=\times.\end{cases} \tag{5.15}$$

We find that the dimensionless spectral energy density of GWs associated with secondary tensor perturbations in the current universe, *viz.* $\Omega_{_\mathrm{GW}}(k)$, can be expressed as

$$h^2\,\Omega_{_\mathrm{GW}}(k) \simeq \frac{1.38\times10^{-5}}{24}\,(k^2\,\eta^2)\,\mathcal{P}_h(k,\eta). \tag{5.16}$$

Note that we had obtained this relation earlier [in Subsec. 1.2.3, *cf.* Eqs. (1.56) and (1.57)]. We shall use this expression to compute $\Omega_{_\mathrm{GW}}$ due to both Gaussian and non-Gaussian contributions to $\mathcal{P}_h(k)$.

As to the non-Gaussian contributions to $\mathcal{P}_h(k)$, let us first consider the contributions at the level of $f_{_\mathrm{NL}}^2$. These terms arise when we introduce $f_{_\mathrm{NL}}$, as defined in Eq. (5.1), in two of $\mathcal{R}_{\boldsymbol{k}}$ terms of the four-point correlation in Eq. (5.12). This gives rise to three types of contributions to $\mathcal{P}_h(k)$, which we shall refer to as $\mathcal{P}_h^{(2-1)}(k)$, $\mathcal{P}_h^{(2-2)}(k)$ and $\mathcal{P}_h^{(2-3)}(k)$. The exact expressions that describe these three contributions are given by

$$
\begin{aligned}
\mathcal{P}_h^{(2-1)}(k) &= 2^5\,\frac{16}{81}\,\frac{9}{25}\,\frac{(2\,\pi^2)^2}{(2\,\pi)^6}\,\frac{1}{k^2\,\eta^2} \\
&\quad\times \int \mathrm{d}^3\boldsymbol{q}_1 \int \mathrm{d}^3\boldsymbol{q}_2\, Q^\lambda(k,q_1)\, Q_\lambda(k,q_2)\, \mathcal{I}(k,q_1)\, \mathcal{I}(k,q_2) \\
&\quad\times k^3\, \frac{\mathcal{P}_{\mathrm{S}}(q_2)\, \mathcal{P}_{\mathrm{S}}(|\boldsymbol{q}_2+\boldsymbol{k}|)\, \mathcal{P}_{\mathrm{S}}(|\boldsymbol{q}_1-\boldsymbol{q}_2|)}{q_2^3\, |\boldsymbol{q}_2+\boldsymbol{k}|^3\, |\boldsymbol{q}_1-\boldsymbol{q}_2|^3} \\
&\quad\times f_{_{\mathrm{NL}}}(\boldsymbol{q}_1, \boldsymbol{q}_2, \boldsymbol{q}_1-\boldsymbol{q}_2)\, f_{_{\mathrm{NL}}}(\boldsymbol{k}-\boldsymbol{q}_1, \boldsymbol{q}_2-\boldsymbol{q}_1, \boldsymbol{k}+\boldsymbol{q}_2), \qquad (5.17\mathrm{a})
\end{aligned}
$$

$$
\begin{aligned}
\mathcal{P}_h^{(2-2)}(k) &= 2^5\,\frac{16}{81}\,\frac{9}{25}\,\frac{(2\,\pi^2)^2}{(2\,\pi)^6}\,\frac{1}{k^2\,\eta^2} \int \mathrm{d}^3\boldsymbol{q}_1 \int \mathrm{d}^3\boldsymbol{q}_2\, Q^\lambda(k,q_1)\, Q_\lambda(k,q_1)\, \mathcal{I}^2(k,q_1) \\
&\quad\times k^3\, \frac{\mathcal{P}_{\mathrm{S}}(|\boldsymbol{k}-\boldsymbol{q}_1|)\, \mathcal{P}_{\mathrm{S}}(q_2)\, \mathcal{P}_{\mathrm{S}}(|\boldsymbol{q}_1-\boldsymbol{q}_2|)}{q_2^3\, |\boldsymbol{k}-\boldsymbol{q}_1|^3\, |\boldsymbol{q}_1-\boldsymbol{q}_2|^3}\, f_{_{\mathrm{NL}}}^2(\boldsymbol{q}_1, \boldsymbol{q}_2, \boldsymbol{q}_1-\boldsymbol{q}_2) \\
&= 2^5\,\frac{16}{81}\,\frac{(2\,\pi^2)}{(2\,\pi)^3}\,\frac{1}{k^2\,\eta^2} \\
&\quad\times \int \mathrm{d}^3\boldsymbol{q}_1\, Q^\lambda(k,q_1)\, Q_\lambda(k,q_1)\, \mathcal{I}^2(k,q_1)\, k^3\, \frac{\mathcal{P}_{\mathrm{C}}(q_1)\, \mathcal{P}_{\mathrm{S}}(|\boldsymbol{k}-\boldsymbol{q}_1|)}{q_1^3\, |\boldsymbol{k}-\boldsymbol{q}_1|^3},
\end{aligned}
\qquad (5.17\mathrm{b})
$$

$$
\begin{aligned}
\mathcal{P}_h^{(2-3)}(k) &= 2^5\,\frac{16}{81}\,\frac{9}{25}\,\frac{(2\,\pi^2)^2}{(2\,\pi)^6}\,\frac{1}{k^2\,\eta^2} \\
&\quad\times \int \mathrm{d}^3\boldsymbol{q}_1 \int \mathrm{d}^3\boldsymbol{q}_2\, Q^\lambda(k,q_1)\, Q_\lambda(k,q_2)\, \mathcal{I}(k,q_1)\mathcal{I}(k,q_2) \\
&\quad\times k^3\, \frac{\mathcal{P}_{\mathrm{S}}(q_1)\, \mathcal{P}_{\mathrm{S}}(q_2)\, \mathcal{P}_{\mathrm{S}}(|\boldsymbol{k}-\boldsymbol{q}_1+\boldsymbol{q}_2|)}{q_1^3\, q_2^3\, |\boldsymbol{k}-\boldsymbol{q}_1+\boldsymbol{q}_2|^3} \\
&\quad\times f_{_{\mathrm{NL}}}(\boldsymbol{k}-\boldsymbol{q}_1, \boldsymbol{q}_2, \boldsymbol{k}-\boldsymbol{q}_1+\boldsymbol{q}_2)\, f_{_{\mathrm{NL}}}(\boldsymbol{k}+\boldsymbol{q}_2, \boldsymbol{q}_1, \boldsymbol{k}_1-\boldsymbol{q}_1+\boldsymbol{q}_2).
\end{aligned}
\qquad (5.17\mathrm{c})
$$

We have used the definition of $\mathcal{P}_{\mathrm{C}}(k)$ in $\mathcal{P}_h^{(2-2)}(k)$ to reduce the first expression and obtain Eq. (5.17b) [*cf.* Eq. (5.8)]. Such a simplification is not possible with $\mathcal{P}_h^{(2-1)}(k)$ or $\mathcal{P}_h^{(2-3)}(k)$. It is useful to note that one can construct Feynman diagrams to represent these integrals (see, for instance, Refs. [190, 295, 298]). If we identify the diagrams with the above integrals, we find that $\mathcal{P}_h^{(2-1)}(k)$ arises from what is called the C-type diagram, whereas $\mathcal{P}_h^{(2-3)}(k)$ arises from the Z-type diagram. The term $\mathcal{P}_h^{(2-2)}(k)$ arises from what is known as the hybrid diagram (see, App. H for the construction of these diagrams). The difference between the integrals presented here and the corresponding ones in the literature is the dependence of $f_{_{\mathrm{NL}}}$ over wave numbers. As mentioned earlier, it has been argued that the terms $\mathcal{P}_h^{(2-1)}(k)$ and $\mathcal{P}_h^{(2-3)}(k)$ shall vanish due to integration over azimuthal angles and it is only the $\mathcal{P}_h^{(2-2)}(k)$ term that survives [189, 238]. However, it was later shown that $\mathcal{P}_h^{(2-1)}(k)$ and $\mathcal{P}_h^{(2-3)}(k)$ do not necessarily vanish when the angular dependences are appropriately accounted for [295].

Next, we shall consider contributions to $\mathcal{P}_h(k)$ at the level of $f_{\rm NL}^4$. These terms arise when we introduce $f_{\rm NL}$, as defined in Eq. (5.1), in all four of $\mathcal{R}_{\boldsymbol{k}}$ terms in the four-point function in Eq. (5.12). In such a case, we obtain three terms, which we shall call $\mathcal{P}_h^{(4-1)}(k)$, $\mathcal{P}_h^{(4-2)}(k)$ and $\mathcal{P}_h^{(4-3)}(k)$. The expressions describing these terms are given by

$$\begin{aligned}
\mathcal{P}_h^{(4-1)}(k) &= 2^5\,\frac{16}{81}\left(\frac{9}{25}\right)^2\frac{(2\,\pi^2)^3}{(2\,\pi)^9}\,\frac{1}{k^2\,\eta^2}\int{\rm d}^3\boldsymbol{q}_1\int{\rm d}^3\boldsymbol{q}_2\,Q^\lambda(k,q_1)\,Q_\lambda(k,q_2)\\
&\quad\times\mathcal{I}(k,q_1)\,\mathcal{I}(k,q_2)\,k^3\int{\rm d}^3\boldsymbol{q}_2'\,\frac{\mathcal{P}_{\rm S}(|\boldsymbol{k}-\boldsymbol{q}_1+\boldsymbol{q}_2-\boldsymbol{q}_2'|)}{|\boldsymbol{k}-\boldsymbol{q}_1+\boldsymbol{q}_2-\boldsymbol{q}_2'|^3}\\
&\quad\times\frac{\mathcal{P}_{\rm S}(q_2')\,\mathcal{P}_{\rm S}(|\boldsymbol{q}_2-\boldsymbol{q}_2'|)\mathcal{P}_{\rm S}(|\boldsymbol{q}_1+\boldsymbol{q}_2'|)}{{q_2'}^3\,|\boldsymbol{q}_2-\boldsymbol{q}_2'|^3|\,\boldsymbol{q}_1+\boldsymbol{q}_2'|^3}\\
&\quad\times f_{\rm NL}(\boldsymbol{q}_1,-\boldsymbol{q}_2',\boldsymbol{q}_1+\boldsymbol{q}_2')\,f_{\rm NL}(\boldsymbol{k}-\boldsymbol{q}_1,\boldsymbol{k}-\boldsymbol{q}_1+\boldsymbol{q}_2-\boldsymbol{q}_2',\boldsymbol{q}_2'-\boldsymbol{q}_2)\\
&\quad\times f_{\rm NL}(\boldsymbol{q}_2,\boldsymbol{q}_2',\boldsymbol{q}_2-\boldsymbol{q}_2')\,f_{\rm NL}(\boldsymbol{k}+\boldsymbol{q}_2,\boldsymbol{q}_1-\boldsymbol{k}-\boldsymbol{q}_2+\boldsymbol{q}_2',-\boldsymbol{q}_1-\boldsymbol{q}_2')
\end{aligned}\tag{5.18a}$$

$$\begin{aligned}
\mathcal{P}_h^{(4-2)}(k) &= 2^5\,\frac{16}{81}\,\frac{(2\,\pi^2)}{(2\,\pi)^3}\,\frac{1}{k^2\,\eta^2}\\
&\quad\times\int{\rm d}^3\boldsymbol{q}_1\,Q^\lambda(k,q_1)\,Q_\lambda(k,q_1)\,\mathcal{I}^2(k,q_1)\,k^3\,\frac{\mathcal{P}_{\rm C}(q_1)\,\mathcal{P}_{\rm C}(|\boldsymbol{k}-\boldsymbol{q}_1|)}{q_1^3\,|\boldsymbol{k}-\boldsymbol{q}_1|^3},
\end{aligned}\tag{5.18b}$$

$$\begin{aligned}
\mathcal{P}_h^{(4-3)}(k) &= 2^5\,\frac{16}{81}\left(\frac{9}{25}\right)^2\frac{(2\,\pi^2)^3}{(2\,\pi)^9}\,\frac{1}{k^2\,\eta^2}\int{\rm d}^3\boldsymbol{q}_1\int{\rm d}^3\boldsymbol{q}_1'\,Q^\lambda(k,q_1)\,\mathcal{I}(k,q_1)\\
&\quad\times k^3\,\frac{\mathcal{P}_{\rm S}(q_1')\,\mathcal{P}_{\rm S}(|\boldsymbol{q}_1-\boldsymbol{q}_1'|)\,\mathcal{P}_{\rm S}(|\boldsymbol{k}-\boldsymbol{q}_1+\boldsymbol{q}_1'|)}{{q_1'}^3\,|\boldsymbol{q}_1-\boldsymbol{q}_1'|^3\,|\boldsymbol{k}-\boldsymbol{q}_1+\boldsymbol{q}_1'|^3}\\
&\quad\times f_{\rm NL}(\boldsymbol{q}_1,\boldsymbol{q}_1',\boldsymbol{q}_1-\boldsymbol{q}_1')\,f_{\rm NL}(\boldsymbol{k}-\boldsymbol{q}_1,-\boldsymbol{q}_1',\boldsymbol{k}-\boldsymbol{q}_1+\boldsymbol{q}_1')\\
&\quad\times\int{\rm d}^3\boldsymbol{q}_2\,Q_\lambda(k,q_2)\,\mathcal{I}(k,q_2)\,\frac{\mathcal{P}_{\rm S}(|\boldsymbol{q}_1'-\boldsymbol{q}_1-\boldsymbol{q}_2|)}{|\boldsymbol{q}_1'-\boldsymbol{q}_1-\boldsymbol{q}_2|^3}\\
&\quad\times f_{\rm NL}(\boldsymbol{q}_2,\boldsymbol{q}_1+\boldsymbol{q}_2-\boldsymbol{q}_1',\boldsymbol{q}_1'-\boldsymbol{q}_1)\\
&\quad\times f_{\rm NL}(-\boldsymbol{k}-\boldsymbol{q}_2,\boldsymbol{q}_1'-\boldsymbol{q}_1-\boldsymbol{q}_2,\boldsymbol{q}_1-\boldsymbol{k}-\boldsymbol{q}_1'|).
\end{aligned}\tag{5.18c}$$

Notice that we have used the definition of $\mathcal{P}_{\rm C}(k)$ to reduce the expression of $\mathcal{P}_h^{(4-2)}(k)$ in terms of $\mathcal{P}_{\rm C}(k)$ [*cf.* Eq. (5.8)]. This is known as the reducible contribution. The other two terms, *viz.* $\mathcal{P}_h^{(4-1)}(k)$ and $\mathcal{P}_h^{(4-3)}(k)$, cannot be rewritten in terms of $\mathcal{P}_{\rm C}(k)$ and they correspond to so-called non-planar and planar Feynman diagrams, respectively (*cf.* App. H; for a discussion in this context, also see Ref. [295]).

We can now utilize Eq. (5.16) to compute the $\Omega_{\rm GW}$ arising from each of these non-Gaussian contributions as well as the Gaussian contributions, and compare them against one another. However, we should note here that, the terms denoted as $\mathcal{P}_h^{(2-i)}(k)$, containing $f_{\rm NL}^2$, involve computation of six dimensional integrals and the terms denoted as $\mathcal{P}_h^{(4-i)}(k)$, containing $f_{\rm NL}^4$, involve performing nine dimensional integrals. Evidently, when we need to compute such integrals numerically, simpler methods such as the Boole's rule on a grid based sampling can be disadvantageous. Also, in such conventional methods, one will require enormous number of sampling points to achieve reasonable level of convergence of integrals in higher dimensions. Hence, one should resort to Monte-Carlo method of integration which circumvents the issue of dimensionality with reasonable number of points [51]. Moreover, at each point of these integrals we require the power spectra and $f_{\rm NL}$ to be evaluated, with their given dependence on wave numbers. Therefore, arriving at numerical estimates of these non-Gaussian contributions for a case of inflation driven by non-trivial potentials is a computationally intensive exercise. There has been an earlier attempt in the literature to compute these contributions [295]. But, we should point out that, in these efforts, the computations involved using analytical templates for the power spectra, such as the Dirac delta function or a lognormal function. Also, the $f_{\rm NL}$ was assumed to be of local form with a given amplitude and without any scale dependence. Hence, the computation of integrals in such cases is relatively easier. However, in this chapter we compute both the power spectra and the $f_{\rm NL}$ numerically from the action governing the perturbations for a given model of interest. Therefore, the computation becomes significantly more intensive and hence takes considerably more time and processing power. Due to this complexity in computation and constraints in implementation, in this chapter, we shall restrict ourselves to calculating the non-Gaussian contributions up to the level of $f_{\rm NL}^2$, *i.e.* terms denoted as $\mathcal{P}_h^{(2-i)}$.

5.5 MODELS FOR ILLUSTRATION

In this section, we shall illustrate the calculation of the correction to the scalar power spectrum and the non-Gaussian contributions to $\Omega_{\rm GW}$ due to a generic $f_{\rm NL}(\boldsymbol{k}_1, \boldsymbol{k}_2, \boldsymbol{k}_3)$ using two models of inflation. These models serve as good examples of a typical scenario of inflation leading to generation of secondary GWs of significant strengths. These models permit a brief epoch of ultra slow roll leading to enhancement of scalar power over small scales. These scalar perturbations source the secondary tensor perturbations and hence amplify the strength of secondary GWs over frequencies corresponding to those scales.

The first model we shall consider is inflation driven by a potential which has a dip introduced to it by hand. Such scenarios where a bump or a dip introduced in a rather smooth potential have been discussed in the literature in the context of PBH formation [237, 251]. Though it may not be well motivated or immediately realized from a high energy theory, it is a toy model that helps achieve a brief epoch of ultra slow roll during inflation and hence enhance the scalar power. We shall work with such a toy model consisting of a dip added to the popular Starobinsky model (1.5). On the introduction of a dip, the potential is given by

$$V(\phi) = V_0 \left[1 - \exp\left(-\sqrt{\frac{2}{3}}\,\frac{\phi}{M_{_{\mathrm{Pl}}}}\right)\right]^2 \left\{1 - \lambda\,\exp\left[-\frac{1}{2}\left(\frac{\phi-\phi_0}{\Delta\phi}\right)^2\right]\right\}, \tag{5.19}$$

where clearly the first part is the potential corresponding to Starobinsky model while the second part (in curly braces) is the Gaussian shaped dip located at ϕ_0 having a coupling strength λ and a width $\Delta\phi$. The values of the parameters involved are set to be $V_0 = 2.25 \times 10^{-10}\, M_{_{\mathrm{Pl}}}^4$, $\lambda = 2.58 \times 10^{-3}$, $\phi_0 = 4.25\, M_{_{\mathrm{Pl}}}$ and $\Delta\phi = 2.8 \times 10^{-2}\, M_{_{\mathrm{Pl}}}$. With the initial value of $\phi_{\mathrm{i}} = 5.6\, M_{_{\mathrm{Pl}}}$, we achieve about 81 e-folds of inflation with the epoch of ultra slow roll occurring when the field crosses and evolves beyond ϕ_0, at around 31 e-folds before the end of inflation. We shall refer to this model as SMD.

Another model we shall consider to illustrate our arguments is a model known as critical-Higgs inflation [300–302]. This model arises when the Higgs field is coupled non-minimally to gravity. The effective potential in this scenario contains a point of inflection which leads to an epoch of ultra slow roll thereby enhancing the scalar power. The potential describing the model is usually written as

$$V(\phi) = V_0\, \frac{\left[1 + a\,(\ln z)^2\right]\, z^4}{\left[1 + c\,(1 + b \ln z)\, z^2\right]^2}\,, \tag{5.20}$$

where $z = \phi/\mu$. We shall choose the values of the parameters to be $\mu = 1\, M_{_{\mathrm{Pl}}}$ and $V_0 = 1.5 \times 10^{-8}\, M_{_{\mathrm{Pl}}}^4$. The parameters a and b are related to c and the location of the point of inflection, say, z_{c}, as follows:

$$a = \frac{4}{1 + c\, z_{\mathrm{c}}^2 + 2\,\log(z_{\mathrm{c}}) - 4\,\log^2(z_{\mathrm{c}})}, \tag{5.21a}$$

$$b = 2\,\frac{1 + c\, z_{\mathrm{c}}^2 + 4\,\log(z_{\mathrm{c}}) + 2\,c\, z_{\mathrm{c}}^2\,\log z_{\mathrm{c}}}{c\, z_{\mathrm{c}}^2 \left[1 + c\, z_{\mathrm{c}}^2 + 2\,\log(z_{\mathrm{c}}) - 4\,\log^2(z_{\mathrm{c}})\right]}. \tag{5.21b}$$

We have set $\{c, z_{\mathrm{c}}\} = \{2.850, 0.784\}$ and arrived at the values of $\{a, b\}$ using the above relations. For these values of the model parameters, and with an initial value of field $\phi_{\mathrm{i}} = 6.0\, M_{_{\mathrm{Pl}}}$, we achieve about 66 e-folds of inflation. The epoch of ultra slow roll occurs as the field crosses the inflection point at $0.784\, M_{_{\mathrm{Pl}}}$ around 35 e-folds before the end of inflation. We shall denote this model as CHI.

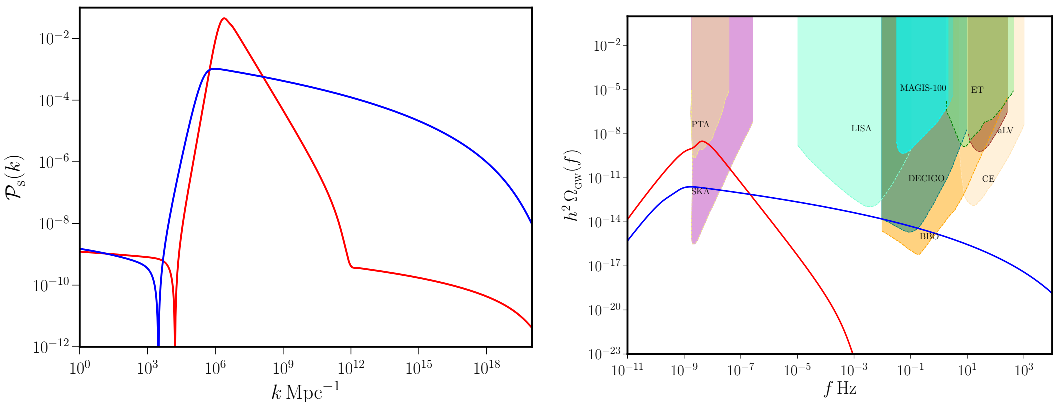

Figure 5.1: The scalar power spectra (on the left) and the corresponding $\Omega_{\rm GW}$ (on the right) generated in the two models of our interest — *viz.* SMD (in red) and CHI (in blue) — have been presented. For the values of parameters chosen for these models, we observe that the peaks of these spectra occur at around $10^6\,\mathrm{Mpc}^{-1}$. The corresponding maxima in the amplitude of $\Omega_{\rm GW}$ occur at around $10^{-9}\,\mathrm{Hz}$. The various constraint and sensitivity curves corresponding to current and upcoming GW missions have also been included as shaded regions (of different colors at the top) in the plot of $\Omega_{\rm GW}$ (on the right). The intersection of $\Omega_{\rm GW}$ curve of the CHI with the sensitivity regions of SKA and BBO indicate predictions for the corresponding future detectors. The intersection of the $\Omega_{\rm GW}$ curve in the case SMD with the observations from PTA indicates the possibility of arriving at constraints on the associated model parameters by comparing with the NANOGrav data [86].

The scalar power spectrum that arises in these models are presented in Fig. 5.1. The power over small scales have been amplified by several orders due to the ultra slow roll epochs in these models. The parameters that we have worked with ensure that the spectra are COBE normalized over the CMB scales. However, we should mention that the predictions of $n_{\rm S}$ and r over these scales have some tension with the constraints on these parameters arrived at by Planck [6]. This issue is known in case of models with enhancement of power over small scales and the tension with data is larger if the peak is closer to CMB scales [18, 161]. Moreover, the rise in power occurs close to the range of scales that can be probed by the effect of spectral distortions in the CMB [306–308]. Hence, there is a possibility of constraining these models using the data from future missions which can probe these effects with improved sensitivity [309]. In this work, we shall focus on the generation of secondary GWs due to the rise in power over small scales and the contributions due to scalar bispectrum.

We first compute the amplitude and behavior of secondary GWs generated from the Gaussian power spectrum in these two models. We present the observable quantity of interest, *viz.* the dimensionless energy density of secondary GWs $\Omega_{\rm GW}$, as a function of frequency f. The spectrum of $\Omega_{\rm GW}(f)$ has been plotted for our models of interest in Fig. 5.1. The peaks in these spectra occur at around $10^6\,{\rm Mpc}^{-1}$ for the choices of parameter values we have worked with. The peak produced in the SMD is sharper than that in the model of CHI. In the figure, we also plot the constraint and sensitivity curves from the current and upcoming observational missions (see Ref. [14] and the associated web-page for the sensitivity curves of various missions). We find that the maximum amplitude of $\Omega_{\rm GW}$ generated is over the range corresponding to PTA and SKA surveys and the curve due to the model of SMD already intersects with the constraints from PTA. This indicates possibility of constraining the model of SMD using the NANOGrav data [85, 86].

Our primary objective in this work is to examine the possible imprints of the scalar non-Gaussianity on the power spectra and on $\Omega_{\rm GW}(f)$ in these models. Hence, we begin by calculating the correction to the power spectrum by the procedure discussed earlier in Sec. 5.3. We first compute the scalar bispectrum for the models. We evaluate all the contributions arising from the third order action governing the scalar perturbations and arrive at the complete form of the scalar bispectrum $G(\boldsymbol{k}_1, \boldsymbol{k}_2, \boldsymbol{k}_3)$ [*cf.* Eqs. (1.23) and (1.24)] for each of the models. We then use the relation (5.5) to obtain the associated $f_{\rm NL}(\boldsymbol{k}_1, \boldsymbol{k}_2, \boldsymbol{k}_3)$. The resulting $f_{\rm NL}(\boldsymbol{k}_1, \boldsymbol{k}_2, \boldsymbol{k}_3)$ is then substituted into Eq. (5.10), to arrive at the correction to the power spectrum $\mathcal{P}_{\rm C}(k)$. Since the bispectra for the models

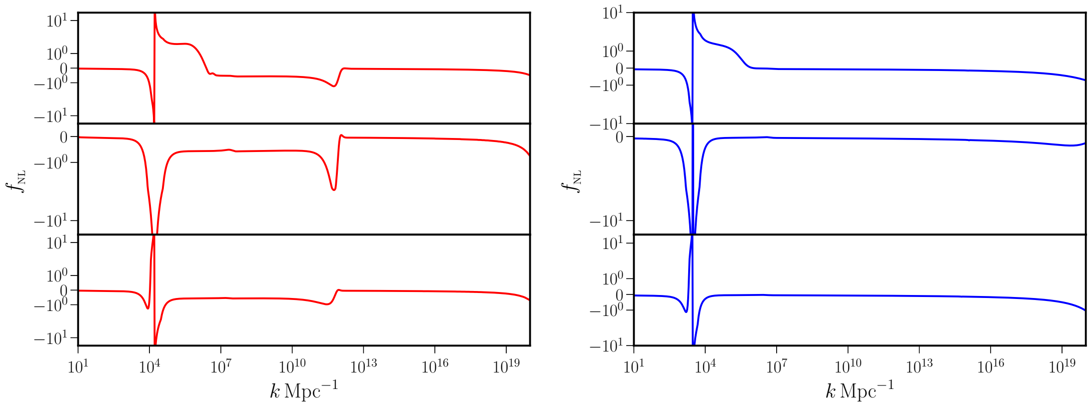

Figure 5.2: We present the non-Gaussianity parameter $f_{\rm NL}(\boldsymbol{k}_1, \boldsymbol{k}_2, \boldsymbol{k}_3)$ for the two models of interest, *viz.* SMD (on the left) and CHI (on the right). We have illustrated the behavior in the squeezed, equilateral and flattened limits (on the top, in the middle and at the bottom panels, respectively). We find that the $f_{\rm NL}(\boldsymbol{k}_1, \boldsymbol{k}_2, \boldsymbol{k}_3)$ has non-trivial scale dependence and it is important to capture its complete behavior while computing the corrections to the power spectrum. There are rather large values of $f_{\rm NL}(\boldsymbol{k}_1, \boldsymbol{k}_2, \boldsymbol{k}_3)$ occurring at the wave numbers corresponding to the location of the sharp downward spike in the power spectra of the respective models. As mentioned, these spuriously large values should be dealt with caution and have to be regulated while using $f_{\rm NL}(\boldsymbol{k}_1, \boldsymbol{k}_2, \boldsymbol{k}_3)$ in further calculations.

of interest are not easy to evaluate analytically, we perform this calculation numerically.

In Fig. 5.2, we illustrate the behavior of the scalar non-Gaussianity parameter $f_{\rm NL}(\boldsymbol{k}_1, \boldsymbol{k}_2, \boldsymbol{k}_3)$ for both the models of interest for various configuration of wave numbers. We have plotted $f_{\rm NL}(\boldsymbol{k}_1, \boldsymbol{k}_2, \boldsymbol{k}_3)$ in the squeezed limit ($k_1 \to 0, k_2 = k_3 = k$), equilateral limit ($k_1 = k_2 = k_3 = k$) and the flattened limit ($k_1 = k_2 = k,\ k_3 = 2\,k$). The parameter exhibits non-trivial behavior close to the wave number corresponding to the peak in the power spectra. The behavior is smoother over scales farther from the peak in the spectra. We also present the density plot of $f_{\rm NL}$ around the peak in the power spectra for these models in Fig 5.3. We find that $f_{\rm NL}$ is largely local in its behavior around the peak. We should note that the value of $f_{\rm NL}$ is lesser than unity over this range of wave numbers close to the peak. However, we notice deviation from these local values as we move further from the peak, *i.e.* as k_1 takes values smaller than k_3. We should mention that there arises a sharp spike in $f_{\rm NL}(\boldsymbol{k}_1, \boldsymbol{k}_2, \boldsymbol{k}_3)$ at the point where

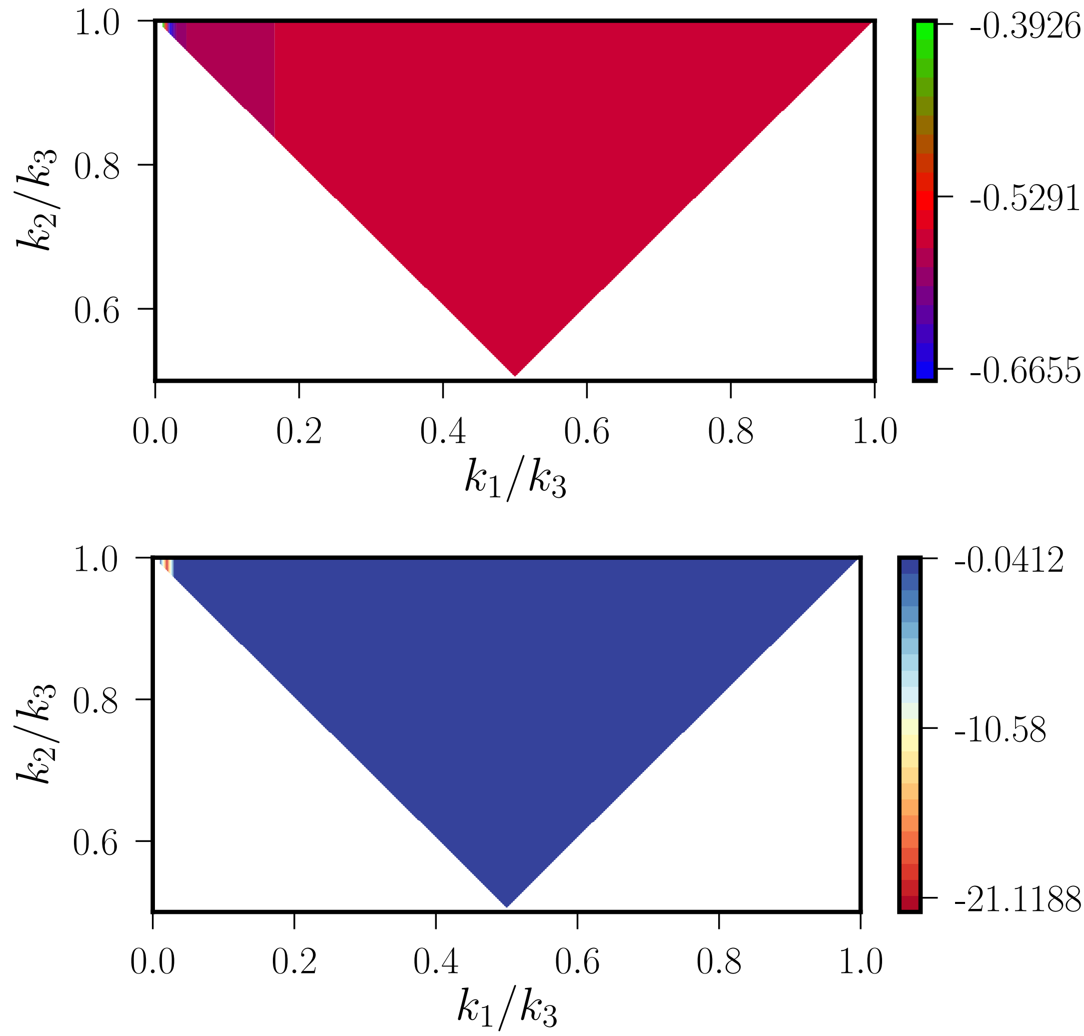

Figure 5.3: The density plots of the scalar non-Gaussianity parameter $f_{\rm NL}(\boldsymbol{k}_1, \boldsymbol{k}_2, \boldsymbol{k}_3)$ illustrating its behavior for a general configuration of wave numbers around a given value of k_3 is presented for the two models of interest, *viz.* SMD (on top) and CHI (at the bottom). The behavior is evidently dependent on the value of k_3, which for both the models is taken to be $k_3 = 10^6\,{\rm Mpc}^{-1}$, corresponding to the wave number close to the peak in the spectra. We find that $f_{\rm NL}(\boldsymbol{k}_1, \boldsymbol{k}_2, \boldsymbol{k}_3)$ in these models are highly local in shape around the peak in the spectra. The value of the parameter is roughly -0.5 in case of SMD, whereas in case of CHI, it turns out to be around -0.04. As we move away from the peak, for $k_1 \ll k_3$, we see that the $f_{\rm NL}$ starts deviating from the local shape and growing larger in value.

there is a sharp downward spike in the power spectrum, occurring before the rise and the peak in the range of wave numbers. This indicates power spectrum reaching very small values. Hence, quantities like $n_{_{\rm S}}(k)$ or $f_{_{\rm NL}}(\boldsymbol{k}_1, \boldsymbol{k}_2, \boldsymbol{k}_3)$ that contain power spectrum in their denominators of their definitions, may incur spuriously large values at this wave number. Therefore, care should be taken when dealing with such anomalous values. In our calculation, we have regulated the value of $f_{_{\rm NL}}$ around the region by introducing a cutoff at 10. This implies that any value of $|f_{_{\rm NL}}|$ which is larger than 10 is taken to be 10.

5.5.1 Calculation of the correction to scalar power spectrum

With $f_{_{\rm NL}}(\boldsymbol{k}_1, \boldsymbol{k}_2, \boldsymbol{k}_3)$ thus computed, we can obtain the correction to the spectrum $\mathcal{P}_{_{\rm C}}(k)$ for both the models. Before we proceed to perform the integrals numerically, we utilize Eq. (5.10) and attempt to arrive at a rough analytical estimate of $\mathcal{P}_{_{\rm C}}(k)$.

Let $k_{\rm f}$ denote the wave number corresponding to the peak in the power spectrum. We know that the maximum amplitude of the integrand occurs around the region where $x = k_{\rm f}/k$ or $y = k_{\rm f}/k$ or $x = y = k_{\rm f}/k$. In Fig. 5.4, we illustrate the range of the integrals involved and the points from which the maximum contribution arises. We shall describe the sharp peak in the behavior of the power spectrum by approximating its form around the peak using a Dirac delta function as follows:

$$\mathcal{P}_{_{\rm S}}(k) = \mathcal{P}_{_{\rm S}}(k_{\rm f})\, \delta^{(1)}(\ln\, k - \ln\, k_{\rm f}). \tag{5.22}$$

Using this approximation, we proceed to calculate the dominant contributions to the integrals. We perform the integral over x in Eq. (5.10) to obtain that

$$\mathcal{P}_{_{\rm C}}(k) = \frac{9}{25}\left(\frac{k}{k_{\rm f}}\right)\mathcal{P}_{_{\rm S}}(k_{\rm f}) \int_{|1-k_{\rm f}/k|}^{1+k_{\rm f}/k} \frac{{\rm d}y}{y^2}\, \mathcal{P}_{_{\rm S}}(ky)\, f_{_{\rm NL}}^2(\boldsymbol{k}, \boldsymbol{k}_{\rm f}, y\boldsymbol{k}). \tag{5.23}$$

To perform this integral, we shall consider the two regimes in wave numbers, *viz.* $k < k_{\rm f}$ and $k > k_{\rm f}$. For the case of $k < k_{\rm f}$, the integrand receives contribution only from the point marked P3 in Fig. 5.4. Due to the narrow range of the integral over y, we may approximate $(k\, y) \simeq k_{\rm f}$ in the arguments of $\mathcal{P}_{_{\rm S}}$ and $f_{_{\rm NL}}$. So, the above integral over y

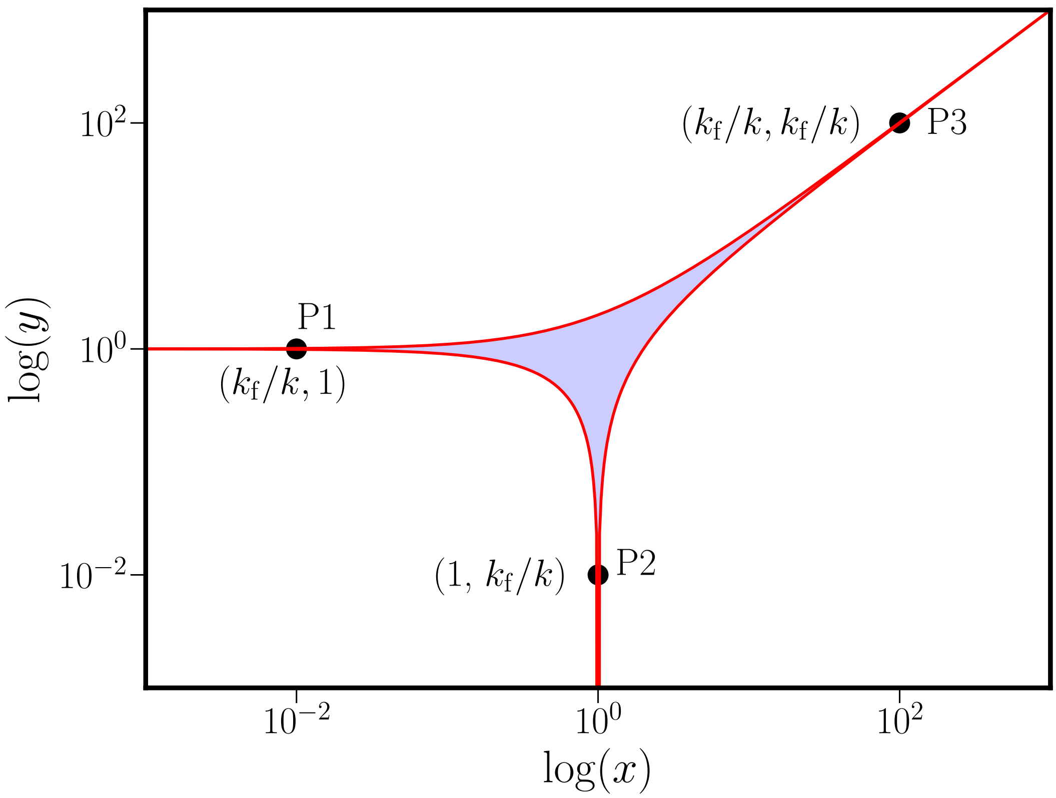

Figure 5.4: The range of integration involved in calculating $\mathcal{P}_{\rm C}(k)$ [*cf.* Eq. (5.10)] is plotted on a logarithmic scale. The shaded region marks the region covered by the limits of the integrals. We mark the three points P1, P2 and P3 at which the integrals derive maximum contribution when there is a strongly localized peak in the power spectrum. The region around the points P1 and P2 contribute when $k > k_{\rm f}$ and the region around P3 contributes when $k < k_{\rm f}$. It is also worth noting that, due to the symmetry of the integrand over the variables x and y, the contributions from P1 and P2 turn out to be equal to one another. For the case of $k \sim k_{\rm f}$, the integrand receives the maximum contribution from the wide region around $x = y = 1$.

simplifies to

$$\begin{aligned}\mathcal{P}_{\rm C}(k) &\simeq \frac{9}{25}\left(\frac{k}{k_{\rm f}}\right)\left[\mathcal{P}_{\rm S}(k_{\rm f})\, f_{\rm NL}(\boldsymbol{k},\boldsymbol{k_{\rm f}},\boldsymbol{k_{\rm f}})\right]^2 \int_{|1-k_{\rm f}/k|}^{1+k_{\rm f}/k}\frac{{\rm d}y}{y^2}\\ &= \frac{18}{25}\left(\frac{k}{k_{\rm f}}\right)^3\left[\mathcal{P}_{\rm S}(k_{\rm f})\, f_{\rm NL}(\boldsymbol{k},\boldsymbol{k_{\rm f}},\boldsymbol{k_{\rm f}})\right]^2, \end{aligned} \tag{5.24}$$

where we have used the fact that $k_{\rm f}/k > 1$. It is interesting to note the combination of wave numbers appearing in the argument of $f_{\rm NL}$. We know that $k < k_{\rm f}$. Hence, $f_{\rm NL}(\boldsymbol{k},\boldsymbol{k_{\rm f}},\boldsymbol{k_{\rm f}})$ denotes that the parameter has to be evaluated in the squeezed limit of the configuration of wave numbers. This further simplifies the expression because we know that the consistency condition relating the $f_{\rm NL}$ and the scalar spectral index $n_{\rm S}(k)$ is obeyed in these models [18, 299]. Therefore, we utilize the consistency relation

$$f_{\rm NL}(\boldsymbol{k},\boldsymbol{k_{\rm f}},\boldsymbol{k_{\rm f}}) = \frac{5}{12}[n_{\rm S}(k_{\rm f})-1]. \tag{5.25}$$

In this expression, strictly speaking, $[n_{\rm S}(k_{\rm f})-1]$ vanishes identically since it is the slope of the spectrum at its peak. However, we shall take it to be a small non-vanishing value close to the peak in the spectrum for the purpose of our calculation. Therefore expression for $\mathcal{P}_{\rm C}(k)$ reduces to

$$\mathcal{P}_{\rm C}(k) = \frac{1}{8}\left(\frac{k}{k_{\rm f}}\right)^3\left\{\mathcal{P}_{\rm S}(k_{\rm f})\,[n_{\rm S}(k_{\rm f})-1]\right\}^2. \tag{5.26}$$

We find that $\mathcal{P}_{\rm C}(k)$ shall be proportional to k^3 over the scales with $k < k_{\rm f}$.

We then consider the case of $k > k_{\rm f}$. For these wave numbers, there arise contributions from the two points P1 and P2 marked in Fig. 5.4. We shall first evaluate the contribution at P1 using the approximation of the spectrum in Eq. (5.22). The expression for $\mathcal{P}_{\rm C}(k)$ becomes

$$\begin{aligned}\mathcal{P}_{\rm C}(k) &\simeq \frac{9}{25}\left(\frac{k}{k_{\rm f}}\right)\mathcal{P}_{\rm S}(k_{\rm f})\,\mathcal{P}_{\rm S}(k)\, f_{\rm NL}^2(\boldsymbol{k},\boldsymbol{k_{\rm f}},\boldsymbol{k}) \int_{|1-k_{\rm f}/k|}^{1+k_{\rm f}/k}\frac{{\rm d}y}{y^2}\\ &= \frac{18}{25}\,\mathcal{P}_{\rm S}(k_{\rm f})\,\mathcal{P}_{\rm S}(k)\, f_{\rm NL}^2(\boldsymbol{k},\boldsymbol{k},\boldsymbol{k_{\rm f}}), \end{aligned} \tag{5.27}$$

where we have used the smallness of $k_{\rm f}/k$. We again note that the arguments of $f_{\rm NL}$ suggest that it is evaluated in the squeezed limit but now with $k_{\rm f}$ acting as the squeezed mode. We shall use the consistency relation again, where

$$f_{\rm NL}(\boldsymbol{k},\boldsymbol{k},\boldsymbol{k_{\rm f}}) = \frac{5}{12}[n_{\rm S}(k)-1]. \tag{5.28}$$

Upon using this relation, the expression for $\mathcal{P}_{\mathrm{C}}(k)$ reduces to be

$$\mathcal{P}_{\mathrm{C}}(k) = \frac{1}{8}\,\mathcal{P}_{\mathrm{S}}(k_{\mathrm{f}})\,\mathcal{P}_{\mathrm{S}}(k)\,\left[n_{\mathrm{S}}(k) - 1\right]^2. \tag{5.29}$$

Due to the fact that the form of the integral in Eq. (5.10) remains unchanged under the exchange of x and y, the contribution from the point P2 shall be the same as from P1 which we computed above. So, we have the total value of $\mathcal{P}_{\mathrm{C}}(k)$ for $k > k_{\mathrm{f}}$ to be

$$\mathcal{P}_{\mathrm{C}}(k) = \frac{1}{4}\,\mathcal{P}_{\mathrm{S}}(k_{\mathrm{f}})\,\mathcal{P}_{\mathrm{S}}(k)\,\left[n_{\mathrm{S}}(k) - 1\right]^2. \tag{5.30}$$

We find that $\mathcal{P}_{\mathrm{C}}(k)$ over the regime of $k > k_{\mathrm{f}}$ shall be proportional to $\mathcal{P}_{\mathrm{S}}(k)$. Hence, if $\mathcal{P}_{\mathrm{S}}(k)$ turns nearly scale invariant away from the peak over large wave numbers, then we can expect a corresponding $\mathcal{P}_{\mathrm{C}}(k)$ with nearly constant amplitude. In summary, we have the analytical estimate of $\mathcal{P}_{\mathrm{C}}(k)$ to be

$$\mathcal{P}_{\mathrm{C}}(k) = \begin{cases} \dfrac{1}{8}\left(\dfrac{k}{k_{\mathrm{f}}}\right)^3 \left\{\mathcal{P}_{\mathrm{S}}(k_{\mathrm{f}})\left[n_{\mathrm{S}}(k_{\mathrm{f}}) - 1\right]\right\}^2, & \text{for}\, k < k_{\mathrm{f}}, \\ \dfrac{1}{4}\,\mathcal{P}_{\mathrm{S}}(k_{\mathrm{f}})\,\mathcal{P}_{\mathrm{S}}(k)\,\left[n_{\mathrm{S}}(k) - 1\right]^2, & \text{for}\, k > k_{\mathrm{f}}. \end{cases} \tag{5.31}$$

Having obtained these analytical expressions, we proceed to compute the exact numerical estimates of $\mathcal{P}_{\mathrm{C}}(k)$. We shall briefly discuss certain aspects of numerical evaluation of the integrals involved. The integral involved in $\mathcal{P}_{\mathrm{C}}(k)$ [*cf.* Eq. (5.10)] is evaluated ensuring that the regimes around $x = k_{\mathrm{f}}/k$ and $y = k_{\mathrm{f}}/k$ are well sampled. Due to the wide range of the integral over x, the integration is performed over log scale. The limits are chosen such that the range of integration is centered at k_{f}/k and spans two decades on either side of the point. For given values of $k\,x$ and $k\,y$, the power spectra are evaluated numerically. Besides, each point on this x-y plane provides a triangular configuration of wave numbers for which $f_{\mathrm{NL}}(\boldsymbol{k}, x\boldsymbol{k}, y\boldsymbol{k})$ is calculated numerically. This is the most time consuming part of the calculation. Once computed, the integrand is summed over to obtain $\mathcal{P}_{\mathrm{C}}(k)$. The exercise is repeated for the complete range of wave numbers.

5.5.2 Calculation of non-Gaussian contributions to Ω_{GW}

The behavior of $\mathcal{P}_{\mathrm{C}}(k)$ may give us an idea of the effect of f_{NL} on the scalar power spectrum. It may further give us an insight about the amplitude of one of the non-Gaussian contributions [*cf.* Eqs. (5.17)]. Having obtained the $\mathcal{P}_{\mathrm{C}}(k)$ in the models of interest, we proceed to compute the non-Gaussian contributions $\mathcal{P}_h^{(2-i)}$ to the $\Omega_{\rm GW}$ in these cases.

At the outset, we should note that, the non-trivial dependence of $f_{\rm NL}$ over different combination of wave numbers in $\mathcal{P}_h^{(2-1)}(k)$ and $\mathcal{P}_h^{(2-3)}(k)$ do not allow us to easily obtain an analytical estimate as we did for $\mathcal{P}_{\rm C}(k)$. Hence, as mentioned earlier, we numerically perform these integrals involved using the Monte-Carlo method of integration to obtain the estimates. Let us now mention a few details about the procedure. We first identify the region of maximum amplitude of the integrands in the range of integration, for a given wave number k. Interestingly, we find that the integrands have maximum values around the wave number $k_{\rm f}$, if the wave number of interest $k < k_{\rm f}$, while they peak around k if $k > k_{\rm f}$. We also find that the nature of integrands are very localized in the range of k allowing us to set the range of integrals to be two decades on either side of the peaks of the integrands. The respective angular integrals were performed over the entire range *viz.* $\cos\theta_i \in [-1, 1]$ and $\phi_i \in [0, 2\,\pi]$. During the performance of integration, each point corresponded to a numerical evaluation of a combination of power and bi-spectra with their appropriate arguments of wave numbers. The computation of $f_{\rm NL}$ at each point of integration was the time consuming part of this process. The integrals were performed using 10^5 points and checked for convergence.

We should also note an interesting property of these contributions. The integrand describing $\mathcal{P}_h^{(2-2)}(k)$ is positive definite and hence the contribution shall be positive. However, the integrand characterizing the contributions $\mathcal{P}_h^{(2-1)}(k)$ and $\mathcal{P}_h^{(2-3)}(k)$ can be negative, because of their dependence over the polar angles (as noted earlier in Ref. [295]). This property should be accounted for while comparing them against $\Omega_{\rm GW}$ from the Gaussian contribution.

5.5.3 Results

First, we present the $\mathcal{P}_{\rm C}(k)$, obtained both the analytically and numerically, against the original spectra, $\mathcal{P}_{\rm S}(k)$, in Fig. 5.5. We observe that $\mathcal{P}_{\rm C}(k)$ is smaller than the original $\mathcal{P}_{\rm S}(k)$ particularly around the peak and over the range $k > k_{\rm f}$. There appears a region close to the dip in the spectrum where $\mathcal{P}_{\rm C}(k)$ is greater than $\mathcal{P}_{\rm S}(k)$. This is mainly due to the sharp spike occurring in $f_{\rm NL}$ that we mentioned earlier. But apart from this effect, there arises no significant correction to the original power spectrum. Moreover, the analytical estimate fairly mimics the exact numerical behavior of $\mathcal{P}_{\rm C}(k)$. The behavior of k^3 over large scales and near scale invariance over small scales is well

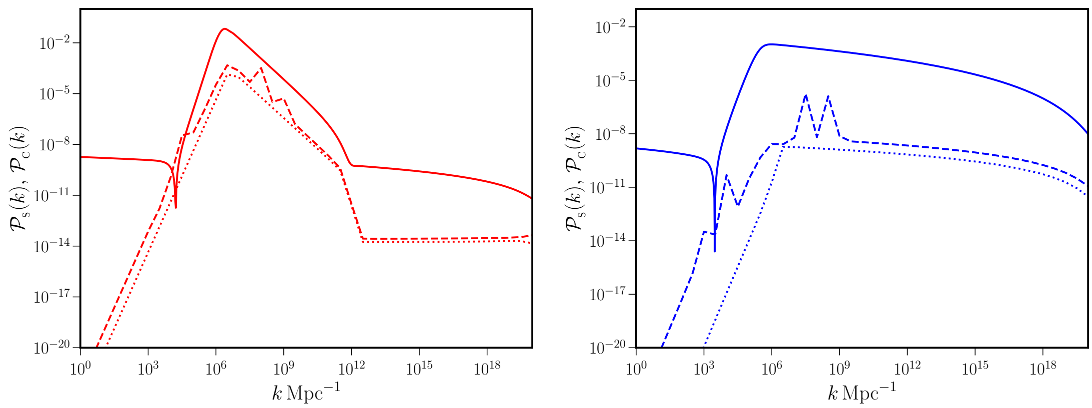

Figure 5.5: The original scalar power spectra $\mathcal{P}_{\rm S}(k)$ (as solid lines) and the non-Gaussian corrections $\mathcal{P}_{\rm C}(k)$ due to the bispectrum (as dashed lines) have been plotted here for the models of interest, *viz.* . SMD (on the left) and CHI (on the right). Evidently, the $\mathcal{P}_{\rm C}(k)$ computed is lower in amplitude than $\mathcal{P}_{\rm S}(k)$. We have also plotted the analytical estimate of $\mathcal{P}_{\rm C}(k)$ for these two models (as dotted lines). The analytical estimate matches the numerical behavior better in the case of SMD than CHI since the spectrum is more sharply peaked in the first model than in the second model. The complete spectrum corrected for $\mathcal{P}_{\rm C}(k)$ shall effectively be the same as the original $\mathcal{P}_{\rm S}(k)$, particularly around $k_{\rm f}$ and over $k > k_{\rm f}$.

captured in the numerical result thereby assuring the validity of the analytical estimates over wave numbers far from the peak. The match is better for the model SMD. This can be understood because its spectrum is closer in resemblance to the Dirac delta function used in the analytical calculation. The original spectrum $\mathcal{P}_{\rm S}(k)$ in case of CHI has a rather broad peak with slower descent over the range of wave numbers. This behavior leads to the difference between numerical and analytical estimates of $\mathcal{P}_{\rm C}(k)$ around the peak in this model. However, for $k > k_{\rm f}$, the analytical estimate matches better even in case of such a broad peak. The rugged nature of the numerical result is due to the limited number of points taken for evaluation over the range of wave numbers.

We present the behavior of the non-Gaussian contributions to $\Omega_{\rm GW}$ at the level of $f_{\rm NL}^2$, *viz.* due to $\mathcal{P}_h^{(2-i)}(k)$, in Fig. 5.6. We focus particularly around the peak amplitude of $\Omega_{\rm GW}$ and find that the non-Gaussian contributions are significant for SMD. These contributions dominate the $\Omega_{\rm GW}$ from the Gaussian spectrum for wave numbers $k \leq k_{\rm f}$. However, they become sub-dominant for $k > k_{\rm f}$. In case of CHI, the non-Gaussian contributions become briefly comparable over the range of $k \simeq k_{\rm f}$. But they are sub-dominant for wave numbers $k < k_{\rm f}$ as well as $k > k_{\rm f}$. Thus, we learn that the behavior

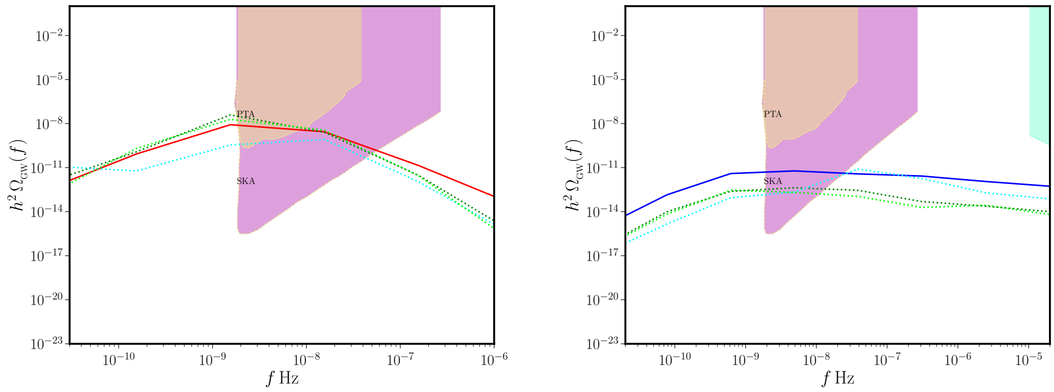

Figure 5.6: We present the non-Gaussian contributions to $\Omega_{\rm GW}$ arising due to $f_{\rm NL}$ (as dotted lines), against the original Gaussian contribution (as solid lines) for the models SMD (on left) and CHI (on right), focusing over the range of frequencies containing the maximum amplitude. The contributions arising from the terms $\mathcal{P}_h^{(2-1)}(k)$ (in green), $\mathcal{P}_h^{(2-2)}(k)$ (in cyan), $\mathcal{P}_h^{(2-3)}(k)$ (in lime) are presented for both the models of interest.

of $\Omega_{\rm GW}$ arising from non-Gaussian contributions are model dependent and significant in case of power spectrum with highly localized behavior around the peak. However, as we move farther from the peak, these contributions become lesser in amplitude compared to the Gaussian contribution. Therefore, these models illustrate that the non-Gaussian contributions to $\Omega_{\rm GW}$ have to be computed and consistently accounted for, especially around the peak, in models of interest.

5.6 DISCUSSION

There have been attempts in the literature to account for scalar non-Gaussianity in the calculation of the spectral density of the secondary GWs, $\Omega_{\rm GW}(f)$, for specific cases of $f_{\rm NL}$ assuming certain shapes or limits of the bispectrum. In this work, we have presented a method to account for a general scalar bispectrum with non-trivial scale dependence in such a calculation. We have presented the correction to the scalar power spectrum that may arise due to the scalar bispectrum. We have also attempted an analytical estimate of the correction to be expected from models with a localized peak in the power spectrum. We have found that it is the squeezed limit of $f_{\rm NL}$ that contributes the most to the correction for wave numbers away from the peak in the power spectrum. We have then presented the non-Gaussian contributions to $\Omega_{\rm GW}(f)$ that arise due to $f_{\rm NL}$. We have computed terms that are reducible in terms of $\mathcal{P}_{\mathrm{C}}(k)$ as well as those that are not reducible so. We have consistently accounted for the scale dependence of f_{NL}, arising from the modified definition of the parameter, in computing these contributions.

We then illustrated our method using two models of inflation. These are models driven by canonical scalar fields that permit brief epochs of ultra slow roll and hence lead to significant amplitudes of secondary GWs. We have computed the correction to the power spectrum arising from f_{NL} and find that it is largely sub-dominant to the original power spectrum. Moreover, the analytical estimate of the correction agrees fairly well with the exact numerical estimate in these cases. We have then computed the non-Gaussian contributions to the $\Omega_{\mathrm{GW}}(f)$ and compared them against the Gaussian contribution. We have computed these contributions up to the level of f_{NL}^2. We have found that the non-Gaussian contributions are non-trivial and slightly different from the shape of the original $\Omega_{\mathrm{GW}}(f)$. The non-Gaussian contributions arising in the case of SMD have been found to dominate the original amplitudes of $\Omega_{\mathrm{GW}}(f)$ around the frequencies corresponding to the wave number k_{f} containing the peak in the power spectrum, as well as smaller wave numbers, *i.e.* over $k < k_{\mathrm{f}}$. But, these contributions decrease farther from the peak and become sub-dominant to the Gaussian contribution for wave numbers with $k > k_{\mathrm{f}}$. In the case of CHI, the non-Gaussian contribution become briefly comparable to and dominant over the Gaussian contribution around k_{f}, but remain sub-dominant farther from k_{f} on either side. Since the models serve as examples typical models of inflation that are considered in this context of generation of secondary GWs, we can argue that the non-Gaussian contributions arising from f_{NL} may turn out to be significant, particularly around the peak amplitude of Ω_{GW}. Hence, they have to be computed and accounted for in the estimates of Ω_{GW}.

Besides, we should emphasize that the method used for calculation has its value in being able to capture the complete behavior of $f_{\mathrm{NL}}(\boldsymbol{k}_1, \boldsymbol{k}_2, \boldsymbol{k}_3)$ in any non-trivial scenario of inflation. Moreover, the analytical estimate of the correction to the power spectrum, $\mathcal{P}_{\mathrm{C}}(k)$, serves as a good approximation for the exact estimate, without directly computing the bispectrum. This greatly reduces the time taken for the calculation of f_{NL} and provides a quick estimate of $\mathcal{P}_{\mathrm{C}}(k)$ to be expected from just the shape of the spectrum for any model with a peak in its scalar power. Importantly, the non-negligible levels of non-Gaussian contributions to Ω_{GW} obtained in these models indicate the necessity to capture the exact scale dependence of f_{NL} as presented in this method.

As to the caveats of this work, we should mention that we have restricted the computation of non-Gaussian contributions to Ω_{GW} up to terms involving f_{NL}^2 due to the complexity of numerical implementation. We are currently working on addressing the complexity and accounting for terms involving $f_{_{\rm NL}}^4$ in the calculation. Secondly, there arises a spike like behavior in the shape of $f_{_{\rm NL}}$ [*cf.* Fig. 5.2]. This occurs due to the presence of $\mathcal{P}_{_{\rm S}}(k)$ in the denominator of the expression of $f_{_{\rm NL}}$ in terms of power and bi-spectra [*cf.* Eq. (5.5)]. As $\mathcal{P}_{_{\rm S}}(k)$ reaches extremely small values, this spike occurs and it has to be regulated to a finite value during the computation. This has an effect in our results as one may see a corrugated shape of $\mathcal{P}_{_{\rm C}}(k)$ computed using $f_{_{\rm NL}}$. Hence, to avoid such artefacts in computation, it may be preferable to modify this method to utilize the bispectrum directly in the calculation of $\mathcal{P}_{_{\rm C}}(k)$ as well as the non-Gaussian contributions to $\Omega_{_{\rm GW}}$. We are presently working on these issues.

In summary, we argue that the method we have discussed is a robust way to account for the exact form of primordial scalar non-Gaussianity at the level of three-point correlation in the calculation of $\Omega_{_{\rm GW}}$ arising from models of inflation. Since we infer a significant non-Gaussian contribution to $\Omega_{_{\rm GW}}$ in the models considered, it would be interesting to employ this method for non-canonical models that can potentially produce larger amplitudes and different shapes of scalar non-Gaussianities. Such scenarios may even lead to significant non-Gaussian corrections to the power spectra along with large non-Gaussian contributions to $\Omega_{_{\rm GW}}$. Moreover there are efforts to account for the contribution of higher order non-Gaussianities, such as the trispectrum, to the secondary tensor power spectrum. It would be interesting to explore the effects of non-Gaussianities with non-trivial scale dependence in such higher order calculations.

CHAPTER 6

CONCLUSIONS

6.1 SUMMARY

The objective of this thesis has been to examine the observational signatures of non-trivial models of inflation and constrain them using the corresponding data. We have investigated models containing unique features in their power spectra and have computed the corresponding observational imprints. We had focused on models which are degenerate at the level of power spectra and found that they possess distinguishing features at the level of bispectra. We had further examined these distinct features and had attempted to consistently account for them in the estimation of the associated observables. We have discussed these investigations and have presented the findings of these analyses in detail in the preceding chapters. In this section, we shall briefly summarize the essential results of the our analyses.

In Chap. 2, we had investigated models leading to the suppression of scalar power over the largest CMB scales. We had considered the scenario of kinetically dominated initial conditions and contrasted it against other models such as the Starobinsky model (2.2) and the punctuated inflation model (2.5) which lead to similar features. We had also compared these models against the latest CMB data from Planck and arrived at constraints on the respective model parameters. We had further examined the associated scalar bispectrum in models with kinetically dominated initial conditions and had found that it contains unique signatures. In particular, we had shown that the consistency relation is violated over large scales in such models where suppression of power occurs in the scalar spectrum. These interesting aspects can serve to potentially discriminate this scenario from other models when we have more precise constraints on primordial non-Gaussianity from future CMB missions and large scale structure surveys.

In Chap. 3, we had focused on models leading to enhancement of scalar power on small scales and hence giving rise to significant amounts of PBHs and detectable amplitudes of secondary GWs. The class of models we had considered, *viz.* the ultra slow roll and punctuated inflationary models, lead to power spectra which are largely similar in shape and amplitude. We had also reproduced similar spectra in scenarios reconstructed from the behavior of the first slow roll parameter ϵ_1. Such reconstructions had allowed us to understand the essentials of the inflationary dynamics leading to enhanced scalar power and had also permitted us to tune the location and shape of the feature more easily. Moreover, we had learnt that these models lead to a non-trivial scalar bispectrum and yet, surprisingly, satisfy the consistency relation in the squeezed limit. These properties shall become crucial when one attempts to account for non-Gaussianities in the estimates of PBHs and GWs generated from such models. Besides, we had illustrated that the bispectrum associated with the secondary tensor perturbations contains remarkable signatures that can shed light on the characteristics of GWs. The associated shape function, if detected by upcoming GW missions, can lend further insight into the dynamics of the models giving rise to them.

In Chap. 4, we had explored a novel mechanism for the production of PBHs and secondary GWs. We had considered evolving scalar perturbations from excited initial states, in particular, squeezed initial states, rather than the standard Bunch-Davies vacuum. We had calculated the scalar bispectrum in this scenario analytically and had shown that, in the squeezed limit, the non-Gaussianity parameter $f_{\rm NL}$ is inversely proportional to the squeezed mode. Hence, the consistency condition is seriously violated and $f_{\rm NL}$ could reach large values. We had utilized such large amplitudes of $f_{\rm NL}$ to compute the associated correction to the power spectrum. This had lead to significant production of PBHs and secondary GWs in this scenario. However, we had also found that the issue of backreaction imposes a severe limit on this mechanism. We had estimated the energy density of perturbations backreacting on the background and had arrived at a stringent constraint on the parameter quantifying the deviation of the initial state from the Bunch-Davies vacuum.

In Chap. 5, we had presented a method to account for the complete behavior of the scalar bispectrum in the calculation of secondary GWs. We had used a modified definition of $f_{\rm NL}$ that generalizes the parameter beyond any particular template or limit. We had computed the correction to the scalar power spectrum due to such an $f_{\rm NL}$ and had also computed the non-Gaussian contributions to the amplitude of secondary GWs. We had illustrated this method using two inflationary models involving the canonical scalar field that are representative of models often considered in this context. We had argued that the method is robust, free from assumptions and generalizes earlier approaches in this regard. Hence, it can be applied to any given scenario of inflation that may give rise to a strongly scale dependent scalar bispectrum and substantial amplitude of secondary GWs.

6.2 OUTLOOK

The theme of this thesis has been investigation of models leading to non-trivial features at level of power and bi-spectra, across a wide range of scales. The constituent efforts discussed thus far can be extended further in many directions. We shall highlight below a few such possibilities for further exploration.

The non-Gaussianities we had examined had involved the auto-correlations, *i.e.* the bispectra of the scalar and tensor perturbations. It is of great interest and possibly of equal significance to investigate the non-Gaussianities arising from the cross-correlation of the scalar and tensor perturbations in the models discussed (for related efforts, see Refs. [310–312]). Accounting for such contributions to the total non-Gaussianity in the estimates of predictions of observables can be highly insightful. It can also help us to jointly constrain the associated non-Gaussianity parameters using the available and forthcoming observational datasets.

The phenomenon of production of PBHs is particularly interesting in the context of models giving rise to non-trivial non-Gaussianities. Recall that, the population of PBHs produced is exponentially sensitive to the amplitude of the scalar power around the peak. Hence, any minor correction to it can have significant effect on the amount PBHs produced. Further, a large primordial scalar non-Gaussianity can alter the underlying distribution governing the field of density contrast during the subsequent epochs (for related efforts, see Refs. [80, 182, 187]). This can, in turn, drastically modify the estimate of the population of PBHs formed in a given epoch [232, 313]. Therefore, the effect of scalar non-Gaussianity on the formation of PBHs in the context of the models of our interest is an interesting avenue to explore.

Another potential aspect of future investigation arises from the upcoming field of observational astronomy, *viz.* the detection of $21\,\mathrm{cm}$ signals from the epoch of reionization (for current efforts, see Refs. [314, 315]). This is an observational probe corresponding to scales between $10^{-1}\,\mathrm{Mpc}$ and $100\,\mathrm{Mpc}$. This range is intermediate to the large scales of the CMB and the small scales probed by PBHs and GWs. Therefore, examining the predictions of models over this regime complements our analyses thus far. Such efforts may therefore help us complete our understanding of the dynamics of inflation throughout its duration (see for instance, Refs. [316, 317]). Further, as these observations grow more precise, an interesting possibility would be to constrain models using a comprehensive dataset comprising of variety of observables that span the complete range of scales.

We are presently working on some these issues.

APPENDIX A

Signatures of initial kinetic domination across models

To illustrate that the imprints of initial kinetic domination arise across all inflationary modes, in this appendix, we shall consider two other models of inflation, *viz.* a small field model and so-called the axion monodromy model, which are described by the following potentials:

$$V(\phi) = V_0 \left[1 - \left(\frac{\phi}{\phi_0}\right)^4\right], \tag{A.1a}$$

$$V(\phi) = \mu^3 \left[\phi + b\,\phi_0 \cos\left(\frac{\phi}{\phi_0}\right)\right]. \tag{A.1b}$$

We work with parameters and initial conditions for the background such that the power spectra are COBE normalized around the pivot scale and the suppression on large scales occurs as in QPa. The corresponding power spectra are illustrated in Fig. A.1, and it is clear that, despite the different choice of potentials, the power spectra have the same shape at large and small scales across models. In Fig. A.2, we have plotted the behavior of the non-Gaussianity parameter $f_{_{\rm NL}}$ in the squeezed limit in these cases. Clearly, the behavior of the parameter is similar to that encountered in the cases of QP and SMI. The restoration of the consistency condition is well illustrated in the case of the axion monodromy model, wherein both the power and bispectra exhibit continued oscillations even at small scales [132, 318].

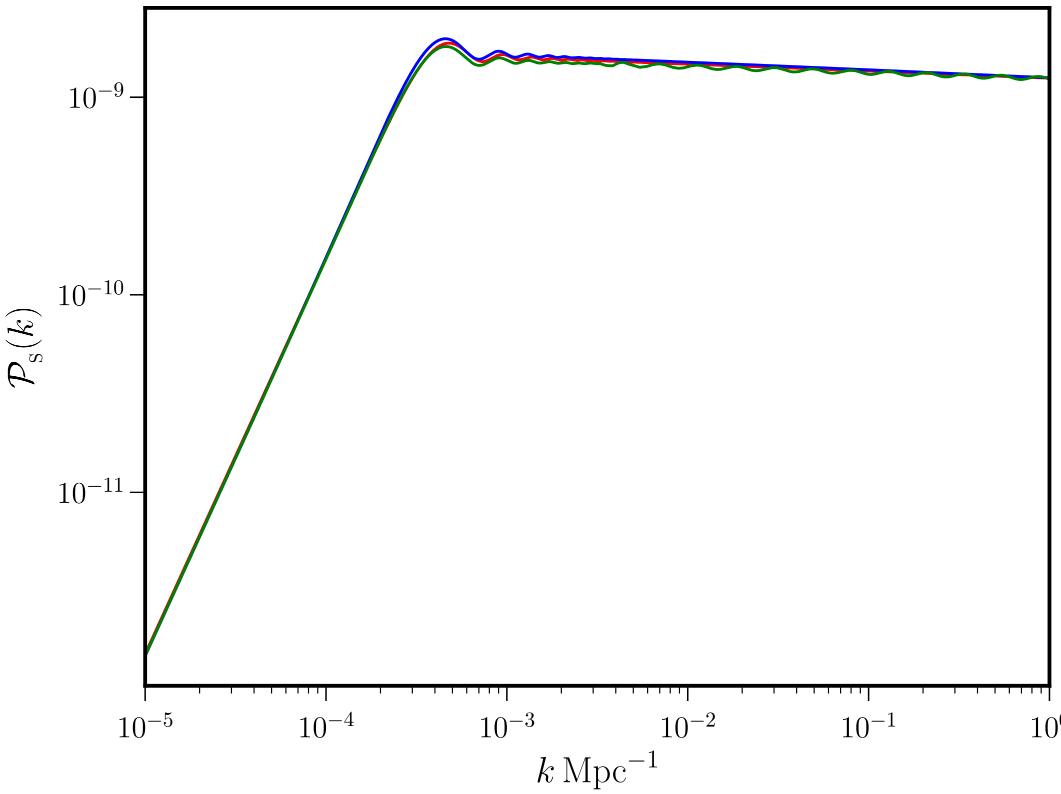

Figure A.1: The scalar power spectra in a small field inflationary model (in blue) and the axion monodromy model (in green) with kinetically dominated initial conditions have been plotted along with the power spectrum in the case of QPa (in red). The parameters have been chosen so that the features of the power spectra match at large scales.

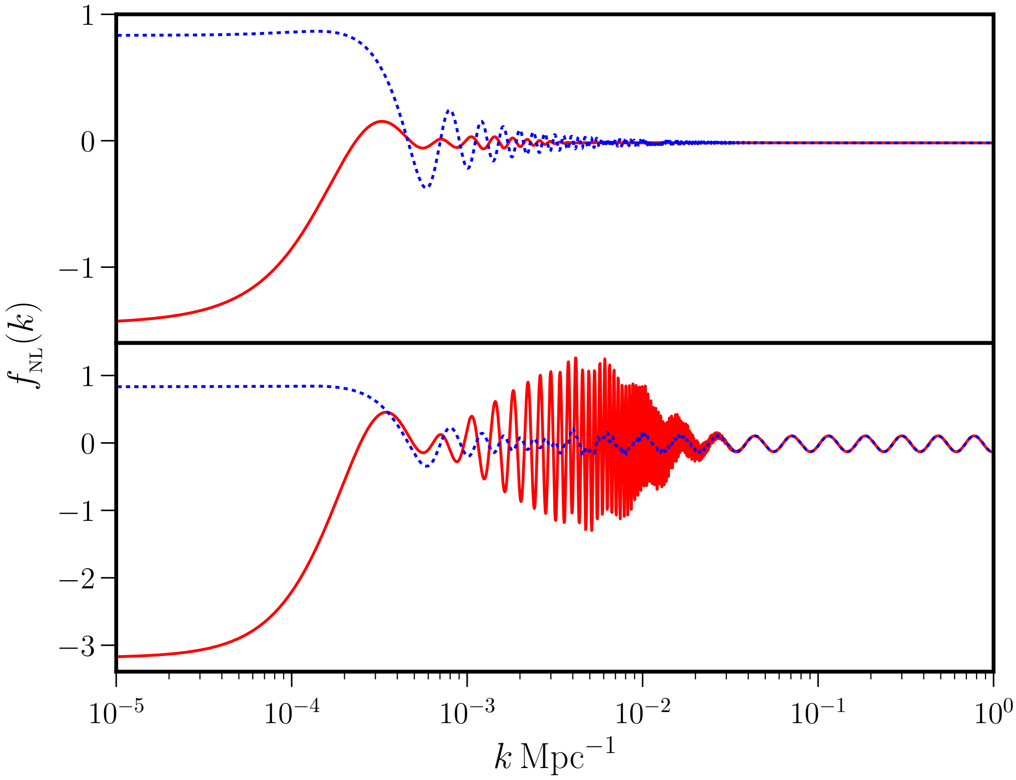

Figure A.2: The behavior of the scalar non-Gaussianity parameter $f_{\rm NL}$ in the squeezed limit has been plotted (in red) for the small field inflationary model (on top) and the axion monodromy model (at the bottom). Just as we had done earlier, we have also plotted the quantity $f_{\rm NL}^{\rm CR}$ (in blue). As in the cases of QP and SMI, while the consistency condition is violated at large scales, it is restored at small scales. This is clearly evident in the case of the axion monodromy model which is known to exhibit oscillations in the power spectrum as well as in the bispectrum even at small scales.

APPENDIX B

The dichotomy of ultra slow roll and punctuated inflation

With the help of an example, in this appendix, we shall illustrate that a given inflationary potential can permit ultra slow roll as well as punctuated inflation for different sets of parameters. The potential that we shall consider, when expressed in terms of the quantity $x = \phi/v$ that we had introduced in the context of USR1, is given by [161]

$$V(\phi) = V_0 \, \frac{\alpha\, x^2 - \beta\, x^4 + \gamma\, x^6}{(1 + \delta\, x^2)^2}. \tag{B.1}$$

In Fig. B.1, we have plotted the evolution of the first slow roll parameter ϵ_1 in the above potential for the following two sets of parameters: $V_0/M_{\rm Pl}^4 = 1.3253 \times 10^{-9}$, $\gamma = 1$, $\delta = 1.5092$ and $(v/M_{\rm Pl}, \alpha, \beta) = (4.3411, 8.522 \times 10^{-2}, 0.469)$ and $(10, 8.53 \times 10^{-2}, 0.458)$. We obtain about 75 e-folds of inflation in these cases for $\phi_{\rm i} = 17.245\, M_{\rm Pl}$ and $\phi_{\rm i} = 13.4\, M_{\rm Pl}$. It is clear from the figure that, while the first set of parameters lead to punctuated inflation, the second set does not permit an interruption of inflation until the very end. This example illustrates the point that a potential itself cannot be classified as an ultra slow roll or a punctuated inflationary model.

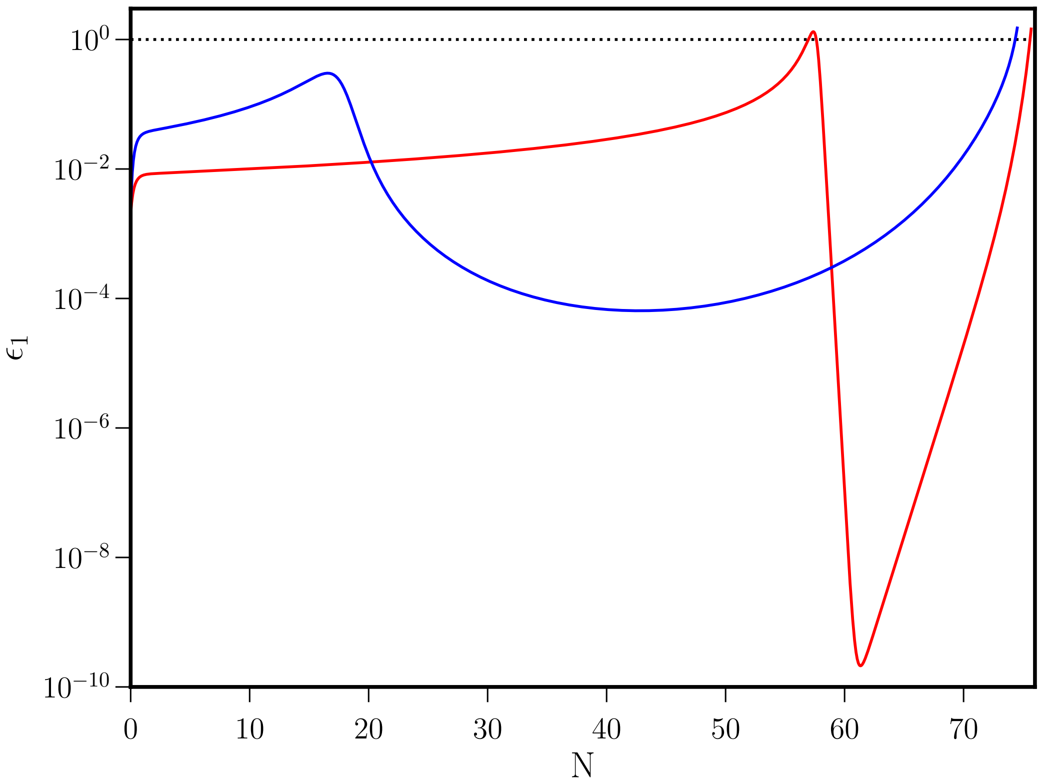

Figure B.1: The behavior of the first slow roll parameter ϵ_1 has been plotted for two sets of parameters describing the potential (B.1) and suitable initial conditions that lead to about 75 e-folds of inflation. Note that the first set of values for the parameters leads to punctuated inflation with ϵ_1 (plotted in red) crossing unity (indicated as a dotted horizontal line) twice, once prior to the regime of ultra slow roll and eventually when inflation terminates. The second set of parameters leads to an extended period of ultra slow roll (plotted in blue) without any interruption of inflation until the very end.

APPENDIX C

The functional forms of the polarization factors

Recall that, $e^\lambda(\boldsymbol{k},\boldsymbol{p}) = e^\lambda_{ij}(\boldsymbol{k})\, p^i\, p^j$. For our choice of $(\boldsymbol{k}_1,\boldsymbol{k}_2,\boldsymbol{k}_3)$ and $(\boldsymbol{p}_1,\boldsymbol{p}_2,\boldsymbol{p}_3)$ [*cf.* Eqs. (3.18) and (3.19)], we find that $e^\lambda(\boldsymbol{k},\boldsymbol{p})$ can be evaluated to be

$$e^+(\boldsymbol{k}_1,\boldsymbol{p}_1) = \frac{1}{4\sqrt{2}}\left(3\,p_{1x}^2 + p_{1y}^2 - 2\sqrt{3}\,p_{1x}\,p_{1y} - 4\,p_{1z}^2\right), \tag{C.1a}$$

$$e^+(\boldsymbol{k}_2,\boldsymbol{p}_2) = \frac{1}{4\sqrt{2}}\Bigg(3\,p_{1x}^2 + 3\,k^2 + p_{1y}^2 + 2\sqrt{3}\,p_{1x}\,p_{1y} - 6\,k\,p_{1x} \tag{C.1b}$$

$$- 2\sqrt{3}\,k\,p_{1y} - 4\,p_{1z}^2\Bigg), \tag{C.1c}$$

$$e^+(\boldsymbol{k}_3,\boldsymbol{p}_3) = \frac{1}{\sqrt{2}}\left(p_{1y}^2 - p_{1z}^2\right), \tag{C.1d}$$

$$e^\times(\boldsymbol{k}_1,\boldsymbol{p}_1) = -\frac{1}{\sqrt{2}}\left(\sqrt{3}\,p_{1x} - p_{1y}\right)\,p_{1z}, \tag{C.1e}$$

$$e^\times(\boldsymbol{k}_2,\boldsymbol{p}_2) = \frac{1}{\sqrt{2}}\left[\sqrt{3}\,(p_{1x} - k) + p_{1y}\right]\,p_{1z}, \tag{C.1f}$$

$$e^\times(\boldsymbol{k}_3,\boldsymbol{p}_3) = -\sqrt{2}\,p_{1y}\,p_{1z}. \tag{C.1g}$$

APPENDIX D

A closer examination of the consistency relation

We had pointed out that, in the squeezed limit, *i.e.* when $k_1 \to 0$ and $k_2 \simeq k_3 = k$, the scalar non-Gaussianity parameter $f_{_{\rm NL}}$ is expected to satisfy the consistency condition (2.11). In the results presented earlier (in Figs. 3.11 and 3.12), we had worked with $k_1 = 10^{-3}\, k$ to arrive at $f_{_{\rm NL}}$ in the squeezed limit. While we find that the consistency condition is satisfied to better than 5% over a wide range of scales, we notice that there is some departure around wave numbers corresponding to the peak in the scalar power spectrum. To investigate this point more closely, in Fig. D.1, we have plotted the numerical results around the peak in the scalar power spectrum for the original choice of k_1 as well as for $k_1 = 10^{-1}\, k$ and $k_1 = 10^{-5}\, k$ in the case of the model PI3. We have considered the case of $k_1 = 10^{-1}\, k$ since we find that roughly a decade of modes exit the Hubble radius during the ultra slow roll phase. Evidently, such a value of k_1 would be insufficient for it to be considered a squeezed mode. We find that the value of $f_{_{\rm NL}}$ remains of order unity even when we confine to modes which leave the Hubble radius during the period of ultra slow roll. Also, as one would expect, we find that the consistency condition is satisfied better and better as we work with a smaller value of k_1. We should clarify that adequate care needs to be taken while evaluating the integrals involved in the calculation of the bispectrum during the ultra slow roll regime. Since there occur rapid changes in the slow roll parameters during this epoch, we should regulate the integrals with an appropriate choice for the cut-off parameter κ, especially for the dominant contribution $G_4(\boldsymbol{k}_1, \boldsymbol{k}_2, \boldsymbol{k}_3)$ [*cf.* Eqs. (1.24)]. With an appropriate cut-off and with smaller values for the squeezed mode k_1, we find that the match between $f_{_{\rm NL}}$ and $f_{_{\rm NL}}^{_{\rm CR}}$ indeed improves. Nevertheless, even with a smaller of choice of k_1, we still notice some difference near the peak in the power spectrum. We feel that this is an artefact and we believe that the difference can be overcome with a further smaller value for k_1. However, working with a very small k_1 poses certain numerical challenges, and we will leave it for future investigation. We should mention that this is an independent issue and stress that it does not affect our main conclusions related to PBHs and GWs.

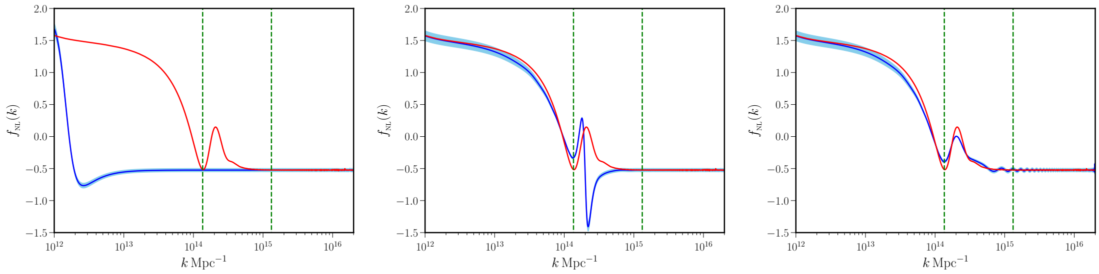

Figure D.1: The non-Gaussianity parameter $f_{\rm NL}$ in the squeezed limit (in blue) and the consistency condition $f_{\rm NL}^{\rm CR}$ (in red) have been plotted for the model PI3 over wave numbers around the peak in the scalar power spectrum. We have set the squeezed mode to be $k_1 = 10^{-1}\,k$ (on the left), $k_1 = 10^{-3}\,k$ (in the middle) and $k_1 = 10^{-5}\,k$ (on the right) in plotting these figures. We have also indicated the 5% uncertainty in our numerical estimate as bands (in blue). Moreover, we have demarcated the range of modes (by vertical, dashed, green lines) that leave the Hubble radius during the epoch of ultra slow roll in the model. Obviously, the choice of $k_1 = 10^{-1}\,k$ is insufficient for k_1 to be considered a squeezed mode. Such a choice has been made to illustrate the point that the value of $f_{\rm NL}$ proves to be of order unity even when we confine to modes that leave the Hubble radius during the period of ultra slow roll. Evidently, there is an improvement in the extent to which the consistency condition is satisfied when we choose to work with smaller and smaller values of k_1. Though the match improves as we work with a smaller k_1, we still seem to notice some deviation. This is possibly an artefact arising due to the reason that, numerically, we are unable to work with an adequately small value of k_1.

APPENDIX E

Asymptotic behavior of the curvature perturbations

As we mentioned, it has been shown that an indefinite ultra slow roll regime of inflation leads to the violation of the consistency condition [137, 138]. Since all the models of our interest contain an ultra slow roll phase, one may wonder if a violation of the consistency condition would occur in these cases. As we have seen, the consistency condition is satisfied in all the cases we have considered. This is primarily due to the fact that the ultra slow roll phase lasts only for a finite duration in our models, permitting the eventual freezing of the amplitude of the curvature perturbations.

In this appendix, we shall illustrate this point with the aid of a truncated version of the scenario RS1. We shall consider the following two functional forms for $\epsilon_1(N)$:

$$\epsilon_1^{\mathrm{III}}(N) = \left[\epsilon_{1a}\,(1+\epsilon_{2a}\,N)\right]\left[1-\tanh\left(\frac{N-N_1}{\Delta N_1}\right)\right], \tag{E.1a}$$

$$\epsilon_1^{\mathrm{IV}}(N) = \left[\epsilon_{1a}\,(1+\epsilon_{2a}\,N)\right]\left[1-\tanh\left(\frac{N-N_1}{\Delta N_1}\right)\right] + \epsilon_{1b}. \tag{E.1b}$$

Evidently, while the first choice leads to an indefinite period of ultra slow roll beyond the e-fold N_1, the second choice restores slow roll when $\epsilon_1(N)$ attains the value of ϵ_{1b}. In Fig. E.1, we have plotted the behavior of these slow roll parameters as well as the evolution of the curvature perturbation for three modes which leave the Hubble radius just prior to and after the onset of the ultra slow roll phase. We have worked with the following values for parameters involved in plotting the figure: $\epsilon_{1a} = 10^{-4}$, $\epsilon_{2a} = 0.05$, $N_1 = 42$, $\Delta N_1 = 0.5$ and $\epsilon_{1b} = 10^{-10}$. It should be clear that, while the amplitude of the curvature perturbations grow indefinitely when the ultra slow roll continues, the amplitude freezes when slow roll inflation is restored.

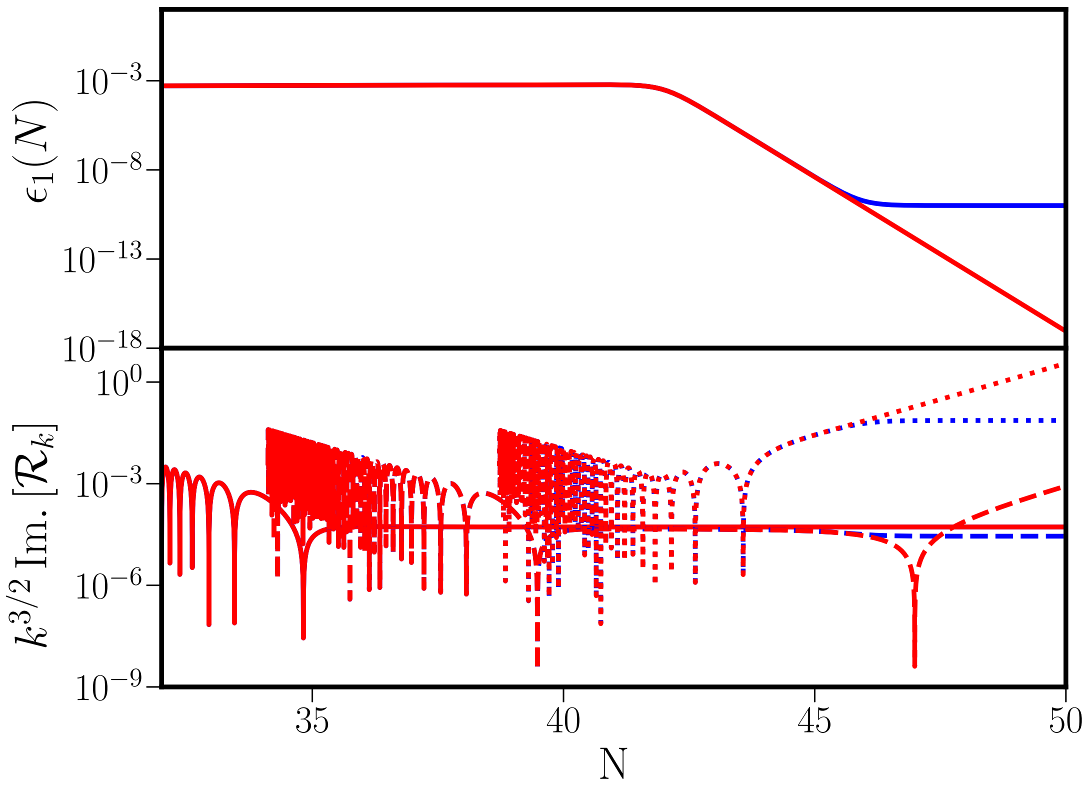

Figure E.1: The functional forms $\epsilon_1^{\rm III}(N)$ (in red) and $\epsilon_1^{\rm IV}(N)$ (in blue) for the first slow roll parameter have been plotted as a function of e-folds (on top). We have also illustrated the evolution of the dominant imaginary part of the curvature perturbation $\mathcal{R}_k$ for three representative modes in these two scenarios (as solid, dashed and dotted curves, in red and blue, respectively, at the bottom). It is easy to see that (upon comparison of, say, the dotted red and blue curves) that the end of the ultra slow phase ensures that the amplitude of the curvature perturbations eventually freeze.

APPENDIX F

The steepest growth of the scalar power spectrum

In models of ultra slow roll and punctuated inflation, we have seen that the scalar power grows rapidly from its COBE normalized values on the CMB scales to higher values at smaller scales over wave numbers that leave the Hubble radius during the transition from slow roll to ultra slow roll. An interesting issue that is worth understanding is the steepest such growth that is possible in models of inflation driven by a single, canonical scalar field. It has been argued that the fastest growth will have $n_{\rm s} - 1 \simeq 4$ over this range of wave numbers (in this context, see Ref. [194]; also see Ref. [199]). We find that the reconstructed scenarios RS1 and RS2 easily permit us to examine this issue. Recall that, in these scenarios, the parameter ΔN_1 determines the rapidity of the transition from the slow roll to the ultra slow roll regime [*cf.* Eqs. (3.10)]. We find that it is this parameter that dictates the steepness of the growth in the corresponding scalar power spectra, with smaller ΔN_1 producing a faster rise. We have examined the rate of growth in the cases of RS1 and RS2 by varying ΔN_1 over a certain range, while keeping the other parameters fixed. In Fig. F.1, we have illustrated the spectra for four values of ΔN_1 which are relatively smaller than those we had used for the reconstructions discussed earlier. It should be clear from the figure that, in the case of RS1, the rise is fairly steady as the value of ΔN_1 is made smaller, with $n_{\rm s} - 1 \simeq 4$ over the growing regime. In the case of RS2, we find that $n_{\rm s} - 1$ varies between 4 and 6 over the growing regime and therefore corresponds to a steeper but non-uniform growth of the spectra.

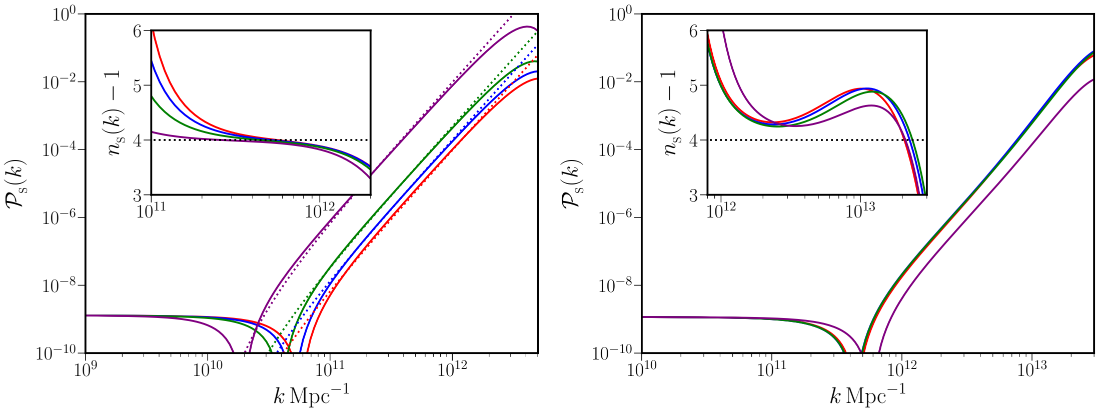

Figure F.1: The scalar power spectra around the region where they exhibit the sharpest growth have been plotted in the cases of RS1 (on the left) and RS2 (on the right) for a set of values of ΔN_1. We have plotted the spectra for the following four values of ΔN_1: $(0.1, 0.08, 0.05, 0.01)$ (in red, blue, green and purple, respectively). The insets illustrate the corresponding spectral indices $n_{\rm s}-1$. We have also indicated the k^4 behavior in the case of RS1 (as dotted lines of corresponding colors on the left) to show how well it matches the spectra during the growth. It should be evident that, while RS1 leads to a growth corresponding to $n_{\rm s}-1 \simeq 4$, RS2 permits a steeper but non-uniform growth with $n_{\rm s}-1$ varying between 4 and 6 over the relevant wave numbers.

APPENDIX G

The dominant contributions to the scalar bispectrum

In this appendix, we shall provide the complete expressions describing the dominant contributions to the scalar bispectrum evaluated in a squeezed initial state. For a generic $\alpha(k)$ and $\beta(k)$, these contributions are given by the following expressions (in this context, see for example, Refs. [264, 268, 270, 271]):

$$
\begin{aligned}
G_1(\boldsymbol{k}_1,\boldsymbol{k}_2,\boldsymbol{k}_3) &= \frac{H_{_\mathrm{I}}^4}{32\,M_{_\mathrm{Pl}}^4\,\epsilon_1}\,\frac{\vert\alpha_1\vert^2\,\vert\alpha_2\vert^2\,\vert\alpha_3\vert^2}{k_1\,k_2\,k_3}\,\frac{(1-\delta_1)\,(1-\delta_2)\,(1-\delta_3)}{k_1^2}\\
&\quad\times\Biggl[\frac{1+\delta_1^\ast\,\delta_2^\ast\,\delta_3^\ast}{k_{_\mathrm{T}}}\,\left(1+\frac{k_1}{k_{_\mathrm{T}}}\right)\\
&\quad+\frac{\delta_1^\ast+\delta_2^\ast\,\delta_3^\ast}{k_1-k_2-k_3}\,\left(1+\frac{k_1}{k_1-k_2-k_3}\right)\\
&\quad+\frac{\delta_2^\ast+\delta_1^\ast\,\delta_3^\ast}{k_2-k_1-k_3}\,\left(1-\frac{k_1}{k_2-k_1-k_3}\right)\\
&\quad+\frac{\delta_3^\ast+\delta_1^\ast\,\delta_2^\ast}{k_3-k_1-k_2}\,\left(1-\frac{k_1}{k_3-k_1-k_2}\right)\Biggr]\\
&\quad+\mathrm{complex\ conjugate}+\mathrm{two\ permutations}, \qquad\qquad (\mathrm{G.1a})\\
G_2(\boldsymbol{k}_1,\boldsymbol{k}_2,\boldsymbol{k}_3) &= -\frac{H_{_\mathrm{I}}^4}{64\,M_{_\mathrm{Pl}}^4\,\epsilon_1}\,\frac{(k_1^2+k_2^2+k_3^2)}{(k_1\,k_2\,k_3)^3}\\
&\quad\times\vert\alpha_1\vert^2\,\vert\alpha_2\vert^2\,\vert\alpha_3\vert^2\,\left(1-\delta_1\right)\,\left(1-\delta_2\right)\,\left(1-\delta_3\right)\\
&\quad\times\Biggl\{\Biggl[\frac{i}{\eta_\mathrm{e}}\Biggl(\mathrm{e}^{i\,k_{_\mathrm{T}}\,\eta_\mathrm{e}}-\delta_1^\ast\,\mathrm{e}^{i\,(-k_1+k_2+k_3)\,\eta_\mathrm{e}}\\
&\quad-\delta_2^\ast\,\mathrm{e}^{i\,(k_1-k_2+k_3)\,\eta_\mathrm{e}}-\delta_3^\ast\,\mathrm{e}^{i\,(k_1+k_2-k_3)\,\eta_\mathrm{e}}\\
&\quad+\delta_2^\ast\,\delta_3^\ast\,\mathrm{e}^{-i\,(-k_1+k_2+k_3)\,\eta_\mathrm{e}}+\delta_1^\ast\,\delta_3^\ast\,\mathrm{e}^{-i\,(k_1-k_2+k_3)\,\eta_\mathrm{e}}\\
&\quad+\delta_1^\ast\,\delta_2^\ast\,\mathrm{e}^{-i\,(k_1+k_2-k_3)\,\eta_\mathrm{e}}-\delta_1^\ast\,\delta_2^\ast\,\delta_3^\ast\,\mathrm{e}^{-i\,k_{_\mathrm{T}}\,\eta_\mathrm{e}}\Biggr)\Biggr]_{\eta_\mathrm{e}\to 0}\\
&\quad+\left(1+\delta_1^\ast\,\delta_2^\ast\,\delta_3^\ast\right)\,\frac{(k_1\,k_2+k_2\,k_3+k_1\,k_3)}{k_{_\mathrm{T}}}\\
&\quad+\left(\delta_1^\ast+\delta_2^\ast\,\delta_3^\ast\right)\,\frac{(k_1\,k_2-k_2\,k_3+k_1\,k_3)}{(-k_1+k_2+k_3)}\\
&\quad+\left(\delta_2^\ast+\delta_1^\ast\,\delta_3^\ast\right)\,\frac{(k_1\,k_2+k_2\,k_3-k_1\,k_3)}{(k_1-k_2+k_3)}\\
&\quad+\left(\delta_3^\ast+\delta_1^\ast\,\delta_2^\ast\right)\,\frac{(-k_1\,k_2+k_2\,k_3+k_3\,k_1)}{(k_1+k_2-k_3)}\\
&\quad+k_1\,k_2\,k_3\,\Biggl[\frac{1+\delta_1^\ast\,\delta_2^\ast\,\delta_3^\ast}{k_{_\mathrm{T}}^2}+\frac{(\delta_1^\ast+\delta_2^\ast\,\delta_3^\ast)}{(-k_1+k_2+k_3)^2}
\end{aligned}
$$

$$
\begin{aligned}
& \quad + \frac{(\delta_2^* + \delta_1^*\,\delta_3^*)}{(k_1 - k_2 + k_3)^2} + \frac{(\delta_3^* + \delta_1^*\delta_2^*)}{(k_1 + k_2 - k_3)^2}\Bigg] \\
& \quad + \text{complex conjugate}, \qquad \text{(G.1b)} \\
G_3(\boldsymbol{k}_1, \boldsymbol{k}_2, \boldsymbol{k}_3) &= -\frac{H_{\rm I}^4}{32\,M_{\rm Pl}^4\,\epsilon_1}\,\frac{|\alpha_1|^2\,|\alpha_2|^2\,|\alpha_3|^2}{k_1\,k_2\,k_3}\,\frac{(1-\delta_1)\,(1-\delta_2)\,(1-\delta_3)}{k_1^2} \\
& \quad \times \frac{(k_2^2 - k_3^2)^2 - k_1^2\,(k_2^2 + k_3^2)}{2\,k_2^2\,k_3^2} \\
& \quad \times \Bigg[\frac{1 + \delta_1^*\,\delta_2^*\,\delta_3^*}{k_{\rm T}}\,\left(1 + \frac{k_1}{k_{\rm T}}\right) \\
& \quad + \frac{\delta_1^* + \delta_2^*\,\delta_3^*}{k_1 - k_2 - k_3}\,\left(1 + \frac{k_1}{k_1 - k_2 - k_3}\right) \\
& \quad + \frac{\delta_2^* + \delta_1^*\,\delta_3^*}{k_2 - k_1 - k_3}\,\left(1 - \frac{k_1}{k_2 - k_1 - k_3}\right) \\
& \quad + \frac{\delta_3^* + \delta_1^*\,\delta_2^*}{k_3 - k_1 - k_2}\,\left(1 - \frac{k_1}{k_3 - k_1 - k_2}\right)\Bigg] \\
& \quad + \text{complex conjugate} + \text{two permutations}, \qquad \text{(G.1c)} \\
G_7(\boldsymbol{k}_1, \boldsymbol{k}_2, \boldsymbol{k}_3) &= \frac{H_{\rm I}^4\,\epsilon_2}{32\,M_{\rm Pl}^4\epsilon_1^2}\,\Bigg[\frac{1}{(k_1\,k_2)^3}\,|\alpha_1|^2\,|\alpha_2|^2 \\
& \quad \times\,(1-\delta_1)\,\,(1-\delta_1^*)\,\,(1-\delta_2)\,\,(1-\delta_2^*) \\
& \quad + \text{two permutations}\Bigg], \qquad \text{(G.1d)}
\end{aligned}
$$

where $k_{\rm T} = k_1 + k_2 + k_3$ and, for convenience, we have set $\alpha(k_i) = \alpha_i$ and $\delta(k_i) = \delta_i$ for $i = \{1, 2, 3\}$. Note that, we can write

$$
|\alpha(k)|^2 = \left[1 - |\delta(k)|^2\right]^{-1} \qquad \text{(G.2)}
$$

so that the complete bispectrum can be expressed in terms of the function $\delta(k)$, which in turn is determined by the feature $g(k)$ in the power spectrum [*cf.* Eqs. (4.6) and (4.7)].

APPENDIX H

Feynman diagrams for non-Gaussian contributions to $\Omega_{\rm GW}$

In order to understand various non-Gaussian contributions to the secondary GWs, one can construct Feynman diagrams representing these contributions (see, for instance, Refs. [190, 295, 298]). In this appendix, we shall define the elements constituting these diagrams and present the diagrams corresponding to the contributions we discussed in Sec. 5.4.

The basic elements that we shall be using for the diagrams are the scalar power spectrum $\mathcal{P}_{\rm S}(k)$, secondary tensor power spectrum $\mathcal{P}_h(k)$, the scalar non-Gaussianity parameter $f_{\rm NL}(\boldsymbol{k}_1, \boldsymbol{k}_2, \boldsymbol{k}_3)$ and the correction to the scalar power spectrum $\mathcal{P}_{\rm C}(k)$. These diagrams are presented in Fig. H.1. Note that the diagram representing the secondary tensor power spectrum $\mathcal{P}_h(k)$ indicates that it is a first loop correction to the primary tensor power specrum $\mathcal{P}_{\rm T}(k)$, due to the interaction between the tensor and scalar perturbations at the second order (as expected from our discussion in Subsec. 1.2.3). The functions $\mathcal{I}(k, k')$ and $Q^\lambda(k, k')$ arising out of the transfer function and polarization tensor, can be accounted at the vertices connecting the secondary tensor and scalar modes in the diagram of $\mathcal{P}_h(k)$. The diagram of $f_{\rm NL}(\boldsymbol{k}_1, \boldsymbol{k}_2, \boldsymbol{k}_3)$ represents the interaction of scalar perturbations $\mathcal{R}_{\boldsymbol{k}}$ at the cubic order (as can be expected from our discussions in Subsec. 1.1.3 and Sec. 5.2). Further, the diagram of $\mathcal{P}_{\rm C}(k)$ indicates that it is a one loop correction to the scalar power spectrum $\mathcal{P}_{\rm S}(k)$ due to such cubic order interaction. It involves two vertices of $f_{\rm NL}$ and hence we readily infer that $\mathcal{P}_{\rm C}(k)$ shall be proportional to $f_{\rm NL}^2$. Using these elements we can construct the diagrams for higher order contributions to secondary tensor power spectrum $\mathcal{P}_h(k)$ due to scalar non-Gaussianity. These shall be higher order loop diagrams arising due to introduction of the vertex of $f_{\rm NL}$ in each arm of the loop in the diagram of $\mathcal{P}_h(k)$.

The diagrams representing non-Gaussian contributions to $\mathcal{P}_h(k)$ at the level of $f_{\rm NL}^2$, $\mathcal{P}_h^{(2-i)}(k)$, are presented in Fig. H.2. These diagrams arise due to the introduction of $f_{\rm NL}$ in two of the four arms of the loop in the diagram of $\mathcal{P}_h(k)$. They are called as C-type, hybrid and Z-type diagrams [295].

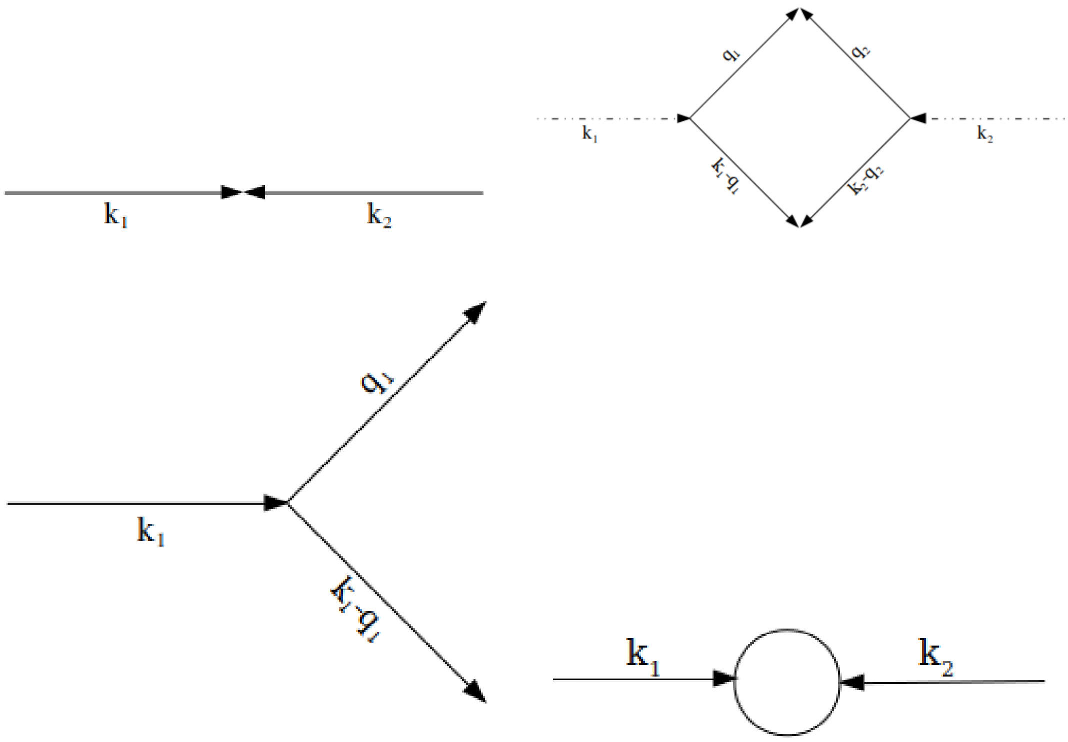

Figure H.1: The Feynman diagrams representing the scalar power spectrum $\mathcal{P}_{\mathrm{S}}(k_1)$ (on top left), secondary tensor power spectrum $\mathcal{P}_h(k_1)$ (on top right) are presented. We also present the diagrams for the scalar non-Gaussianity parameter $f_{\mathrm{NL}}(\boldsymbol{k}_1, \boldsymbol{q}_1, \boldsymbol{k}_1 - \boldsymbol{q}_1)$ (on bottom left) and the correction to the scalar power $\mathcal{P}_{\mathrm{C}}(k_1)$ (on bottom right). We use solid lines to represent the scalar mode $\mathcal{R}_{\boldsymbol{k}}$ and dashed-dotted line to represent the secondary tensor mode $h_{\boldsymbol{k}}$.

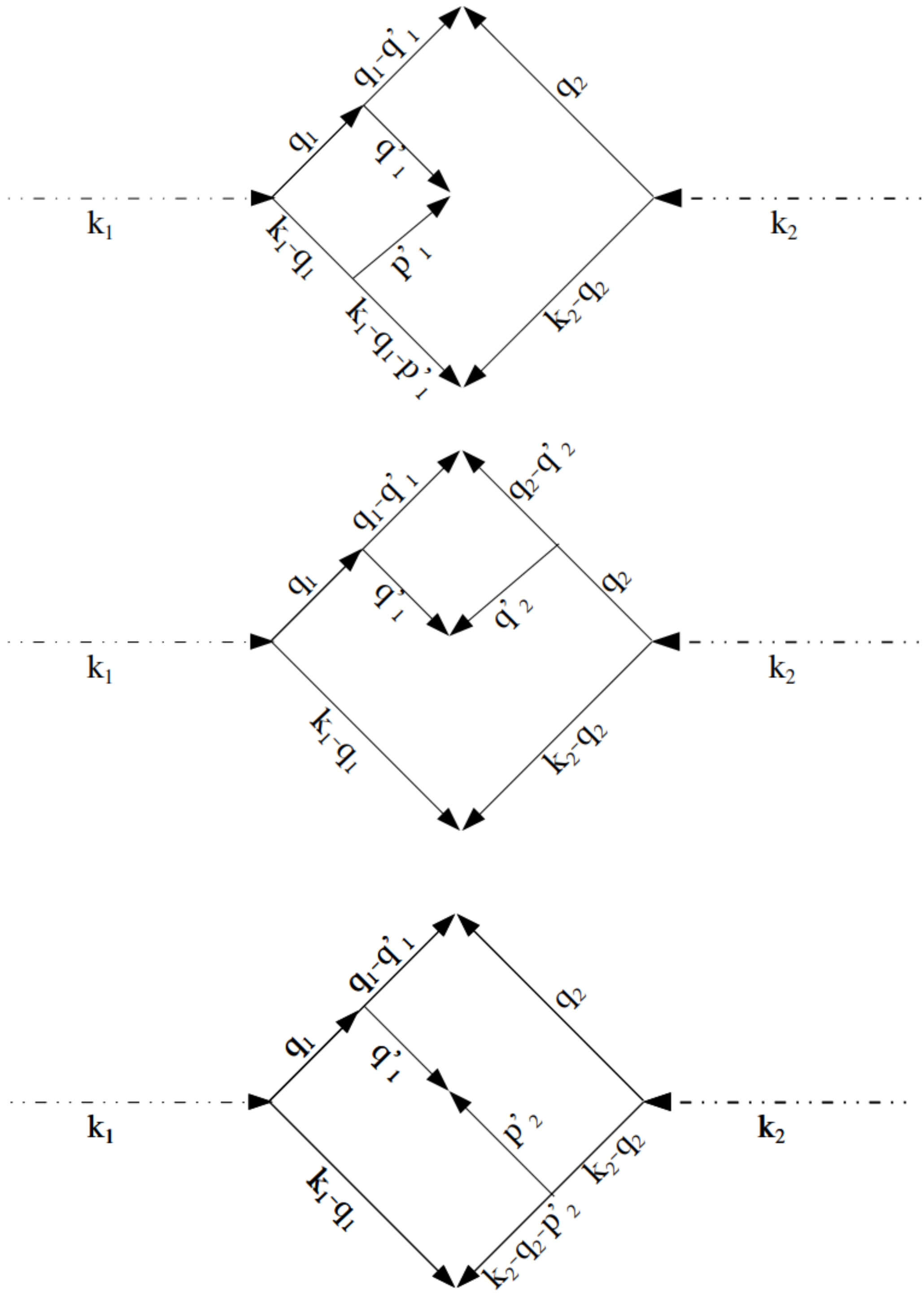

Figure H.2: The Feynman diagrams representing the non-Gaussian contributions at the level of $f_{\rm NL}^2$ are presented. The term denoted as $\mathcal{P}_h^{(2-1)}(k)$ corresponds to the C-type diagram (on top) and the term denoted as $\mathcal{P}_h^{(2-2)}(k)$ corresponds to the diagram known as the hybrid type (in the middle). The term denoted as $\mathcal{P}_h^{(2-3)}(k)$ corresponds to the Z-type diagram (at the bottom).

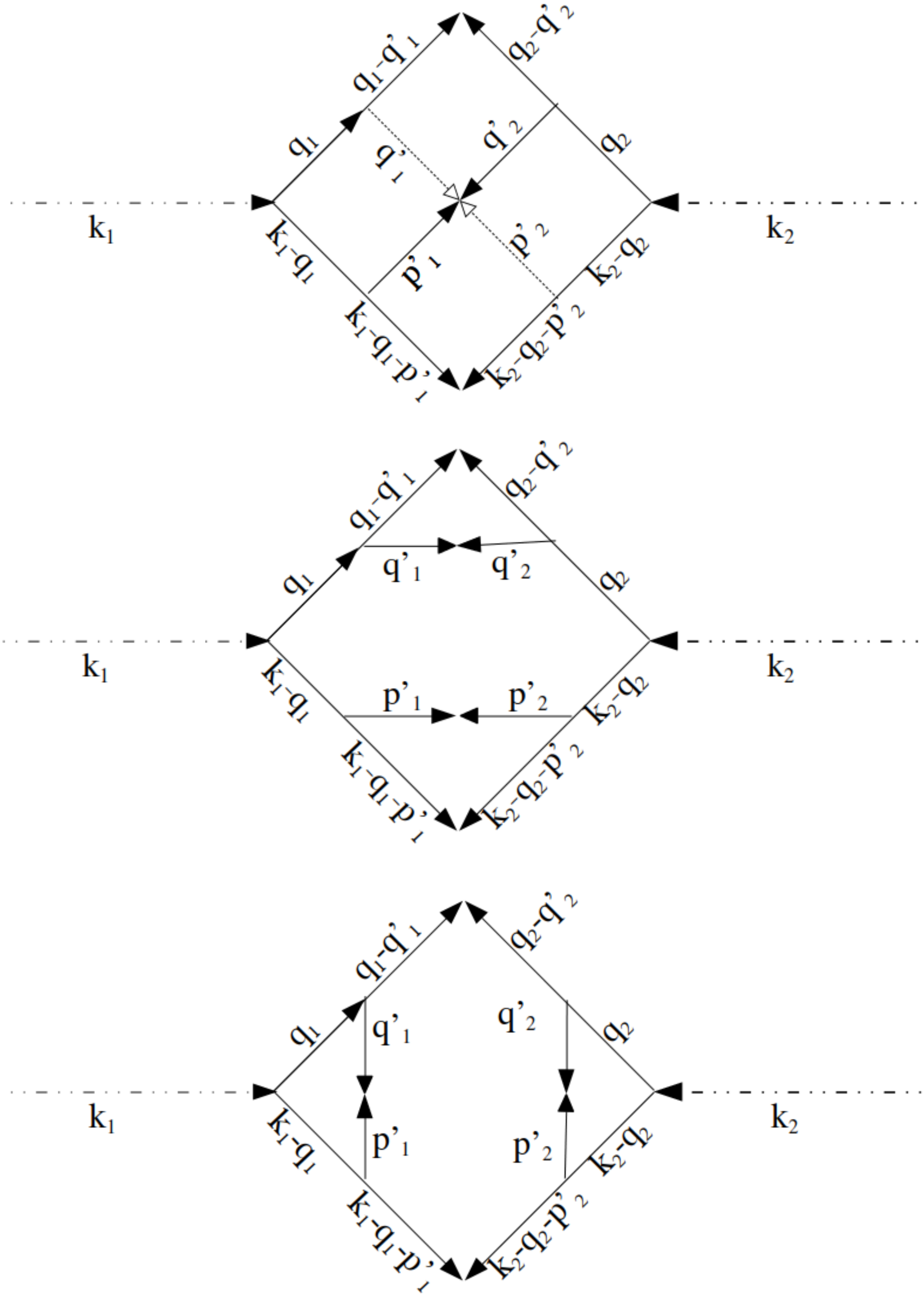

Figure H.3: The Feynman diagrams representing the non-Gaussian contributions at the level of $f_{\rm NL}^4$ are presented. The term denoted as $\mathcal{P}_h^{(4-1)}(k)$ corresponds to non-planar diagram (on top) and the term denoted as $\mathcal{P}_h^{(4-2)}(k)$ corresponds to the diagram known as reducible term (in the middle). The term denoted as $\mathcal{P}_h^{(4-3)}(k)$ corresponds to the planar diagram (at the bottom).

The diagrams representing non-Gaussian contributions to $\mathcal{P}_h(k)$ at the level of $f^4_{\rm NL}$ *i.e.* $\mathcal{P}_h^{(4-i)}(k)$, are presented in Fig. H.3. These diagrams arise when we introduce of $f_{\rm NL}$ in all the four arms of the loop in the diagram of $\mathcal{P}_h(k)$. They are called as non-planar, reducible and planar diagrams [295].

REFERENCES

[1] V. F. Mukhanov, H. A. Feldman, and R. H. Brandenberger, Phys. Rept. **215**, 203 (1992).

[2] A. D. Linde, *Particle physics and inflationary cosmology*, Vol. 5 (1990) arXiv:hep-th/0503203.

[3] J. Martin, *Particles and fields. Proceedings, 24th National Meeting, ENFPC 24, Caxambu, Brazil, September 30-October 4, 2003*, Braz. J. Phys. **34**, 1307 (2004), arXiv:astro-ph/0312492 [astro-ph].

[4] D. Baumann, in *Physics of the large and the small, TASI 09, proceedings of the Theoretical Advanced Study Institute in Elementary Particle Physics, Boulder, Colorado, USA, 1-26 June 2009* (2011) pp. 523–686, arXiv:0907.5424 [hep-th].

[5] L. Sriramkumar, (2009), arXiv:0904.4584 [astro-ph.CO].

[6] Y. Akrami *et al.* (Planck), Astron. Astrophys. **641**, A10 (2020), arXiv:1807.06211 [astro-ph.CO].

[7] J. Martin, C. Ringeval, and V. Vennin, Phys. Dark Univ. **5-6**, 75 (2014), arXiv:1303.3787 [astro-ph.CO].

[8] B. J. Carr and S. W. Hawking, Mon. Not. Roy. Astron. Soc. **168**, 399 (1974).

[9] B. Carr, F. Kuhnel, and M. Sandstad, Phys. Rev. D **94**, 083504 (2016), arXiv:1607.06077 [astro-ph.CO].

[10] M. Maggiore, Phys. Rept. **331**, 283 (2000), arXiv:gr-qc/9909001.

[11] K. Inomata and T. Nakama, Phys. Rev. D **99**, 043511 (2019), arXiv:1812.00674 [astro-ph.CO].

[12] B. J. Carr, K. Kohri, Y. Sendouda, and J. Yokoyama, Phys. Rev. **D81**, 104019 (2010), arXiv:0912.5297 [astro-ph.CO].

[13] B. Carr, K. Kohri, Y. Sendouda, and J. Yokoyama, (2020), arXiv:2002.12778 [astro-ph.CO].

[14] C. Moore, R. Cole, and C. Berry, Class. Quant. Grav. **32**, 015014 (2015), arXiv:1408.0740 [gr-qc].

[15] S. Clesse, J. García-Bellido, and S. Orani, (2018), arXiv:1812.11011 [astro-ph.CO].

[16] H. V. Ragavendra, D. Chowdhury, and L. Sriramkumar, Springer Proc. Phys. **248**, 39 (2020), arXiv:1906.03942 [astro-ph.CO].

[17] H. V. Ragavendra, D. Chowdhury, and L. Sriramkumar, (2020), arXiv:2003.01099 [astro-ph.CO].

[18] H. V. Ragavendra, P. Saha, L. Sriramkumar, and J. Silk, Phys. Rev. D **103**, 083510 (2021), arXiv:2008.12202 [astro-ph.CO].

[19] H. V. Ragavendra, L. Sriramkumar, and J. Silk, JCAP **05**, 010, arXiv:2011.09938 [astro-ph.CO].

[20] H. V. Ragavendra, (2021), arXiv:2108.04193 [astro-ph.CO].

[21] E. W. Kolb and M. S. Turner, *The Early Universe* (Addison-Wesley, Redwood City, California, 1990).

[22] S. Dodelson, *Modern Cosmology* (Academic Press, Amsterdam, 2003).

[23] V. Mukhanov, *Physical Foundations of Cosmology* (Cambridge University Press, Cambridge, England, 2005).

[24] S. Weinberg, *Cosmology* (Oxford University Press, Oxford, England, 2008).

[25] R. Durrer, *The Cosmic Microwave Background* (Cambridge University Press, Cambridge, England, 2008).

[26] D. H. Lyth and A. R. Liddle, *The Primordial Density Perturbation: Cosmology, Inflation and the Origin of Structure* (Cambridge University Press, Cambridge, England, 2009).

[27] H. Mo, F. v. d. Bosch, and S. White, *Galaxy Formation and Evolution* (Cambridge University Press, Cambridge, England, 2010).

[28] P. Peter and J.-P. Uzan, *Primordial Cosmology*, Oxford Graduate Texts (Oxford University Press, Oxford, England, 2013).

[29] D. Baumann and L. McAllister, *Inflation and String Theory*, Cambridge Monographs on Mathematical Physics (Cambridge University Press, Cambridge, England, 2015) arXiv:1404.2601 [hep-th].

[30] J. Martin, *Planck scale effects in astrophysics and cosmology. Proceedings, 40th Karpacs Winter School, Ladek Zdroj, Poland, February 4-14, 2004*, Lect. Notes Phys. **669**, 199 (2005), arXiv:hep-th/0406011 [hep-th].

[31] B. A. Bassett, S. Tsujikawa, and D. Wands, Rev. Mod. Phys. **78**, 537 (2006).

[32] D. Baumann and H. V. Peiris, Adv. Sci. Lett. **2**, 105 (2009), arXiv:0810.3022 [astro-ph].

[33] W. H. Kinney, (2009), arXiv:0902.1529 [astro-ph.CO].

[34] L. Sriramkumar, in *Vignettes in Gravitation and Cosmology*, edited by L. Sriramkumar and T. R. Seshadri (World Scientific, Singapore, 2012) pp. 207–249.

[35] A. Linde, in *Proceedings, 100th Les Houches Summer School: Post-Planck Cosmology: Les Houches, France, July 8 - August 2, 2013* (2015) pp. 231–316, arXiv:1402.0526 [hep-th].

[36] J. Martin, *The Cosmic Microwave Background*, Astrophys. Space Sci. Proc. **45**, 41 (2016), arXiv:1502.05733 [astro-ph.CO].

[37] G. Hinshaw *et al.* (WMAP), Astrophys. J. Suppl. **208**, 19 (2013), arXiv:1212.5226 [astro-ph.CO].

[38] N. Aghanim *et al.* (Planck), Astron. Astrophys. **641**, A6 (2020), arXiv:1807.06209 [astro-ph.CO].

[39] L. Amendola *et al.* (Euclid Theory Working Group), Living Rev. Rel. **16**, 6 (2013), arXiv:1206.1225 [astro-ph.CO].

[40] R. Scaramella *et al.* (Euclid), (2021), arXiv:2108.01201 [astro-ph.CO].

[41] J. N. Grieb *et al.* (BOSS), Mon. Not. Roy. Astron. Soc. **467**, 2085 (2017), arXiv:1607.03143 [astro-ph.CO].

[42] T. M. C. Abbott *et al.* (DES), Phys. Rev. D **98**, 043526 (2018), arXiv:1708.01530 [astro-ph.CO].

[43] M. J. Chapman *et al.*, (2021), arXiv:2106.14961 [astro-ph.CO].

[44] A. G. Riess *et al.*, (2021), arXiv:2112.04510 [astro-ph.CO].

[45] D. M. Scolnic *et al.* (Pan-STARRS1), Astrophys. J. **859**, 101 (2018), arXiv:1710.00845 [astro-ph.CO].

[46] D. Scolnic *et al.*, (2021), arXiv:2112.03863 [astro-ph.CO].

[47] E. Di Valentino, A. Melchiorri, and J. Silk, Astrophys. J. Lett. **908**, L9 (2021), arXiv:2003.04935 [astro-ph.CO].

[48] W. Yang, S. Pan, E. Di Valentino, O. Mena, and A. Melchiorri, JCAP **10**, 008, arXiv:2101.03129 [astro-ph.CO].

[49] A. A. Starobinsky, JETP Lett. **30**, 682 (1979).

[50] E. Fehlberg, *Low-order classical Runge-Kutta formulas with stepsize control and their application to some heat transfer problems*, Vol. 315 (National Aeronatics and Space Administration, Washington D.C., 1969).

[51] W. H. Press, S. A. Teukolsky, W. T. Vetterling, and B. P. Flannery, *Numerical Recipes: The Art of Scientific Computing*, 3rd ed. (Cambridge University Press, Cambridge, England, 2007).

[52] J. M. Maldacena, JHEP **05**, 013, arXiv:astro-ph/0210603 [astro-ph].

[53] D. Seery and J. E. Lidsey, JCAP **0506**, 003, arXiv:astro-ph/0503692 [astro-ph].

[54] H. Collins, (2011), arXiv:1101.1308 [astro-ph.CO].

[55] X. Chen, R. Easther, and E. A. Lim, JCAP **0804**, 010, arXiv:0801.3295 [astro-ph].

[56] D. K. Hazra, L. Sriramkumar, and J. Martin, JCAP **1305**, 026, arXiv:1201.0926 [astro-ph.CO].

[57] P. Ade *et al.* (Planck), Astron. Astrophys. **594**, A17 (2016), arXiv:1502.01592 [astro-ph.CO].

[58] Y. Akrami *et al.* (Planck), (2019), arXiv:1905.05697 [astro-ph.CO].

[59] X. Chen, Adv. Astron. **2010**, 638979 (2010), arXiv:1002.1416 [astro-ph.CO].

[60] J. Martin and L. Sriramkumar, JCAP **1201**, 008, arXiv:1109.5838 [astro-ph.CO].

[61] F. Arroja and T. Tanaka, JCAP **1105**, 005, arXiv:1103.1102 [astro-ph.CO].

[62] N. Aghanim *et al.* (Planck), Astron. Astrophys. **641**, A5 (2020), arXiv:1907.12875 [astro-ph.CO].

[63] A. Lewis and S. Bridle, Phys. Rev. D **66**, 103511 (2002), arXiv:astro-ph/0205436.

[64] A. Lewis, A. Challinor, and A. Lasenby, Astrophys. J. **538**, 473 (2000), arXiv:astro-ph/9911177.

[65] A. Lewis, (2019), arXiv:1910.13970 [astro-ph.IM].

[66] P. Creminelli, A. Nicolis, L. Senatore, M. Tegmark, and M. Zaldarriaga, JCAP **05**, 004, arXiv:astro-ph/0509029.

[67] L. Senatore, K. M. Smith, and M. Zaldarriaga, JCAP **01**, 028, arXiv:0905.3746 [astro-ph.CO].

[68] E. Komatsu, Class. Quant. Grav. **27**, 124010 (2010), arXiv:1003.6097 [astro-ph.CO].

[69] P. A. R. Ade *et al.* (BICEP, Keck), Phys. Rev. Lett. **127**, 151301 (2021), arXiv:2110.00483 [astro-ph.CO].

[70] S. Chongchitnan and G. Efstathiou, JCAP **01**, 011, arXiv:astro-ph/0611818.

[71] J. Garcia-Bellido and E. Ruiz Morales, Phys. Dark Univ. **18**, 47 (2017), arXiv:1702.03901 [astro-ph.CO].

[72] C. Germani and T. Prokopec, Phys. Dark Univ. **18**, 6 (2017), arXiv:1706.04226 [astro-ph.CO].

[73] B. Carr, M. Raidal, T. Tenkanen, V. Vaskonen, and H. Veermäe, Phys. Rev. D **96**, 023514 (2017), arXiv:1705.05567 [astro-ph.CO].

[74] B. Carr and J. Silk, Mon. Not. Roy. Astron. Soc. **478**, 3756 (2018), arXiv:1801.00672 [astro-ph.CO].

[75] M. Sasaki, T. Suyama, T. Tanaka, and S. Yokoyama, Class. Quant. Grav. **35**, 063001 (2018), arXiv:1801.05235 [astro-ph.CO].

[76] B. Carr and F. Kuhnel, Ann. Rev. Nucl. Part. Sci. **70**, 355 (2020), arXiv:2006.02838 [astro-ph.CO].

[77] B. J. Carr, Astrophys. J. **201**, 1 (1975).

[78] A. M. Green, A. R. Liddle, K. A. Malik, and M. Sasaki, Phys. Rev. **D70**, 041502 (2004), arXiv:astro-ph/0403181 [astro-ph].

[79] C. Germani and I. Musco, Phys. Rev. Lett. **122**, 141302 (2019), arXiv:1805.04087 [astro-ph.CO].

[80] C. Germani and R. K. Sheth, Phys. Rev. D **101**, 063520 (2020), arXiv:1912.07072 [astro-ph.CO].

[81] A. Escrivà, Phys. Dark Univ. **27**, 100466 (2020), arXiv:1907.13065 [gr-qc].

[82] A. Escrivà, C. Germani, and R. K. Sheth, Phys. Rev. D **101**, 044022 (2020), arXiv:1907.13311 [gr-qc].

[83] A. Escrivà, C. Germani, and R. K. Sheth, (2020), arXiv:2007.05564 [gr-qc].

[84] P. Ade *et al.* (Planck), Astron. Astrophys. **594**, A13 (2016), arXiv:1502.01589 [astro-ph.CO].

[85] Z. Arzoumanian *et al.* (NANOGRAV), Astrophys. J. **859**, 47 (2018), arXiv:1801.02617 [astro-ph.HE].

[86] Z. Arzoumanian *et al.* (NANOGrav), Astrophys. J. Lett. **905**, L34 (2020), arXiv:2009.04496 [astro-ph.HE].

[87] N. Bartolo *et al.*, JCAP **12**, 026, arXiv:1610.06481 [astro-ph.CO].

[88] K. N. Ananda, C. Clarkson, and D. Wands, Phys. Rev. **D75**, 123518 (2007), arXiv:gr-qc/0612013 [gr-qc].

[89] D. Baumann, P. J. Steinhardt, K. Takahashi, and K. Ichiki, Phys. Rev. **D76**, 084019 (2007), arXiv:hep-th/0703290 [hep-th].

[90] R. Saito and J. Yokoyama, Phys. Rev. Lett. **102**, 161101 (2009), [Erratum: Phys.Rev.Lett. 107, 069901 (2011)], arXiv:0812.4339 [astro-ph].

[91] R. Saito and J. Yokoyama, Prog. Theor. Phys. **123**, 867 (2010), [Erratum: Prog.Theor.Phys. 126, 351–352 (2011)], arXiv:0912.5317 [astro-ph.CO].

[92] G. Domènech, Int. J. Mod. Phys. D **29**, 2050028 (2020), arXiv:1912.05583 [gr-qc].

[93] N. Bartolo, V. De Luca, G. Franciolini, A. Lewis, M. Peloso, and A. Riotto, Phys. Rev. Lett. **122**, 211301 (2019), arXiv:1810.12218 [astro-ph.CO].

[94] N. Bartolo, V. De Luca, G. Franciolini, M. Peloso, D. Racco, and A. Riotto, Phys. Rev. D **99**, 103521 (2019), arXiv:1810.12224 [astro-ph.CO].

[95] J. R. Espinosa, D. Racco, and A. Riotto, JCAP **1809**, 012, arXiv:1804.07732 [hep-ph].

[96] K. Kohri and T. Terada, Phys. Rev. D **97**, 123532 (2018), arXiv:1804.08577 [gr-qc].

[97] S. L. Bridle, A. M. Lewis, J. Weller, and G. Efstathiou, Mon. Not. Roy. Astron. Soc. **342**, L72 (2003), arXiv:astro-ph/0302306 [astro-ph].

[98] A. Shafieloo and T. Souradeep, Phys. Rev. D **70**, 043523 (2004), arXiv:astro-ph/0312174.

[99] P. Hunt and S. Sarkar, Phys. Rev. D **70**, 103518 (2004), arXiv:astro-ph/0408138.

[100] P. Hunt and S. Sarkar, Phys. Rev. D **76**, 123504 (2007), arXiv:0706.2443 [astro-ph].

[101] D. K. Hazra, A. Shafieloo, and G. F. Smoot, JCAP **1312**, 035, arXiv:1310.3038 [astro-ph.CO].

[102] J. M. Cline, P. Crotty, and J. Lesgourgues, JCAP **0309**, 010, arXiv:astro-ph/0304558 [astro-ph].

[103] C. R. Contaldi, M. Peloso, L. Kofman, and A. D. Linde, JCAP **0307**, 002, arXiv:astro-ph/0303636 [astro-ph].

[104] R. Sinha and T. Souradeep, Phys. Rev. D **74**, 043518 (2006), arXiv:astro-ph/0511808.

[105] B. A. Powell and W. H. Kinney, Phys. Rev. D **76**, 063512 (2007), arXiv:astro-ph/0612006.

[106] D. Boyanovsky, H. J. de Vega, and N. G. Sanchez, Phys. Rev. D **74**, 123007 (2006), arXiv:astro-ph/0607487.

[107] D. Boyanovsky, H. J. de Vega, and N. G. Sanchez, Phys. Rev. D **74**, 123006 (2006), arXiv:astro-ph/0607508.

[108] G. Nicholson and C. R. Contaldi, JCAP **0801**, 002, arXiv:astro-ph/0701783 [astro-ph].

[109] R. K. Jain, P. Chingangbam, and L. Sriramkumar, JCAP **0710**, 003, arXiv:astro-ph/0703762 [astro-ph].

[110] R. K. Jain, P. Chingangbam, J.-O. Gong, L. Sriramkumar, and T. Souradeep, JCAP **0901**, 009, arXiv:0809.3915 [astro-ph].

[111] R. K. Jain, P. Chingangbam, L. Sriramkumar, and T. Souradeep, Phys. Rev. D **82**, 023509 (2010), arXiv:0904.2518 [astro-ph.CO].

[112] D. K. Hazra, A. Shafieloo, G. F. Smoot, and A. A. Starobinsky, Phys. Rev. Lett. **113**, 071301 (2014), arXiv:1404.0360 [astro-ph.CO].

[113] D. K. Hazra, A. Shafieloo, G. F. Smoot, and A. A. Starobinsky, JCAP **1408**, 048, arXiv:1405.2012 [astro-ph.CO].

[114] J. White, Y.-l. Zhang, and M. Sasaki, Phys. Rev. D **90**, 083517 (2014), arXiv:1407.5816 [astro-ph.CO].

[115] M. H. Qureshi, A. Iqbal, M. A. Malik, and T. Souradeep, JCAP **1704**, 013, arXiv:1610.05776 [astro-ph.CO].

[116] S. Pi, Y.-l. Zhang, Q.-G. Huang, and M. Sasaki, JCAP **05**, 042, arXiv:1712.09896 [astro-ph.CO].

[117] E. Ramirez and D. J. Schwarz, Phys. Rev. D **85**, 103516 (2012), arXiv:1111.7131 [astro-ph.CO].

[118] E. Ramirez, Phys. Rev. D **85**, 103517 (2012), arXiv:1202.0698 [astro-ph.CO].

[119] M. Cicoli, S. Downes, B. Dutta, F. G. Pedro, and A. Westphal, JCAP **12**, 030, arXiv:1407.1048 [hep-th].

[120] L. T. Hergt, W. J. Handley, M. P. Hobson, and A. N. Lasenby, Phys. Rev. D **100**, 023502 (2019), arXiv:1809.07185 [astro-ph.CO].

[121] L. T. Hergt, W. J. Handley, M. P. Hobson, and A. N. Lasenby, Phys. Rev. D **100**, 023501 (2019), arXiv:1809.07737 [astro-ph.CO].

[122] A. A. Starobinsky, JETP Lett. **55**, 489 (1992), [Pisma Zh. Eksp. Teor. Fiz.55,477(1992)].

[123] J. S. Horner and C. R. Contaldi, (2013), arXiv:1303.2119 [astro-ph.CO].

[124] W. J. Handley, S. D. Brechet, A. N. Lasenby, and M. P. Hobson, Phys. Rev. **D89**, 063505 (2014), arXiv:1401.2253 [astro-ph.CO].

[125] J. S. Horner and C. R. Contaldi, (2014), arXiv:1407.6948 [astro-ph.CO].

[126] F. Arroja and M. Sasaki, JCAP **1208**, 012, arXiv:1204.6489 [astro-ph.CO].

[127] J. Martin, L. Sriramkumar, and D. K. Hazra, JCAP **1409** (09), 039, arXiv:1404.6093 [astro-ph.CO].

[128] S. Dodelson and L. Hui, Phys. Rev. Lett. **91**, 131301 (2003), arXiv:astro-ph/0305113 [astro-ph].

[129] A. R. Liddle and S. M. Leach, Phys. Rev. D **68**, 103503 (2003), arXiv:astro-ph/0305263.

[130] Y.-F. Cai, J.-O. Gong, D.-G. Wang, and Z. Wang, JCAP **10**, 017, arXiv:1607.07872 [astro-ph.CO].

[131] Y.-F. Cai, X. Chen, M. H. Namjoo, M. Sasaki, D.-G. Wang, and Z. Wang, JCAP **1805**, 012, arXiv:1712.09998 [astro-ph.CO].

[132] V. Sreenath, D. K. Hazra, and L. Sriramkumar, JCAP **1502** (02), 029, arXiv:1410.0252 [astro-ph.CO].

[133] V. Sreenath, R. Tibrewala, and L. Sriramkumar, JCAP **1312**, 037, arXiv:1309.7169 [astro-ph.CO].

[134] V. Sreenath and L. Sriramkumar, JCAP **1410** (10), 021, arXiv:1406.1609 [astro-ph.CO].

[135] P. Creminelli and M. Zaldarriaga, JCAP **0410**, 006, arXiv:astro-ph/0407059 [astro-ph].

[136] C. Cheung, A. L. Fitzpatrick, J. Kaplan, and L. Senatore, JCAP **0802**, 021, arXiv:0709.0295 [hep-th].

[137] M. H. Namjoo, H. Firouzjahi, and M. Sasaki, EPL **101**, 39001 (2013), arXiv:1210.3692 [astro-ph.CO].

[138] J. Martin, H. Motohashi, and T. Suyama, Phys. Rev. D **87**, 023514 (2013), arXiv:1211.0083 [astro-ph.CO].

[139] X. Chen, H. Firouzjahi, M. H. Namjoo, and M. Sasaki, EPL **102**, 59001 (2013), arXiv:1301.5699 [hep-th].

[140] P. Adshead, W. Hu, C. Dvorkin, and H. V. Peiris, Phys. Rev. D **84**, 043519 (2011), arXiv:1102.3435 [astro-ph.CO].

[141] S. Basu, D. J. Brooker, N. C. Tsamis, and R. P. Woodard, Phys. Rev. D **100**, 063525 (2019), arXiv:1905.12140 [gr-qc].

[142] W. Sohn and J. Fergusson, Phys. Rev. D **100**, 063536 (2019), arXiv:1902.01142 [astro-ph.CO].

[143] B. Abbott *et al.* (LIGO Scientific, Virgo), Phys. Rev. Lett. **116**, 131103 (2016), arXiv:1602.03838 [gr-qc].

[144] B. Abbott *et al.* (LIGO Scientific, Virgo), Phys. Rev. D **93**, 122003 (2016), arXiv:1602.03839 [gr-qc].

[145] B. Abbott *et al.* (LIGO Scientific, Virgo), Phys. Rev. Lett. **116**, 241102 (2016), arXiv:1602.03840 [gr-qc].

[146] B. P. Abbott *et al.* (LIGO Scientific, Virgo), Phys. Rev. Lett. **116**, 061102 (2016), arXiv:1602.03837 [gr-qc].

[147] B. P. Abbott *et al.* (LIGO Scientific, Virgo), Phys. Rev. Lett. **116**, 241103 (2016), arXiv:1606.04855 [gr-qc].

[148] B. P. Abbott *et al.* (LIGO Scientific, VIRGO), Phys. Rev. Lett. **118**, 221101 (2017), [Erratum: Phys. Rev. Lett.121,no.12,129901(2018)], arXiv:1706.01812 [gr-qc].

[149] B. P. Abbott *et al.* (LIGO Scientific, Virgo), Astrophys. J. Lett. **851**, L35 (2017), arXiv:1711.05578 [astro-ph.HE].

[150] B. P. Abbott *et al.* (LIGO Scientific, Virgo), Phys. Rev. Lett. **119**, 141101 (2017), arXiv:1709.09660 [gr-qc].

[151] B. P. Abbott *et al.* (LIGO Scientific, Virgo), Phys. Rev. Lett. **119**, 161101 (2017), arXiv:1710.05832 [gr-qc].

[152] R. Abbott *et al.* (LIGO Scientific, Virgo), Phys. Rev. D **102**, 043015 (2020), arXiv:2004.08342 [astro-ph.HE].

[153] B. P. Abbott *et al.* (LIGO Scientific, Virgo), Astrophys. J. Lett. **892**, L3 (2020), arXiv:2001.01761 [astro-ph.HE].

[154] R. Abbott *et al.* (LIGO Scientific, Virgo), Astrophys. J. **896**, L44 (2020), arXiv:2006.12611 [astro-ph.HE].

[155] V. De Luca, G. Franciolini, P. Pani, and A. Riotto, JCAP **06**, 044, arXiv:2005.05641 [astro-ph.CO].

[156] K. Jedamzik, JCAP **09**, 022, arXiv:2006.11172 [astro-ph.CO].

[157] K. Jedamzik, Phys. Rev. Lett. **126**, 051302 (2021), arXiv:2007.03565 [astro-ph.CO].

[158] P. Ade *et al.* (Planck), Astron. Astrophys. **594**, A20 (2016), arXiv:1502.02114 [astro-ph.CO].

[159] G. Ballesteros and M. Taoso, Phys. Rev. D **97**, 023501 (2018), arXiv:1709.05565 [hep-ph].

[160] I. Dalianis, A. Kehagias, and G. Tringas, JCAP **01**, 037, arXiv:1805.09483 [astro-ph.CO].

[161] N. Bhaumik and R. K. Jain 10.1088/1475-7516/2020/01/037 (2019), [JCAP2001,037(2020)], arXiv:1907.04125 [astro-ph.CO].

[162] D. Roberts, A. R. Liddle, and D. H. Lyth, Phys. Rev. D **51**, 4122 (1995), arXiv:astro-ph/9411104.

[163] S. M. Leach and A. R. Liddle, Phys. Rev. D **63**, 043508 (2001), arXiv:astro-ph/0010082.

[164] S. M. Leach, M. Sasaki, D. Wands, and A. R. Liddle, Phys. Rev. D **64**, 023512 (2001), arXiv:astro-ph/0101406.

[165] K. Kannike, L. Marzola, M. Raidal, and H. Veermäe, JCAP **09**, 020, arXiv:1705.06225 [astro-ph.CO].

[166] S. Pi and M. Sasaki, JCAP **09**, 037, arXiv:2005.12306 [gr-qc].

[167] B. P. Abbott *et al.* (LIGO Scientific, Virgo), Phys. Rev. Lett. **118**, 121101 (2017), [Erratum: Phys.Rev.Lett. 119, 029901 (2017)], arXiv:1612.02029 [gr-qc].

[168] M. V. Sazhin, Vestn. Mosk. Univ. Fiz. Astron. **18**, 82 (1977).

[169] S. L. Detweiler, Astrophys. J. **234**, 1100 (1979).

[170] P. Amaro-Seoane *et al.* (LISA), (2017), arXiv:1702.00786 [astro-ph.IM].

[171] E. Barausse *et al.*, Gen. Rel. Grav. **52**, 81 (2020), arXiv:2001.09793 [gr-qc].

[172] J. Crowder and N. J. Cornish, Phys. Rev. D **72**, 083005 (2005), arXiv:gr-qc/0506015.

[173] V. Corbin and N. J. Cornish, Class. Quant. Grav. **23**, 2435 (2006), arXiv:gr-qc/0512039 [gr-qc].

[174] J. Baker *et al.*, (2019), arXiv:1907.11305 [astro-ph.IM].

[175] S. Kawamura *et al.*, *Laser interferometer space antenna. Proceedings, 8th International LISA Symposium, Stanford, USA, June 28-July 2, 2010*, Class. Quant. Grav. **28**, 094011 (2011).

[176] S. Kawamura (DECIGO working group), PoS **KMI2019**, 019 (2019).

[177] M. Punturo *et al.*, *Proceedings, 14th Workshop on Gravitational wave data analysis (GWDAW-14): Rome, Italy, January 26-29, 2010*, Class. Quant. Grav. **27**, 194002 (2010).

[178] B. Sathyaprakash *et al.*, *Gravitational waves. Numerical relativity - data analysis. Proceedings, 9th Edoardo Amaldi Conference, Amaldi 9, and meeting, NRDA 2011, Cardiff, UK, July 10-15, 2011*, Class. Quant. Grav. **29**, 124013 (2012), [Erratum: Class. Quant. Grav.30,079501(2013)], arXiv:1206.0331 [gr-qc].

[179] D. Seery and J. Hidalgo, JCAP **07**, 008, arXiv:astro-ph/0604579.

[180] J. Hidalgo, (2007), arXiv:0708.3875 [astro-ph].

[181] H. Motohashi and W. Hu, Phys. Rev. D **96**, 063503 (2017), arXiv:1706.06784 [astro-ph.CO].

[182] V. Atal and C. Germani, Phys. Dark Univ. **24**, 100275 (2019), arXiv:1811.07857 [astro-ph.CO].

[183] G. Franciolini, A. Kehagias, S. Matarrese, and A. Riotto, JCAP **03**, 016, arXiv:1801.09415 [astro-ph.CO].

[184] A. Kehagias, I. Musco, and A. Riotto, JCAP **12**, 029, arXiv:1906.07135 [astro-ph.CO].

[185] V. Atal, J. Cid, A. Escrivà, and J. Garriga, JCAP **05**, 022, arXiv:1908.11357 [astro-ph.CO].

[186] V. De Luca, G. Franciolini, A. Kehagias, M. Peloso, A. Riotto, and C. Ünal, JCAP **07**, 048, arXiv:1904.00970 [astro-ph.CO].

[187] S. Passaglia, W. Hu, and H. Motohashi, Phys. Rev. D **99**, 043536 (2019), arXiv:1812.08243 [astro-ph.CO].

[188] J. M. Ezquiaga, J. García-Bellido, and V. Vennin, JCAP **03**, 029, arXiv:1912.05399 [astro-ph.CO].

[189] R.-g. Cai, S. Pi, and M. Sasaki, Phys. Rev. Lett. **122**, 201101 (2019), arXiv:1810.11000 [astro-ph.CO].

[190] C. Unal, Phys. Rev. D **99**, 041301 (2019), arXiv:1811.09151 [astro-ph.CO].

[191] R.-G. Cai, S. Pi, S.-J. Wang, and X.-Y. Yang, JCAP **10**, 059, arXiv:1907.06372 [astro-ph.CO].

[192] C. Yuan and Q.-G. Huang, (2020), arXiv:2007.10686 [astro-ph.CO].

[193] M. P. Hertzberg and M. Yamada, Phys. Rev. D **97**, 083509 (2018), arXiv:1712.09750 [astro-ph.CO].

[194] C. T. Byrnes, P. S. Cole, and S. P. Patil, JCAP **06**, 028, arXiv:1811.11158 [astro-ph.CO].

[195] H. Motohashi, S. Mukohyama, and M. Oliosi, JCAP **03**, 002, arXiv:1910.13235 [gr-qc].

[196] R. Allahverdi, K. Enqvist, J. Garcia-Bellido, A. Jokinen, and A. Mazumdar, JCAP **06**, 019, arXiv:hep-ph/0610134.

[197] I. Dalianis and K. Kritos, Phys. Rev. D **103**, 023505 (2021), arXiv:2007.07915 [astro-ph.CO].

[198] O. Özsoy, S. Parameswaran, G. Tasinato, and I. Zavala, JCAP **07**, 005, arXiv:1803.07626 [hep-th].

[199] O. Özsoy and G. Tasinato, JCAP **04**, 048, arXiv:1912.01061 [astro-ph.CO].

[200] C. Gordon, D. Wands, B. A. Bassett, and R. Maartens, Phys. Rev. D **63**, 023506 (2000), arXiv:astro-ph/0009131.

[201] S. Unnikrishnan and L. Sriramkumar, Phys. Rev. D **81**, 103511 (2010), arXiv:1002.0820 [astro-ph.CO].

[202] M. Cicoli, V. A. Diaz, and F. G. Pedro, JCAP **1806** (06), 034, arXiv:1803.02837 [hep-th].

[203] S. Pi, M. Sasaki, and Y.-l. Zhang, JCAP **06**, 049, arXiv:1904.06304 [gr-qc].

[204] G. D'Amico and N. Kaloper, JCAP **08**, 058, arXiv:2011.09489 [hep-th].

[205] G. Tasinato, Phys. Rev. D **103**, 023535 (2021), arXiv:2012.02518 [hep-th].

[206] A. Barnacka, J. F. Glicenstein, and R. Moderski, Phys. Rev. D **86**, 043001 (2012), arXiv:1204.2056 [astro-ph.CO].

[207] A. Katz, J. Kopp, S. Sibiryakov, and W. Xue, JCAP **1812**, 005, arXiv:1807.11495 [astro-ph.CO].

[208] K. Griest, A. M. Cieplak, and M. J. Lehner, Phys. Rev. Lett. **111**, 181302 (2013).

[209] R. Allsman *et al.* (Macho), Astrophys. J. Lett. **550**, L169 (2001), arXiv:astro-ph/0011506.

[210] P. Tisserand *et al.* (EROS-2), Astron. Astrophys. **469**, 387 (2007), arXiv:astro-ph/0607207 [astro-ph].

[211] L. Wyrzykowski *et al.*, Mon. Not. Roy. Astron. Soc. **416**, 2949 (2011), arXiv:1106.2925 [astro-ph.GA].

[212] M. Ricotti, J. P. Ostriker, and K. J. Mack, Astrophys. J. **680**, 829 (2008), arXiv:0709.0524 [astro-ph].

[213] T. D. Brandt, Astrophys. J. **824**, L31 (2016), arXiv:1605.03665 [astro-ph.GA].

[214] A. M. Green and B. J. Kavanagh, J. Phys. G **48**, 043001 (2021), arXiv:2007.10722 [astro-ph.CO].

[215] P. Montero-Camacho, X. Fang, G. Vasquez, M. Silva, and C. M. Hirata, JCAP **1908**, 031, arXiv:1906.05950 [astro-ph.CO].

[216] R. Laha, Phys. Rev. Lett. **123**, 251101 (2019), arXiv:1906.09994 [astro-ph.HE].

[217] B. Dasgupta, R. Laha, and A. Ray, Phys. Rev. Lett. **125**, 101101 (2020), arXiv:1912.01014 [hep-ph].

[218] R. Laha, J. B. Muñoz, and T. R. Slatyer, Phys. Rev. D **101**, 123514 (2020), arXiv:2004.00627 [astro-ph.CO].

[219] J. Coleman (MAGIS-100), PoS **ICHEP2018**, 021 (2019), arXiv:1812.00482 [physics.ins-det].

[220] B. Abbott *et al.* (LIGO Scientific, Virgo), Phys. Rev. D **100**, 061101 (2019), arXiv:1903.02886 [gr-qc].

[221] B. P. Abbott *et al.* (LIGO Scientific), Class. Quant. Grav. **34**, 044001 (2017), arXiv:1607.08697 [astro-ph.IM].

[222] E. Thrane and J. D. Romano, Phys. Rev. D **88**, 124032 (2013), arXiv:1310.5300 [astro-ph.IM].

[223] B. Abbott *et al.* (LIGO Scientific, VIRGO), Nature **460**, 990 (2009), arXiv:0910.5772 [astro-ph.CO].

[224] M. Tsuneto, A. Ito, T. Noumi, and J. Soda, JCAP **03**, 032, arXiv:1812.10615 [gr-qc].

[225] C. Powell and G. Tasinato, JCAP **01**, 017, arXiv:1910.04758 [gr-qc].

[226] L. Iacconi, M. Fasiello, H. Assadullahi, and D. Wands, JCAP **12**, 005, arXiv:2008.00452 [astro-ph.CO].

[227] H. Motohashi, A. A. Starobinsky, and J. Yokoyama, JCAP **09**, 018, arXiv:1411.5021 [astro-ph.CO].

[228] R. Bravo and G. A. Palma, (2020), arXiv:2009.03369 [hep-th].

[229] E. Pajer, JCAP **01**, 023, arXiv:2010.12818 [hep-th].

[230] E. Komatsu and D. N. Spergel, Phys. Rev. D **63**, 063002 (2001), arXiv:astro-ph/0005036.

[231] C. T. Byrnes, E. J. Copeland, and A. M. Green, Phys. Rev. **D86**, 043512 (2012), arXiv:1206.4188 [astro-ph.CO].

[232] M. Taoso and A. Urbano, JCAP **08**, 016, arXiv:2102.03610 [astro-ph.CO].

[233] F. Riccardi, M. Taoso, and A. Urbano, JCAP **08**, 060, arXiv:2102.04084 [astro-ph.CO].

[234] Y. Tada and V. Vennin, JCAP **02**, 021, arXiv:1609.08876 [astro-ph.CO].

[235] T. Suyama, Y. Tada, and M. Yamaguchi, (2020), arXiv:2008.13364 [astro-ph.CO].

[236] S. Matarrese, L. Pilo, and R. Rollo, (2020), arXiv:2007.08877 [astro-ph.CO].

[237] S. S. Mishra and V. Sahni, JCAP **04**, 007, arXiv:1911.00057 [gr-qc].

[238] R.-G. Cai, S. Pi, S.-J. Wang, and X.-Y. Yang, JCAP **05**, 013, arXiv:1901.10152 [astro-ph.CO].

[239] R.-G. Cai, Z.-K. Guo, J. Liu, L. Liu, and X.-Y. Yang, JCAP **06**, 013, arXiv:1912.10437 [astro-ph.CO].

[240] A. Ashoorioon, A. Rostami, and J. T. Firouzjaee, JHEP **07**, 087, arXiv:1912.13326 [astro-ph.CO].

[241] J. Lin, Q. Gao, Y. Gong, Y. Lu, C. Zhang, and F. Zhang, Phys. Rev. D **101**, 103515 (2020), arXiv:2001.05909 [gr-qc].

[242] Z. Yi, Y. Gong, B. Wang, and Z.-h. Zhu, Phys. Rev. D **103**, 063535 (2021), arXiv:2007.09957 [gr-qc].

[243] G. A. Palma, S. Sypsas, and C. Zenteno, Phys. Rev. Lett. **125**, 121301 (2020), arXiv:2004.06106 [astro-ph.CO].

[244] J. Fumagalli, S. Renaux-Petel, J. W. Ronayne, and L. T. Witkowski, (2020), arXiv:2004.08369 [hep-th].

[245] M. Braglia, D. K. Hazra, F. Finelli, G. F. Smoot, L. Sriramkumar, and A. A. Starobinsky, JCAP **08**, 001, arXiv:2005.02895 [astro-ph.CO].

[246] R. Abbott *et al.* (LIGO Scientific, Virgo), Phys. Rev. Lett. **125**, 101102 (2020), arXiv:2009.01075 [gr-qc].

[247] V. Domcke, F. Muia, M. Pieroni, and L. T. Witkowski, JCAP **07**, 048, arXiv:1704.03464 [astro-ph.CO].

[248] P. Pina Avelino, Phys. Rev. D **72**, 124004 (2005), arXiv:astro-ph/0510052.

[249] K. Inomata, M. Kawasaki, K. Mukaida, Y. Tada, and T. T. Yanagida, Phys. Rev. D **96**, 043504 (2017), arXiv:1701.02544 [astro-ph.CO].

[250] N. Bhaumik and R. K. Jain, Phys. Rev. D **104**, 023531 (2021), arXiv:2009.10424 [astro-ph.CO].

[251] V. Atal, J. Garriga, and A. Marcos-Caballero, JCAP **09**, 073, arXiv:1905.13202 [astro-ph.CO].

[252] A. Y. Kamenshchik, A. Tronconi, T. Vardanyan, and G. Venturi, Phys. Lett. **B791**, 201 (2019), arXiv:1812.02547 [gr-qc].

[253] G. Ballesteros, J. Beltran Jimenez, and M. Pieroni, JCAP **06**, 016, arXiv:1811.03065 [astro-ph.CO].

[254] Z. Zhou, J. Jiang, Y.-F. Cai, M. Sasaki, and S. Pi, (2020), arXiv:2010.03537 [astro-ph.CO].

[255] J. Fumagalli, S. Renaux-Petel, and L. T. Witkowski, (2020), arXiv:2012.02761 [astro-ph.CO].

[256] Y.-F. Cai, X. Tong, D.-G. Wang, and S.-F. Yan, Phys. Rev. Lett. **121**, 081306 (2018), arXiv:1805.03639 [astro-ph.CO].

[257] C. Chen and Y.-F. Cai, JCAP **10**, 068, arXiv:1908.03942 [astro-ph.CO].

[258] A. E. Romano, (2020), arXiv:2006.07321 [astro-ph.CO].

[259] B. Carr, K. Dimopoulos, C. Owen, and T. Tenkanen, Phys. Rev. D **97**, 123535 (2018), arXiv:1804.08639 [astro-ph.CO].

[260] S. Bhattacharya, S. Mohanty, and P. Parashari, Phys. Rev. D **102**, 043522 (2020), arXiv:1912.01653 [astro-ph.CO].

[261] R. H. Brandenberger and J. Martin, Int. J. Mod. Phys. A **17**, 3663 (2002), arXiv:hep-th/0202142.

[262] L. Sriramkumar and T. Padmanabhan, Phys. Rev. D **71**, 103512 (2005), arXiv:gr-qc/0408034.

[263] R. Holman and A. J. Tolley, JCAP **05**, 001, arXiv:0710.1302 [hep-th].

[264] P. D. Meerburg, J. P. van der Schaar, and P. S. Corasaniti, JCAP **05**, 018, arXiv:0901.4044 [hep-th].

[265] P. Meerburg, J. P. van der Schaar, and M. G. Jackson, JCAP **02**, 001, arXiv:0910.4986 [hep-th].

[266] I. Agullo and L. Parker, Phys. Rev. D **83**, 063526 (2011), arXiv:1010.5766 [astro-ph.CO].

[267] P. Meerburg, R. Wijers, and J. P. van der Schaar, Mon. Not. Roy. Astron. Soc. **421**, 369 (2012), arXiv:1109.5264 [astro-ph.CO].

[268] J. Ganc, Phys. Rev. D **84**, 063514 (2011), arXiv:1104.0244 [astro-ph.CO].

[269] S. Kundu, JCAP **02**, 005, arXiv:1110.4688 [astro-ph.CO].

[270] R. H. Brandenberger and J. Martin, Class. Quant. Grav. **30**, 113001 (2013), arXiv:1211.6753 [astro-ph.CO].

[271] S. Kundu, JCAP **04**, 016, arXiv:1311.1575 [astro-ph.CO].

[272] A. Shukla, S. P. Trivedi, and V. Vishal, JHEP **12**, 102, arXiv:1607.08636 [hep-th].

[273] K. H. Seleim, A. A. El-Zant, and A. Abdel-Moneim, Phys. Rev. D **102**, 063505 (2020), arXiv:2002.06656 [astro-ph.CO].

[274] S. Clesse and J. García-Bellido, Phys. Rev. D **92**, 023524 (2015), arXiv:1501.07565 [astro-ph.CO].

[275] A. D. Gow, C. T. Byrnes, and A. Hall, Phys. Rev. D **105**, 023503 (2022), arXiv:2009.03204 [astro-ph.CO].

[276] J. Garcia-Bellido, M. Peloso, and C. Unal, JCAP **1709** (09), 013, arXiv:1707.02441 [astro-ph.CO].

[277] C. Ünal, E. D. Kovetz, and S. P. Patil, Phys. Rev. D **103**, 063519 (2021), arXiv:2008.11184 [astro-ph.CO].

[278] S. Shankaranarayanan and L. Sriramkumar, Phys. Rev. D **70**, 123520 (2004), arXiv:hep-th/0403236.

[279] U. H. Danielsson, Phys. Rev. D **66**, 023511 (2002), arXiv:hep-th/0203198.

[280] J. Martin and C. Ringeval, Phys. Rev. D **69**, 083515 (2004), arXiv:astro-ph/0310382.

[281] J. Martin and C. Ringeval, JCAP **01**, 007, arXiv:hep-ph/0405249.

[282] S. Hashiba and Y. Yamada, JCAP **05**, 022, arXiv:2101.07634 [hep-th].

[283] M. Braglia, X. Chen, and D. K. Hazra, JCAP **03**, 005, arXiv:2012.05821 [astro-ph.CO].

[284] G. N. Felder, L. Kofman, and A. D. Linde, JHEP **02**, 027, arXiv:hep-ph/9909508.

[285] L. Wang and A. Mazumdar, JCAP **05**, 012, arXiv:1302.2637 [astro-ph.CO].

[286] S. Lu, Y. Wang, and Z.-Z. Xianyu, JHEP **02**, 011, arXiv:1907.07390 [hep-th].

[287] J. S. Schwinger, Phys. Rev. **82**, 664 (1951).

[288] J. Audretsch and G. Schaefer, J. Phys. A **11**, 1583 (1978).

[289] M. Porrati, Phys. Lett. B **596**, 306 (2004), arXiv:hep-th/0402038.

[290] H. Collins and R. Holman, Phys. Rev. D **74**, 045009 (2006), arXiv:hep-th/0605107.

[291] A. Albrecht, N. Bolis, and R. Holman, (2018), arXiv:1806.00392 [hep-th].

[292] B. Allen and A. Folacci, Phys. Rev. D **35**, 3771 (1987).

[293] P. R. Anderson, W. Eaker, S. Habib, C. Molina-Paris, and E. Mottola, Phys. Rev. D **62**, 124019 (2000), arXiv:gr-qc/0005102.

[294] A. Bedroya, R. Brandenberger, M. Loverde, and C. Vafa, Phys. Rev. D **101**, 103502 (2020), arXiv:1909.11106 [hep-th].

[295] P. Adshead, K. D. Lozanov, and Z. J. Weiner, JCAP **10**, 080, arXiv:2105.01659 [astro-ph.CO].

[296] T. Nakama, J. Silk, and M. Kamionkowski, Phys. Rev. D **95**, 043511 (2017), arXiv:1612.06264 [astro-ph.CO].

[297] D. Seery and J. E. Lidsey, JCAP **01**, 008, arXiv:astro-ph/0611034.

[298] V. Atal and G. Domènech, JCAP **06**, 001, arXiv:2103.01056 [astro-ph.CO].

[299] F. Zhang, J. Lin, and Y. Lu, Phys. Rev. D **104**, 063515 (2021), arXiv:2106.10792 [gr-qc].

[300] J. M. Ezquiaga, J. Garcia-Bellido, and E. Ruiz Morales, Phys. Lett. B **776**, 345 (2018), arXiv:1705.04861 [astro-ph.CO].

[301] F. Bezrukov, M. Pauly, and J. Rubio, JCAP **02**, 040, arXiv:1706.05007 [hep-ph].

[302] M. Drees and Y. Xu, Eur. Phys. J. C **81**, 182 (2021), arXiv:1905.13581 [hep-ph].

[303] F. Schmidt and M. Kamionkowski, Phys. Rev. D **82**, 103002 (2010), arXiv:1008.0638 [astro-ph.CO].

[304] I. Agullo, D. Kranas, and V. Sreenath, Front. Astron. Space Sci. **8**, 703845 (2021), arXiv:2105.12993 [gr-qc].

[305] K. Inomata, M. Kawasaki, K. Mukaida, Y. Tada, and T. T. Yanagida, Phys. Rev. D **95**, 123510 (2017), arXiv:1611.06130 [astro-ph.CO].

[306] J. Chluba, A. L. Erickcek, and I. Ben-Dayan, Astrophys. J. **758**, 76 (2012), arXiv:1203.2681 [astro-ph.CO].

[307] D. Jeong, J. Pradler, J. Chluba, and M. Kamionkowski, Phys. Rev. Lett. **113**, 061301 (2014), arXiv:1403.3697 [astro-ph.CO].

[308] T. Kite, A. Ravenni, S. P. Patil, and J. Chluba, Mon. Not. Roy. Astron. Soc. **505**, 4396 (2021), arXiv:2010.00040 [astro-ph.CO].

[309] J. Chluba *et al.*, Exper. Astron. **51**, 1515 (2021), arXiv:1909.01593 [astro-ph.CO].

[310] P. Adshead, N. Afshordi, E. Dimastrogiovanni, M. Fasiello, E. A. Lim, and G. Tasinato, Phys. Rev. D **103**, 023532 (2021), arXiv:2004.06619 [astro-ph.CO].

[311] A. Malhotra, E. Dimastrogiovanni, M. Fasiello, and M. Shiraishi, JCAP **03**, 088, arXiv:2012.03498 [astro-ph.CO].

[312] G. Orlando, P. D. Meerburg, and S. P. Patil, (2021), arXiv:2109.01095 [astro-ph.CO].

[313] S. Young, I. Musco, and C. T. Byrnes, JCAP **1911** (11), 012, arXiv:1904.00984 [astro-ph.CO].

[314] R. Ansari *et al.* (Cosmic Visions 21 cm), (2018), arXiv:1810.09572 [astro-ph.CO].

[315] A. Weltman *et al.*, Publ. Astron. Soc. Austral. **37**, e002 (2020), arXiv:1810.02680 [astro-ph.CO].

[316] X. Chen, P. D. Meerburg, and M. Münchmeyer, JCAP **09**, 023, arXiv:1605.09364 [astro-ph.CO].

[317] D. Karagiannis, J. Fonseca, R. Maartens, and S. Camera, Phys. Dark Univ. **32**, 100821 (2021), arXiv:2010.07034 [astro-ph.CO].

[318] M. Aich, D. K. Hazra, L. Sriramkumar, and T. Souradeep, Phys. Rev. D **87**, 083526 (2013), arXiv:1106.2798 [astro-ph.CO].